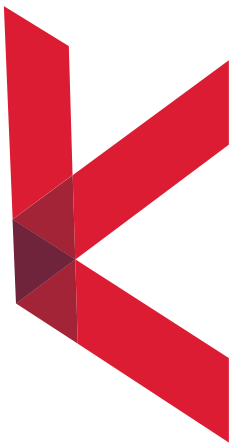

Brno University of Technology
Faculty of Mechanical Engineering
Institute of Machine and Industrial Design

Vysoké učení technické v Brně
Fakulta strojního inženýrství
Ústav konstruování

# COMPUTATIONAL MODELS FOR NON-LINEAR MECHANICAL LOADING ANALYSES OF LATTICE STRUCTURES MADE BY LASER POWDER BED FUSION

## VÝPOČTOVÉ MODELY PRO NELINEÁRNÍ ANALÝZY ZATĚŽOVÁNÍ MIKRO-PRUTOVÝCH STRUKTUR VYROBENÝCH TECHNOLOGIÍ LASEROVÉ FÚZE S PRÁŠKOVÝM LOŽEM

**Ing. Ondřej Červinek**
Author
Autor práce

**doc. Ing. Daniel Koutný, Ph.D.**
Supervisor
Vedoucí práce

Dissertation Thesis
Dizertační práce

Brno 2022


Brno University of Technology
Faculty of Mechanical Engineering
Institute of Machine and Industrial Design

Vysoké učení technické v Brně
Fakulta strojního inženýrství
Ústav konstruování

# COMPUTATIONAL MODELS FOR NON-LINEAR MECHANICAL LOADING ANALYSES OF LATTICE STRUCTURES MADE BY LASER POWDER BED FUSION

VÝPOČTOVÉ MODELY PRO NELINEÁRNÍ ANALÝZY ZATĚŽOVÁNÍ MIKRO-PRUTOVÝCH STRUKTUR VYROBENÝCH TECHNOLOGIÍ LASEROVÉ FÚZE S PRÁŠKOVÝM LOŽEM

**Ing. Ondřej Červinek**
Author
Autor práce

**doc. Ing. Daniel Koutný, Ph.D.**
Supervisor
Vedoucí práce

Dissertation Thesis
Dizertační práce

Brno 2022

# STATEMENT

I hereby declare that I have written the PhD thesis *Computational models for non-linear mechanical loading analyses of lattice structures made by laser powder bed fusion* on my own according to advice of my supervisor doc. Ing. Daniel Koutný, Ph.D., and using the sources listed in the references.

Brno, _____ .....

Ing. Ondřej Červinek

# BIBLIOGRAPHICAL REFERENCE

ČERVINEK, O. *Computational models for non-linear mechanical loading analyses of lattice structures made by powder laser bed fusion*. Brno, 2022, 160 p. PhD thesis. Brno University of Technology, Faculty of Mechanical Engineering, Institute of Machine and Industrial Design. Supervisor: doc. Ing. Daniel Koutny, Ph.D.

# ACKNOWLEDGEMENT

I would like to thank all people who supported me during my doctoral studies. First, I want to mention my supervisor doc. Daniel Koutný, Ph.D., who guided me through the entire period of my Ph.D. studies. Further, I would like to thank my colleagues from the RIAT group who stand with me side by side in good times and bad times. I want to thank to my colleagues at TU Wien who made friendly workplace for me and taught me a lot. Thank to doc. David Paloušek, Ph.D. for his advice. Many thanks to my family, friends and especially to my girlfriend for support. Without you finishing my studies would not be possible.

# ABSTRACT

The development of additive technologies in recent years has enabled the manufacturing of metamaterials with porous internal architecture, called lattice structures, from several types of metal alloys. With these structures, it is possible to develop lightweight parts with potential in the field of mechanical energy absorption. Their implementation in vehicle deformation zones can increase the safety of passengers. The properties of structures allow to design absorbers with specific type of behavior which reduce the overload applied on the vehicle crew during an accident. To use these parts for specific applications, it is necessary to estimate their deformational behavior. Recent research has shown that the parent material of these structures has properties different from those of conventional bulk components produced by the same technologies. It means that, for efficient use of lattice structures, their specific properties and deformation characteristics must be accurately mathematically described. However, a mathematical model that would consider a description of all significant deformation characteristics of lattice structures is not available. Therefore, this thesis focuses on development of non-linear numerical model of lattice structures loading with inclusion of the most significant geometrical imperfections, specific properties of multi-strut samples and dynamic effects. The structures are made of aluminum alloy $AlSi_{10}Mg$ and stainless steel 316L using the selective laser melting technology. Two different finite element analysis approaches are used to create the geometry model that allows inspection of the deformation features in detail. The results of both models confirm that geometrical imperfections related to a change in shape and cross-sectional area of the strut have a significant impact on the resulting mechanical properties. Their inclusion in the geometry model improves the accuracy of the simulation results. Furthermore, the mechanical properties of lattice structures determined by multi-strut samples significantly better represent properties of structures for quasi-static and dynamic loading. The final parameter verification simulation of lattice structures loading at several velocities shows good agreement between the experiment and the computational solution. A similar parametrical study can lead to the finding of efficient structure configurations determined for a specific amount of absorbed energy without prior manufacturing and testing.

# KEYWORDS

Non-linear finite element analysis, Split Hopkinson bars test, laser powder bed fusion, lattice structures, geometrical imperfections

# ABSTRAKT

Rozvoj aditivních technologií v posledních letech umožnil výrobu meta materiálů s porézní vnitřní architekturou zvaných mikro-prutové struktury z několika typů kovových slitin. Za pomoci těchto struktur je možné vyvíjet lehké komponenty s potenciálem v oblasti absorpce mechanické energie. Jejich implementací do deformačních zón vozidel může být docíleno zvýšení bezpečnosti posádky. Vlastnosti mikro-prutových struktur umožňují navrhnout absorbéry se specifickým typem chování, které redukuje přetížení působící na posádku vozidla v případě nehody. Pro využití těchto dílů pro specifické aplikace je nutné odhadnout jejich deformační chování. Nedávný výzkum ukázal, že základový materiál těchto struktur má odlišné vlastnosti v porovnání s konvenčními objemovými komponentami vyrobenými stejnou technologií. To znamená, že pro efektivní využití mikro-prutových struktur je zapotřebí matematicky přesně popsat jejich specifické vlastnosti a deformační charakteristiky. Nicméně matematický model, který by zahrnoval popis všech významných charakteristik deformace mikro-prutových struktur, není k dispozici. Proto se tato práce zaměřuje na vývoj nelineárního numerického modelu zatěžování mikro-prutových struktur se zahrnutím efektů spojených s nejvýznamnějšími geometrickými imperfekcemi, specifickými vlastnostmi multi-prutových vzorků a dynamickými efekty. Struktury jsou vyrobeny z hliníkové slitiny $AlSi_{10}Mg$ a nerezové oceli 316L s využitím technologie selektivního laserového tavení. Dva odlišné přístupy jsou použity k vytvoření modelu geometrie, což umožňuje detailní inspekci deformačního charakteru. Výsledky obou modelů potvrzují, že geometrické imperfekce spojené se změnou tvaru a velikosti průřezu prutu mají významný vliv na výsledné mechanické vlastnosti. Jejich zahrnutí do modelu geometrie zvyšuje přesnost výsledků simulace. Navíc mechanické vlastnosti mikro-prutových struktur stanovené pomocí multi-prutových vzorků výrazně lépe representují vlastnosti struktur pro kvazistatické i dynamické zatěžování. Finální parametrická ověřovací simulace zatěžování mikro-prutové struktury při několika rychlostech ukazuje dobrou shodu experimentu a výpočtového řešení. Podobná parametrická studie může v budoucnu vést k nalezení efektivních strukturovaných konfigurací pro specifické množství absorbované energie bez předchozí výroby a testování.

# KLÍČOVÁ SLOVA

Nelineární analýza metody konečných prvků, test Hopkinsonových dělených tyčí, laserová fúze s práškovým ložem, mikro-prutové struktury, geometrické imperfekce

# CONTENT

# 1 INTRODUCTION

For fast energy absorption, e.g., in vehicle crashes, plastically deformed absorbers are used from specially shaped profiles made of mild steels and aluminum alloys. Their main purpose is the dissipation of kinetic energy during impact. Changes in shape and material allow tailoring of absorbers for a specific application. Their implementation in vehicle deformation zones increases the safety of the crew in case of an accident. However, customization of specially shaped profiles has certain limitations given by manufacturing technology.

Highly specialized applications use components precisely designed for a specific kind of deformation. In this category, a porous metamaterial with regularly repeated architecture can be included. These are, for example, aluminum foams or structures of honeycomb type. Metamaterials with internal architecture include a large volume fraction of pores (75-95%), which in the event of impact loading serves as a flexible damper and increases energy absorption capacity. However, these components are usually limited to a specific amount of energy absorbed and cannot be adapted for wide range of deformation loads.

The solution provides structures with internal architecture produced by additive technologies, e.g., selective laser melting (SLM). Using SLM technology allows to efficiently combine multiple absorption characteristics by geometry changes like gradient volume fraction. The precise control of the structure shape enables tuning associated mechanical properties. As a result, components that protect passengers against collisions of varying intensity can be produced. Multifunctional absorbers with enhanced energy absorption capabilities can be designed for better adaptation to different types of car accidents. Furthermore, a large freedom of shapes in the internal architecture with a lightweight design can be obtained. Compared to metal foams, a wider range of metallic materials, such as titanium alloys ($Ti_6Al_4V$) or tool steels (1.2709), can be processed.

To effectively design and use lattice structures for energy absorption, it is necessary to mathematically describe their deformation behavior. This description can be done with analytical equations or, more efficiently, with computational software based on finite element methods (FEM). Research has shown that these structures have a specific type of behavior compared to bulk components. Therefore, to obtain a description of the behavior of the lattice structures, it is necessary to define specific input parameters of the material model, geometry and boundary conditions (contacts) involving non-linear effects. A precise numerical model that would reflect the influence of non-linearities of all types and at the same time the effect of imperfections and dynamic loading has not been the subject of studies yet. Therefore, this dissertation focuses on the development of a model that builds on existing knowledge in the field of FEM models and combines all the aspects described above. It allows to obtain precise estimation of lattice structure properties under dynamic loading similar to those during vehicle crash. As a result, energy absorbers with a graduated deformation pattern can be achieved, which reduces the applied overload on the passenger.

# 2 STATE OF THE ART

Specially shaped profiles made of metal sheets and tubes are frequently used to absorb mechanical energy in deformation zones of vehicles in the transport industry. A suitable shaping of their geometry can increase the amount of energy that the absorber is able to dissipate during its deformation [1–3]. However, this procedure has limitations [4, 5]. Changing shape can rapidly increase stiffness. It leads to a stepwise change in force at the beginning of the plastic deformation, causing a force peak (stress peak respectively $\sigma_{peak}$; see Fig. 2-1) [6]. This force reaction peak is undesirable because it indicates step deformation deceleration, leading to a steep overload that can endanger the vehicle crew.

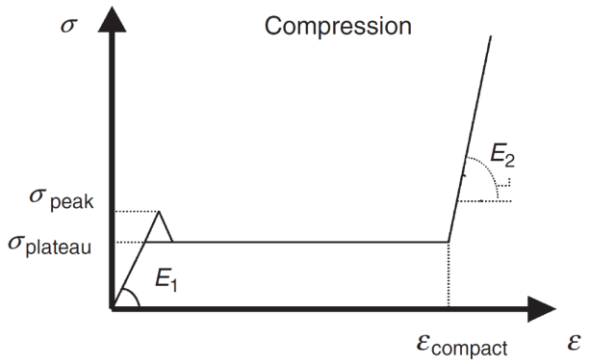


Fig. 2-1 Idealized stress-strain curve of lattice structure compression [6]

New applications combine these conventional absorbers with porous metamaterials [7–10] to increase their absorption capabilities and reduce the force peak [11, 12]. In the optimal course of deformation, a smooth transition from the elastic to the uniform plastic deformation area can be observed. The plastic deformation should have uniform plateau character $\sigma_{plateau}$ and last until the compaction $\varepsilon_{compact}$ of the porous material (see Fig. 2-2) [13]. This area, sometimes described as the area of progressive collapse, is most significant in active absorption. The engineering stress in this phase should be constant or possibly monotonically increasing [14]. It should be followed by a material densification area where the absorber is no longer able to efficiently dissipate energy. Some of the current metal foams approximate this model [15].

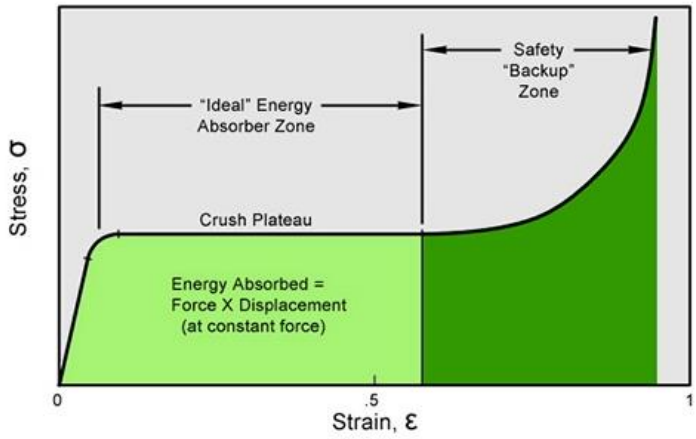


Fig. 2-2 Optimal stress-strain dependence of the energy absorber [16]

The development of additive technologies in recent years allowed the use of new types of porous materials that have potential in applications considering the absorption of mechanical energy [17–19]. These are lattice structures produced by SLM technology [13, 20]. Comparison of lattice structures with conventional porous materials such as extruded honeycomb and aluminum foams showed [21, 22] that they can achieve similar potential in the field of mechanical energy absorption. Furthermore, a wide range of materials can be used to produce these structures (SS316L [13], $Ti_6V_4Al$ [23], $AlSi_{10}Mg$, $AlSi_7Mg_{0.6}$ [24, 25]. The geometry of the lattice structures can be controlled relatively precisely by several parameters and designed for the desired type of deformation, or the amount of energy absorbed [18, 26]. It allows the tailoring of highly specialized parts which dissipate a specific energy shock with the required characteristics of deformation behavior.

For an efficient estimation of the lattice structure properties, it is necessary to perform a detailed FEM analysis that includes quasi-static and dynamic loading [27, 28]. The model must contain knowledge about the properties of the structures obtained by mechanical testing [22]. It includes tensile and compression tests of the lattice structure material performed at several strain-rates [21].

Software that works with implicit and explicit FEM solvers is used for simulations of lattice structure deformation behavior [29–32]. These analyzes are based on the computational solution of the interactions of solid bodies or shock waves with structured blocks, which reflect the conditions of the experiments [33]. Using simulations allows to make changes of the geometry (material) model and observe their impact on the behavior of the structure with minimizing the production efforts.

The following studies describe different types of non-linear computational FEM analysis development, including the determination of the input parameters of the material model, the geometry model, and the initial and boundary conditions. For this type of analysis, the influence of the non-linearities of material, geometry and contact conditions must be considered. The inclusion of these non-linearities together with the precise definition of the geometry allows to achieve numerical predictions of the structure's deformation behavior with high accuracy.

## 2.1 Computational approaches and models of geometry

Luxner et al. [34–36] published pioneering studies in the field of the deformation behavior of lattice structures produced by additive technologies. The studies focused on quasi-static uniaxial compression loading of several structures produced by stereolithography (SLA; a blend of acrylates and epoxy-based resins) and selective laser sintering (SLS; polyamide powder). The simulation approaches were compared with those of the experiment, especially in terms of the structure modulus of elasticity.

The first approach used the geometry model described by 3D beam elements with a quadratic interpolation function based on Timoshenko beam theory. It allowed for consideration of large deformations, bending stresses, transverse shear deformations, and tensile stresses. The model was computationally cheap, but its accuracy was reduced because of several simplifications. The contact of the beam struts in the nodes was reduced to a single point, which did not fully reflect the actual contact conditions. For this reason, a stiffness correction was introduced in the vicinity of the nodes using elements with artificially increased stiffness (1000 times higher). At least four elements were used to discretize each strut between two nodal regions. Twenty-four Gaussian integration points were used across the beam cross-section (eight points around the circumference times three in the radial direction).

The second approach used a model for detailed representation created with tetrahedron solid elements with a quadratic interpolation function. It allowed the study of a high-resolved stress and strain field in the vicinity of the nodes. The element edge length was not larger than 1/6 of the strut diameter (1/12 in the nodes). The high number of degrees of freedom led to a computationally expensive simulation with significant limitations in the model size.

A comparison of simulations for different loading directions showed significantly lower values of the structure's normalized modulus of elasticity $E^*/E^s$ for the approach using beam elements without stiffness correction (see Fig. 2-3 (a), Finite, without adapt. beams) [35]. In contrast, the simulation that considered beam elements with stiffness correction (Finite, adapt. beams) was close to the computational model with volume elements, which was considered as a reference (unit cell, continuum elements). A comparison of computational models with the experiment for the most of tested structures produced by both technologies showed good agreement (see Fig. 2-3 (b)).

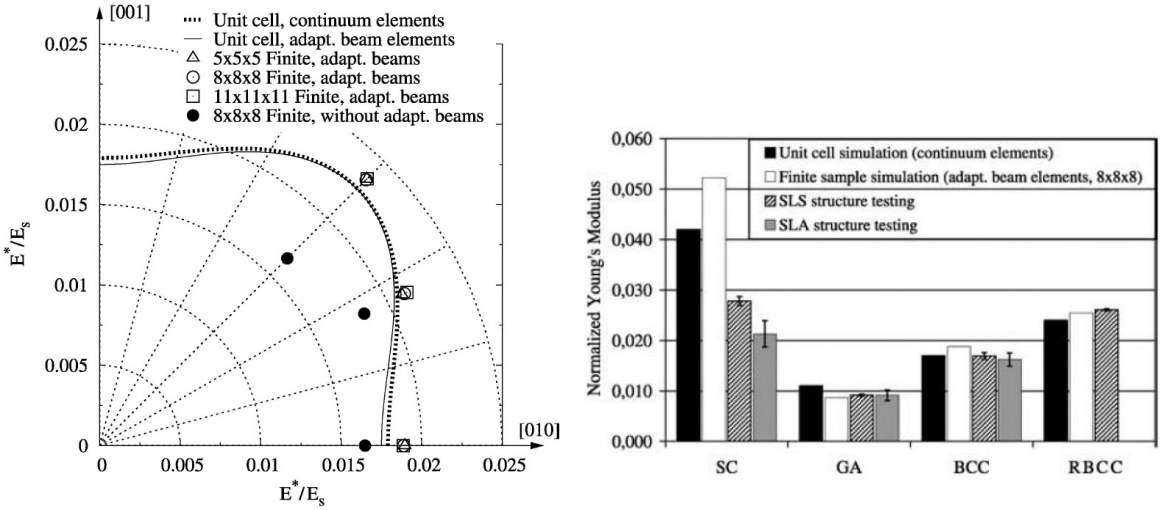


(a) (b)

Fig. 2-3 Comparison of (a) simulations in terms of normalized modulus of elasticity for the BCC structure; (b) uniaxial pressure experiment and simulation for Simple Cubic (SC), Gibson Ashby (GA), BCC and Reinforced BCC structure [35]

Labeas et al. [6] continued with simulations of dynamic loading of lattice structures. Two numerical models were developed to predict the deformation of the BCC structure under low-velocity loading up to 5 $m \cdot s^{-1}$ (316L made by SLM). The first type used beam elements BEAM 188 based on Timoshenko beam theory with quadratic shape function suitable for problems that involved geometrical non-linearities and plasticity. The circular strut cross-section was divided into sixteen circumferential areas with four integration points per area. To compensate for a higher material concentration around the strut junction points, the strut cross-section was increased by 40% on 1/10 of the strut length. The simulation of the drop test was performed in an explicit solver with the following conditions:

- Four beam elements per strut were used for heavily loaded areas.
- For less loaded areas, two beam elements per strut were used.
- The edge plates were meshed with SHELL 163 four-node layered shell elements of the degenerated biphase type. It allows for the bending and tearing of the plates under impact force.
- A self-intersecting contact was defined for the struts of the structure.

- Node-surface contact was defined between the indenter and the top plate in the impact region.

The second type replaced the lattice structure with eight-node brick elements SOLID 164 with *x*, *y* and *z* degrees of freedom referring to translations, velocities, and acceleration suitable for explicit analysis [13]. The method was called homogenization – the model provided the solution to complex contact problems of structure's interactions with foreign bodies under dynamic loading (see Fig. 2-4 (a)).

A comparison of the simulations and the experiment (see Fig. 2-4 (b)) showed that the beam element model can better reflect the experiment (Detailed FE model). The model appeared to be suitable for studying the mechanisms of structural damage, stiffness, and strength of the struts. On the contrary, the model with homogenized structure representation (Homogenized core FE model) suffered from significant inaccuracies caused by nonrealistic structure deformation.

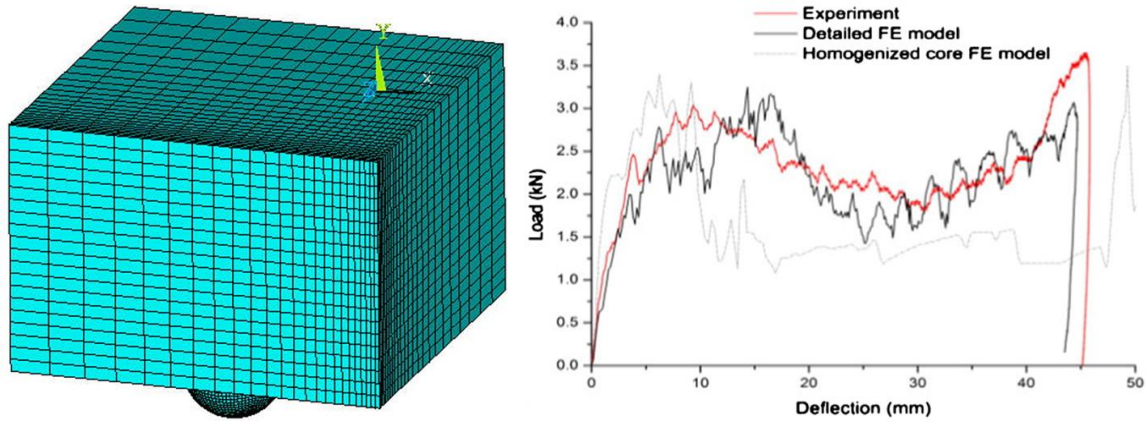


(a) (b)

Fig. 2-4 (a) polygonal mesh of homogenized structure; (b) numerical and experimental load-deflection curves of BCC structure for 99 J impact [13]

Ravari et al. [37] presented a novel approach to include geometrical imperfections for the BCCz structure produced by fused deposition modeling (FDM) made of polylactid acid (PLA). The method used the Python 6.6.6 script to create a geometry model. The first model used 3D shear deformable beam elements B32 with quadratic interpolation function. The second model used second-order tetrahedral elements C3D10M to capture the complex geometry of the struts, especially at the nodal points (see Fig. 2-5 (a)). Both models considered the circular strut cross-section with the trapezoidal rule applied for integration points (three in the radial direction and eight in the circumferential direction).

The script split each strut into the required number of equivalent sections, which allowed to change the diameter independently for each section. The average diameters of the struts were changed according to the probability index assigned for each section of the strut (see Fig. 2-5 (b)). The diameter assignment was based on a pseudorandom distribution of the specific values range from previous measurements. To capture the effect of material concentration on the nodes, the diameter of the struts near the nodes was assigned to the four largest diameter ranges.

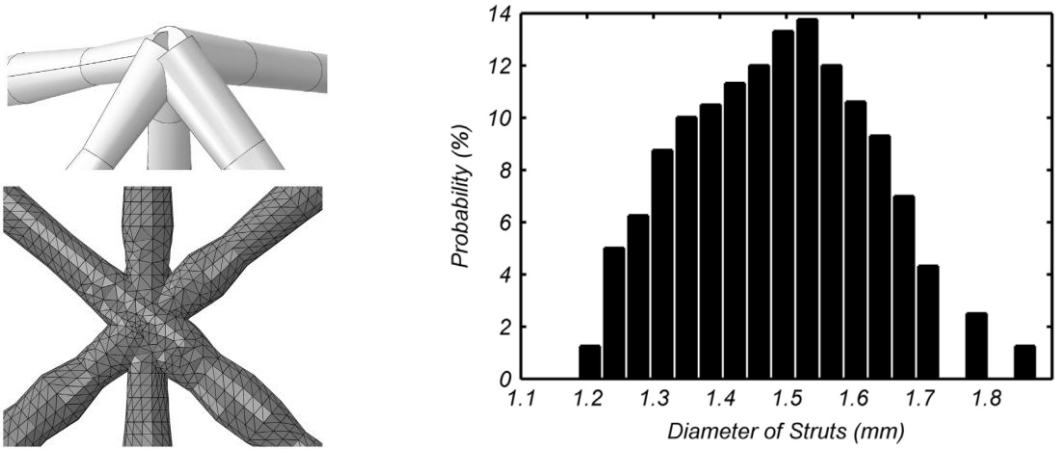


(a) (b)

Fig. 2-5 (a) overlaps of the beam and solid element struts at a conjunction; (b) probabilities for diameter of struts [37]

The comparison showed that the model with solid elements was closer to the experimental results than the model with beam elements. The same result was observed for both, constant and variable cross-sections. At least ten intervals with variable diameters were required to obtain a valid value of the modulus of elasticity or deformation stress according to the sensitivity study.

Persistent problems with node connectivity were investigated by Dong et al. [38], who tried to model strut connections using the so-called joint stiffening concept for Cubic-centered and Vintiles structures. The proposed method was applied to determine the effect of joint connections and stiffness of the struts produced from acrylonitrile butadiene styrene (ABS) by FDM. At first, each strut was divided into three segments meshed with four-node tetrahedrons C3D4 (very stiff, one integration point) and 3D two-node beam B31 (linear interpolation function) elements. The segments at the ends of the strut were represented by joint elements (see Fig. 2-6). The middle segment represented the actual length of the strut reduced by the radii of the nodes. The stiffness matrix of the proposed element was derived by rearranging the displacement and the load vector. Some parameters, e.g., the diameter of the strut, were parametrically changed to achieve the required rigidity of the proposed joint element. A self-contained beam element solver was written in Matlab with integrated joint stiffening parameters to solve the proposed model.

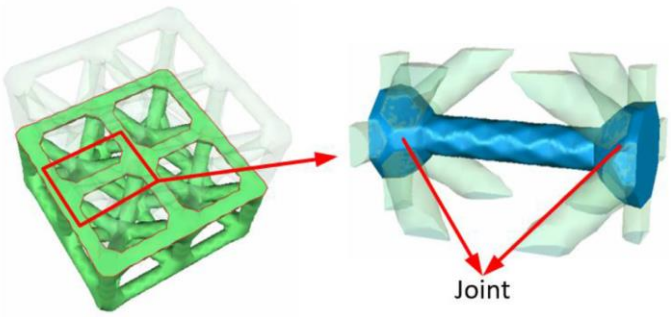


Fig. 2-6 The geometrical model of the joint stiffening element inside a lattice structure [38]

The experimental and computational approaches were compared for uniaxial tensile and bending loading. The results showed that the model with the proposed joint connection with parametrically changed properties can better reflect the actual stiffness of the lattice structure even for beam elements [39]. Better compliance with the results was observed for stretching-dominated structures, where axial loads played a significant role, and the joint stiffening effect was not that significant.

Geng et al. [40] tried to reduce computational effort using beam elements (Timoshenko – shear flexible) but preserve the level of accuracy achievable for solid elements (C3D10 second-order tetrahedral). The study was carried out as an investigation of the deformation behavior of the rhombic dodecahedron and BCCz lattice structures made of $AlSi_{10}Mg$ alloy by SLM technology. A geometry model was created by a combination of both types of elements. By replacing the beam elements of a specific unit cell in the middle of the structure with solid elements, a hybrid model was created. It allowed to make local changes in the geometry of the struts and closely monitor their effects on the stress response (see Fig. 2-7). To connect the beam elements with the solid elements, a bond called a multipoint constraint was used (MPC – allowed constraint to be imposed between different degrees of freedom; can be non-linear or nonhomogeneous), which reflected the actual conditions of the strut connection. Depending on the structure, each strut was divided into 3, 4 or 6 elements.

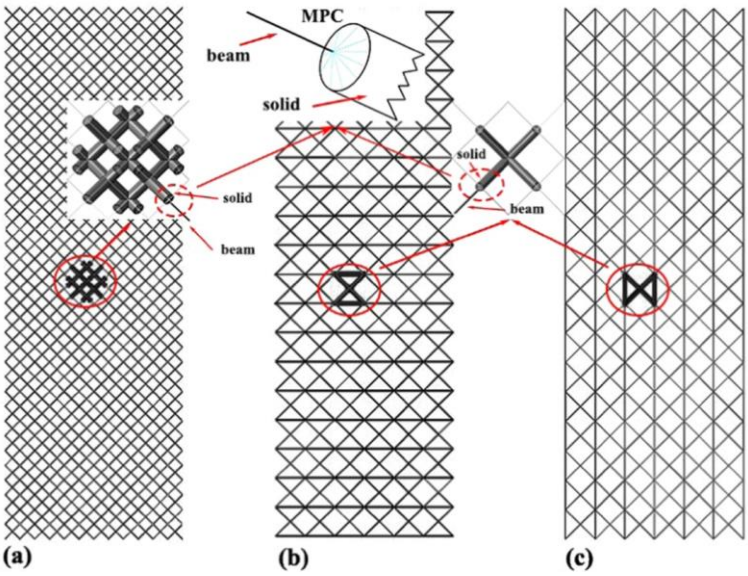


Fig. 2-7 Combined models of geometry (a) rhombic dodecahedron; (b) BCCz1; (c) BCCz2 [40]

The comparison of the experiment and the hybrid simulation showed good agreement not only in the modulus of elasticity but also for plastic deformation. The unit cell meshed with solid elements did not affect the overall behavior of the loaded structure. Small differences between the experiment and the calculations were attributed to geometric imperfections of lattice manufacturing that were not included in the analyzes.

Lei et al. [41] took the next step in the inclusion of different geometric imperfections in the computational model of quasi-static compression loading of lattice structures produced by SLM (BCC and BCCz structures made of $AlSi_{10}Mg$). Structures were subjected to micro-computed tomography (μ-CT) to capture actual information about the geometry of the struts [42]. The results of the μ-CT analysis showed that the diameter of the strut changed with its location in the structure and the manufacturing angle (similar to the findings of Koutny et al.) [43]. For each strut, 160 cross-sections were measured perpendicular to the axis. The boundary shape of the cross-section was fitted with a circle using the least squares' method [44]. The measured diameters showed significant deviations along the length compared to the designed CAD data.

The models were prepared with an automatic Python script that served to generate lattice structure models using 3D B31 beam elements (see Fig. 2-8) [37]. The first computational approach was used with idealized strut diameters according to the original CAD design. The second approach used the average strut diameter value based on statistical processing of the μ-CT scanned data. Another method considered pseudo-random assignment according to the Gaussian distribution of diameters for individual segments similar to Ravari et al. [37]. Furthermore, the strut diameter was defined based on reconstructed μ-CT scans and the fitting function with fast Fourier transformation (FFT, see Fig. 2-9).

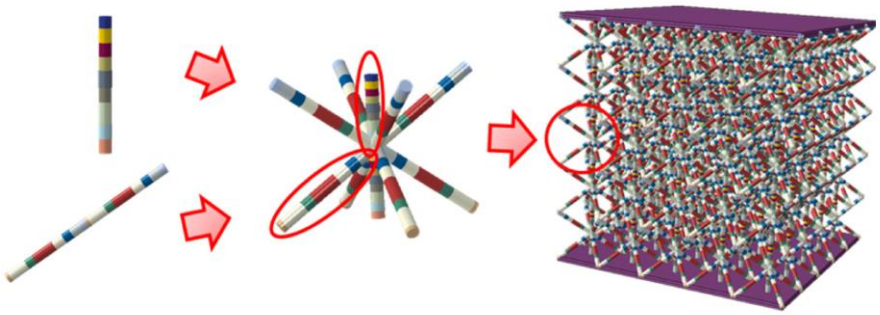

Fig. 2-8 BCC lattice structure model of geometry including geometric imperfections [41]

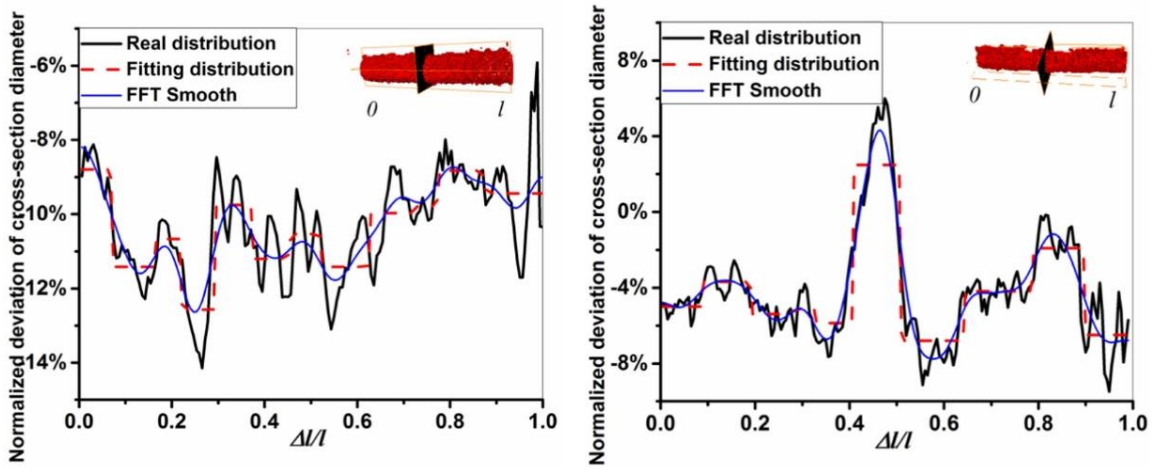


(a) (b)

Fig. 2-9 Distribution of diameter deviation along the length Δl/l of strut: (a) diagonal strut; (b) vertical strut [41]

The models were tested for compression loading of structures with different numbers of unit cell layers. A comparison showed that the inclusion of geometric imperfections using a method that used reconstructed data from μ-CT and a fitting function led to the most accurate numerical prediction for different numbers of unit cell layers.

Liu et al. [45] tried to increase the efficiency of computations to predict the quasi-static loading behavior of the multilayer BCC structure. To create a simulation, an explicit Abaqus 6.14-1 module was used, which is commonly used for simulations of dynamic processes. A similar procedure was used by Lei et al. [41] in a previous study.

To guarantee the quasi-static response of the structure, the loading time was 10 times increased. Furthermore, two energy principles were followed according to the recommendations of the Abaqus developers [46]. The ratio of increase in artificial energy to internal energy was kept below 5% to guarantee minimization of the hourglass effect. Furthermore, the ratio of kinetic energy to internal energy was monitored with the same boundary criterion during structure compression to maintain the dynamic effects at a negligible level. An optimum element size was determined according to the convergence test developed by Becker et al. [47].

Based on the settings, acceptable compliance with theoretical results in terms of stress-strain was achieved for the quasi-static compression of the lattice structure.

Gümrük et al. [27] introduced a similar approach for further investigation of the mechanical properties of lattice structures (BCC made of 316L by SLM) under quasi-static compressive loading. An analytical approach based on Timoshenko theory was formulated and two numerical approaches were developed.

The first approach used 1-D 3-noded Hughes Liu beam elements that allowed for finite deformation and shear effects [48]. A lack of stiffness in the vicinity of the vertices was compensated by increasing Young's modulus by about 50%, similar to Luxner et al. [35]. The length of the elements at the ends was equal to 50% of the diameter. The length of other elements changed according to the size of the unit cell (e.g., the cell side 2.5mm – 10 el.; 1.25 mm – 6 el.;). For each strut thickness 16 integration points were used across the cross-section. The second approach used solid 3-D 4-node tetrahedron elements with rotational degrees of freedom.

For preliminary study, the symmetry boundary conditions were applied by the constrained Node Set option. It allowed for the connection of preferred degrees of freedom in a node group to each other, i.e., the translational movements of the nodes on the symmetric surface in parallel to the normal of the surface. Movement of the nodes in parallel to the symmetric surface was possible, but rotations were not allowed. The translation movement of the symmetric nodes on the bottom surface in the normal direction of the surface was fixed to prevent rigid body movement (see Fig. 2-10).

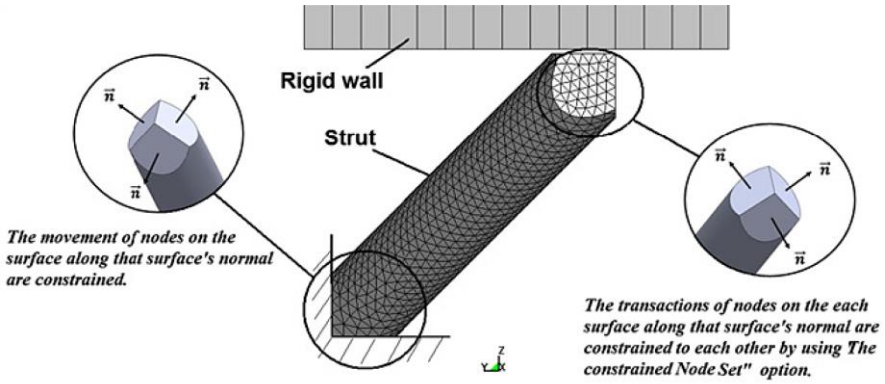


Fig. 2-10 The boundary conditions and finite element model of 3D strut [27]

The quasi-static loading simulation was created in the LS-DYNA explicit solver by an artificially increased loading rate while minimizing the effects of inertia. The velocity of the deformation member in the form of a rigid wall for the solid element model was given by the initial velocity of 1 $m \cdot s^{-1}$. For the beam element model, the rigid wall was modeled with a velocity defined by the equation:

$$v(t) = \frac{U}{t^*}\left[1 - \cos\left(\frac{\pi}{2t^*}t\right)\right] \ [m \cdot s^{-1}] \quad (2\text{-}1)$$

where t* is the total loading time and U is the axial displacement. After 4 ms, the loading speed was fixed to the maximal value achieved according to the equation. To increase the explicit time step, the density of the parent material was scaled 100 times. The criterion of quasi-static conditions was defined as the equal reaction forces between the loading and the bottom surface of the structure. Furthermore, the criterion of minimizing kinetic energy was used during the simulation, similar to that of Liu et al. [45].

Lozanovski et al. [49] continued by including manufacturing deviations and defects in the computational geometry models of the FCC and FCCz structures made of Inconel 625 by SLM technology. The material model was based on Yadroitsev et al. [50]. Simulations with models based on μ-CT scans were compared with simulations considering nominal geometry and experiment. The μ-CT scans were performed with a 7.5 μm voxel size undergoing thresholding and 3D reconstruction. A binary image stack of cross-sectional views was generated at 8 μm intervals. A custom algorithm was developed to analyze the image stack and extract scaled cross-sectional boundary data. The extracted cross-section included Cartesian coordinates of centroid position, centroidal principal area moments of inertia and the axis principal inclination angle. The data from each cross-sectional image were considered valid if they were within the three standard deviation intervals from the mean value.

The simulation was prepared as a quasi-static compressive loading of cubes using 4-node linear C3D4 and 8-node quadratic tetrahedral C3D8 (isoparametric) element models [51]. Scanned data, including detailed information on the geometry of the struts, were divided into sections. The sections were intersected with a series of ellipses that approximated the actual shape of the struts (see Fig. 2-11). The ellipses differed in each section in size, position, and rotation of the axes. Therefore, they had to be intertwined to create the geometry of the struts that reflected the imperfections and strut waviness.

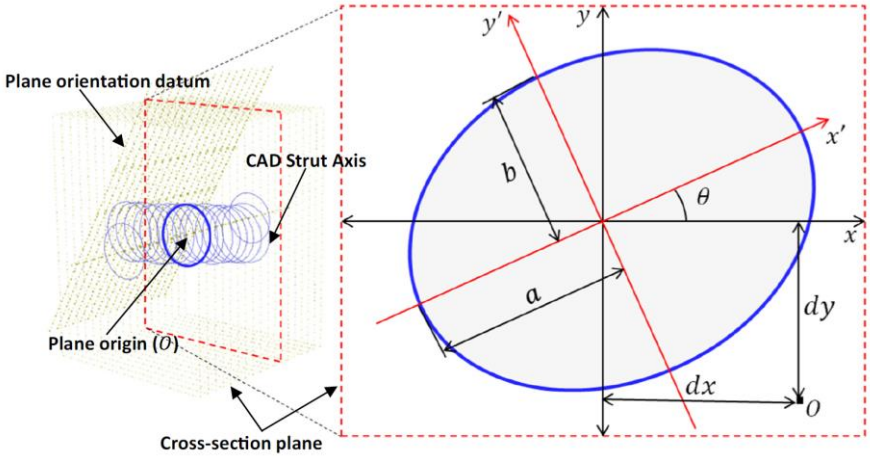


Fig. 2-11 Elliptical cross-section of the strut including variable parameters defining the dimensions and shape of the ellipse: *a*, *b* – radii of axes; $d_x$, $d_y$ – vertical and horizontal displacement of the center of gravity with respect to the theoretical axis of the strut; *x'*, *y'* – rotated cross-section axis [49]

A comparison of the Young's modulus and yield strength for different structure sizes showed that simulations of larger structures were closer to the experimental results. The study compared simulations with nominal geometry called 'Idealized' and geometry with imperfections called 'AM Representative Geometry' (see Fig. 2-12). The solid element models showed better compliance with the experiment. The deviations were probably caused by the material model, which was determined for different process parameters and bulk bodies.

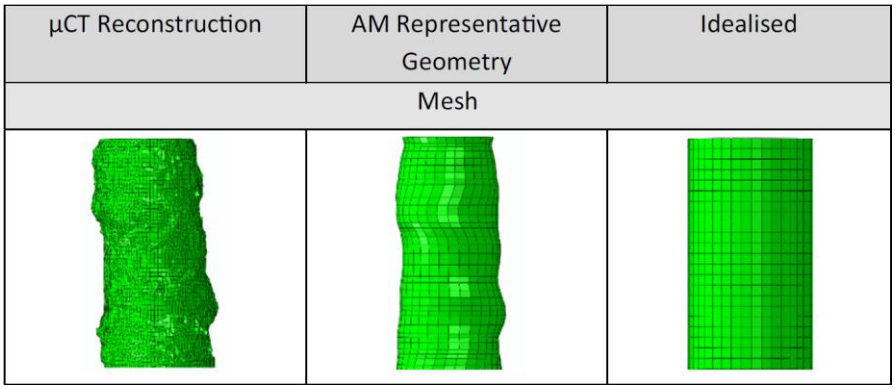


Fig. 2-12 Finite element mesh of µ-CT Reconstruction, AM representative and Idealized geometries [49]

## 2.2 Models of material

Experimental testing of lattice structures showed that thin struts have different material characteristics compared to bulk components despite the same manufacturing procedure and the same parent material used. Tsopanos et al. [21] determined the relative deformation, Young's modulus and the plastic deformation at 5 % of the BCC structure (made by SLM of SS 316L) using experimental and computational approaches. The properties of the parent material were determined by tensile tests of single-strut samples and compression tests of the structures. For the tensile samples, the elongation was subtracted in two ways.

According to the first, an extension of the sample was determined directly from the crosshead displacement. For testing, a low-capacity load cell (50 N) was used in combination with friction grips with a loading rate of $10^{-4}$ $s^{-1}$. The results showed an elasticity modulus of approximately 5 GPa, which corresponded to approximately 3% of the Young's modulus of the bulk material. This significant deviation was attributed to an inaccurate measurement of the elongation of the thin strut caused by slippage of a sample in the grips' jaws. Therefore, it was decided to make corrections to the elastic modulus using finite element analysis in the LS-DYNA software.

The second method used displacement measurement with a touch extensometer with 8 mm clip gauge length. The results showed an average modulus of elasticity of 40 GPa, which indicated only 21% of the Young's modulus of the bulk material. For this reason, a similar correction was made as in the previous case. The study highlighted problems with the accuracy of measuring the mechanical properties of thin strut samples. The authors mentioned the variability of the strut geometry and its metallographic structure as one of the main problems (see Fig. 2-13).

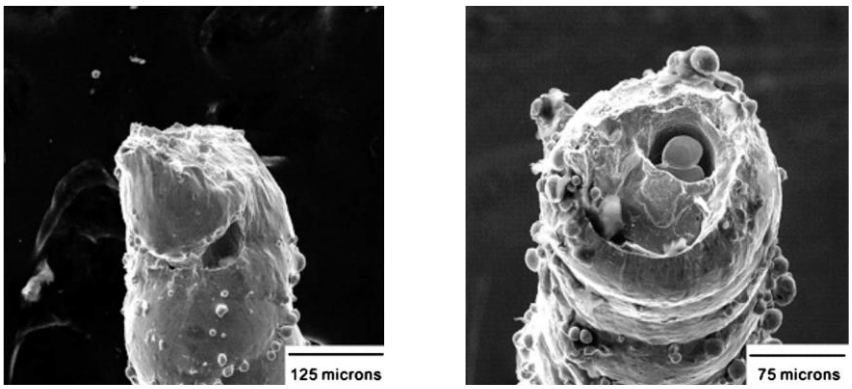


(a) (b)

Fig. 2-13 Scanning electron micrographs of struts failure with laser power (a) 140W; (b) 70 W [21]

To tune the simulation material model, the structures were subjected to a compression test (using Hughes-Liu beam elements) [52]. The Young's modulus of the parent material was parameterized until good agreement of the experimental and computational compression modulus of the structure was reached. The resulting value of Young's modulus of the parent material corresponded to 140 GPa, which is equal to 74%.

Smith et al. [51] built on previous research by creating mathematical models of 2-noded beams and 8-noded brick elements to predict the deformational behavior of the BCC and BCCz structures produced by SLM technology. The diameter of the struts near the nodes was increased to achieve a higher stiffness of the model, similar to the Luxner study [35].

Due to the small diameters of the struts, it was difficult to determine the properties of the material based on tensile tests. Manufacturing phenomena causing changes in the diameter of the strut led to inaccurate measurement and determination of mechanical properties. Therefore, the material properties of the Tsopanos study were taken over [53]. Instead of changing material properties, reverse engineering methods were used to adjust the diameter of the strut in the simulation. At first, the initial diameter of the strut of 0.2 mm was chosen for simulation. Then the diameter of the strut varied until the compliance between the experiment and the simulation was achieved for both the model definitions for most unit cell sizes.

The results showed that the behavior of lattice structures under non-linear quasi-static loading can be accurately captured using beam element simulations in the certain range of strut radius ($K$) to strut length ($L$) ratios (for BCC see Fig. 2-14).

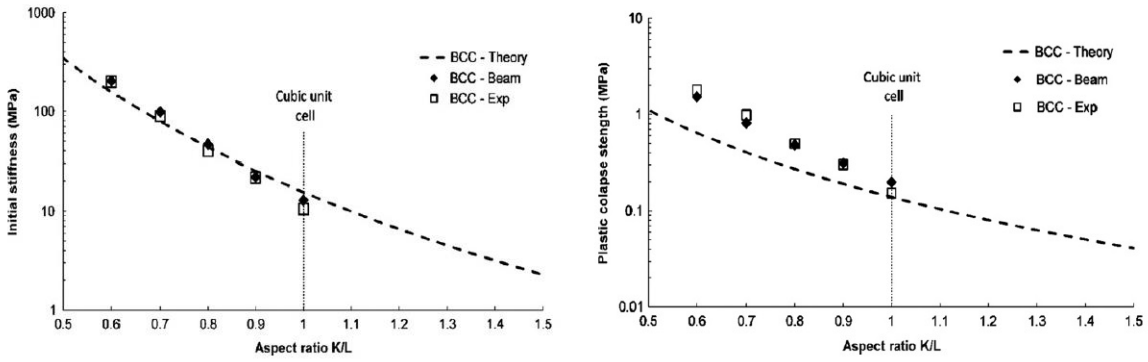


(a) (b)

Fig. 2-14 (a) comparison of initial structure's stiffness; (b) plastic deformation depending on the strut diameter to length ratio for the BCC structure [51]

Li et al. [28] continued with the precise determination of the mechanical properties of the lattice structures. A simulation was developed that mapped the macroscopic deformations of a BCC structure made of SS 316L by SLM technology. The elastic-plastic material model was based on stress-strain curves of a single strut tensile test with a nominal diameter corresponding to the diameter of the structure strut. The elongation of the strut was deduced from the displacement of the test head with the gripping clamps specially developed for the strut samples (500 N load cell and ~ $10^{-4}$ $s^{-1}$ strain-rate). Furthermore, due to the difficulty of measuring properties described in the Tsopanos study [53], one end of the strut was captured by a high-resolution camera mapping the sample deformation.

It allowed to perform deformation correction using the camera images. By the corrections, the deformation was increased approximately 1.3 times in the plastic area (see Fig. 2-15 (a)) and 1.9 times in the elastic area (see Fig. 2-15 (b)). Despite the relatively large roughness of the struts and the teeth of the test head jaws, the slippage of the ends proved to be significant. Compared to contact measurement, the deformation of non-contact sample scanning allowed to eliminate the slip effect.

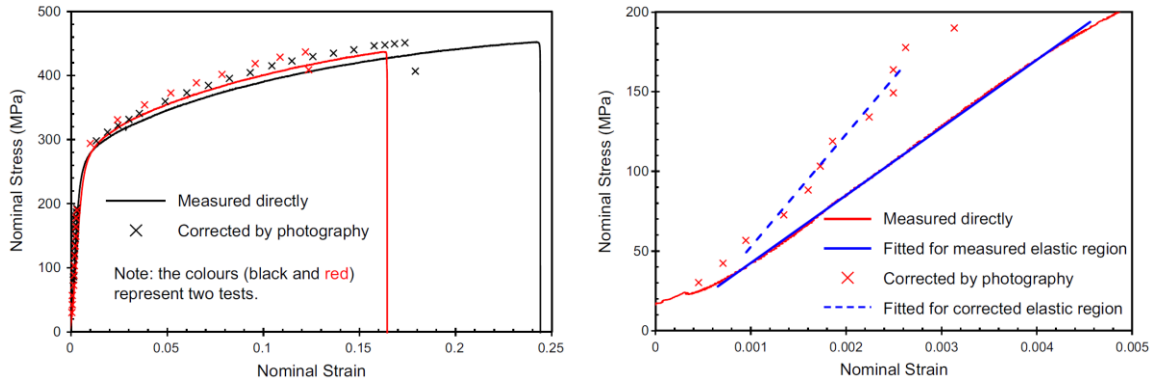


(a) (b)

Fig. 2-15 (a) Nominal stress as a function of the strain measured directly during the tensile test and indirectly by means of image corrections; (b) curves fitted in the elastic region to one of the curves [28]

The elastic deformation was subjected to linear regression analysis to determine the true value of Young's modulus. The results showed a value of $E$=71±7 GPa, which differed significantly from Young's modulus of the bulk material ($E$=190-200 GPa). This result indicated a significant degradation of the material, probably due to the influence of pores in the struts [54]. The contractual yield strength at 0.2% plastic strain was $\sigma_Y$=280±14 MPa.

Li et al. [55, 56] continued with the development of a non-linear elastic-plastic material model with isotropic hardening for the quasi-static compression simulation of the BCCz structure. The input parameters of the $AlSi_{10}Mg$ alloy were determined based on tensile tests of strut samples with the same nominal diameter as the structure struts diameter (1 mm at a loading rate of 0.5 $mm \cdot min^{-1}$) similar to Labeas et al. [13]. The geometry model in the simulation was created using a Python script. The FEM simulations were compared with analytical calculations based on the Gibson-Ashby [57] model and experiments.

In addition, conventional tensile struts with a diameter of 5 mm were produced and tested. The results showed Young's modulus values of 70 GPa, a tensile strength of 350 MPa and maximal elongation at a break of 5.5%. The corresponding properties of the strut were 40 GPa, 276 MPa and 3.5%. Despite the equivalent production conditions and the same process parameters, significant differences were observed, similar to previous studies [14, 58]. These differences have been attributed to the effects of different heat transfers to thin struts and bulk material [55]. For each new layer built, a smaller strut diameter requires a shorter scan time. Insufficient heat accumulation caused by short melting time could lead to reduction of actual diameters, which degrades mechanical properties. However, overheating of the melted cross-section could lead to large amounts of partially melted particles.

A similar approach was used by Labeas et al. [13], who focused on the investigation of compression properties of BCC and FCC-based structures produced by SLM (SS 316L). The geometry model was created with Timoshenko beam elements (BEAM 188) for detailed simulation and hexahedral elements (SOLID 164) for homogenized representations. For the beam elements, a bilinear elastic-plastic model of material with kinematic hardening Mat03 was prepared based on the quasi-static tensile test of struts with corrections. Corrections were determined using the calibration procedure suggested by Mines et al. [59].

To obtain material properties, a lattice structure was tested with compression and shear loading. For the linear phase, the unit cell was considered isotropic. The elastic tensor values assumed that the average stress-strain response of homogenized material is identical to the stress-strain response of the lattice structure.

For the homogenized representation, Mat26 (Mat Honeycomb) was used. Its mathematical formulation consisted of two almost independent deformation phases (see Fig. 2-16). In the first uncompacted phase (see Fig. 2-16 (a)), stresses and strains were uncoupled in all three directions. Each element behaved like six independent one-dimensional elements – three compressions and three shears. The second fully compacted phase (see Fig. 2-16 (b)) prevented the hexagonal element from becoming a zero volume. The stresses were a function of relative volume or volumetric strain.

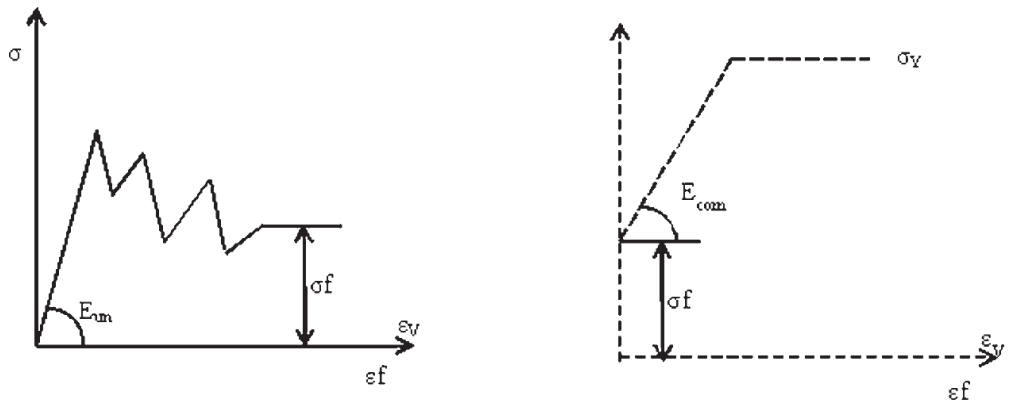


(a) (b)

Fig. 2-16 Material model used for homogenized representation (a) uncompacted; (b) compacted phase [20]

In the later stages of the research, the material model was replaced by the non-linear orthotropic Mat40 (*Mat_Nonlinear_Orthotropic) [20]. The input parameters were based on the six independent non-linear stress-strain curves – three normal and three shear stresses. The elastic moduli required for the stress update in the model were used from the stress-strain curves and coincide with the values calculated from the linear phase of homogenization.

An experimentally performed drop test was used to validate the FEM simulations. The results of both simulations in comparison with the experiment showed a similar course in the elastic region and the region of progressive deformations. During the onset of material compaction, the simulations no longer reflected experimental trends.

Harris et al. [60] compared different approaches to modeling lattice structure plasticity. The approaches were used to assess the impact of the process parameters and changes in geometry on the mechanical properties of the structure under dynamic loading (316L made by SLM). The main object of interest became a special honeycomb structure with artificially increased porosity created by replacing walls with struts that maintained the same relative density.

Properties were determined by tensile tests of the dogbone tensile coupon with gauge section of width 3 mm, length 20 mm and thickness 1 mm. The curves of the actual stress $\sigma_t$ depending on the logarithmic deformation $\varepsilon_p$ were interpolated by the curves of the constitutive relations of plastic hardening (see Fig. 2-17). Each of them represented a different stress-strain response. The parameters $n_i$ and $C_i$ obtained by interpolation were used to describe these relationships:

Hollomon [61] $$\sigma_t = C_1 \varepsilon_p^{n_1} \ [MPa] \quad (2\text{-}2)$$

Ludwik [62] $$\sigma_t = C_2 + C_1 \varepsilon_p^{n_1} \ [MPa] \quad (2\text{-}3)$$

Voce [63] $$\sigma_t = C_2 - (C_2 - C_1)exp(-n_1\varepsilon_p)\ [MPa] \quad (2\text{-}4)$$

Ludwigson [64] $$\sigma_t = C_1\varepsilon_p^{n_1} + exp(C_2 + n_2\varepsilon_p)\ [MPa] \quad (2\text{-}5)$$

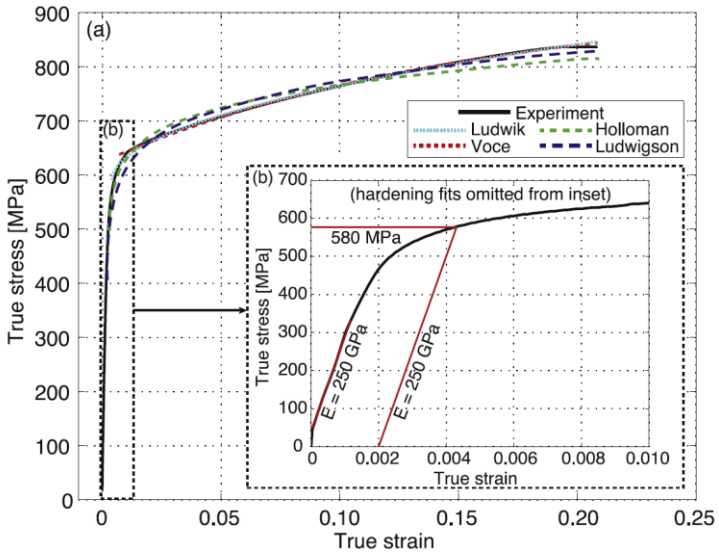


Fig. 2-17 a) Tensile stress-strain response of a dogbone sample with alternative models for strain hardening superimposed; b) a magnification of the curve at the onset of yielding [60]

Amani et al. [65] introduced an even more sophisticated material model for simulation of the BCC structure ($AlSi_{10}Mg$) produced by SLM technology. The deformation process of the structures was scanned in-situ and ex-situ by X-ray tomography, capturing macroscopic changes in the structure geometry and local micro-porosity (see Fig. 2-18). The detector with 1920 x 1536 square sensitive pixels and a relatively low resolution of 20 µm pixel size was able to capture entire structure. The three-dimensional images were then used to create a simplified geometric representation of the structures, including manufacturing imperfections.

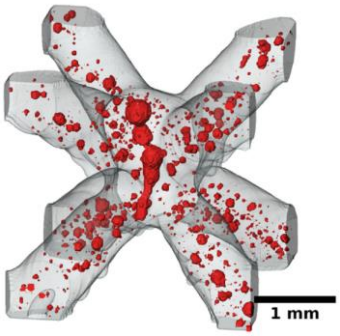


Fig. 2-18 Scan of basic BCC unit cell with red highlighted local pores [65]

The internal porosity information obtained by tomography was introduced via a Gurson-Tvergaard-Needleman (GTN) model of the material which assigned local porosity data to each element. The GTN model was based on von Mises yield criteria for ductile porous materials that included void nucleation and growth [66]. The basic equation of this model was defined as [66, 67]:

$$\Phi\left(\sigma_{eq}, \sigma_y, \sigma_H, f\right) = \left(\frac{\sigma_{eq}}{\sigma_y}\right)^2 + 2fq_1 cosh\left(\frac{3q_2\sigma_H}{2\sigma_y}\right) - (1 + q_3 f^2) = 0 \tag{2-6}$$

where $\Phi$ is the yield function, $\sigma_{eq}$ is the von Mises equivalent stress, $\sigma_y$ is the yield stress, $\sigma_H$ is the hydrostatic stress, $q_1$, $q_2$, and $q_3$ are calibrating parameters, and $f$ is the void volume fraction in the matrix starting from an initial void volume fraction $f_0$ defined as:

$$\dot{f} = \dot{f}_{gr} + \dot{f}_{nucl} = (1 - f)tr(\dot{\varepsilon}^{pl}) + \frac{f_N}{s_N\sqrt{2\pi}}\, exp\left[-\frac{1}{2}\left(\frac{\varepsilon_{eq}^{pl} - \varepsilon_N}{s_N}\right)^2\right]\dot{\varepsilon}_{eq}^{pl} \tag{2-7}$$

where $\dot{f}_{gr}$ represents the void growth rate based on mass conservation and proportional to the hydrostatic plastic strain-rate tensor $\dot{\varepsilon}^{pl}$ and equivalent plastic strain $\varepsilon_{eq}^{pl}$. In additional, $\varepsilon_N$ is the mean value and $s_N$ standard deviation of the normal nucleation distribution. $f_N$ represents the volume fraction of nucleated voids. The power law hardening was defined by following equation [68]:

$$\frac{\sigma_y}{\sigma_0} = \left(\frac{\sigma_y}{\sigma_0} + \frac{3G}{\sigma_0}\varepsilon^{pl}\right)^N \tag{2-8}$$

where $\sigma_y$ is the flow stress, $\sigma_0$ is the initial yield stress, *N* in the hardening exponent and *G* represents the elastic shear modulus.

As a result, two computational models were created: the first considered a homogeneous distribution of the average measured porosity across all struts and the second a heterogeneous distribution depending on the area of actual pore occurrence. First-order volume tetrahedral elements were used to create a polygonal mesh for both approaches (Avizo software) [65].

Except for the two models of the GTN material, the nonporous J2 isotropic plasticity model was used and compared with the experiment (see Fig. 2-19). The comparison showed that the simulations using J2 plasticity overestimated the stress values. The micro-pores in the struts and nodes of the structure slightly reduced Young's modulus and its strength significantly. The simulation using homogeneous GTN led to lower stress levels compared to the experiment, while the simulation with heterogeneous GTN was in good agreement. This result indicated a correct representation of the micro-porosity distribution.

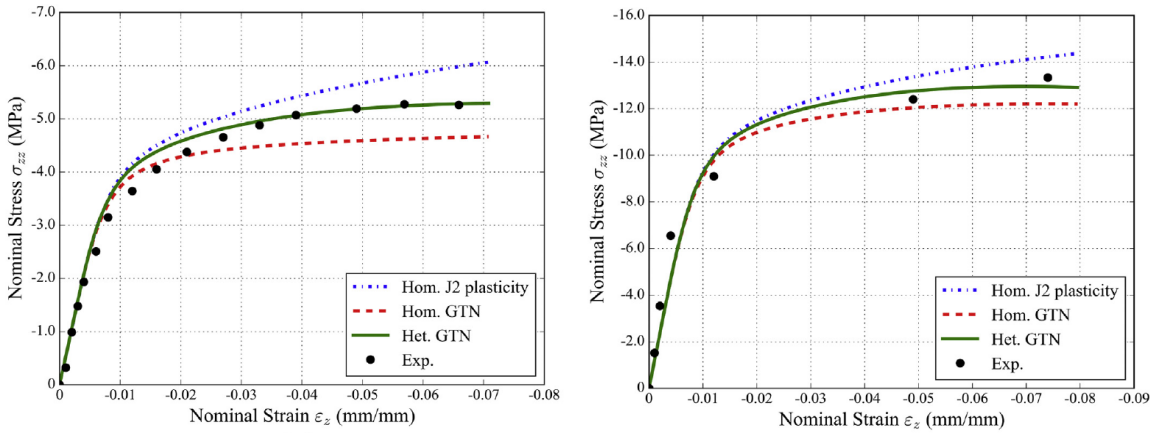


Fig. 2-19 Nominal stress $\sigma_{zz}$ as a function of strain $\varepsilon_z$ obtained by experiment and simulation (a) for structure with thin struts (0.66±0.56); (b) for structure with thick struts (0.79±0.59) [65]

The model of material with constitutive law for the simulation of lattice structure under dynamic loading was presented by Chen et al. [24]. The main focus was to increase the stiffness, strength, and energy absorption capacity of the lattice structures with a negative Poisson's ratio. More specifically, it was desired to achieve transverse expansion of the structures under tensile loading by the implementation of different types of rib to conventional structures (see Fig. 2-20 (a-d)).

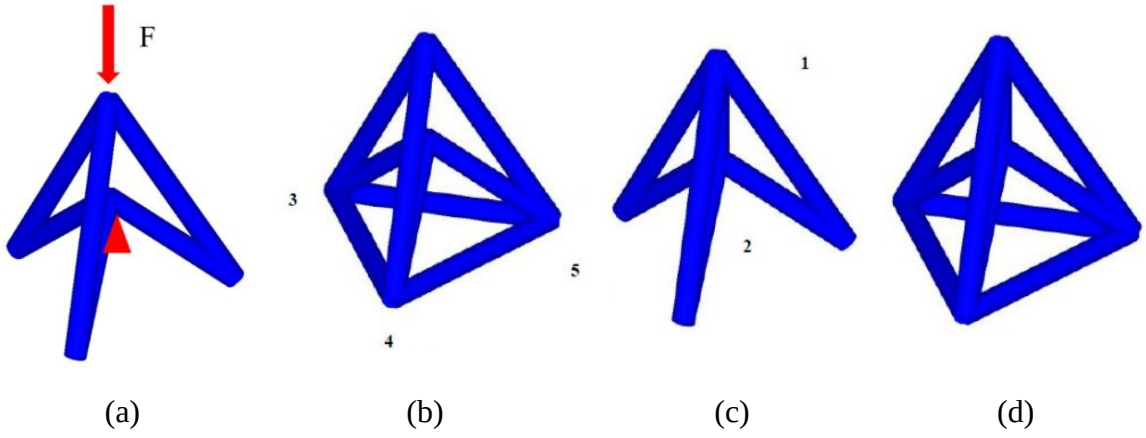


Fig. 2-20 Unit cells of structure with negative value of Poisson's ratio [24]

Linear elastic behavior was defined as the standard aluminum alloy 7075 with Young's modulus of 70 GPa and Poisson's ratio of 0.27. Plasticity was represented by the constitutive law of simplified Johnson-Cook (J-C, MAT-98) [48] considering the deformation hardening effect and the strain-rate, but neglecting the effect of temperature:

$$\sigma = (A + B\varepsilon^n)(1 + C ln\frac{\dot{\varepsilon}}{\dot{\varepsilon}_0}) \quad [MPa] \tag{2-9}$$

where $\sigma$ is resulting stress value, $\dot{\varepsilon_0}$ is quasi-static strain-rate, $\dot{\varepsilon}$ is dynamic strain-rate, A (448 MPa) is yield strength, B (343 MPa) is hardening modulus, C (0.01) strain-rate hardening coefficient and n (0.41) is hardening exponent.

Due to the computational effort of the solid elements, Belytschko-Schwer beam elements reflecting plastic bends, elongations, and torsional loading were used. A series of tests were performed to determine the effect of changes in geometry and mechanical properties. A comparison of the parametric simulation with the experiment showed small differences in the acting stress.

The full version of the J-C constitutive law was used by Grytten et. al [33] and Zmindak et. al [30, 69] to model the high velocity impact on aluminum (6061-T6) and steel (4340-C30) plates at intermediate strain-rates $10^2$–$10^3$ $s^{-1}$. The model was given by the equation where isotropic hardening in which von Mises stress $\bar{\sigma}$ was expressed as a function of the equivalent plastic strain $\bar{\varepsilon}^{pl}$, equivalent plastic strain-rate $\dot{\bar{\varepsilon}}^{pl}$, a homologous temperature $T^*$ and $m$ coefficient of thermal softening [70]:

$$\bar{\sigma} = [A + B(\bar{\varepsilon}^{pl})^n]\left[1 + Cln\left(\frac{\dot{\bar{\varepsilon}}^{pl}}{\dot{\varepsilon}_0}\right)\right](1 - T^{*m}) \quad [MPa] \tag{2-10}$$

where $\dot{\bar{\varepsilon}}^{pl}/\dot{\varepsilon}_0$ is the normalized equivalent plastic strain-rate usually to 1.0 $s^{-1}$. The homologous temperature $T^*$ is the defined as [69]:

$$T^* = \frac{(T - T_{room})}{(T_{melt} - T_{room})} \quad [-] \tag{2-11}$$

where $T$ is the material temperature, $T_{melt}$ is the melting temperature, and $T_{room}$ is the room temperature. The equation for equivalent plastic deformation is given as:

$$\bar{\varepsilon}^{pl} = \left[d_1 + d_2 exp\left(d_3 \frac{p}{\bar{\sigma}}\right)\right]\left[1 + d_4 ln\left(\frac{\dot{\bar{\varepsilon}}^{pl}}{\dot{\bar{\varepsilon}}_0^{pl}}\right)\right](1 - d_5) \quad [MPa] \tag{2-12}$$

where $p$ is pressure and $d_1$ – $d_5$ are experimentally determined constants.

Gümrük et al. [19] continued the development of a simpler strain-rate-dependent computational model to estimate the dynamic compression behavior of the BCC structure made of SS 316L by SLM technology. The model considered the dynamic effect that represented the sensitivity of the parent material to the strain-rate in the area of plastic deformations. This dependence was introduced by means of the Cowper-Symonds (C-S) constitutive law supplemented with the isotropic elasticity behavior [1]. The basic equation can be described as follows [71]:

$$\frac{\sigma_o'}{\sigma_o} = 1 + \left(\frac{\dot{\varepsilon_p}}{D}\right)^{\frac{1}{q}} \ [s^{-1}] \ pro \ \sigma_o' \geq \sigma_o \tag{2-13}$$

where $\sigma_o'$ is the dynamic yield or ultimate tensile stress at uniaxial plastic deformation with strain-rate $\dot{\varepsilon_p}$. $\sigma_o$ is the static stress and $D$ and $q$ are the constant material parameters.

To determine the input parameters of the constitutive law, the strut tensile tests were performed in the range of $10^{-3}$ $s^{-1}$ to $6 \cdot 10^3$ $s^{-1}$. Low-velocity dynamic tensile tests (up to 80 $s^{-1}$) were performed on a modified Instron E3000 hydraulic device (Instron, Norwood, Massachusetts, USA) using single strut samples. Significant oscillations of the system transmitted to the strain gauge record were observed with increasing loading velocities. This problem was described in a study by Fang et al. [8]. A modified Hopkinson device was used for high-velocity tensile testing [72–74] (see Fig. 2-21 a)). Special multi-strut bodies (21 struts; see Fig. 2-21 b)) were used similarly to those used by Dong et al. [38] for polymer materials. Based on the results, the stress, strain, and strain-rate values were obtained using the following equations [75, 76]:

$$\sigma = \frac{A_0 E_0}{A} \varepsilon_t(t) \ \ [MPa] \tag{2-14}$$

$$\varepsilon(t) = -\frac{2C_0}{L} \int_0^t \varepsilon_t \, dt \ \ [-] \tag{2-15}$$

$$\dot{\varepsilon} = -\frac{2C_0}{L} \varepsilon_r \ \ [s^{-1}] \tag{2-16}$$

where $\varepsilon_t(t)$ and $\varepsilon_r(t)$represented the transmitted wave and the reflected wave, respectively. $A_0$ indicated the cross-sectional area, $E_0$ the elasticity modulus of the bars, $A$ the cross-sectional area of a micro-strut, $L$ the size of the samples, and $C_0$ the elastic wave velocity given by equation [75]:

$$C_0 = \sqrt{\frac{E_0}{\rho_0}} \tag{2-17}$$

where $\rho_0$ is the density of the bars. The obtained values of dynamic yield strength ($Y_s$) or ultimate tensile stress (UTS) for different strain-rates were fitted with curves. Constants $D$ and $q$ were determined as parameters of the polynomial function describing the fitting curve.

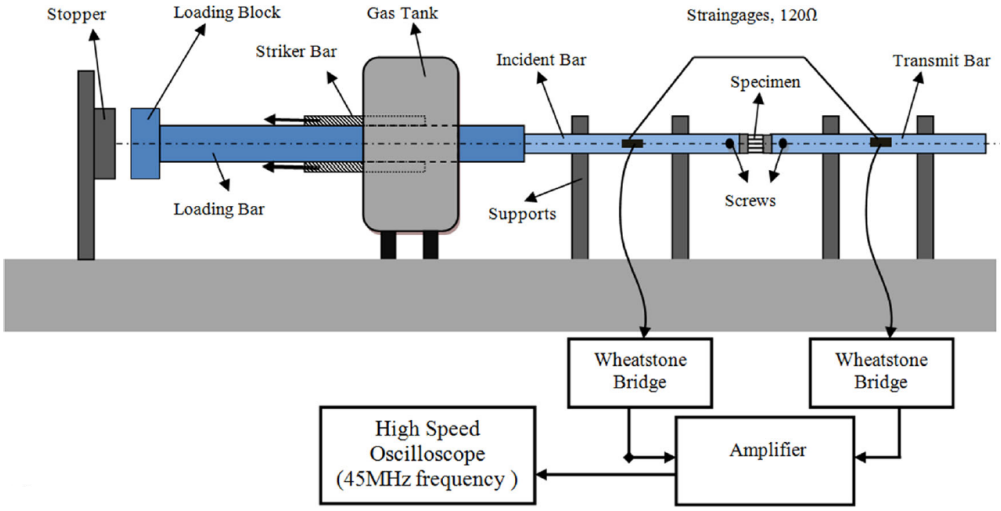


(a)

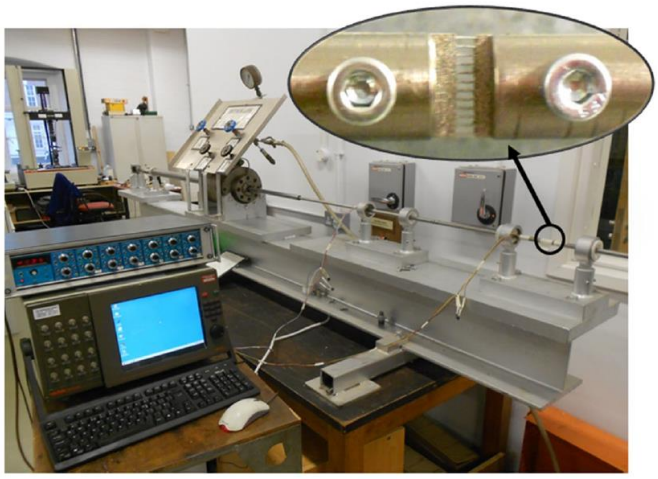

(b)

Fig. 2-21 (a) Schematic of a Hopkinson device adapter for high-speed tensile tests; (b) attachment of a sample designed for the test [19]

For verification, a drop test was simulated in the LS-DYNA 3D software with settings from a previous study [27]. The geometry of the structure struts was created using Hughes-Liu beam elements with sixteen integration points across the cross-section. Each strut consisted of eight elements. Rotational degrees of freedom were removed from the struts in the nodes.

Xiao et al. [23] used a similar evaluation of the split Hopkinson pressure bars test (SHPB, Kolsky bars) for dynamic compression of lattice structures. The tests were performed for relative strain-rates up to $10^3$ $s^{-1}$. Based on the one-dimensional stress wave theory and homogeneous hypothesis, nominal stress, strain and strain-rate were obtained using the following formula:

$$\sigma(t) = \frac{F_{input} + F_{output}}{2A_0} = \frac{E_B A_B}{2A_0} \left(\varepsilon_i(t) + \varepsilon_r(t) + \varepsilon_t(t)\right) \quad [MPa] \tag{2-18}$$

$$\varepsilon(t) = \frac{\Delta L}{L_0} = \frac{C_0}{L_0}\int_0^t \big(\varepsilon_i(\tau) - \varepsilon_r(\tau) - \varepsilon_t(\tau)\big)d\tau \quad [-] \tag{2-19}$$

$$\dot{\varepsilon}(t) = \frac{d\varepsilon(t)}{dt} = \frac{C_0}{L_0}\left(\varepsilon_i(\tau) - \varepsilon_r(\tau) - \varepsilon_t(\tau)\right) \quad [s^{-1}] \tag{2-20}$$

where $E_B$, $A_B$, and $C_0$ are elastic modulus, cross-section area and sound speed of the bars, respectively. $\varepsilon_i(t)$, $\varepsilon_r(t)$ and $\varepsilon_t(t)$ represent the elastic strain obtained for the incident wave, the reflected wave, and the transmitted wave. $F_{input}$ and $F_{output}$ represent the input and output force history at the bar-sample interface. $L_0$ is the initial length of the sample and $\Delta L$ is the relative displacement of the bar-sample interface.

## 2.3 Performance of lattice structures

In order to quantify and compare the performance of lattice structures with those of other porous metamaterials, research teams started to develop their metrics. Most of them focused on stress-strain dependence, plateau stress, energy absorption, or structure efficiency. Ushijima et al. [22] focused on the analytical and numerical estimation of the BCC structure properties and their comparison with the experiment. The study highlighted the main mechanisms that influenced the behavior of the structure, for example, elastic and plastic buckling, axial and bending plasticity, rupture, etc. [77]. It also mentioned that the struts were primarily deformed by axial tension or bending, whereas the effect of torsion was assumed to be negligible. One of the most important comparative metrics was the initial stiffness of the BCC structure $E^*_{BCC}$ based on classical beam theory given as:

$$E^*_{BCC} = \sqrt{3}\pi E \cdot \frac{(d/L)^2}{1 + 2(L/d)^2} = \frac{\rho^*}{\rho_s} \cdot \frac{E}{1 + 2(L/d)^2} \quad [MPa] \tag{2-21}$$

where $E$ is the Young's modulus of the parent material, $d$ is the diameter of the strut, $L$ is the length of unit cell, and $\rho^*/\rho_s$ is the relative density with $\rho_s$ density of parent material and $\rho^*$ actual overall density of structure. Applying this metric assumed for symmetry boundary conditions and constraint of rotation at strut nodes. Another important metric was the plastic collapse strength $\sigma^*_{pl,BCC}$ which was defined as the initiation of fully plastic hinges [6]. This metric was mathematically described by the following equation:

$$\sigma^*_{pl,BCC} = \frac{4\sqrt{2\sigma_0}}{3}\left(\frac{d}{L}\right)^3 = \frac{\rho^*}{\rho_s} \cdot \frac{4\sqrt{6\sigma_0}}{9} \cdot \frac{d}{L} \quad [MPa] \tag{2-22}$$

where $\sigma_0$ is the flow stress. The application of this metric assumed that the elastic deformation was not affected by the growth of plasticity. It allowed to estimate plastic collapse strength for different *d/L* ratios and compare them with simulation and experiment. For relatively small values *d/L*<0.1, a good agreement of the prediction was achieved with the simulation of the beam and solid elements and the experiment. However, for a large ratio *d/L*>0.1 analytical calculation and the beam element simulation became inaccurate.

Mines et al. [17] continued with the development of the analytical approach for estimation the actual diameter of the BCC structure strut based on the weight of the structure. It allowed the detection of anisotropic imperfections related to changes in the geometry of struts [27]. The calculated diameter of the struts is given as:

$$d = \sqrt{\frac{m_b}{\rho_p \pi N^3 L \sqrt{3}}} \quad [mm] \tag{2-23}$$

where $m_b$ is the measured sample weight, $\rho_p$ is the parent material density, *N* is the number of cells along the side length of the structure, and *L* is the side length of unit cell. The disadvantage of the method was considering only the circular cross-section of the struts, which was constant along its entire length and did not correspond to the actual shape accurately.

Furthermore, the study focused on the energy absorption performance of different types of porous materials. A drop-weight test was used to compare the properties of BCC and BCCz structures made of SS 316L and $Ti_6Al_4V$ by SLM with a honeycomb aluminum structure (Hexcel CR111-1/4-5056-0.001N-2.3) [78] and aluminum foam (Alporas, Shinko Wire Company, Amagasaki, Japan). To achieve an equivalent comparison of metamaterials with different volume fractions, the energy dissipated during deformation (see Fig. 2-22) was divided by the average density of the sample – specific impact energy (SIE). The results showed a similar amount of SIE for several types of structures tested, with the honeycomb type reaching the highest values for various dent depths.

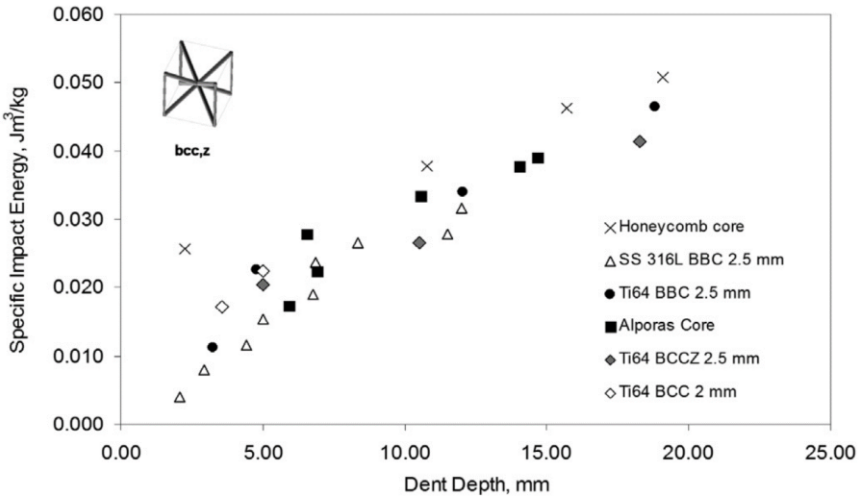


Fig. 2-22 Specific impact energy dissipated for the deformation of several types of porous structures [79]

A similar approach was offered by Tancogne-Dejean et al. [14], who mapped the deformation behavior of octet truss lattice structures made of SS 316L by SLM technology under quasi-static and dynamic loading. The study assumed that a suitable parabolic narrowing of the struts (see Fig. 2-23) can lead to higher energy absorption capabilities and an increase in stiffness.

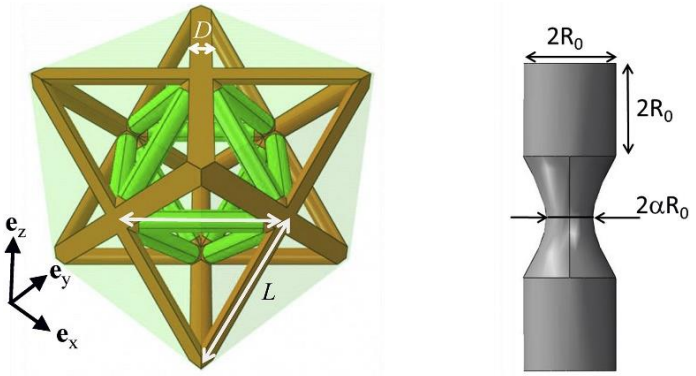


(a) (b)

Fig. 2-23 (a) Basic cell of octet truss structure without constriction; (b) constricted geometry of a single strut [14]

The energy absorption was evaluated as the dissipated energy dependent on the relative density based on simulations – specific energy absorption (SEA). The relative density $\bar{\rho}$ was defined by the ratio of the average density of the structure $\rho$ and the density of the parent material $\rho_s$:

$$\bar{\rho} = \frac{\rho}{\rho_s} \quad [-] \tag{2-24}$$

SEA up to 0.3 strain was defined by the following equation:

$$\psi = \frac{W}{\rho} \quad [J \cdot m^{-3}] \tag{2-25}$$

with

$$W = \int_0^{0.3} \sigma \, d\varepsilon \; [J \cdot kg^{-1}] \tag{2-26}$$

where $W$ is the work performed on the structure compression, $\sigma$ is the axial stress and $\varepsilon$ is the axial strain. The results showed that the SEA was a monotonically increasing function of the relative density with the highest absorption capacity for the fully dense parent material SS 316L $\psi_s = 26.6\, J \cdot g^{-1}$. If SEA of the structure was normalized by SEA of fully dense material the relative SEA was obtained, which was proportional to the relative density:

$$\frac{\psi}{\psi_s} = \frac{\rho}{\rho_s} \quad [-] \tag{2-27}$$

Since the SEA was already normalized by the density, the absorbed energy was a quadratic function of the density. Therefore, it was concluded that the energy absorption of the lattice structures increases substantially for higher densities, and the following equation was formulated:

$$W = \psi\rho = \left(\frac{\psi_s}{\rho_s}\right)\rho^2 \quad [J \cdot kg^{-1}] \tag{2-28}$$

The assessed strength of the lattice structure increased by approximately 30% as the rate of relative deformation changed from $10^{-3}$ $s^{-1}$ to $10^{3}$ $s^{-1}$. This phenomenon was mainly attributed to the sensitivity of the parent material to the deformation rate.

Harris et al. [60] investigated the impact of process parameters and geometry changes on the mechanical properties of lattice structures produced by the SLM technology of SS 316L under dynamic loading. The special honeycomb structure was designed, with artificially increased porosity created by replacing walls with struts that maintained the same relative density (see Fig. 2-24). Structure performance was expressed in terms of normalized stress, normalized SEA, and energy absorption efficiency. Normalized stress was described as follows:

$$\bar{\sigma} = \frac{\sigma}{\bar{\rho}\sigma_y} \quad [-] \tag{2-29}$$

where $\sigma$ is the nominal compressive stress defined as the total force divided by sample cross-section, $\bar{\rho}$ is the measured relative density of the sample and $\sigma_y = 580\ MPa$ is the yield stress of the SLM produced SS 316L (thin-walled material). Normalized SEA was defined as:

$$\bar{W}(\varepsilon_1) = \frac{W(\varepsilon_1)}{\bar{\rho}\rho_s} \quad [-] \tag{2-30}$$

where SEA is evaluated to strain $\varepsilon_1 = 0.5$. The energy absorption efficiency was described as:

$$\eta(\varepsilon_d) = \frac{1}{\sigma_m} \int_0^{\varepsilon_d} \sigma d\varepsilon \quad [-] \tag{2-31}$$

where $\sigma_m$ is the maximum nominal compressive stress in the range of $0 \leq \varepsilon \leq \varepsilon_d$ with $\varepsilon_d$ indicating the maximum strain achieved. The normalized energy absorption efficiency was further defined by the following equation:

$$\bar{\eta} = \frac{\eta}{\bar{\rho}} \quad [-] \tag{2-32}$$

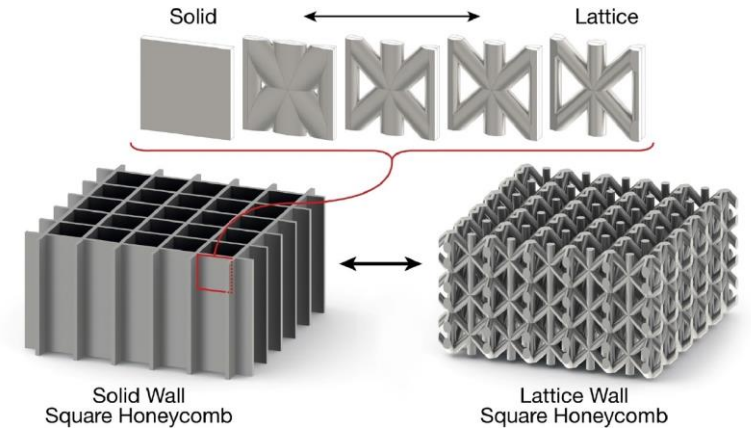


Fig. 2-24 Hybrid geometry concept: replacing the walls of a square honeycomb structure with strut elements (with equal relative density) [37]

For quasi-static and dynamic loading, the hybrid geometry of Fine lattice-walled square honeycomb (FLW-SHC) and Lattice-walled square honeycomb (LW-SHC) significantly outperformed lattice structures produced in previous studies (see Fig. 2-25) [22, 80–82]. An increase in mechanical properties was observed for the strength of the structure, the SEA, and the absorption efficiency. However, compared to the square honeycomb (SHC) produced by additive technologies, these values were lower [83].

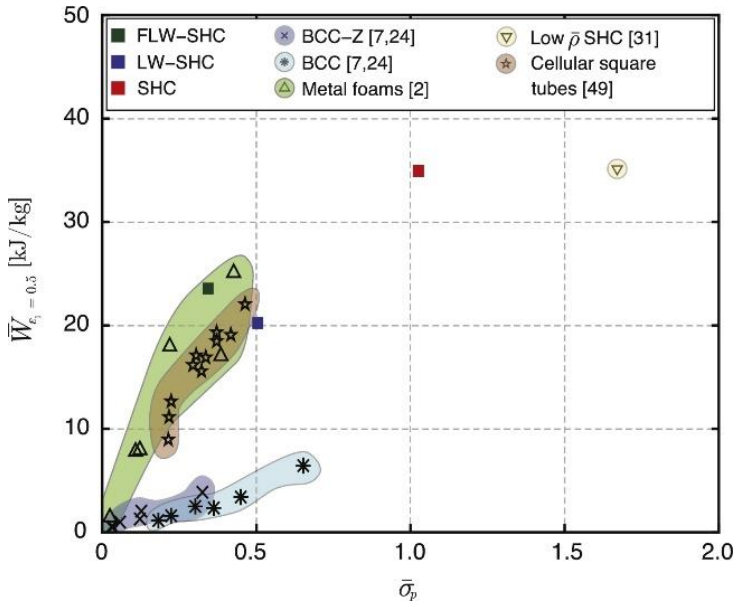


Fig. 2-25 SEA to 50% nominal compressive strain vs normalized initial peak stress $\bar{\sigma}_p$ [37]

Similar metric to eq. 2-27 was used by Wang et al. [7] for the assessment of the energy absorption capabilities of connectors with curved plates and aluminum foam. The stress and strain were replaced with force and displacement. Therefore, the energy absorption capacity of the connector was determined by integrating the force as:

$$E_a = \int_0^{x_D} F(x)dx \quad [J] \tag{2-33}$$

Then the specific energy absorption was calculated as:

$$SEA = \frac{E_a}{m_{ct}} \quad [J] \tag{2-34}$$

where $m_{ct}$ is total mass of aluminum foam and plates. The energy absorption efficiency was defined by:

$$\eta(x) = \frac{1}{F(x)H} \int_{x_y}^{x} F(x)dx \quad [-] \tag{2-35}$$

where $F(x)$ represents compressive force, $H$ is the height of aluminum foam and $x_y$ is the displacement at yield. The densification displacement $x_D$ was determined according two principles. The first of them the displacement $x_D'$ corresponding to the point at which the energy absorption efficiency reached a maximum value was chosen:

$$\left.\frac{d\eta(x)}{dx}\right|_{x=x'_D} = 0 \quad [-] \tag{2-36}$$

In the second of them the maximal force $F_{max}$ within the displacement from 0 to $x'_D$ was found. The densification displacement $x_D$ was determined as the displacement corresponding to the first maximum force, $F_{max}$ after $x'_D$. Then, the mean force reaction $F_m$ was calculated as:

$$F_m = \frac{\int_0^{x_D} F(x)dx}{x_D} \quad [N] \tag{2-37}$$

Similar metric to eq. 2-25 was used by Xiao et al. [23, 84, 85]. The study focused on increasing energy absorption for the BCC structure with a step change in the volume fraction (made with $Ti_6Al_4V$ SLM technology) under quasi-static and dynamic loading. Differences in volume fraction were achieved by changing the length of unit cells of the structure in the direction of loading (see Fig. 2-26). One of the main goals was to verify the hypothesis that a step-change volume fraction can lead to a reduction of the force peak at the beginning of impact loading and increases the energy absorption capacity.

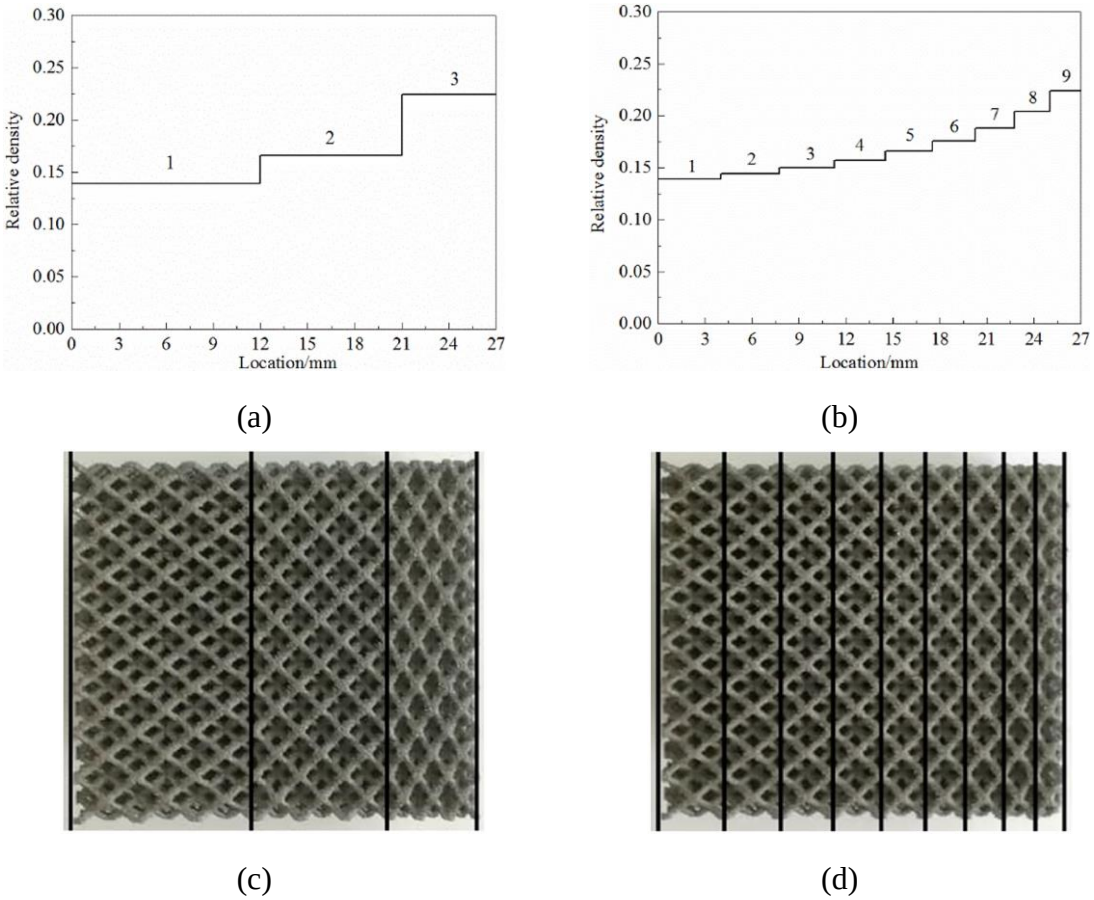


Fig. 2-26 Step change in volume fraction of the BCC structure shown graphically (a-b) and on the corresponding sample (c-d) [23]

The collapse strength metrics mentioned above [22] and energy absorption [14] were supplemented with specific strength $\sigma^*$ and specific plateau stress $\sigma_{pl}^*$. The collapse strength $\sigma$ was defined according to Gibson and Ashby [86, 87] for porous materials with solid struts and related to the relative density in a simple form:

$$\sigma = C\sigma_s\left(\frac{\rho}{\rho_s}\right)^{\frac{3}{2}} \quad [MPa] \tag{2-38}$$

where $\sigma_s$ and $\rho_s$ represent strength and density of the bulk material respectively, and C is constant which can be determined by experiments. The specific strength $\sigma^*$related to the material density was defined as follows:

$$\sigma^* = \frac{\sigma}{\rho} = C\frac{\sigma_s}{\rho_s}\left(\frac{\rho}{\rho_s}\right)^{\frac{1}{2}} \quad [MPa] \tag{2-39}$$

where $\rho$ denotes density of the lattice sample and $\rho_s$ density of parent material. The specific plateau stress $\sigma_{pl}^*$ was defined as follows:

$$\sigma_{pl}^* = \frac{\sigma_{pl}}{\rho}\int_{\varepsilon_s}^{\varepsilon_d}\sigma(\varepsilon)d\varepsilon/\rho \quad [MPa] \tag{2-40}$$

where $\sigma_{pl}$ denotes plateau stress, $\varepsilon_s$ strain related to collapse strength and $\varepsilon_d$=0.65 in the densification strain which corresponded to the origin of the rapid increase of stress.

The loading process was monitored by two high-speed cameras FASTCAM SA5 (frequency 50 KHz) to assess the deformation mechanisms characteristic of the lattice structures by 2D digital imaging correlation (DIC). The least squares search algorithm was used to analyze images using 27-pixel subsets with a step size of 2 pixels. The experimental study was supplemented by a numerical simulation in the LS-DYNA software. The modeling methods were taken from the Ozdemir study [26, 88].

A comparison of the experimental results with uniform conventional BCC structures showed that the specific strength and SEA were higher for structures with a gradient relative density. For the area of uniform deformations, before compaction of the material, the SEA was approximately 28% higher. The type of structure transition or the inclination of the load direction (in the vertical direction) did not have a significant impact on energy absorption in the range of tested velocities.

Tancogne-Dejean et al. [18] evaluated the deformation behavior of BCC structures produced by SLM technology (SS 316L) using analytical and numerical calculations. The author increased the values of Young's modulus and SEA of the structure by suitable strut tapering (see Fig. 2-27) [14].

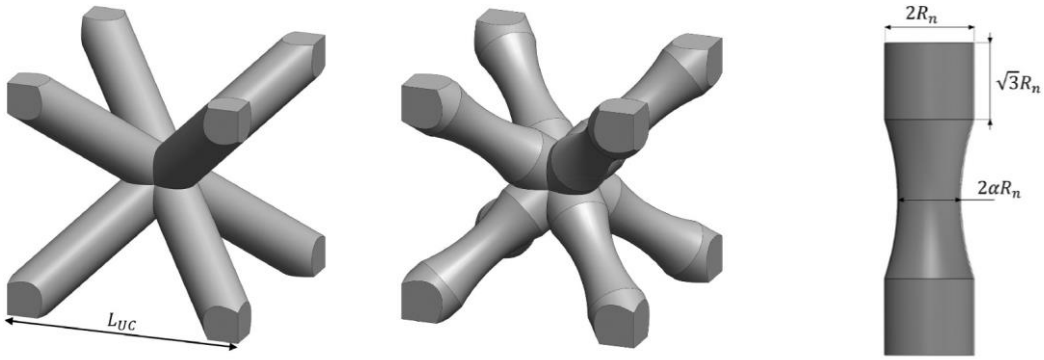


(a) (b) (c)

Fig. 2-27 Unit cell of BCC structure composed of (a) struts with constant circular cross-section (α = 1; unit cell length $L_{UC}$), (b) tapered struts (α = 0,7); (c) parameters describing strut geometry (strut diameter $R_n$) [18]

The dynamic response (Hopkinson test, 480 $s^{-1}$) of the material was similar to the quasi-static. The difference was described by a coefficient called the dynamic increase factor (DIF). An approximately 30% stress difference was observed for the structure with 10% volume fraction and different strut tapering. The DIF values confirmed the findings of the previous study [23] for the same parent material. Furthermore, it was determined that the DIF of the lattice structure was caused primarily by the sensitivity of the material to the strain-rate (not the topological configuration).

Zhao et al. [89] determined the properties of a mathematically defined modification of the BCC structure using a triply periodic minimal surface (TPMS) representation. Smooth transitions between neighboring struts were achieved by mathematical shape definition, resulting in a more favorable distribution of the applied stress when loading the structure (see Fig. 2-28) [90, 91]. The structure samples were subsequently made by SLM technology from $Ti_6Al_4V$, subjected to quasi-static pressure tests and compared with a conventional BCC structure.

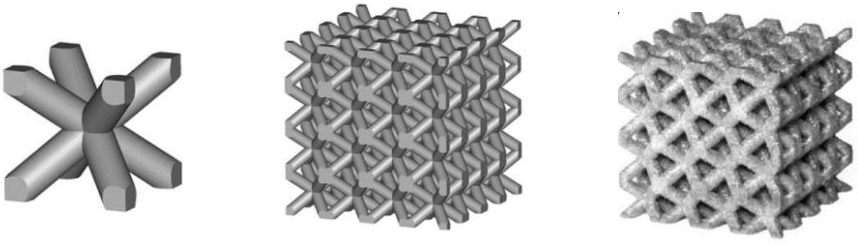

a) b) c)

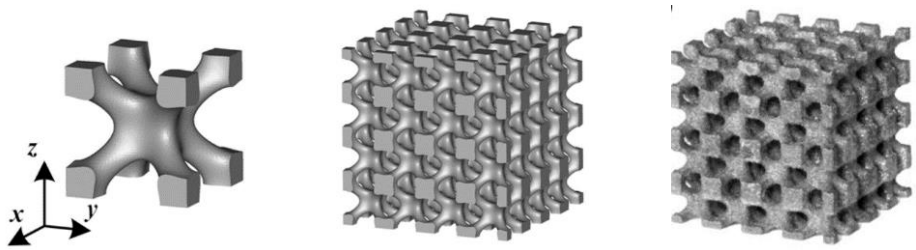


d) e) f)

Fig. 2-28 (a-c) conventional BCC structure, (d-f) modified BCC TPMS structure [89]

The energy absorption of the structures was determined by numerical integration of the stress curve up to 50% deformation according to ISO 13314: 2011 [92]. The similar method up to 30% strain was used by Dejean-Tancogne et al. (see eq. 2-22) [14]. To compare the load-bearing capacity after the first plastic failure, the coefficient K was presented by the following equation:

$$K = \frac{\sigma_{min}}{\sigma_b} \quad [-] \tag{2-41}$$

where $\sigma_{min}$ is the first lowest value of stress after the initial plastic failure and $\sigma_b$ is the compression strength and regarded as the first stress peak. The BCC TPMS structure achieved the larger amount of absorbed energy compared to the convention BCC configuration with the desired course of absorption (see Fig. 2-29).

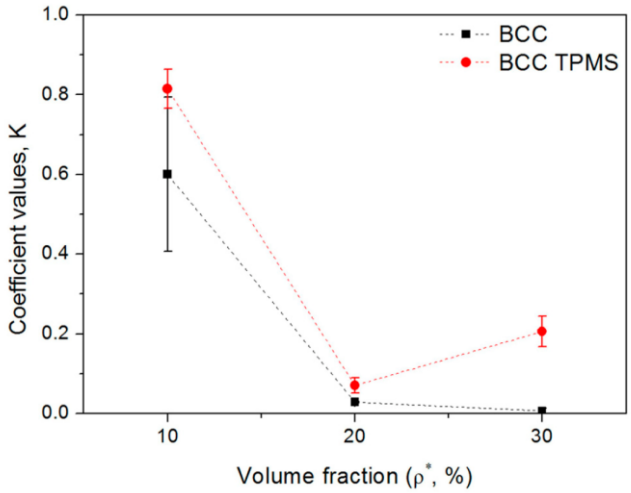


Fig. 2-29 Load-bearing capability of BCC and BCC TPMS after first plastic failure (three samples, means and standard deviations) [89]

The changes in the absorbed energy $W_v$ at different strain $\varepsilon$ was assessed:

$$W_v = a\varepsilon^b \quad [J] \tag{2-42}$$

where the coefficient *a* refers to the initial energy absorption capacity and the exponent *b* represents the increasing rate of cumulative absorption. The coefficient values increased with increasing volume fraction. The same author [84] used a similar procedure for more TPMS structures.

# 3 ANALYSIS AND CONCLUSION OF LITERATURE REVIEW

The following section describes the analysis of knowledge based on research papers from the field of non-linear structural FEM simulations, which consider the loading of lattice structures produced by additive technologies. It describes the most important modeling strategies and highlights their advantages and weaknesses. The key fragments of the analysis that require further investigation are summarized in the subsection at the end of this section.

## 3.1 Computational approaches

To understand the properties of lattice structures during mechanical loading, a series of FEM simulations was developed working with different representations of the structure geometries. The main aim of computational approaches was to explore the deformation pattern and estimate the behavior of the lattice structure. One of the first descriptions [34, 35] used beam elements based on Timoshenko's theory with a quadratic interpolation function suitable for simulation of larger structures. The model considered large deformations, allowed for bending, transverse shear deformations, and strut stretching [36, 93]. The simulations were computationally cheap, but the beam representation was unable to provide accurate results because of several simplifications. For this reason, a stiffness correction was introduced near the nodal points by implementing elements with artificially increased Young's modulus [27, 93]. Furthermore, it was recommended to modify the diameter and mass of the strut so that the beams in the vicinity of the nodes were equal to those of the real structure [13, 37]. At least four elements were used to discretize the non-modified middle part of each strut for linear elastic loading [51]. Despite the modification, the beam element model definition was accurate only in a certain range of strains.

To represent the topology of the lattice structure in detail, a tetrahedron element model of geometry with a quadratic interpolation function was created [27, 34]. This model provided a detailed description of the stress evolution across the strut cross-section. Its disadvantages were the high demands on hardware and computing times that limited the size of the structure and scope of the simulation.

An alternative option was to use the so-called homogenized model of geometry [13, 20]. This concept used hexahedral elements with independent mechanical properties in each loading direction which were equal to the properties of the lattice structure defined by compression tests. This approach allowed to solve computational problems of large structure deformations with omitting of complex interactions among struts in structures. On the other hand, its use for non-linear computations was shown to be significantly inaccurate.

One of the progressive approaches for the creation of a geometry model allowed the Python programming language [37]. The tool enabled the assembly of the beam element and tetrahedron element models with the actual measured shape of the strut. Furthermore, Python scripting made it possible to prepare code that divided struts of any cross-sectional shape into equivalent intervals with different diameter sizes [49, 90]. Individual diameters were assigned to the struts according to the experimentally measured probability intervals [37].

Persistent issues with the connectivity of the struts were investigated in concept using the modeling and loading of only a single strut enclosed in a lattice structure [38]. The approach was used to determine the effect of different joint connections of the struts on the stiffness of the lattice structure for solid or beam elements [42]. A similar method used in the following study [40] worked with models based on a combination of both types of elements. Some of the beam elements (Timoshenko representation) in the central cells of the loaded structure were replaced with tetrahedron elements. By this step, a so-called hybrid model was created. It provided a detailed overview of the development of stresses in the structure while maintaining low computational demands.

To achieve higher accuracy of simulations, the methods that allowed to implement manufacturing imperfections based on actual structure measurement were developed. One of the methods used μ-CT to capture actual information about the shape of the strut surface, including imperfections [44, 90, 94]. The Python script was used to automatically generate a beam element model. Therefore, the actual distribution of imperfections was considered when the geometry model was generated. It was in contrast to the approach described above [37] that works with the random assignment of strut diameters to individual segments [37]. Another similar model captured the waviness of the struts that vary along their length using a series of elliptical cross-sections created from μ-CT scan measurements [49].

Usually, software that worked with explicit solvers was used for computational tasks of dynamic events such as drop tests or impacts [13, 56, 60]. The explicit algorithm allowed to achieve longer duration of simulations considering large deformations until the structure densification. Then metrics that compared the performance of the structure, such as energy absorption, were applied. To achieve a similar comparison for quasi-static simulations, some authors used explicit solvers to simulate slow events with an artificial quasi-static condition (see eq. 2-1) [27, 41, 44, 45, 55]. The ratio of artificially increased energy and internal energy, as well as the ratio of kinetic energy, and internal energy, was kept below 5%. Sometimes, the equilibrium of the force reaction was required on the loaded side and on the opposite side of the structure [27]. Applied criteria allowed to create a simulation neglecting dynamic effects.

## 3.2 Models of material

The correctly defined material model was crucial for the simulation of the parent material behavior under mechanical loading. The model was represented by a mathematical description that determined the response of the material to mechanical excitations. Its development for the purpose of non-linear loading of lattice structures produced by additive technologies has been studied by many research teams [14, 20, 23, 27].

Most of the initial approaches worked with the definition of a bilinear elastic-plastic material model based on the tensile tests of the conventional sample produced according to DIN standards [51]. Unfortunately, the material parameters obtained by the tests of these samples did not accurately represent the structure behavior and the overestimated mechanical properties [28, 55]. Therefore, the samples were replaced with thin long strut samples [21] similar to struts of lattice structures [21]. Some authors directly used the same nominal strut diameter for samples and the corresponding structure [13, 55] to obtain the correct material parameters. However, the resulting parameters were strongly underestimated, as single strut samples tended to fragile fractures caused by local defects. Therefore, these tests were supplemented with a quasi-static compression of the structure [51]. Based on the compression test, the material properties were adjusted until the simulation and the experiment achieved compliance in terms of the deformation curve. It was concluded that this procedure was limiting in terms of material properties measurement accuracy and therefore had to be further modified.

Another issue was the exact measurement of the elongation of the struts under tensile loading [28]. Measurement was usually considered as the reading of the elongation directly from the displacement of the head of the test machine [21]. However, this procedure did not consider the slippage of a small circular sample in the jaws. An alternative type of measurement considered taking high-resolution images that captured the elongation of the test sample independently of the slip in the jaws [28]. The measurement method allowed to do the correction of the measured data in the post-processing.

The following methods offered the performance of tensile tests using samples composed of multiple struts joined to a single sample [19, 38]. According to the authors, the configuration of multi-strut samples better reflected the behavior of the corresponding structure because several struts participated in the load transfer. This method seemed to be sufficiently accurate and representative to obtain input parameters of a bilinear elastic-plastic model of the material (even for the J2-plasticity model) [14].

In addition to the approaches mentioned above, the literature offered the formulation of more complex models. Based on tensile tests and additional calibration, it was possible to construct a piece-wise linear (multi-linear) model with isotropic hardening [14]. This model allowed to better capture the development of stresses depending on the deformation of complex geometry. A more accurate representation was achieved using a so-called homogeneous isotropic Levy-von Mises model, which combined ideal plasticity with isotropic strain hardening [18]. However, the model did not consider the effect of possible anisotropy, loading rate, kinematic hardening, and martensitic phase transformation [27]. Other strain hardening models that used different fitting parameters were developed by Hollomon (see eq. 2-2) [61], Ludwik (see eq. 2-3) [62], Voce (see eq. 2-4) [63], and Ludwigson (see eq. 2-5) [60, 64].

The most advanced model of the material reflecting the loading of the lattice structure was the model called porous plastic GTN (in the Abaqus environment; see eqs. 2-6, 2-7, 2-8) [65, 66]. The input values of this model were obtained by compression test of structures and X-ray tomography. The deformation process of the structure was captured by in-situ and ex-situ tomography showing macroscopic structural and local micro-porosity. The reconstructed 3D images were then used to create a geometry model of the structure. A special procedure was used to assign local porosity properties to individual elements based on tomography images. Based on the results, models using a homogeneous matrix with an average initial porosity and a heterogeneous porosity distribution were prepared. The authors stated that the use of models for low porosity could have less effect on the resulting behavior of the loaded structure.

The above-described material models achieved different accuracy for lattice structure behavior estimation. However, even the most sophisticated model did not consider the effects of dynamic loading. Therefore, some of these models were supplemented by other constitutive laws that consider the dynamic effect. One of these laws was known as Cowper-Symonds [72], which reflected the strain-rate sensitivity of the parent material (see eq. 2-13). The input values of this law were obtained by a dynamic tensile test of special multi-strut samples [19]. An example was Hopkinson Bars specially modified to perform a tensile test (see eqs. 2-14, 2-15, 2-16) [75, 76].

An alternative constitutive law was Johnson-Cook (see eq. 2-10) [30, 33, 56]. In addition to the effect of the strain-rate, this law also included the effect of material thermal softening of the material and the effect of large plastic strains (strain hardening) [95]. The law was supplemented with a corresponding damage criterion based on the formation of a crack in the material when the critical strain value was reached (see eq. 2-12). Its input parameters were obtained using the Taylor test [7, 29, 33, 96]. For lower strain-rates where neglect of the thermal effect was possible, a simplified version was used that considered only the strain-rate and the large plastic strain effect (see eq. 2-9) [23, 24, 48].

## 3.3 Performance of lattice structures

The state of the art in the previous section showed that the non-linear FEM simulations used to estimate the deformation behavior of the lattice structures allowed to assess the energy absorption capabilities [23, 60]. Using validated computational models made it possible to test individual designs with changes in material, geometry, or loading conditions without the need of their production. Based on the software output data, the most efficient configurations were chosen [89]. It usually indicated the structures with the highest SEA (see eqs. 2-25, 2-34) [14, 17, 83]. However, this property was not the only determining parameter for a specific configuration selection. Other key characteristics included the course of absorption or its efficiency (see eqs. 2-31, 2-35) [14, 60]. The preferred type was uniform energy absorption under constant stress during progressive collapse of the structure [16, 20]. A stable stress level without extreme fluctuations (peaks) was especially required before the first plastic deformations occurred [1, 11, 97].

The stability of energy absorption was an issue that arose (see eqs. 2-26, 2-33) [18] when fragile materials with low ductility were used for the production of structures ($Ti_6Al_4V$, $AlSi_{10}Mg$) [23, 89]. During structure compression, the struts were loaded with combined stress [98]. The highest stress concentration occurred in the transition between the nodes and the struts. When the yield strength was exceeded, the strut-node interfaces started to rotate and were changed to plastic hinges. It caused cracks followed by fragmentation of the struts in the transition in the early stage of the deflection of the structure. As a dominant consequence, a collapse of the structure occurred along the slip planes [89]. Therefore, it was appropriate to prevent this phenomenon by using materials with high elongation at break, e.g., 316L stainless steel [14]. The natural properties of steel allowed for a large deflection of the structure until densification without fragmentation of the struts.

Except for the choice of parent material, the absorption of energy and the deformation pattern were fundamentally affected by the geometry of the basic elements of the structure called unit cells [99]. If these cells had high initial stiffness, usually caused by struts with an axis perpendicular to the loading direction, a step increase in applied stress occurred at the beginning of loading [13, 49]. The stress increased until buckling failure was achieved accompanied by plastic deformation of the struts (see eqs. 2-22; 2-38). This was followed by a rapid fluctuation of stress, usually associated with the collapse of several unit cells, unless the structure collapsed along the slip planes [100]. Therefore, it appeared to be efficient to use cells with lower initial stiffness and further modify them to increase absorption efficiency [18, 89]. An example of such a structure was the BCC lattice structure, which had already been partially modified for these purposes [23]. In addition, the use of the modified structure allowed to increase the capacity of the absorbed energy with a monotonically increasing stress during deformation [18].

## 3.4 Lack of knowledge – key points

Based on the analysis of the fundamental findings, certain aspects of lack of knowledge were drawn. Together with them, assumptions were raised for the supplementation of knowledge. Both are summarized in the following bullets:

- The development of non-linear computational models of lattice structures loading for quasi-static and dynamic deformation became an interest of many research teams. However, the model that would consider together aspects of important geometrical deviations, deformation behavior specifics of structures, thin strut material characteristics and dynamic effects does not exist. Including all the mentioned features would lead to a robust computational model that would be able to accurately estimate the deformation behavior of lattice structures.
- The input parameters of the material model for quasi-static loading of lattice structures are difficult to define based on the tensile test of single strut samples. Research results indicate that by using specially designed multi-strut samples with a nominal strut diameter that corresponds to the nominal strut diameter of the structure, a better representation of structure properties could be achieved. Additionally, it should eliminate problems with sample slip in jaw grips.
- The plasticity of a lattice structure made of 316L stainless steel by SLM technology could be represented by the linear or multi-linear dependency of a material model. For loading in an elastic area, a standard linear isotropic elasticity should mathematically sufficiently describe the loading until the yield strength is reached.
- As the loading velocity increases, the accuracy of the simulation decreases because the material model specified for quasi-static loading does not capture the effects of phenomena associated with dynamic loading. It should be sufficient to use a constitutive law known as the Cowper-Symonds or Johnson-Cook law to include the behavior of the metamaterial at elevated velocities. Their input parameters could be obtained using a high velocity tensile test (SHPB, Taylor test).
- The geometry of the structures created by the beam elements should include corrections of stiffness or diameters near the nodes to compensate for the actual contact of the struts in this area. The results of the modified simulation should be compared and verified by an equivalent simulation using the volume elements.
- Simulations of lattice structure loading require large deformations of samples to evaluate the absorbed energy. Solvers working with explicit algorithms commonly used for simulations of dynamic processes could be efficiently used even for quasi-static loading rates.

- Incorporating geometric imperfections of the manufacturing process related to a change of strut cross-section shape and area into the simulation should increase accuracy. It should be appropriate to use μ-CT scanning, X-ray tomography, or surface digitization methods to obtain input data of geometric deviations based on actual geometry. The measured data could be evaluated using automated Python or APDL language scripts and implemented in the geometry model as a constant or variable deviation.
- For structure production, it is necessary to use topologies and materials that lead to deformation characteristics corresponding to idealized energy absorption. This behavior could be described by the elastic deformation area followed by a smooth transition to the uniform plastic deformation area until the material compaction. Using the BCC lattice structure and its modifications made of SS 316L appears to be suitable for achieving the described characteristics.

Based on some of the assumptions for supplementing lack of knowledge, scientific questions and hypotheses were formulated. To test the hypotheses, the partial aims of the thesis were defined giving together the overall aim.

# 4 AIM OF THE THESIS

This dissertation thesis aims at developing a computational model that represents the deformational behavior of mechanically loaded lattice structures produced by SLM technology, primarily from stainless steel 316L. This model should include non-linearities arising from large deformations, the most significant manufacturing imperfections, and knowledge about the mechanisms of structural damage and failure for quasi-static and dynamic loading. To achieve the main goal of this thesis, the following steps must be taken:

- Identification and execution of experimental procedures required for the determination of the mechanical properties of thin struts.
- Identification and execution of procedures required to obtain actual geometry, including imperfections in the shape of the strut.
- Development of non-linear quasi-static FEM analysis using solid and beam elements.
- Calibration of the stiffness of the nodal connection for the beam element model to achieve compliance with the solid element model.
- Implementation of geometrical imperfections related to change of strut cross-section shape and area to FEM simulation.
- Determination of the dynamic behavior of the thin strut material and implementation of constitutive law reflecting the dynamic loading effects to the material model.
- Verification of computational strategy for different loading velocities and structure topologies.

## 4.1 Scientific questions

Upon analysis and review of the literature, the following scientific questions were identified:

Q1 How do geometric imperfections of the cross-sectional shape and size affect the compression response of the lattice structures with a nominal strut diameter in the range of 0.6-1.2 mm?

Q2 How does the non-linear material model based on multi-strut tensile samples with stiffness corrections influence the deformation behavior of the lattice structure with nominal strut diameter in the range of 0.3-1.0 mm made of 316L stainless steel by SLM technology?

Q3 How does the implementation of strain-rate sensitivity into the model of material influence the behavior of the 316L stainless steel lattice structure under dynamic compression loading in the range of $10^2$-$10^3$ $s^{-1}$ strain-rate?

## 4.2 Hypothesis

Each scientific question was tested through working hypothesis formulated on the basis of the state of the art and previous research.

**Working hypothesis 1**

H1 Lattice structures produced by SLM technology show signs of anisotropic behavior due to the layer-wise building process that leads to non-uniform geometric imperfections arising on the struts during production. The phenomenon is associated primarily with an increase in the load-bearing cross-section height of the strut, which leads to an increase in the mechanical properties in the direction of the building. As a consequence, a higher stiffness of the structure is expected to be observed. The most significant imperfections are expected for struts with smaller diameters, where a high energy input related to the melted area is delivered during production. With increasing diameters of the struts, the significance of imperfections is expected to decrease. However, in the range of investigated diameters, these imperfections have not yet been minimized to consider the mechanical properties change to be negligible.

Fundamental explanation: After manufacturing, inspections of the lattice structures revealed imperfections of several types. These are mainly the waviness of the struts [49], the rough surface, the change in the shape and diameter of the cross-section [17] or the internal porosity [65]. The occurrence of these imperfections is different for each material, structure type, and set of process parameters. The biggest influence on mechanical properties should have a combination of factors associated with the change in the diameter and cross-sectional shape of the strut [101]. As a result of the transfer of heat to the surrounding environment in the SLM production process, the powder particles of the raw building material are partially melted onto the surfaces of the struts. Most of them remain melted on the lower side of the struts [102, 103]. This causes a change (very often an increase) in the cross-section in the vertical direction, which is usually also the direction of structure loading. Changes in properties are the most significant for small diameters, where overheating can occur [55].

H2. LPBF scanning strategies applied to sample production create a different internal architecture for the subsurface and internal space of components with different material properties. The different proportions of subsurface and internal space for thin struts and DIN samples are expected to lead to a distinction in mechanical properties that cannot be neglected. It can be assumed that performing a tensile test of samples that contain a series of thin struts with nominal strut diameter similar to the struts of the structure is necessary. Furthermore, due to the simplified contact definition for the beam element model, a compression test of the structure should be required to reveal detailed characteristics of the deformation behavior. Based on the findings, stiffness corrections need to be done in the vicinity of the nodes to achieve the desired accuracy.

Fundamental explanation: The determination of the non-linear model of the material in the past showed that conventional tensile samples cannot fully reflect the deformation properties of the lattice structure [21, 37]. Detailed analysis of the samples revealed differences between the porosity of the subsurface layer and the internal volume part of the bodies [17]. These properties were attributed to applied scanning strategies. It led to a change in mechanical properties, namely, a weakening of the subsurface part with a higher proportion of porosity. In the case of conventional tensile samples, the ratio of the subsurface layer to the internal volume is negligible and therefore the weakening of the mechanical properties is not significant. Different situations occur in the case of struts, where the ratio of subsurface area to internal area is much higher and the weakening of mechanical properties increases. Therefore, the properties of the lattice structures should be obtained based on struts with the corresponding geometry [19, 38]. It includes the use of a similar strut diameter and manufacturing angle for the lattice structure and tensile sample. In addition, the models of geometry proposed for the lattice structure can suffer from several simplifications. As a consequence of these simplifications, inaccuracies occur in the structure deformation pattern and the resulting deformation response. To compensate for these simplifications, local corrections of the material model are required. A lattice structure compression test should be performed to determine the level of corrections required [51]. According to the experimental results, the stiffness of the elements around the nodes can be changed to ensure the calibration of the computational model [34].

H3 Monitoring of the 316L stainless steel properties under dynamic loading showed increased stress compared to quasi-static loading, even at a relatively low strain-rate of about $10^2$ $s^{-1}$. A similar effect is expected in the case of thin strut structures produced by SLM technology, assuming the same parent material. The stress difference between quasi-static and dynamic loading should increase with increasing strain-rate. Dynamic effects such as the sensitivity of the parent material on strain-rate, micro-inertia, dynamic strengthening, thermal softening, or large deformation effects become amplified. However, for low strain-rates, most of these effects have a negligible level compared to the strain-rate sensitivity, which becomes dominant. Therefore, it is expected that the inclusion of this effect into the material model of the structure will significantly increase the level of dynamic stress for intermediate strain-rates ($10^2$-$10^3$ $s^{-1}$) and improve the simulation accuracy.

Fundamental explanation: The behavior of the lattice structures under dynamic loading is relatively complex and differs from that of the base material [18]. At higher velocities, the effects of large deformations, micro-inertia, dynamic strengthening, etc. begin to rise [17, 60, 79]. The behavior of the parent material affects the sensitivity of the parent material to relative deformation. This effect can be described, for example, by the Cowper-Symonds [19] constitutive law. The input values of this law can be obtained by a dynamic tensile test of strut samples (SHPB) [75, 104]. Its advantage is relative simplicity; on the other hand, it considers only the sensitivity of the parent material to the strain-rate. To consider other influences, it is possible to use a combination of similar laws or replace them with more complex ones. For example, the Johnson-Cook constitutive law [24] accounts in addition for the large deformation effect and the temperature softening effect.

## 4.3 Thesis layout

The main part of the dissertation thesis consists of three scientific papers published in peer-reviewed journals with an impact factor. The first paper [I.] focuses on answering the first scientific question of how geometric imperfections of shape and size affect the mechanical properties of the lattice structure. To test the hypothesis, several lattice structures with different strut diameters were tested by a dynamic impact test in experimental and two computational regimes. FEM analyses allowed to investigate the influence of individual imperfections separately. The second paper [II.] answers the second scientific question on how the input parameters of the non-linear material model based on multi-strut tensile samples with stiffness corrections influence the deformation behavior of the lattice structure. In the first step, conventional and special strut tensile samples were designed and tested. The stress-strain results were evaluated using optical digitization methods. In the second step, lattice cubes with a wide range of volume ratios were designed and tested. The data were used for verification of the solid element model. Furthermore, information on the deformation pattern was used for local adjustments of the properties of the beam element model material. The third paper [III.] focuses on the third scientific question asking how the implementation of strain-rate sensitivity into the model of material influences the behavior of the lattice structure under dynamic compression loading. To test the hypothesis, data determined by several authors in the past were combined with results of dynamic tests of special multi-strut tensile samples. Based on curve fitting, regression parameters of the constitutive C-S law were obtained. The C-S effect was computationally tested for different structures at several loading velocities and further verified with the experiment.

I. VRÁNA, R.; ČERVINEK, O.; MAŇAS, P.; KOUTNÝ, D.; PALOUŠEK, D. Dynamic Loading of Lattice Structure Made by Selective Laser Melting-Numerical Model with Substitution of Geometrical Imperfections

*Journal impact factor = 3.748, Quartile Q2, CiteScore = 4.7*
*Author's contribution: 20% (40%)*

II. ČERVINEK, O.; WERNER, B.; KOUTNÝ, D.; VAVERKA, O.; PANTĚLEJEV, L.; PALOUŠEK, D. Computational Approaches of Quasi-Static Compression Loading of SS316L Lattice Structures Made by Selective Laser Melting. Materials, 2021, vol. 14, no. 9, p. 1-24. ISSN: 1996-1944.

*Journal impact factor = 3.748, Quartile Q2, CiteScore = 4.7*
*Author's contribution: 55%*

III. ČERVINEK, O.; PETTERMANN, H.; TODT, M.; KOUTNÝ, D.; VAVERKA, O. Non-linear dynamic finite element analysis of micro-strut lattice structures made by laser powder bed fusion. Journal of Materials Research and Technology, 2022, vol. 18, no. 1, p. 3684-3699. ISSN: 2238-7854.

*Journal impact factor = 6.267, Quartile Q1, CiteScore = 5.9*
*Author's contribution: 65%*

# 5 MATERIALS AND METHODS

To test hypotheses formulated on scientific questions, it was necessary to perform various types of experiments and FE analyses (see Fig. 5-1). The following section describes the equipment, methods, and experiments that were used to develop and verify a non-linear computational FEA of lattice structure loading, including dynamic effects and the most significant geometrical imperfections of manufactured structures. In the first step, dimensional analysis was performed on single strut samples and unit cells with different topologies to determine the actual deviations of the struts. Based on this measurement, the geometry models were prepared using the APDL programming language and Python scripts. In the second step, the mechanical tests of multi-strut samples were performed to determine the material model under quasi-static loading. The tests were supplemented with dynamic loading of similarly designed samples to obtain input parameters of a constitutive law for fast loading of structures. Then series of compression experiments with lattice structures were performed under strain-rates and compared with the computational model.

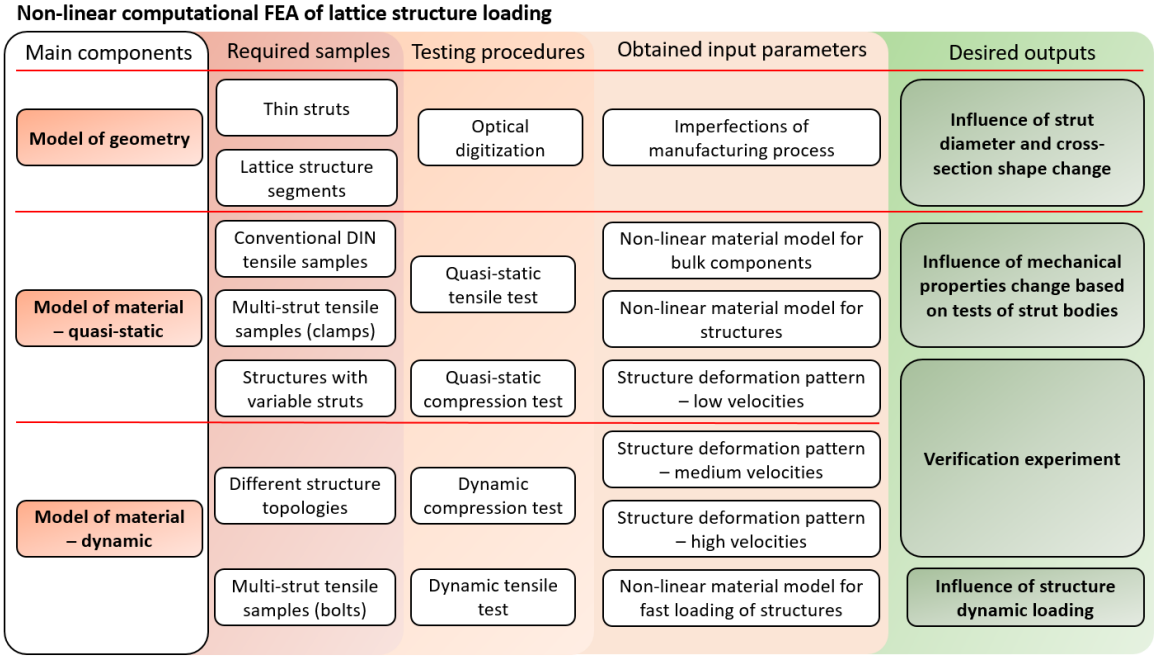


Fig. 5-1 Scheme of the most important methods and procedures used

## 5.1 Laser powder bed fusion

### 5.1.1 Process parameters

All samples for experimental testing were produced by SLM 280$^{HL}$ (SLM Solutions GmbH, Lübeck, Germany; building area 280 x 280 x 350 mm). The device was equipped with a YLR-400-WC-Y11 ytterbium fiber laser (IPG Photonics, Oxford, USA), which has a maximum power of 400 W with a Gaussian energy distribution in the focus spot with a diameter of 82 µm. Process parameters were selected primarily as a series of settings recommended by the machine provider for the SS 316L and $AlSi_{10}Mg$ materials (see Tab. 5-1). The selected scanning strategy was referred to as bidirectional hatching with two contours. The laser paths for each layer were rotated to each other about an angle of 67°. Setting equal parameters and production conditions for each manufacturing trial should guarantee equivalent mechanical properties and comparable deviations from the geometry of the samples.

Tab. 5-1 Basic process parameters of stainless steel 316L and $AlSi_{10}Mg$

| **Parameters** | **SS 316L** | **$AlSi_{10}Mg$** | **Unit** |
|---|---|---|---|
| Platform temperature | 100 | 150 | °C |
| Inert atmosphere | $N_2$ (> 0.2 % $O_2$) | $N_2$ (> 0.2 % $O_2$) | - |
| Layer thickness | 50 | 50 | µm |
| *Borders* | | | |
| Laser power | 100 | 300 | W |
| Scanning speed | 300 | 600 (500) | $mm \cdot s^{-1}$ |
| *Hatching* | | | |
| Laser power | 275 | 350 | W |
| Scanning speed | 700 | 1150 (930) | $mm \cdot s^{-1}$ |
| *Fill contours* | | | |
| Laser power | 150 | 250 | W |
| Scanning speed | 400 | 555 | $mm \cdot s^{-1}$ |
| Hatch distance | 120 | 170 (150) | µm |

Note: Values in brackets indicate parameters based on previous research used in the study.

### 5.1.2 Powder material

SS 316L and $AlSi_{10}Mg$ supplied by TLS Technik GmbH (Bitterfeld, Germany) were selected for sample production. Their chemical composition (see Tab. 5-2) was close to that of the materials produced by SLM Solutions. The particle distribution before the first recycling cycle was $Q_{10}$=10.07 µm, $Q_{50}$=29.44 µm and $Q_{90}$=48.21 µm for steel and $Q_{10}$=25.2 µm, $Q_{50}$=40.7 µm and $Q_{90}$=58.0 µm for $AlSi_{10}Mg$. The manufacturability of both materials has been tested with good results at the Institute of Machine and Industrial Design in the past. Therefore, the powders were found to be suitable for further research. It was decided not to continue with the development of the process parameters to maintain constant conditions. The powder materials were dried in an oven before each production.

Tab. 5-2 Result of chemical analysis of stainless steel 316L and $AlSi_{10}Mg$ powders

| **SS 316L** | | | | | | | |
|---|---|---|---|---|---|---|---|
| Elem. | Fe | C | Si | Mn | Cr | Mo | Ni |
| wt-% | Bal. | 0.03 | 0.8 | 1.8 | 17.5 | 2.2 | 11.3 |
| **$AlSi_{10}Mg$** | | | | | | | |
| Elem. | Al | Si | Mg | Fe | Ni+Cu | Other | |
| wt-% | Bal. | 9.8 | 0.35 | 0.14 | <0.02 | <0.1 | |

### 5.1.3 Samples

Models of samples for production were prepared in Inventor software (Autodesk, San Rafael, Californie, USA). Assignment of process parameters and data slicing was performed in Magics software (Materialize, Leuven, Belgium).

**Single struts for optical digitization** – were manufactured as 20 mm long distributed in the corners of the platform. Originally, the struts for optical inspection were produced as part of structures. The struts were manufactured with the same nominal diameter as the structure struts that cover all manufacturing angles of the struts in the structures (35.26°, 40.89°, 90°, etc.).

**Samples for tensile test (quasi-static, DIN 50125:2009-07)** – to compare mechanical properties with thin struts, conventional tensile samples were produced with a manufacturing angle of 90°. The effect of surface and subsurface porosity was eliminated by machining.

**Samples for tensile test (quasi-static, multi-strut)** – consisted of 12 parallel struts with a length of 28 mm in an arrangement of 3 x 4 struts (the minimum length for mounting the extensometer jaws was 20 mm) [105]. The multi-strut configuration was supposed to prevent a local weakening of the sample caused by pores in the strut that occur during the production. Additionally, the design of the samples was expected to better reflect the situation of the structure, where multiple struts participate in the transmission of applied forces [19, 38].

The samples were designed with a nominal strut diameter of 0.6 mm, which was further considered as a reference [55]. The manufacturing angle was set at 35.26° so that any geometric deviations and properties were mainly comparable to the properties of the BCC structure struts.

**Samples for tensile test (dynamic, multi-strut)** – were manufactured in a configuration similar to multi-strut samples for quasi-static tests. The length of the struts was preserved, but the arrangement of the struts and the fastening part was adjusted to the Hopkinson device (2 x 6 struts configuration) [19, 38].

**Structures for compression test (quasi-static, dynamic)** – were designed as lattice structure cubes of the BCC or FCC based type* [3, 27, 29], their combinations, and modifications with vertical struts [5, 99, 105, 106]. The dimensions of the structures were 20 x 20 x 20 mm with a unit cell side length of 4 mm. The strut diameter and the volume fraction differed according to the objective of the individual sample series. Due to the equivalent width to height dimensions, it was possible to observe whether slip planes occur on the sample diagonals during the pressure test [107]. Regarding the production method, solid cone-shaped supports were used to attach the lowest positioned nodes in the structure to build the plate (height 5 mm).

*Note: The basic cubic element called the unit cell of the BCC structure consists of eight struts. These struts correspond in their arrangement to the body diagonals that intersect at its center. The FCC unit cell consists of struts that correspond to the face diagonals. Both are self-supported (with limited side length).

## 5.2 Model of geometry

To obtain actual dimensions of the struts, the samples were digitized (see Fig. 5-2) after production with a blue light projection scanner ATOS Triple Scan (GOM GmbH, Braunschweig, Germany) [102, 108]. The scanner was equipped with MV170 optical lenses calibrated according to the VDI/VDE 2634 standard. Before scanning, the samples were coated with antireflective titanium dioxide (approx. 5 µm height layer) [109]. The resulting data in the form of 3D scans were evaluated using GOM Inspect (SR1, GOM GmbH, Braunschweig, Germany) [100, 110–112].

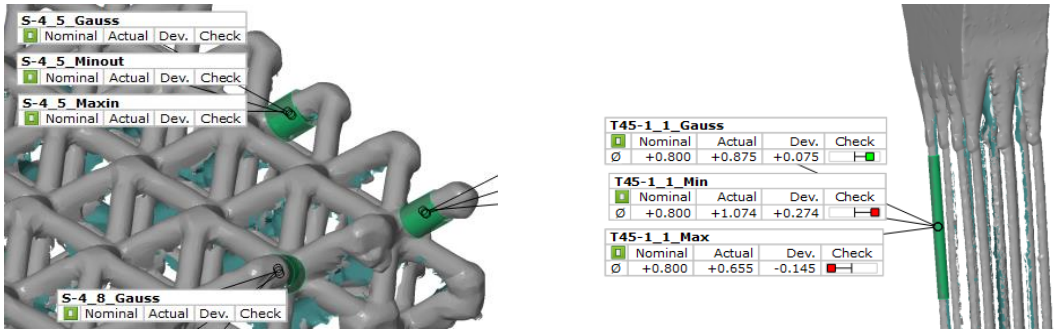


(a) (b)

Fig. 5-2 Example of strut part selection for inspection – (a) on structure; (b) on tensile sample

Scans of individual struts were divided into sections using a semi-automated GOM script. These sections were intersected with simple geometric shapes such as a circle or ellipse, which were used to approximate the actual shape of the strut [49]. The shapes were measured and statistically evaluated to achieve the average values of simplified cross-sections representing the actual geometry. Based on the simplified shapes, geometry models were created in the FEM software. The geometry of the struts was designed with constant or variable cross-sections depending on the aim of simulation.

After production, the structures were weighed with Sartorius MA35 (Sartorius, Göttingen, Germany) with a resolution of ±0.5 mg. According to the measurement, an estimation of the actual volume fraction was made using eq. 2-23. Together with information on the actual dimensions of the struts, it was possible to approximately calculate the porosity and/or the amount of powder aggregated on the struts [17].

## 5.3 Model of material

### 5.3.1 Determination of mechanical properties

To estimate the behavior of the lattice structure under mechanical loading considering plastic deformation, it was necessary to perform experiments with a thin strut material. Furthermore, to verify the computational models, structures were required to be compressed under different loading rates.

**Material properties (quasi-static)** – to obtain material properties of stainless steel for quasi-static loading uniaxial tests on a Zwick Z250 (ZwickRoell GmbH & Co. KG, Ulm, Germany) with a maximum force 250 kN was performed at strain-rate $10^{-3}$ $s^{-1}$ (see Fig. 5-3). At this strain-rate no inertia effect was expected. The tests were performed as compression of lattice structures (see Fig. 5-3 (a)) and tension of standard DIN and multi-strut tensile samples (see Fig. 5-3 (b)). The deformation of the samples was read from the clip-on extensometer attached directly to the sample. The transition of the measurement values from the sample to the sensor was short and stiff, resulting in a high level of accuracy.

To determine the engineering stress-strain curves of multi-strut samples, the force reaction was divided by the overall cross-sectional area of the struts in the sample determined by optical digitization before testing. Based on sample scans the actual cross-sections were calculated. The true stress-strain curves were determined using FEA. Based on the compression test results, a correction of stiffness in the near area of the nodes was made for the beam element model.

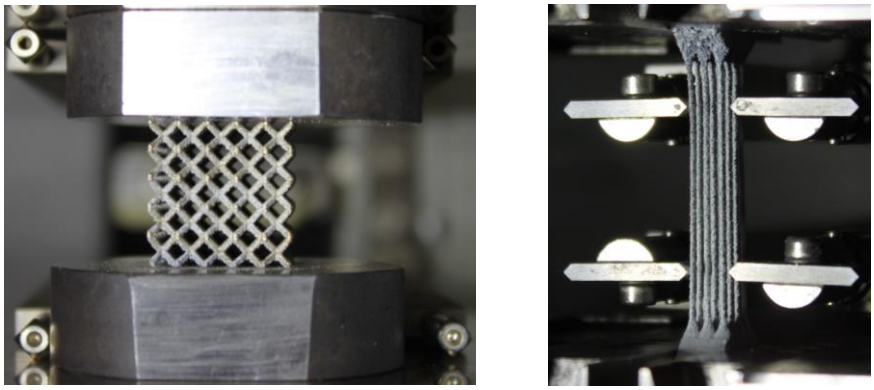

(a) (b)

Fig. 5-3 Mounting of the samples in Zwick – (a) compression test; (b) tensile test

**Material properties (dynamic)** – were carried out using modified split Hopkinson tensile bars (SVS FEM, Brno, Czech Republic) to determine the mechanical properties of 316L stainless steel under dynamic loading [19, 60]. The initial loading velocity was 30 m $s^{-1}$ (equal to approx. 175-250 $s^{-1}$). The samples were attached between the bars of the device using a bolt connection. Semiconductor strain gauges EP140-3-35-G (VTS Zlín s.r.o., Zlín, Czech Republic) with a nominal resistance of 350 Ω, a grid length of 3 mm, and a k-factor of +140 were placed in pairs in the middle of both bars. The strain gauges were connected in the half Wheatstone bridge configuration to eliminate any flexural stress on the bars. The signal emitted from the Wheatstone bridge was strengthened with amplifiers. The signal was further recorded with a high-speed oscilloscope with a recording frequency of 10 MHz.

The signals from the gauges were evaluated assuming uniaxial stress wave theory in the form of engineering stress $\sigma$ according to eq. 2-14, strain $\varepsilon$ according to eq. 2-15, and strain-rate $\dot{\varepsilon}$ according to eqs. 2-16, 2-17 [30, 72].

### 5.3.2 Constitutive law

The model of material was defined as a non-linear elastic-plastic model [5] based on tensile tests of multi-strut samples (see Tab. 5-3). For quasi-static simulations, the behavior of the material after exceeding the yield point was described as linear isotropic hardening [13]. Unlike the Grytten study [33], the model was not supplemented with a damage criterion (plastic strain failure or other), because SS 316L was ductile with high elongation at break and showed no signs of strut fragmentation even for large deformations [20, 27].

Tab. 5-3 Parameters of non-linear model of material

| **Parameters** | **Value** | **Unit** |
|---|---|---|
| *Isotropic elasticity* | | |
| Density | 7750 | $kg \cdot m^{-3}$ |
| Poisson's ratio | 0.3 | - |
| Young's modulus | 94 | GPa |
| *Bilinear plasticity* | | |
| Yield strength | 338 | MPa |
| Tangent modulus | 787 | MPa |
| *Hollomon plasticity* | | |
| Strength coefficient | 481 | MPa |
| Hardening exponent | 0.0656 | - |
| *Cowper-Symonds* | | |
| *D* | 80737 | $s^{-1}$ |
| *q* | 5.0075 | - |

The dynamic properties were described using a Cowper-Symonds constitutive law (see eq. 2-13) that considered the effect of the strain-rate, which was described for lattice structures by Ahmad et al. and Gümrük et al. [19, 113]. The law was combined with plasticity description using the Hollomon equation (see eq. 2-2) [60, 61].

### 5.3.3 Verification experiments

In order to verify the computational model at different loading rates, a comparative series of experiments were performed and compared to FEA.

**Quasi-static compression** (strain-rate approx. $10^{-3}$ $s^{-1}$) – was performed as a compression test of lattice structure cubes on Zwick described in section 5.3.1.. They were placed without fixing between the plate adapters of the device. The lower adapter was fixed on a movable bar in a vertical direction, and the upper adapter was mounted on a static joint connection to allow slight tilting.

**Dynamic compression** (strain-rate approx. $10^{2}$ $s^{-1}$) – was performed as a drop-weight test on the impact tester (Impactor 2.1, BUT, Brno, Czechia) with a maximum weight of 13.45 kg and a fall height of 1.1 m [114, 115]. For these parameters, a crosshead was able to achieve a drop velocity of approximately 3.5 $m \cdot s^{-1}$ [69], equal to impact energy of 60.5 J [17, 43, 90]. The device was equipped with a Phantom V710 high-speed camera (Vision Research, Wayne, New Jersey) and a strain gauge XY31-3/120 (HBM GmbH, Darmstadt, Germany). The strain gauge measured the reaction force during the deformation of the lattice sample, whereas the high-speed camera measured the position of the marker on the falling head to capture the deformation of the sample. A strain gauge signal was recorded using the Quantum MX410B data acquisition system (HBM GmbH, Darmstadt, Germany). The high-speed camera used Phantom Camera Control software version 3.5 for recording (Vision Research, Wayne, NJ). Both records were compounded and evaluated in MATLAB R2021a software (MathWorks, Natick, Massachusetts). An indenter placed on the head was flat with a diameter of 32 mm.

**Dynamic compression** (strain-rate approx. $10^{3}$ $s^{-1}$) – was performed on a Hopkinson device similar to that described in Section 5.3.1.. The device was based on the principle of moving bars toward each other, causing high-speed dynamic compression of the structures, as described by Nolting et al. [72, 75].

## 5.4 Computational approaches

Non-linear simulations of structure compression were created in the ANSYS Workbench software (Ansys Inc., Canonsburg, Pennsylvania, USA) using several approaches. Geometries for solid element models was created in the Inventor software. For beam element models, APDL and later Python script API v19 were used. Scripting allowed to accurately model geometry of struts including geometrical imperfections and define material properties on single element resolution. The quasi-static simulations were prepared in a module called Static Structural using the Mechanical solver, while the dynamic simulations were prepared in the module Explicit Dynamics [55, 89] using the AUTODYN solver. Both types of simulation, quasi-static and dynamic, were prepared using two different approaches.

The first of them used solid tetrahedron elements type SOLID 187 with quadratic base function for discretization of modeled geometry. It allowed a detailed assessment of the development of stress in individual struts and geometrical transitions between struts and nodes. The model was considered as a reference and was used to simulate the loading of smaller structures and mild non-linearities.

The second model used beam elements type BEAM 189 based on Timoshenko's beam theory to create more extensive parametric studies. It allowed to monitor the development of energy absorption for different structure configurations. In this model, the stiffness of the elements in the vicinity of the nodes was modified according to the experiment and the reference solid element model to simulate the real contact of the struts (see Fig. 5-4) [35].

Special attention was paid to the quality of the polygonal mesh, which can have a high impact on the validity of the results. Furthermore, both types of models were subjected to a mesh sensitivity study to determine the appropriate number of elements to divide the strut length or its cross-section [14, 34, 51].

The other setup was related to the loading conditions. The structure was placed between rigid plates with artificially increased stiffness that represented surfaces of static support and deformational member similar to the experiment. For the discretization of both plates, shell elements of type SHELL 93 were used [45, 65]. Both plates were modeled in proximity to the structure to shorten computational times and eliminate the inaccuracies that would occur when the indenter passed through free space.

Subsequently, frictional contacts that allowed sliding and separation on the target surface were defined at the interfaces of the deformation member-structure and the structure-static support. Tabular values for the steel-steel contact for both static and dynamic friction coefficients (dry degreased surface – static 0.15-0.2 and dynamic 0.1 for the steel-steel interface) were considered. In the next steps, the boundary conditions, load velocity, and other computational settings were defined according to the specific purpose of the task.

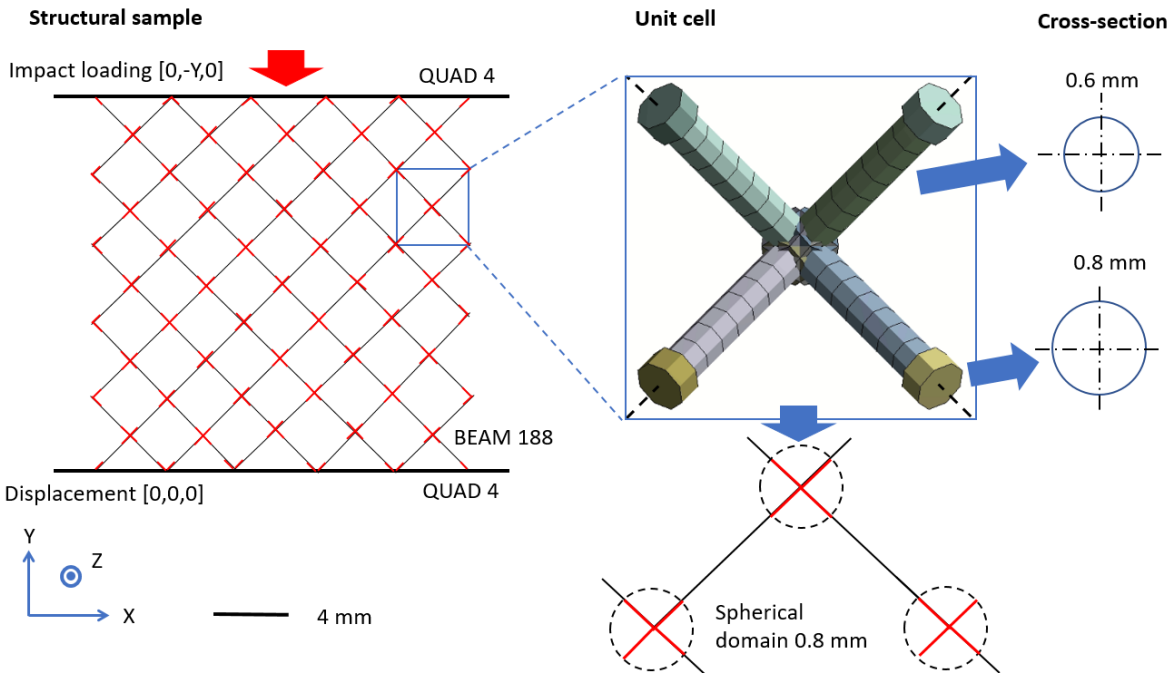


Fig. 5-4 Beam element model of BCC lattice structures with stiffness corrections and diameter changes

# 6 RESULTS AND DISCUSSION

The following section presents a summary of the most important results, especially in the field of non-linear computational modeling strategies that involve quasi-static and dynamic loading of lattice structures. The first part is divided into three subsections according to the main research papers. The subsections focus on the geometry model with the inclusion of the most significant geometrical imperfections, determination of the accurate model of material that represents properties of lattice structures, and constitutive law that reflects dynamic effects of structure deformation. Each subsection is dedicated to testing one of the above-mentioned scientific hypotheses. The second part consists of full versions of research papers in which the results are discussed in detail.

## 6.1 Research paper I

The key findings of Research Paper I were related to the geometry model. Most of the attention was paid to a novel approach to include geometrical imperfections of the manufacturing process. The proposed methodology workflow was based on optical digitization of structure segments after the manufacturing process. The scanned struts were cut in several cross-sections and interlaced by several simplified shapes of a circle and ellipse. This step allowed to accurately find the actual cross-section shape and its dimensions. Simplified shapes were used to make an equivalent comparison of geometries and create models suitable for FEM analyzes.

In the paper, the BCC lattice structure made of aluminum alloy $AlSi_{10}Mg$ with different parameters was investigated using an impact test and corresponding FEM analysis. In the first step, digitization of the structure segments was performed with a nominal strut diameter of 0.8 mm (section 5.2.). After digitization cross-sections were done in the mid-length of chosen struts. These cross-sections formed significantly irregular shapes similar to a water drop. In the next step, they were interlaced with circles according to several governing rules: maximum inscribed, minimum circumscribed, and circle with Gaussian distribution (with three-sigma accuracy). Additionally, an elliptical approximation of the actual cross-sectional shape was included because it better approximated the shape of the water drop.

The measurement results were consistent (0.94±0.08 mm for the circle with Gaussian distribution), but the different governing rules of the cross-sectional approximation showed significant differences in the measured diameters. The largest differences were observed for the diameters of the maximum inscribed and minimum circumscribed circle diameters (0.74±0.08 mm for the maximum inscribed circle and 1.25±0.17 for the minimum circumscribed circle). The result was attributed to the significant non-circularity of the measured sections (average minor/major axis ratio 0.71). Therefore, it was decided to compare experiment with FEM simulations for nominal geometry, geometry created with Gaussian distribution and elliptical cross-section. It allowed to assess the influence of imperfections independently.

The results were compared in terms of force reaction, duration of deformation, and deformation pattern. Initial comparison of experiment and simulation with nominal geometry of struts showed a significant underestimation of deformation resistance. The geometry was, therefore, modified according to the measurements, and the simulation was recalculated. It was shown that simulation considering the cross-section with circular Gaussian distribution achieved lower values of force reaction at the beginning of the plastic deformation compared to the experiment (approx. 12% difference). In addition, the duration of the deformation differed about 21%. In contrast, geometry created with elliptical cross-section achieved a good agreement of the force reaction compared to the experiment (approx. 2% difference). The comparison also showed a similar deformation pattern.

In the next step, a similar optical measurement and experimental testing procedure were performed for structures with nominal strut diameters in the range of 0.6-1.2 mm. Measured data were extrapolated with the linear function to show general trends. The percentage difference between the measured Gaussian and nominal diameters was concluded to decrease with increasing nominal diameters: 29% for 0.6 mm, 16% for 0.8 mm, 9% for 1.0 mm, and 4% for 1.2 mm. Based on the measurement results, the simulations with circular Gaussian and elliptical cross-sections were prepared for the remaining diameters equivalent to 0.6 mm, 1 mm, and 1.2 mm.

The results showed a good agreement between the experimental data and the numerical models that used elliptical geometry. Differences in terms of structure reaction forces were 29% for 0.6 mm, 6% for 1 mm, and 1% for 1.2 mm nominal diameter equivalent and deformation differences were 5% for 0.6 mm, 14% for 1 mm, and 5% for 1.2 mm nominal diameter equivalent. Bigger overall differences were observed for geometries that used circular cross-sections with Gaussian distribution. For reaction forces were 16% for 0.6 mm, 16% for 1 mm, and 14% for 1.2 mm nominal diameter equivalent and for deformations were 6% for 0.6 mm, 21% for 1 mm, and 23% for 1.2 mm nominal diameter equivalent. The last findings showed that the geometrical imperfections differed according to the strut diameter. It confirmed that the inclusion of manufacturing imperfections must be considered individually for each geometry, material and manufacturing setup. Furthermore, it showed that the inclusion of imperfections related to the shape and size of the cross-section can be sufficient to achieve accurate results.

## 6.2 Research paper II

The key findings of Research Paper II were related to the model of the material. The main aim was focused on the determination of material properties specific to thin struts of lattice structures and the assembly of the non-linear material model. The proposed workflow was based on the development of a special multi-strut tensile sample that was able to reflect conditions of lattice structure under loading. The course of the elastic-plastic response of loaded samples gave a detailed overview of which mathematical equations were required for the description of material behavior. The model developed for this purpose was adopted by simulations that used the solid and beam element model. Both types of simulations were further compared with the experiment and evaluated by several metrics.

The study focused on the BCC lattice structure made of 316L stainless steel using SLM technology under quasi-static loading. The nominal diameter of the strut changed in the range of 0.3-1.0 mm.

In the first step, special multi-strut tensile samples were designed with a nominal strut diameter of 0.6 mm determined by the state of the art [19, 38]. In the next step, special samples were manufactured together with conventional samples and tested on the Zwick device.

The comparison of the different tensile samples showed a significant difference. Although the properties of conventional tensile samples (DIN 50125:2009-07, $E$=166±15 GPa, $Ys$=450±5 MPa) were comparable to the properties provided by SLM Solutions (DIN EN 10088:2014, ASTM A276, $E$=178 GPa, $Ys$=529 MPa, [116]), multi-strut tensile samples showed a decrease in the observed properties ($E$=94±10 GPa, $Ys$=338±20 MPa). Further investigation of multi-strut samples showed a 49% lower Young's modulus compared to the single strut test with the numerical corrections performed by Smith et al. [51]. In contrast, a comparison of the dual mode module described by Li et al. [28] showed an increase of approximately 30%. A good agreement of Young's modulus and other properties was achieved for the study by Gümrük et al. [27] who used similar samples. The wide range of properties can be explained by the different process parameters and geometry. These factors play an important role, especially in the production of thin-walled samples.

In the following step, the non-linear elastic-plastic material model based on the results of multi-strut tensile samples was adopted by numerical simulation. An optical digitization procedure similar to the previous study was performed to obtain manufacturing imperfections. Based on findings geometry models with circular Gaussian and elliptical cross-sections were prepared.

The first simulation considered only the linear elastic behavior of the material without including imperfections. For this setup, one solid element and two beam element models [34, 117] were compared with the experiment in terms of structure compressive modulus. One of the beam element models was prepared with modification of the nodal stiffness according to the Luxner study (1000 times higher Young's modulus) [34]. The radius of correction for stiffness in the vicinity of the node was determined as a value of the nominal strut diameter +0.2 mm. The comparison showed that the compressive modulus of the structure without modifications was in good agreement with the experiment for all tested strut diameters (with an average error of 14%) [117]. In contrast to this, the beam element model with stiffness corrections was in good agreement with the experiment only for smaller strut diameters up to 0.6 mm. The compressive modulus then increased significantly. A similar behavior was observed for the solid element model, which was according to expectations in compliance with the beam element model that included stiffness corrections.

Then the non-linear behavior was included in the material model. For this setup, four beam element models were compared: the model with nominal geometry [117], the model with nominal geometry and stiffness corrections [34], the model with circle Gaussian cross-sections and stiffness corrections, and the model with elliptical cross-sections and stiffness corrections. This time, both models with nominal geometry were shown to be consistent with the experiment in terms of compressive modulus (with average error of 18% and 10%, respectively). On the other hand, models with modified cross-sections manifested higher stiffness compared to experimental values, especially for intermediate strut diameters (approx. twice in the range of 0.5-0.8 mm nominal diameter equivalent). It indicated that the different nominal cross-sections were influenced by the imperfections irregularly.

Three of these models were further compared with the experiment in the area of plastic deformations in terms of initial collapse stress, plateau stress at 30% strain and volume energy absorbed up to 30% strain (see eqs. 2-22, 2-26, 2-40). The model with nominal geometry [117] appeared to have insufficient stiffness compared to the experiment. The lack of stiffness became significant with increasing strut diameter, and therefore the model was eliminated. Contrary to that, results closer to the experiment showed models with nodal stiffness modification and Gaussian, respectively, elliptical cross-section even for higher strut diameters. The most accurate results were achieved with elliptical cross-section and stiffness corrections, which confirmed findings from the previous study and justified the model of material developed in this research paper. Differences that occurred for simulations with larger strut diameters were caused by slightly different material properties for each diameter.

In the last step, a larger lattice structure was produced and tested in a similar way. A comparison of the experiment and the finite element analysis confirmed the functionality of the simulation using a non-linear model of the material based on multi-strut tensile samples with the inclusion of local modifications and geometrical imperfections (up to 11% difference in terms of stress at 0.3 strain).

## 6.3 Research paper III

The key findings of Research Paper III were related to the inclusion of dynamic loading effects in the material model. The study focused on the determination of the strain-rate sensitivity of the parent material for thin struts and its mathematical description. The proposed methodology workflow was based on the fast tensile test of multi-strut samples on a modified Hopkinson bars device. The result of this test quantified the differences between dynamic and quasi-static behavior determined in the previous study. Both series tested at different velocities were supplemented with data from other authors [19, 73, 74] and fitted with curves. According to the polynomial description of the curves, the most accurate input parameters of the constitutive C-S law were found. The material model containing this constitutive law was applied for simulations of lattice structure compression at different loading velocities.

In the paper, several BCC and FCC based lattice structures made of stainless steel 316L with different parameters were investigated using experiment and FEM analysis of compression tests with different strain-rates. The governing nominal diameter was chosen at 0.6 mm for all struts, which led to a different volume fraction depending on the type of structure. Furthermore, the stand-alone struts were manufactured with different manufacturing angles, representing the angles of the struts in the structures. The struts were further digitized and geometry models were prepared based on measurement results similar to those of previous studies.

The results of the dynamic tensile test showed good agreement with three sets of C-S law parameters from the author that tested thin struts in a similar multi-strut composition [19]. The parameters set in the original study were defined as 1 – up to 100 $s^{-1}$ based on yield stress; 2 – up to 6600 $s^{-1}$ based on yield stress; 4 – Estimation. All the mentioned sets were adopted by the material model and used in the simulation performed at intermediate strain-rates ($10^2$-$10^3$ $s^{-1}$). The results compared to the experiment of six different structures in terms of initial collapse stress, plateau stress and SEA showed significant differences.

The initial collapse stress was consistent for parameter sets 1 and 2 but differed from the simulation with parameters 4. Compared to the experiment, the simulation with parameters 1 and 2 was much closer to the average values of the experiment. On the other hand, when plateau stress and SEA were compared, parameter setup 4 showed better compliance with the experiment. However, the consistency of the simulations using setups 1 and 2 remained preserved.

In the next part, parameter set 4 was used for simulations of BCC lattice structure compression performed under different strain-rates. To compare them with the experiment, the data from quasi-static testing from the previous study had to be supplemented with intermediate and high loading rates (approx. $2.2 \cdot 10^3$ $s^{-1}$). The comparison of simulation and experiment in terms of initial collapse stress showed a relatively good agreement across the range of tested strain-rates. It showed that a similar approach can be used in the future for different structure topologies or process parameters.

# Dynamic Loading of Lattice Structure Made by Selective Laser Melting-Numerical Model with Substitution of Geometrical Imperfections

**Article** *in* Materials · October 2018

DOI: 10.3390/ma11112129



**5 authors**, including:

Radek Vrana
Brno University of Technology
**9** PUBLICATIONS **14** CITATIONS
SEE PROFILE

Ondřej Červinek
Brno University of Technology
**1** PUBLICATION **0** CITATIONS
SEE PROFILE

Pavel Manas
Univerzita Obrany
**23** PUBLICATIONS **24** CITATIONS
SEE PROFILE

Daniel Koutny
Brno University of Technology
**30** PUBLICATIONS **126** CITATIONS
SEE PROFILE

materials

MDPI

Article

# Dynamic Loading of Lattice Structure Made by Selective Laser Melting-Numerical Model with Substitution of Geometrical Imperfections

**Radek Vrána [1,*], Ondřej Červinek [1], Pavel Maňas [2], Daniel Koutný [1] and David Paloušek [1]**

[1] Institute of Machine and Industrial Design, Faculty of Mechanical Engineering, Brno University of Technology, Technická 2896/2, 616 69 Brno, Czech Republic; Ondrej.Cervinek@vut.cz (O.Č.); Daniel.Koutny@vut.cz (D.K.); David.Palousek@vut.cz (D.P.)

[2] Department of Engineer Technology, Faculty of Military Technology, University of Defence, Kounicova 65, 662 10 Brno, Czech Republic; Pavel.Manas@unob.cz

* Correspondence: Radek.Vrana@vut.cz; Tel.: +420-541-144-927

Received: 9 October 2018; Accepted: 25 October 2018; Published: 29 October 2018

**Abstract:** Selective laser melting (SLM) is an additive technology that allows for the production of precisely designed complex structures for energy absorbing applications from a wide range of metallic materials. Geometrical imperfections of the SLM fabricated lattice structures, which form one of the many thin struts, can lead to a great difference in prediction of their behavior. This article deals with the prediction of lattice structure mechanical properties under dynamic loading using finite element method (FEA) with inclusion of geometrical imperfections of the SLM process. Such properties are necessary to know especially for the application of SLM fabricated lattice structures in automotive or aerospace industries. Four types of specimens from AlSi10Mg alloy powder material were manufactured using SLM for quasi-static mechanical testing and determination of lattice structure mechanical properties for the FEA material model, for optical measurement of geometrical accuracy, and for low-velocity impact testing using the impact tester with a flat indenter. Geometries of struts with elliptical and circular cross-sections were identified and tested using FEA. The results showed that, in the case of elliptical cross-section, a significantly better match was found (2% error in the $F_{max}$) with the low-velocity impact experiments during the whole deformation process compared to the circular cross-section. The FEA numerical model will be used for future testing of geometry changes and its effect on mechanical properties.

**Keywords:** finite element analysis (FEA); low-velocity impact; numerical model; lattice structure; material model; ANSYS Workbench; aluminum alloy AlSi10Mg; energy absorption

## 1. Introduction

Energy absorbers made of porous materials are currently used to absorb mechanical energy caused by impact or high velocity deformation due to their high efficiency of energy absorption and low weight [1–3]. There are several types of commercially produced porous materials, e.g., hexagonal honeycomb structures [4], metal foams [5–7], or laminated composite fiber blocks [8]. Mostly, the aluminum foams are used. They usually have porosity about 75–95% with a large amount of closed gas pockets and irregular porous structure. This material is usually used in the form of sandwich panels to achieve a higher absorption effect through uniform distribution of stress during loading.

An alternative way to produce porous materials with precisely controlled shape of porous geometry is the SLM technology [9]. SLM uses a layer-based production which allows for the manufacturing of the porous material with a complex shape that can be designed directly for the expected amount of impact energy. Using SLM, it is also possible to integrate screw holes or other

fixation elements to the porous material. Unlike conventionally produced materials, SLM allows the production of the porous material from various alloys such as titanium or tool steels alloys [10]. The most commonly used shape of lattice structure produced by SLM is BCC (Body Centered Cubic) [9,11]. BCC geometry corresponds to body diagonals of the cube. It consists of eight struts intersecting in its center. Orientation of the struts in BCC structure is 35.26° compared to $xy$ plane.

During SLM production of the lattice structure, geometrical imperfections occur. They are caused by struts orientation and heat transfer to the surrounding metal powder. Consequently, the laser process parameter needs to be optimized for SLM production of lattice structure [12–19]. Vrana et al. [19] deal with the SLM processing strategy for strut-lattice structure production, which uses only contour lines and various combinations of main process parameters. The authors focused on the evaluation of the influence of a laser scanning strategy on material properties and surface roughness. The best results were achieved with 25% track overlapping, input energy $E_{imp}$ in the range from 9 J to 10.5 J and linear energy $E_{lin}$ from 0.25 to 0.4 J/mm; in particular, the relative density of 99.83% and the surface roughness on the side of the strut of Ra 14.6 μm in an as-built state was achieved. Geometrical imperfections are mainly shape deviations created by sticking of the partly melted powder particles onto the down skin side of struts [19–21], high surface roughness, and internal porosity. Sticking of powder was also dealt with by Koutny et al. [20]. These authors studied the influence of SLM production orientation on the real diameter of struts. The results show a dependence between the struts diameter and production orientation. In the case AlSi10Mg, the diameter of the struts was always larger, and their true diameter changed with orientation of the strut (compared to the platform). Qui et al. [14] also examined the influence of laser process parameters onto the strut diameter. The results show that single struts manufactured by SLM had a larger diameter than nominal. The diameter increased monotonically with higher laser power and it significantly improved compression mechanical properties of the lattice structure compared to the assumption. Similar results were achieved by Vrana et al. [22] in the case of lattice structure under low-velocity impact loading. The results from mechanical testing show a significant improvement of the impact resistance due to the strut diameter increase.

For efficient design of energy absorber, it is necessary to use FEA to predict mechanical properties of the part during impact load. There are two main approaches to the numerical models of porous materials. The former uses a homogenized model of geometry and the latter uses a simplified model of real geometry [2,4,23–27]. The method of how to simplify the real shape of the lattice struts for FEA was described by Suard et al. [21]. They studied the shape of the lattice structure struts produced by EBM technology. A Computed tomography (CT) analysis was used for a detailed 3D scan of the strut surface. For geometry simplification in FEA, the effective volume corresponding with the maximum cylinder inscribed in the strut was defined. Koutny et al. [20] measured the shape of struts specimens using optical measurement. Similar to the previous author, the maximum inscribed diameter was used for the evaluation of mechanical properties.

Porous materials have a specific impact loading behavior due to the topology of core geometry. Therefore, in the case of homogenized geometry, it is necessary to use a suitable material model that considers its deformation behavior. Material models of porous structures, such as honeycomb or metal foam, are usually included in the material library of the FEA software, and it is possible to also use them for lattice structure [10,26–28]. According to Mohmmed et al. [26], a crushable foam material model is suitable for simulation of penetration of porous foam blocks with a damage criterion describing the occurrence of breakdowns between the core and plates. Input material constants can be obtained from uniaxial compression tests according to ASTM D5308. Labeas et al. [27] used both ways; the material model Mat-26 Honeycomb (LS-Dyna) to create a dynamic FEM simulation with a homogenized micro-lattice core and the bilinear (multilinear) material model with micro-lattice BCC structure geometry. The results showed that the simplified core is only suitable for prediction of the first progressive collapse of the lattice structure, while the beam geometry allows for the prediction of the whole deformation process due to the preserving topology of the core. Based on previous studies [10,26,27], it is possible to determine boundary conditions, type and density of

polygonal mesh, type of contact between bodies. It is necessary to consider the difference between the core and plate material model and the damage criterion [19,24,29,30] that needs to be added.

The authors [31–33] examined mechanical properties of AlSi10Mg alloy produced by SLM technology. As tensile specimens, the standard or flat specimens in the as-build or machined condition were usually used. Kempen et al. [33] showed various mechanical properties depending on the SLM production orientation. Specimens with *xy* orientation achieved a higher elongation compared to the z direction. The influence of the strut shape and SLM process parameters was dealt with by Tsopanos et al. [34]. In their study, the single struts from 316L alloy were tested. The results showed significant differences between the mechanical properties of struts with internal porosity or non-melted particles compared to the well melted struts. It is caused by small dimensions of struts compared to the standard tensile specimens. Therefore, special multi-strut tensile specimens were designed in this study.

Porous materials as honeycomb or metal foams are already used as a highly effective absorber in industry. Currently, metal additive technologies such as SLM can be used as one of the ways for production of energy absorbers. Thanks to the additive production, it is possible to customize the absorbers for specific impact loading by the structure shape design (various areas with a different type of structure, gradient structure [35], etc.) or by the used material. SLM technology also has a few technological limitations that should be considered in FEA. In the case of thin struts production, small shape deviations can occur. Due to the high number of the struts inside the lattice structure, these imperfections can influence mechanical properties of whole structure. Therefore, this study deals with the influence of SLM technology imperfections during struts production and their mechanical response in FEA.

## 2. Materials and Methods

### *2.1. Speciments Fabrication Using SLM*

All sets of specimens were manufactured using SLM 280HL machine (SLM Solutions GmbH, Lübeck, Germany) which is equipped with a 400 W Ytterbium fiber laser (YLR-laser) with Gaussian shape of energy distribution and spot diameter 82 μm. Laser scanning speed may reach up to 10.000 $mm \cdot s^{-1}$. During SLM process, the $N_2$ atmosphere was used in a chamber which provides 280 × 280 × 350 mm build envelope. To ensure the same conditions during the manufacturing process, each set of specimens were produced in one build job (Figure 1a). Standard process parameters (SLM Solutions) were used (Figure 1b).

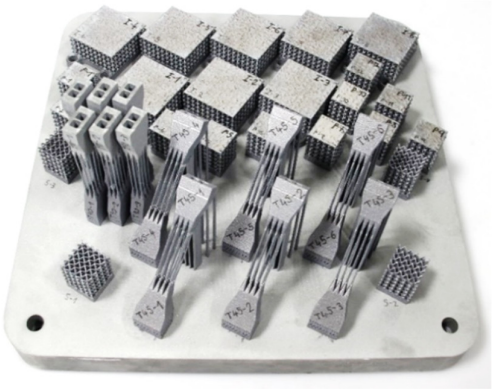

(**a**)

| Selective Laser Melting Process Parameters | |
|---|---|
| Laser power | 350 W |
| Laser speed – borders | 500 $mm \cdot s^{-1}$ |
| Laser speed – volume | 930 $mm \cdot s^{-1}$ |
| Beam compensation | 150 μm |
| Layer thickness | 50 μm |
| Hatch distance | 150 μm |
| Platform preheating | 150 °C |
| Laser spot size | ϕ 82 μm |
| Oxygen level | up to 0.2 % |
| Atmosphere | $N_2$ |

(**b**)

**Figure 1.** (**a**) Single series of mechanical specimens after SLM manufacturing; (**b**) SLM laser process parameters used for specimen fabrication.

### 2.2. Metal Powder Analysis

AlSi10Mg aluminum alloy powder (TLS Technik GmbH, Bitterfeld, Germany) was used for manufacturing all types of specimens. The powder material with almost spherical shape of particles was produced using a gas atomization technology in nitrogen atmosphere (Figure 2b). For quality verification, the particle size distribution was analyzed (Horiba LA–960, Horiba, Kyoto, Japan). Main parameters of the particle size distribution were as follows—median size was 40.7 µm, mean size was 41.4 µm, and standard deviation was 12.9 µm. The particle size up to 25.2 µm represents 10% and the particles up to size of 58 µm represents 90% of particles (Figure 2a). Depending on the particle size distribution of the metal powder, a 50 µm layer was used for fabrication of all specimens.

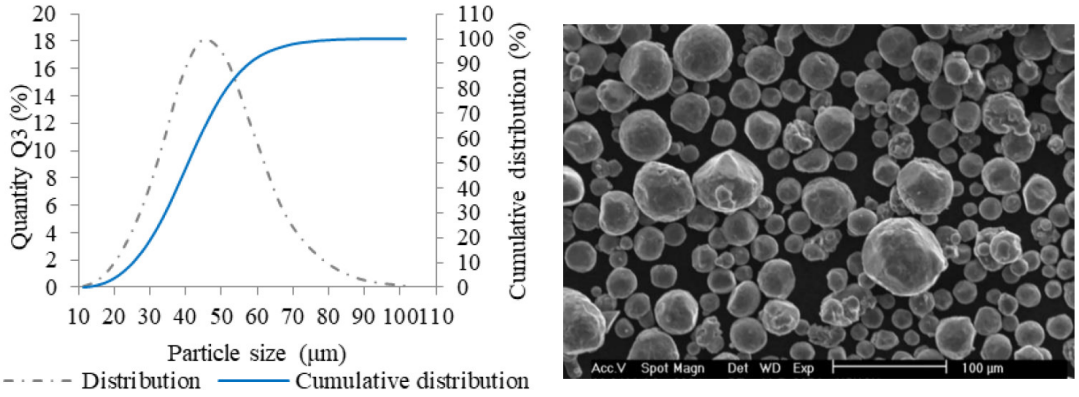


(**a**) (**b**)

**Figure 2.** Selective laser melting (SLM) powder characteristics; (**a**) chart of particle size distribution; (**b**) shape of powder particles (scanning electron microscopy (SEM)).

### 2.3. Specimens for Mechanical Testing

#### 2.3.1. Tensile Specimens

Mechanical properties of thin struts are highly affected by surface roughness and internal material porosity, which locally reduces the strut cross-section and mechanical properties [34]. Therefore, a special (multi-struts) shape of tensile specimens was designed for quasi-static mechanical testing (TS-series; Figure 3d). The multi-strut specimens were composed of 12 struts with diameters of $d = 0.8$ mm and strut lengths of $l = 29$ mm. To describe the material properties depending on specimen's inclination during SLM layer-based fabrication, they were fabricated in orientation of 90° and 45° (relative to the platform). To compare the struts and bulk mechanical properties, standard bulk material specimens (TB-series; Figure 3b) were also fabricated in orientation of 90° and 45° (relative to the platform). All specimens were tested in the as-build condition.

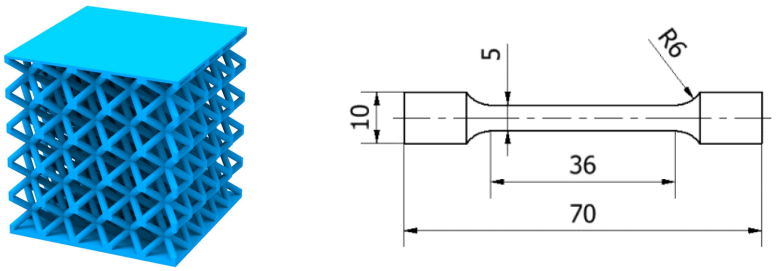


(**a**) (**b**)

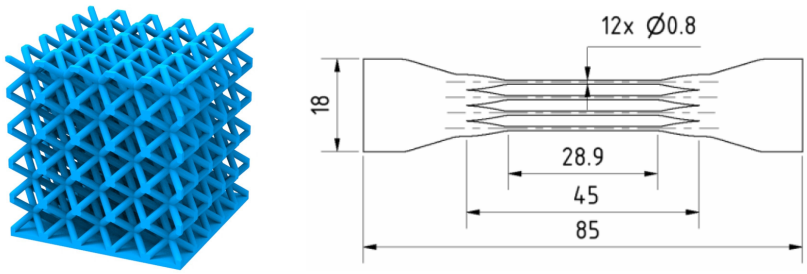


(**c**) (**d**)

**Figure 3.** Specimens for (**a**) quasi-static compressive (C-series) and low-velocity impact testing (IT-series); (**b**) quasi-static tensile testing of bulk material (TB-series); (**c**) optical analysis (O-series); and (**d**) quasi-static tensile testing of multi-strut specimens (TS-series).

#### 2.3.2. Lattice Structure Specimens

For quasi-static compression tests, BCC lattice structure core specimens with dimensions of 20 × 20 × 20.8 mm were used (C-series; Figure 3a). The BCC unit cell was composed of eight struts with diameter $d$ = 0.8 mm and side length $a_{BCC}$ = 4 mm. On the bottom and upper side, the specimens were covered with thin plates $t$ = 0.3 mm. For low-velocity impact testing, a specimen with dimensions of 20 × 20 × 16.8 mm and the same shape of the unit cell was used (IT-series; Figure 3a). To verify the material model based on parameters obtained from quasi-static testing, specimens for low-velocity impact testing with diameters of 0.6, 0.8, 1.0, and 1.2 mm were produced. Specimens for optical measurement were similar to the specimens for mechanical testing but manufactured without the upper plate for better access to the lattice structure core during the optical measurement process (O-series; Figure 3c).

### *2.4. Shape of the Struts Analysis*

To determine the actual dimensions of BCC lattice structure and multi-strut tensile specimens, O-series and TS-series of the specimens were analyzed by ATOS Triple Scan (GOM GmbH, Braunschweig, Germany) optical 3D scanner (MV170 lens; calibration was carried out according to VDI/VDE 2634, Part 3). Before the scanning process, specimens were coated with a thin layer of titanium dioxide powder (approx. 3 μm) [36]. Due to the complex shape of specimens, only four-corner struts could be digitized in the required quality.

The actual dimensions were measured by fitting the ideal cylinders and ellipses into the surface geometry in GOM Inspect software (SR1, GOM GmbH, Braunschweig, Germany, Figure 4)—diameter $d_{in}$ (inscribed cylinder) shows the largest diameter of homogeneous strut without geometrical imperfection and surface roughness; diameter $d_{out}$ (circumscribed cylinder) defines the strut diameter including surface roughness and partially melted powder on the down skin strut surface; diameter $d_{gauss}$ shows the value with the Gaussian distribution.

To include the partially melted powder on the down skin side to the strut geometry, the ellipse geometry, which very well reflects the real shape of the strut cross-section, was used. Ellipse dimensions were measured in three points on the single corner struts, and the average value was used. Measured diameters were used for dimensional analysis of the lattice structure and for the creation of real lattice structure geometry in FEA.

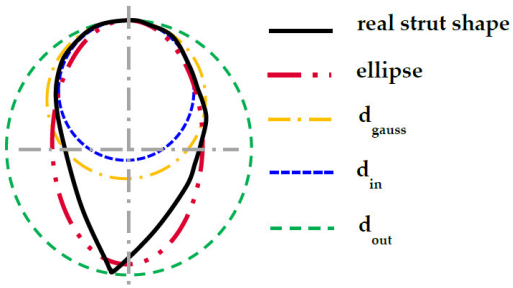


**Figure 4.** Visual 2D representation of elements used for dimensional struts analysis.

## *2.5. Mechanical Testing*

### 2.5.1. Quasi-Static Mechanical Testing

Zwick Z020 device, (Zwick Z020, ZwickRoell GmbH & Co. KG, Ulm, Germany) a universal machine for mechanical testing with maximum force of 20 kN, was used for tensile (TS-series, TB-series) and compression test (C-series). Specimens were pre-loaded with 20 N and loaded with standard loading speed of 2 mm·min$^{-1}$. During tensile testing, specimens were clamped into the jaws and loaded until all struts were broken.

During the pressure testing, the samples were placed between two plates in the testing device. The bottom plate was fixed attached to the device, thereby, movement of the sample in the vertical axis or its rotation was avoided. The upper movable plate was hinged with a rotary joint. This type of connection allowed a slight rotation of the upper (loading) plate during contacting with the sample's surface. This eliminates the possible effect of uneven loads caused by inclined grinding of the sample surface (Figure 5).

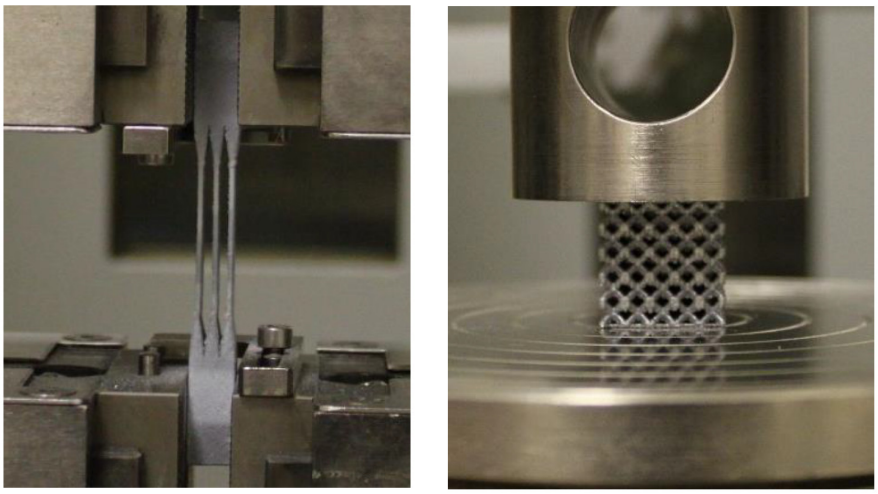

(**a**) (**b**)

**Figure 5.** Mechanical testing using Zwick Z020 machine (**a**) tensile test; and (**b**) compression test.

### 2.5.2. Low-Velocity Impact Test

Low-velocity impact testing of the IT-series was performed on the drop weight impact tester developed at Brno University of Technology (Figure 6a). The system is equipped with high-speed camera Phantom V710 and strain-gauge (XY31-3/120). The strain-gauge measures the reaction force during deformation of the lattice specimens, the high-speed camera measures the position of the marker on the falling head. Signals from the strain gauge were recorded using the data acquisition system Quantum X MX410B (HBM GmbH) with a sampling frequency of 96 kHz, data from the high-

speed camera were recorded in Phantom software with a sampling frequency of 48 kHz. Both records were jointly evaluated in MATLAB software. The main output of measurements are the following dependencies: Force reaction, time (deformation), velocity of falling head, time (deformation), maximum specimen deformation, and deformation duration. The device allows to change the shape of impact body—flat indenter (surface contact; Figure 6b) and ball indenter (point contact; $d$ = 16 mm). During impact testing, the weight of the falling head was $m$ = 7.252 kg and the drop height was $h$ = 1 m. For these parameters, the falling head achieves the maximum drop speed $v_{In}$ = 3.2 m·s$^{-1}$ with maximum energy $E_{In}$ = 71.1 J. The testing device belongs to the group of low-velocity test devices [7,25,26].

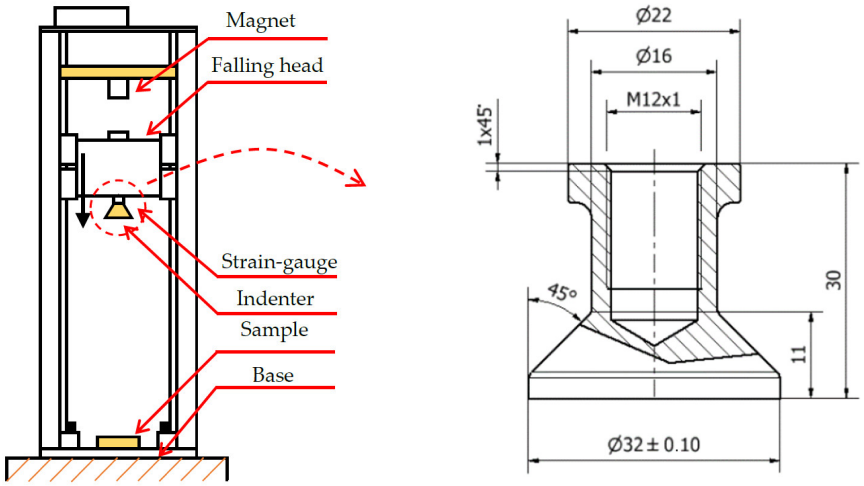


(**a**) (**b**)

**Figure 6.** (**a**) Schema of the low-velocity impact tester; and (**b**) Geometry of the flat indenter.

### *2.6. FEM Numerical Model*

The numerical model of the low-velocity impact test was created in ANSYS Workbench 18.2 software, module Explicit dynamic. Based on previous studies [2,4,23–27], the material model Bilinear isotropic hardening was selected for definition of mechanical properties of lattice core. The geometry was composed of five bodies according to Figure 7a, where the body (3) represents the lattice structured core; bodies (2) and (4) represent bottom and upper plates of the specimen; the body (1) is the indenter, and the body (5) is a solid base.

The initial drop weight impact test was performed to find out the strain rate values for various struts diameters. The obtained results were in range of 80–120 s$^{-1}$. Based on the initial results along with the loading velocity of about of 3 m·s$^{-1}$, the elastic-plastic material model was selected. This model did not further consider sensitivity in the strain-rate effect.

Input parameters for definition of lattice structure core material model were determined from quasi-static tensile and compression tests of the specimen TS- and C-series, specifically from stress-strain curves, which were created based on force—displacement testing data and the geometry results from optical measurement of the specimens (see Section 3.3.1). Mechanical parameters of plates were determined from the tensile test of bulk material (TB-series). The material model was also supplemented with the criterion of damage obtained from the lattice quasi-static compression test. The used limit value corresponds with strain at the maximum stress point ($\varepsilon_{\sigma max}$) before the progressive collapse of the lattice structure. For the indenter and the base body, the standard Structural Steel material model was used in the case of the indenter with rigid behavior.

Numerical model constrains were based on a quarter symmetry in $x$ and $y$ directions. From the bottom to the top in Figure 7a, between the base (5) and the bottom plate (4), the frictional contact

with static frictional coefficient (0.61), and dynamic frictional coefficient of 0.47 were defined. The bottom and upper plates (4, 2) are connected with the lattice core (3) by the bonded contacts. Body self-interaction was involved. To achieve a comparable result with the experiment, only the base body (5), which represents the base plate in the testing device, was limited in $x$, $y$, $z$ direction (rotation was not suppressed). To define the boundary conditions, parameters of the low-velocity impact experiment were used. The falling head ($m$ = 7.25 kg) was represented by the indenter in the numerical model. As in reality, the weight of the indenter is very low compared to the falling head; therefore, the weight of the indenter was increased using a higher density value ($\rho_{Ind}$ = 899,306 kg·m$^{-3}$) to match the weight of the real falling head. The impact velocity was determined using high-speed camera $v$ = 3.1 m·s$^{-1}$. For all bodies, the standard gravitational acceleration g = 9.806 m·s$^{-2}$ was adopted.

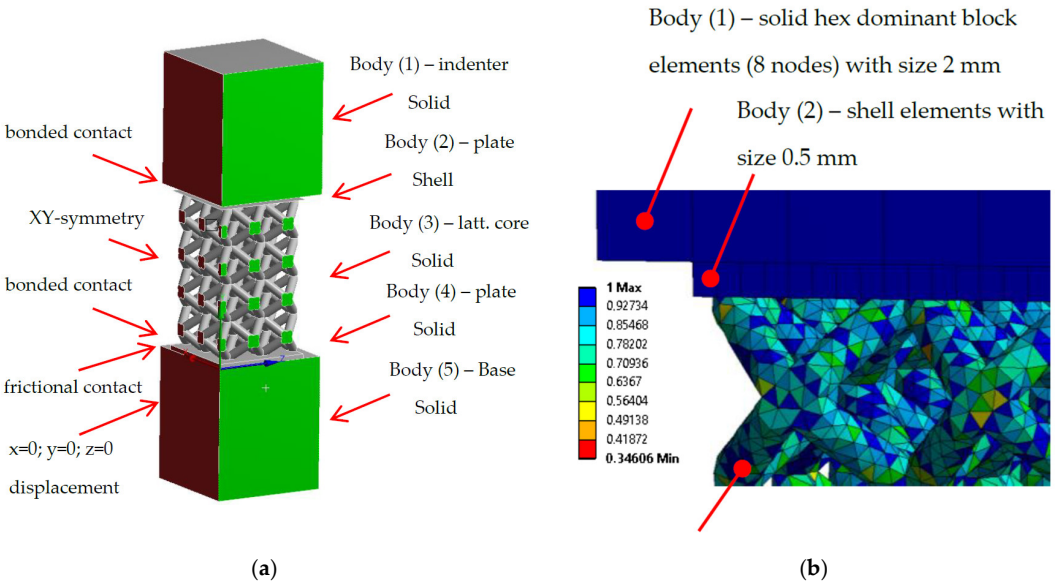


**Figure 7.** Numerical model in the Ansys software (**a**) quarter model with bodies and constrains; (**b**) finite element mesh quality.

A finite element mesh was created with several element types (Figure 7a)—the base and indenter bodies (1, 5) were formed by Hex dominant block elements (8 nodes) with size 2 mm, the bottom plate (4) with Hex Dominant block elements (8 nodes) with a size of 1 mm, the lattice core (3) with solid Tetrahedron (4 nodes) elements, which also well represents the surface roughness of the struts (Figure 7b). Their size was managed by the diameter of struts and the mesh quality parameter. In the case of circular cross-section shape with diameter $d$ = 0.95 mm, tetrahedron element size was 0.4 mm. The shell elements with size of 0.5 mm were used for upper plate (2) to prevent the Hourglass effect (Figure 8a).

In the case of a mid-surface representation, all physical and geometrical information are represented only by the surface of shell elements without thickness (Figure 8b). For the correct physical representation and constrain application between the upper plate and indenter, the shell thickness factor was considered and set to $STF$ = 0.95. This parameter ensures a contact surface in real distance from the mid-surface (Figure 8c).

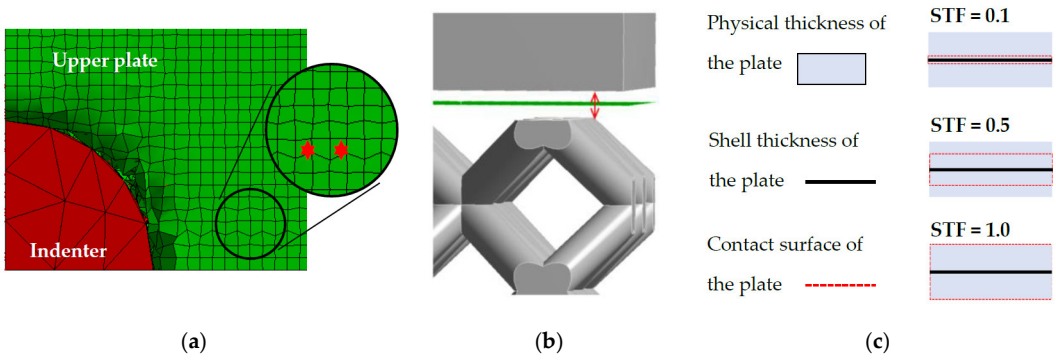


**Figure 8.** (**a**) Hour-glassing energy error; Shell thickness factor—(**b**) Shell mid-surface of the upper plate; and (**c**) Description of the contact surface.

## 3. Results

In presented study, there are a lot of used abbreviations, therefore, the table which summarizes them was created (Table 1).

**Table 1.** The list of used abbreviation.

| Shortcut | Description | Shortcut | Description |
|---|---|---|---|
| *SLM* | Selective laser melting technology | $d_{in}$ | Maximum inscribed cylinder into the strut |
| *FEA* | Finite element analysis | $d_{out}$ | Minimum circumscribed cylinder on the strut surface |
| *FEM* | Finite element method | $A_r$ | Cross-section area of real strut |
| *YLR* | Ytterbium fiber laser | $A_{Din}$ | Cross-section area of maximum inscribed cylinder into a strut |
| *BCC* | Body centered cubic | $A_{Dgauss}$ | Cross-section area of Gauss strut cylinder |
| *NM* | Numerical model | $A_{Dout}$ | Cross-section area of minimum circumscribed cylinder fitted on a strut surface |
| *STF* | Shell thickness factor | $A_{ellipse}$ | Cross-section area of an ellipse fitted to the strut surface |
| *CAD* | Computer aided design | $a$ | Ellipse minor axes |
| *EPS* | Equivalent Plastic Strain | $b$ | Ellipse major axes |
| *BL-I* | Bilinear isotropic hardening model of lattice core | $e$ | Ellipse ratio |
| *BL-II* | Bilinear isotropic hardening model of bottom and upper plates | $F_{max}$ | Maximum force |
| *EBM* | Electron beam melting | $x_{Fmax}$ | Deformation of the specimen at maximum force |
| *CT* | Computed tomography | $\sigma_{max}$ | Maximum engineering stress |
| $a_{BCC}$ | Length of BCC cell edge | $\varepsilon_{\sigma max}$ | Strain at the maximum engineering stress |
| $l$ | Length of the struts in the multi-strut tensile specimen | $E$ | Young's Modulus |
| $d$ | Nominal lattice structure strut diameter | $E_T$ | Tangent Modulus |
| $t$ | Specimen's upper plate thickness | $YTS_{0.2\%}$ | Offset yield strength at strain 0.2% |
| $h$ | Height of the C-series specimens | $UTS$ | Ultimate tensile strength |
| $h_{CAD}$ | Nominal CAD height of the specimen | $E_{In}$ | Initiating impact energy, energy just before impact |
| $t_{UpP}$ | Thickness of the upper plate | $v_{In}$ | Initiating speed, speed just before impact |
| $m_C$ | Weight of the C-series specimens | $m$ | Weight of the falling head |
| $m_{CAD\_0.8}$ | CAD weight of the C-series specimen with nominal struts dimeter | $t_{def}$ | Duration of deformation |
| $m_{CAD\_0.95}$ | CAD weight of the C-series specimen with Gauss stuts diameter and real upper plate thickness | $x_{Dyn}$ | Deformation of the specimens under dynamic loading |
| $\bar{\rho}$ | Measured relative density of C-series | $E_{Abs}$ | Absorbed energy |
| $\bar{\rho}_{CAD\_0.8}$ | Calculated relative density of the CAD model with nominal diameter $d$ = 0.8 mm | $v_{Up}$ | Speed of the rebound |
| $\bar{\rho}_{CAD\_0.95}$ | Calculated relative density of the CAD model with measured Gaussian diameter $d$ = 0.8 mm | $k_{Dyn}$ | Average stiffness of the specimens under dynamic loading |

| | | | |
|---|---|---|---|
| $d_{gauss}$ | Ideal struts Gauss cylinder | $P_{Abs}$ | Absorption power of the specimens under dynamic loading |
| $n$ | Number of the struts in the multi-strut specimen | $h_{ef}$ | Effective length of the tensile specimen |
| $\rho_{Ind}$ | deliberately increased density of the indenter to represent the weight of the whole falling head | $E_{inp}$ | Input energy to the current layer of the lattice structure |
| *SEM* | Scanning electron microscopy | $E_{lin}$ | Linear energy—(laser power/laser speed) |

### *3.1. The Analysis of Initial Weight and Height*

After SLM fabrication, the basic parameters, such as weight and height of C-series, were carried out (nominal struts diameter $d$ = 0.8 mm). The results showed that the weight of the specimens was almost twice as high and the relative density $\bar{\rho}$, which was found comparing the real weight and the theoretical weight of the solid cube, was about 10% higher than that expected by CAD. Therefore, the lattice structure numerical model must have struts diameter larger than the nominal diameter $d$ = 0.8 mm. The deviation was caused by SLM production of larger struts of the lattice structure, as was also described in the study in Reference [14]. Based on these results (Table 2), more detailed analyses using optical measurement were performed.

**Table 2.** The initial analysis of the C-series.

| **(Avg. Values)** | **Measured** | | | | **CAD** | | | | |
|---|---|---|---|---|---|---|---|---|---|
| | $h$ | $t_{UpP}$ | $m$ | $\bar{\rho}$ | $h_{CAD}$ | $m_{CAD\_0.8}$ | $m_{CAD\_0.95}$ | $\bar{\rho}_{CAD\_0.8}$ | $\bar{\rho}_{CAD\_0.95}$ |
| | (mm) | (mm) | (g) | (%) | (mm) | (g) | (g) | (%) | (%) |
| $\bar{x}$ | 21.04 | 0.75 | 6.97 | 31 | 20.80 | 4.72 | 6.94 | 21 | 31 |

### *3.2. Optical Measurement of the Lattice Structure*

The optical system Atos Triple Scan III (GOM GmbH, Braunschweig, Germany) and the lighting microscope Olympus SZX7 (Olympus, Tokyo, Japan) were used for more detailed measurements of the lattice structure. The result shows that there were significant differences between the inscribed and circumscribed cylinders (Table 3, Figures 4 and 9).

**Table 3.** Struts diameter measured using the Atos Triple Scan optical system (O-series; nominal diameter $d$ = 0.8 mm).

| **(mm)** | **Corner Strut** | $d_{gauss}$ | | $d_{in}$ | | $d_{out}$ | | **Ellipse** | | | |
|---|---|---|---|---|---|---|---|---|---|---|---|
| | | | | | | | | **Minor Axis** | | **Major Axis** | |
| **S1** | 1 | 0.94 | 0.95 | 0.74 | 0.73 | 1.26 | 1.21 | 0.79 | 0.79 | 1.1 | 1.12 |
| | 2 | 0.99 | | 0.75 | | 1.19 | | 0.81 | | 1.17 | |
| | 3 | 0.93 | | 0.7 | | 1.24 | | 0.79 | | 1.14 | |
| | 4 | 0.93 | | 0.72 | | 1.16 | | 0.78 | | 1.09 | |
| **S2** | 1 | 0.96 | 0.96 | 0.76 | 0.74 | 1.18 | 1.22 | 0.8 | 0.79 | 1.2 | 1.12 |
| | 2 | 0.92 | | 0.75 | | 1.09 | | 0.79 | | 1.03 | |
| | 3 | 1.02 | | 0.73 | | 1.36 | | 0.8 | | 1.06 | |
| | 4 | 0.94 | | 0.72 | | 1.23 | | 0.77 | | 1.17 | |
| **S3** | 1 | 0.86 | 0.91 | 0.69 | 0.71 | 1.08 | 1.18 | 0.78 | 0.76 | 1.08 | 1.06 |
| | 2 | 0.91 | | 0.69 | | 1.26 | | 0.77 | | 1.05 | |
| | 3 | 0.94 | | 0.76 | | 1.2 | | 0.76 | | 1.13 | |
| | 4 | 0.91 | | 0.7 | | 1.17 | | 0.73 | | 0.97 | |
| **S4** | 1 | 0.97 | 0.97 | 0.82 | 0.74 | 1.27 | 1.31 | 0.86 | 0.84 | 1.27 | 1.16 |
| | 2 | 0.96 | | 0.73 | | 1.31 | | 0.89 | | 1.15 | |
| | 3 | 1.01 | | 0.74 | | 1.43 | | 0.83 | | 1.04 | |
| | 4 | 0.93 | | 0.67 | | 1.23 | | 0.77 | | 1.18 | |
| $\bar{x}$ | | 0.945 | | 0.729 | | 1.229 | | 0.795 | | 1.114 | |

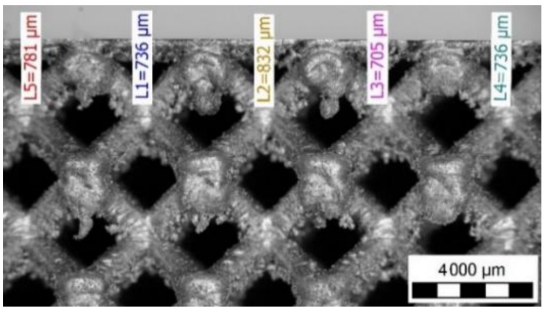


**Figure 9.** Side view on the C-series specimen using the lighting microscope.

### *3.3. Mechanical Properties*

#### 3.3.1. Quasi-Static Mechanical Testing

For evaluation of mechanical properties, the average dimensions of $d_{gauss}$ were used (Table 4; Figure 10). From the stress-strain curves, yield strength $YTS_{0.2\%}$, Young's Modulus $E$, and tangent modulus $E_T$ were evaluated. $YTS_{0.2\%}$ was carried out as an intersection of the stress-strain curve and the parallel line to the linear part of the curve (Hook area) in the strain value *0.002*. $E_T$ tangent modulus was obtained as an interpolation of the part of the plastic area in a stress-strain curve by a line. The same evaluation process was used in the case of bulk material specimens (TB-series). The obtained average values are shown in Table 5.

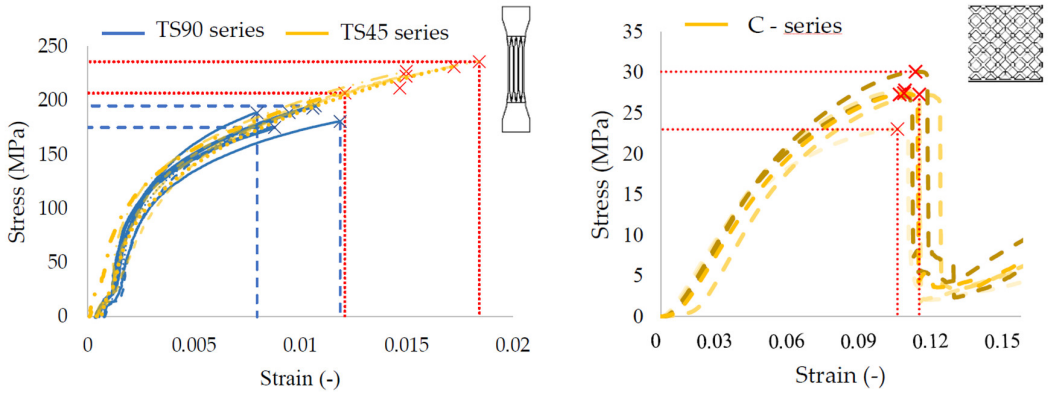


(**a**) (**b**)

**Figure 10.** (**a**) Quasi-static stress-strain curves of the struts tensile specimens; and (**b**) Quasi-static stress-strain curves of the compression specimens.

**Table 4.** The dimensions of the tensile specimen specimens (multi-struts tensile specimens TS-series; bulk tensile specimens TB-series).

| (mm) | TS45 | | | TS90 | | | TB45 | | | TB90 | | |
|---|---|---|---|---|---|---|---|---|---|---|---|---|
| | $d_{gauss}$ | $d_{in}$ | $d_{out}$ | $d_{gauss}$ | $d_{in}$ | $d_{out}$ | $d_{gauss}$ | $d_{in}$ | $d_{out}$ | $d_{gauss}$ | $d_{in}$ | $d_{out}$ |
| 1 | 0.88 | 0.66 | 1.07 | 0.78 | 0.61 | 1.09 | 5.05 | 4.91 | 5.49 | 5.03 | 4.94 | 5.36 |
| 2 | 0.88 | 0.69 | 1.14 | 79 | 0.68 | 1.03 | 5.04 | 4.89 | 5.66 | 5.02 | 4.9 | 5.45 |
| 3 | 0.89 | 0.72 | 1.15 | - | - | - | 5.03 | 4.85 | 5.6 | 5.01 | 4.93 | 5.57 |
| 4 | 0.9 | 0.74 | 1.19 | 0.79 | 0.71 | 0.88 | - | - | - | - | - | - |
| 5 | 0.9 | 0.7 | 1.34 | 0.8 | 0.69 | 1.06 | - | - | - | - | - | - |
| 6 | 0.91 | 0.71 | 1.29 | 0.78 | 0.69 | 0.87 | - | - | - | - | - | - |
| $\bar{x}$ | 0.89 | 0.70 | 1.20 | 0.79 | 0.68 | 0.99 | 5.04 | 4.88 | 5.58 | 5.02 | 4.92 | 5.46 |

**Table 5.** The dimensions of the tensile specimen specimens with different orientation to the platform (multi-struts tensile specimens TS-series; bulk tensile specimens TB-series).

| *Spec.* | $F_{max}$ (N) | $x_{Fmax}$ (mm) | $\sigma_{max}$ (MPa) | $\varepsilon_{\sigma max}$ | *E* (GPa) | $YTS_{0.2\%}$ (MPa) | *UTS* (MPa) | $E_T$ (MPa) |
|---|---|---|---|---|---|---|---|---|
| TS45 | 2270 | 0.462 | - | 0.015 | 71.6 | 131.6 | 224.2 | 6649 |
| TS90 | 1934 | 0.297 | - | 0.010 | 103.7 | 116.6 | 186.8 | 8701 |
| TB45 | 7625 | 1.030 | - | 0.026 | 96.1 | 227.0 | 382.2 | 4858 |
| TB90 | 6453 | 0.809 | - | 0.020 | 147.5 | 187.4 | 326 | 5753.3 |
| C | 10,860 | 2.133 | 27.2 | 0.103 | 483.5 | - | - | - |

### 3.3.2. Low-Velocity Impact Test Results

To find out the absorption characteristics of the BCC lattice structure material and FEA for validation, the low-velocity impact test of the IT-series was carried out using the low-velocity impactor. As was described above, the specimens were produced together in the one build job; however, significant differences in mechanical properties in single sets of specimens, such as maximum reaction force $F_{max}$, maximum deformation $x_{Dyn}$ or duration $t_{def}$ can be observed (Figure 11b). These differences could be caused by a local damage of the lattice structure under loading, the structure which can occur by the material imperfection of SLM fabricated lattice structures such as surface roughness or internal porosity. It can change symmetrical bending of dominate deformation process, which is typical for BCC structures, to an asymmetrical mechanical response [37]. Therefore, in the case of the lattice structure, it is necessary to work with average values of the mechanical properties. For comparison purposes, the average curves of the force-deformation and initial speed-deformation were created (Figure 11c,d). All the low-velocity impact results are shown in Table 6; there is shown that mechanical properties of sets of specimens, such as maximum reaction $F_{max}$ and stiffness of the specimens under dynamic loading $k_{Dyn}$, increase linearly with struts diameter.

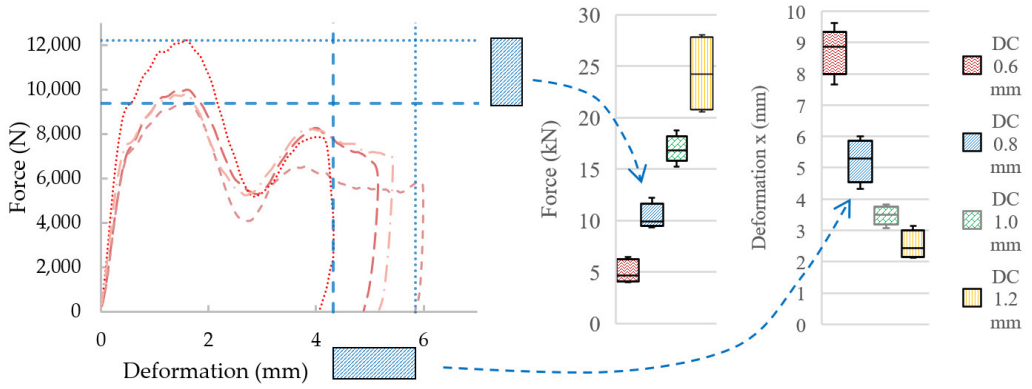


(**a**) (**b**)

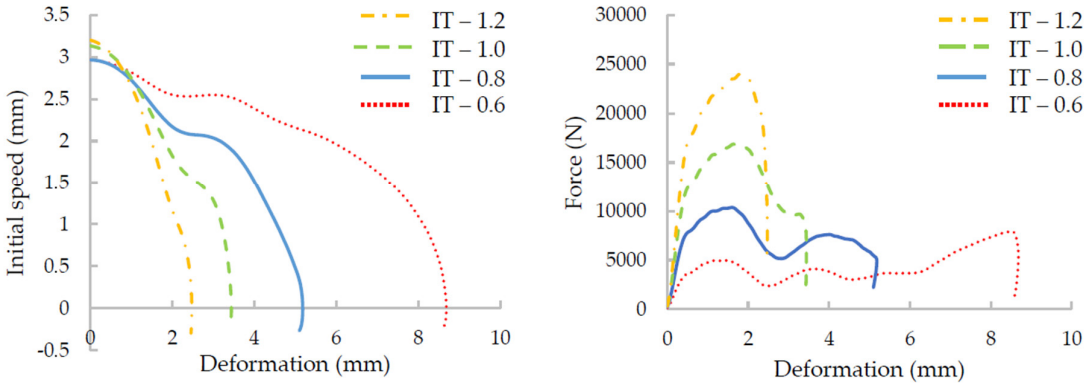


**Figure 11.** The results from low-velocity impact testing: (**a**) Single IT-series with diameter $d$ = 0.8 mm; (**b**) variance of force and deformation of all IT-series; (**c**) average initial speed, deformation curves; and (**d**) average force-deformation curves.

Absorbed energy $E_{Abs}$ was evaluated regarding the real measured initiating speed $v_{In}$ and initiating impact energy $E_{In}$ for each specimen. From Table 5, it is obvious that most of specimens absorbed more than 99% of impact energy, and only in the case of the specimens with nominal diameter $d$ = 1.2 mm, there was a small decline. Therefore, the parameter absorption power $P_{Abs}$ (J·s$^{-1}$), which reflects the deformation and absorbed energy, was defined.

$$P_{Abs} = E_{Abs}/t_{def} \quad (1)$$

The lattice structure with low value of $P_{Abs}$ can absorb energy through long duration and large deformation. It is important e.g., in automotive industry where the car deformation area must be designed for overload not damaging the human body.

**Table 6.** The results of the low-velocity impact.

| # | $F_{max}$ (N) | $t_{def}$ (ms) | $x_{Dyn}$ (mm) | $v_{In}$ (m·s$^{-1}$) | $E_{In}$ (J) | $E_{Abs}$ (J) | $v_{up}$ (m·s$^{-1}$) | $k_{Dyn}$ (N·mm$^{-1}$) | $P_{Abs}$ (J·s$^{-1}$) |
|---|---|---|---|---|---|---|---|---|---|
| IT 0.6 | 4252 | 4.94 | 9.07 | 3.02 | 33.10 | 32.47 | 0.42 | 9005 | 6.58 |
| | 6479 | 4.64 | 7.67 | 2.95 | 31.51 | 31.19 | 0.30 | | 6.73 |
| | 4005 | 5.29 | 9.61 | 2.93 | 31.19 | 30.87 | 0.30 | | 5.83 |
| | 4660 | 5.04 | 8.86 | 2.95 | 31.48 | 31.20 | 0.28 | | 6.19 |
| | 6047 | 4.71 | 8.31 | 2.97 | 32.08 | 31.68 | 0.33 | | 6.73 |
| $\bar{x}$ | 5089 | 4.92 | 8.70 | 2.96 | 31.87 | 31.48 | 0.32 | - | 6.41 |
| | - | - | - | - | - | - | - | - | - |
| IT 0.8 | 9989 | 3.41 | 5.15 | 2.97 | 32.03 | 31.58 | 0.35 | 19,417 | 9.27 |
| | 9368 | 4.05 | 6.00 | 2.93 | 31.91 | 31.71 | 0.24 | | 7.82 |
| | 12,218 | 2.94 | 4.32 | 2.96 | 31.87 | 31.31 | 0.39 | | 10.66 |
| | 9795 | 3.52 | 5.43 | 2.96 | 31.72 | 31.08 | 0.42 | | 8.83 |
| $\bar{x}$ | 10,343 | 3.48 | 5.22 | 2.96 | 31.88 | 31.42 | 0.35 | - | 9.15 |
| IT 1.0 | 15,223 | 2.79 | 3.83 | 3.07 | 34.22 | 33.89 | 0.30 | 29,371 | 12.14 |
| | 17,625 | 2.03 | 3.30 | 3.13 | 35.45 | 35.28 | 0.22 | | 17.37 |
| | 16,437 | 2.16 | 3.66 | 3.15 | 36.09 | 35.56 | 0.38 | | 16.49 |
| | 18,796 | 1.80 | 3.08 | 3.16 | 36.09 | 35.29 | 0.47 | | 19.58 |
| | 16,859 | 2.18 | 3.50 | 3.15 | 35.98 | 35.83 | 0.20 | | 16.46 |
| $\bar{x}$ | 16,988 | 2.19 | 3.47 | 3.13 | 35.57 | 35.17 | 0.31 | - | 16.41 |

| | | | | | | | | | |
|---|---|---|---|---|---|---|---|---|---|
| | 24,205 | 1.49 | 2.43 | 3.19 | 36.93 | 34.87 | 0.75 | | 23.41 |
| | 28,067 | 1.31 | 2.17 | 3.22 | 37.61 | 35.22 | 0.81 | | 26.84 |
| IT 1.2 | 20,597 | 1.89 | 3.14 | 3.21 | 37.30 | 36.44 | 0.48 | 39,006 | 19.33 |
| | 27,627 | 1.31 | 2.13 | 3.21 | 37.28 | 34.92 | 0.81 | | 26.61 |
| | 20,990 | 1.80 | 2.87 | 3.17 | 36.54 | 35.41 | 0.56 | | 19.65 |
| $\bar{x}$ | 24,297 | 1.56 | 2.55 | 3.20 | 37.13 | 35.38 | 0.68 | - | 23.17 |

### *3.4. Finite Element Analysis (FEA)*

#### 3.4.1. FEA Material Models

Based on the quasi-static results, the material model (BL-I) of the BCC lattice structure from AlSi10Mg alloy was created (Table 7). The parameters $E$, $YTS_{0.2\%}$ and $E_T$ of the TS45-series were used to create the Bilinear isotropic hardening material model due to a similar strut build inclination, as in the case of the BCC lattice structure (35.26°) [33]. A damage criterion was obtained from the C-series as the maximum equivalent plastic strain $\varepsilon_{\sigma max}$. The material model (BL-II) of the upper and bottom plate was created using mechanical parameters of the bulk material. The other needed parameters were used from the Ansys material library as the default values.

**Table 7.** Materials model used for lattice structure specimens FEA.

| Parameters | BL-I (BCC) | BL-II (Plate) | Unit |
|---|---|---|---|
| Density | 2680 | 2680 | $kg \cdot m^{-3}$ |
| Isotropic Elasticity | - | - | - |
| Young's Modulus | 70,723 | 96,100 | MPa |
| Poisson's Ratio | 0.334 | 0.334 | - |
| Bulk Modulus | $7.1 \times 10^{10}$ | $9.6 \times 10^{10}$ | Pa |
| Shear Modulus | $2.7 \times 10^{10}$ | $3.6 \times 10^{10}$ | Pa |
| Bilinear Isotropic Hardening | - | - | - |
| Yield Strength | 135 | 227 | MPa |
| Tangent Modulus | 6586 | 4858 | MPa |
| Plastic Strain Failure | - | - | - |
| Max. Equivalent Plastic Strain EPS | 0.1025 | 0.1025 | - |

#### 3.4.2. FEM Model

The results from FEA using the numerical model (NM) of the low-velocity dynamic loading (described above) are shown in Figure 12. From the figure, it is obvious that the force-time curve of the NM with ellipse cross-section (Figure 12b) corresponds better to the experimental results than that with circular cross-section (Figure 12a). The largest deviations can be seen in the middle (between 1.5–4 ms) and towards the end (between 4–5 ms) of the force-time curve. In the case of FEA considering the circular cross-section shape, the deformation time exceeded 5 ms, and the specimen was continually deformed. It does not correspond with the results of the low-velocity testing where the deformation ended at 5 ms. In the case of FEA considering the ellipse cross-section shape, duration and deformation ended at the end of 5 ms. The real and predicted damage of the specimens after low-velocity impact testing is shown in Figures 13 and 14.

The deviations between FEA and the experiment were compared using the maximum force value in the first force peak in the case of FEA, and the average maximum force from the five experimentally tested specimens. The results show that the relative error of FEA with circular cross-section is 12%, while with elliptical cross-section, it is 2% in the case of IT-0.8 series.

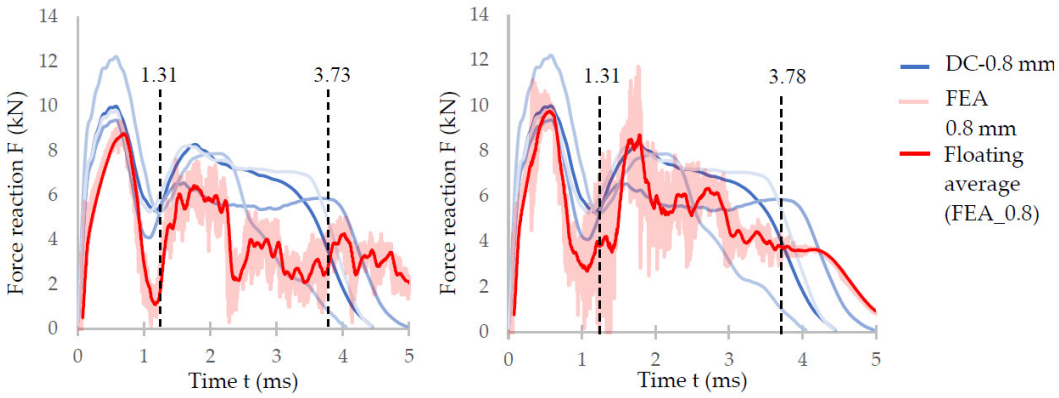


**Figure 12.** (**a**) Comparison of the results of the IT-0.8 series and the numerical simulation with (**a**) circular cross-section; and (**b**) elliptical cross-section.

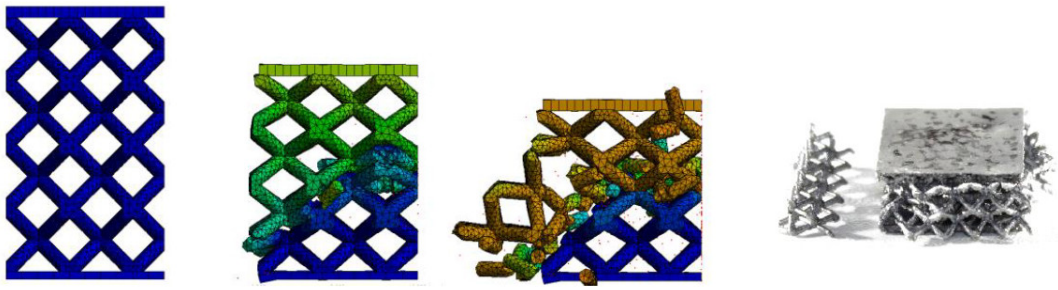


**Figure 13.** Gradual deformation of the specimen with circular strut cross-section in time—(**a**) 0 ms; (**b**) 1.31 ms; (**c**) 3.73 ms; (**d**) real damage of the specimen IT-2 after low-velocity impact test.

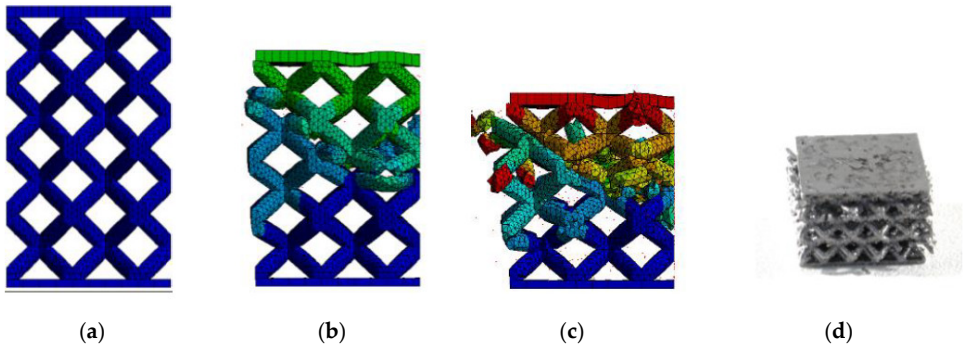


**Figure 14.** Gradual deformation of the specimen with elliptical strut cross-section in tim: (**a**) 0ms; (**b**) 1.31ms, (**c**) 3.78 ms; and (**d**) real damage of the specimen IT-2 after low-velocity impact test.

## 4. Discussion

### *4.1. Substitution of the Strut's Real Cross-Section with the Ideal Cross-Section*

The deformation behavior of numerical model (NM) with the ideal circular cross-section geometry of $d = 0.8$ mm (nominal diameter) showed large differences to the experiment during initial tests. Therefore, the results from weighing and optical measuring of the C-series (Figrue 15a) were

used for finding ideal diameter for using in NM for prediction of the real behavior of the lattice structure.

From the 3D scanned data of the lattice structure(C-series), a cross-section area of the real single strut was calculated (Figure 15b; $A_r$ = 0.712 mm²) and compared with the cross-section area of the fitted ideal cylinders to the strut in the GOM Inspect software ($A_{Din}$ = 0.417 mm²; $A_{Dgauss}$ = 0.701 mm²; $A_{Dout}$ = 1.186 mm²). The results show that the best match is in the case of $d_{Gauss}$. Therefore, this diameter seems to be appropriate to represent the designed diameter $d$ = 0.8 mm in the NM.

A similar result was obtained from weight comparison where the weight of the lattice structure CAD model with $d_{Gauss}$ and the measured weight were compared (Table 2). To the weight of CAD model ($m_{CAD\_0.95}$), the larger thickness of the plates from the lighting microscope was also added. The result show that weight $m$ and $m_{CAD\_0.95}$ are almost identical. Based on these basic analyses, the strut diameter $d_{Gauss}$ was selected for lattice structure simplification using ideal circular cross-section in the numerical model. This result differs from the results of Suart et al. [21], where the diameter equal to $d_{In}$ was used.

During the evaluation of optical measurement, the real shape of the lattice structure struts similar to "water drop" was found (Figure 15b). On the down skin strut surface, surroundings metal powder was melted due to struts orientation and heat transfer [19]. The partially melted powder modifies the strut shape into an elliptical cross-section resulting in an increase of mechanical properties under compression loading (Figure 12). Therefore, if only equivalent circular cross-section is used, the mechanical properties are increase in all directions instead of only Z direction. This will be reflected especially in the FEM model response during the progressive collapse of the lattice structure where deviations from the actual behavior occur, as is shown in Figure 12a. The results of experiment and FEA comparison show that the elliptic cross-section is more suitable for a description of the whole deformation process via FEA (Figure 12b). The circular cross-section can only be used for the estimation of approximate $F_{max}$ reaction force when the lattice structure starts to be damaged.

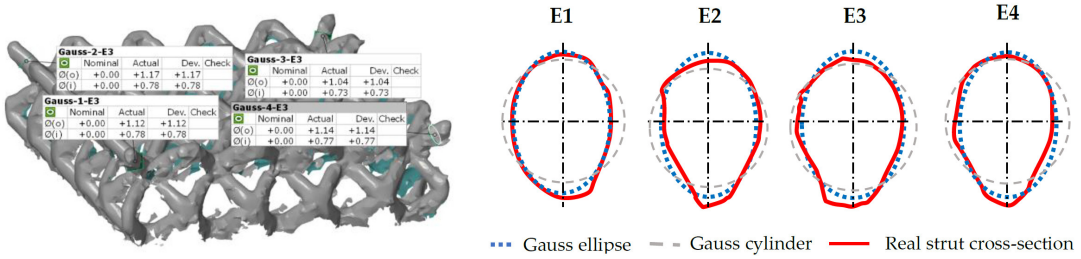


**Figure 15.** Comparison of the real and ideal cylinder cross-section: (**a**) shape analysis in the GOM Inspect software and (**b**) real cross-section in four corner struts.

### *4.2. Application of Numerical Model to BCC Lattice Structures with Struts Diameter between 0.6–1.2 mm*

The material model was created directly for the lattice structure with 0.8 mm nominal diameter; therefore, the other specimens, such as those for optical measurement or quasi-static testing, were fabricated only for this nominal diameter. However, as is shown in Figure 16, the material model of the lattice structure can also be used for diameters between 0.6–1.2 mm, which are commonly used dimensions of lattice structure struts.

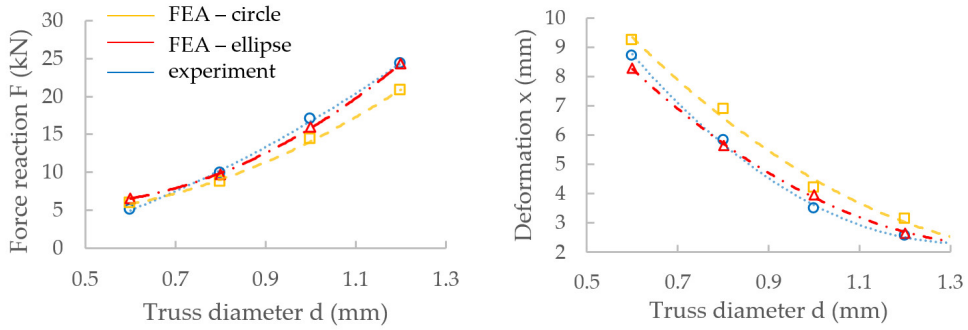


**Figure 16.** Comparison of FEA results and experiment for different strut diameters; (**a**) reaction force; and (**b**) deformation.

To create the FEM geometry in Ansys software, real strut diameters of nominal diameters 0.6, 1.0 and 1.2 mm were obtained from the previous study [20] where the relation between the designed and real strut diameter after SLM processing was described. In order to use the elliptical shape for these diameters (0.6–1.2 mm), the ellipse ratio $e$ from the O-series ($d$ = 0.8 mm) was evaluated and applied to other strut sizes using Equation (6). The $d_{gauss}$ cylinder values from the line equation (Figure 17) [20] were used to calculate the circle cross-section area. Then the elliptical ratio $e$ = 0.71 and the equivalent sizes of circular and elliptical cross-sections were used for calculation of minor and major axes of the ellipse. The elliptical ratio was identified as a ratio between the average minor and major ellipse axes in the O-series test. The re-calculation process is described in Equations (2)–(6). The results also confirm a better compliance with the ellipse cross-section than with the circular one (Figure 16).

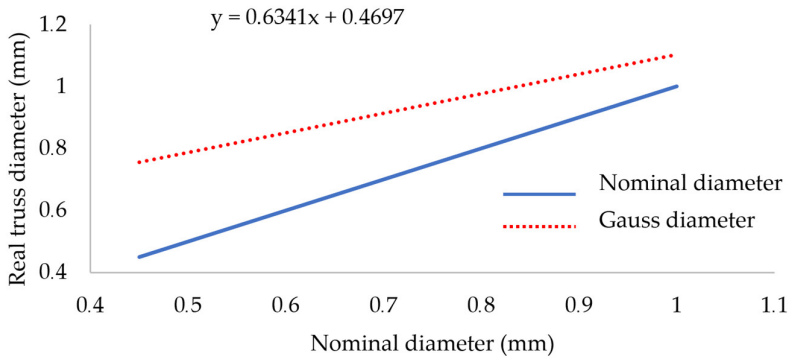


**Figure 17.** Increase of the real strut diameter fabricated by SLM described in the study [20].

$$A_{Dgauss} = A_{ellipse} \tag{2}$$

$$\pi \frac{d_{gauss}^2}{4} = \pi \cdot a \cdot b \tag{3}$$

$$e = \frac{a}{b} = \frac{0.795/2}{1.114/2} = 0.714 \tag{4}$$

$$b = \sqrt{d_{gauss}^2/4 \cdot e} \tag{5}$$

$$a = e \cdot b \tag{6}$$

### *4.3. Mechanical Testing*

In their study [34], the Tsopanos et al. tested single struts of 316L with diameters of about 0.2 mm. The mechanical properties of struts were half as compared to the standard material because the mechanical properties of a single strut mainly decrease porosity and surface roughness. From this, it follows that to find the correct mechanical properties for the numerical model of lattice structure, it is not suitable to use the bulk material tensile specimens.

Nevertheless, during compression loading, a lot of single struts transfer the load in the lattice structure. Therefore, multi-strut tensile specimen, where more struts are also loaded simultaneously were designed. The results of tensile testing show that specimens fabricated by SLM with of 45° orientation have different mechanical properties in comparison with those of 90° orientation − $YTS_{0.2\%}$ + 10%; $UTS$ + 20%; $E$ + 40%; and $E_t$ − 30%. It could be due to a higher porosity level inside the strut in the case of 90° orientation. To obtain the correct mechanical properties during evaluation of strut mechanical properties, it is necessary to use the real dimensions measured e.g., by optical measurement. The strut mechanical properties were compared with bulk material which is not too affected by internal defects. The results show much lower strut mechanical properties and more brittle material. ($YTS_{0.2\%}$ − 40%; $UTS$ − 30%; Young's modulus $E$ − 30% and Tangent modulus $E_t$ + 30 ÷ 50%). It may be mainly caused by significant surface roughness and almost two times higher surface of multi-strut specimens compare to bulk specimens (970/565 mm$^2$, calculated using Gaussian diam. for specimens T45-series $d_{Gauss}$ = 0.89 mm.). The size of specimen's surface is also connected with close to surface porosity which can be expressed using parameter $CtS$ and Equation (7) (for one truss of multi-strut spec., it is of 130; for bulk spec., it is of 29). This parameter expresses the ratio between the surface of the specimen or struts in multi-strut specimen $S$ (mm$^2$) and cross-section of the specimen or strut $A$ (mm$^2$). Its value shows susceptibility to failure due to close to surface porosity.

$$CtS = \frac{S}{A} = \frac{n \cdot \pi \cdot d \cdot h_{ef}}{n \cdot \pi \frac{d^2}{4}} = \frac{4h_{ef}}{d} = 28.8 \quad (7)$$

where $n$ is number of the struts of the specimens (for bulk shape $n$ = 1), $d$ is the strut or bulk specimens' diameter and $h$ is the effective area of the specimen (see Figure 3).

### *4.4. Criterion of Damage*

A damage criterion is the Ansys parameter which defines when the element is excluded from calculation (element erosion) and no longer contributes to load transfer. In the case of presented numerical model, the Equivalent Plastic Strain $EPS$ = 0.1025 was used (Table 6). It means that if the element is deformed more than 10.25%, it is removed.

The true strain value at the area of the damage of tensile specimen is required as input for this criterion in Ansys. From the strut tensile testing, only the global specimen's strain without considering the local damage in the critical area was obtained. There are two reasons: Firstly, it was an atypical shape of the specimens where it was problematic to measure the narrowing of the single struts in the damaged area. Secondly, the used material is very brittle; therefore, the narrowing of the struts was very small and could not be measured with available equipment. For this reason, an alternative method was used; $EPS$ was represented by the strain at the first peak $F_{max}$ in the compression test.

## 5. Conclusions

In this study, all processes of material model creation and final FEA analysis were presented. The results show that the SLM technology allows to produce energy absorbers from AlSi10Mg alloy, which can effectively absorb energy through self-deformation. Due to a good accordance between the numerical model and the experiment, it was possible to use the numerical model of lattice structure for precise design of the absorber in high-performance applications. This model will be used for future testing of geometry changes and their impact on mechanical properties. The

presented process of finding the material model can be employed for various materials used for SLM production.

- The numerical model of BCC micro-lattice structure under dynamic loading with the elliptic strut shape was developed. The results show that the elliptic shape of the lattice structure significantly decreases a deviation between FEA and the measured results compared to the circular cross-section (10%, measured in the first force peak).
- To find the correct mechanical properties for FEA material model, it is necessary to use the struts specimens with appropriate orientation during production due to the influence of internal porosity and surface roughness.
- The orientation during SLM production significantly influences the mechanical properties.
- The shape of the BCC lattice structure was analyzed using optical methods. A distinct "water drop" shape was found in the case of AlSi10Mg alloy.
- A weight comparison of the CAD design and the produced lattice structure shows that for simplification of the "water drop" shape of the strut, the Gaussian strut diameter should be used.
- The results of quasi-static mechanical testing show that the differences between mechanical properties of the 90° and 45° orientation are mainly in the plastic area of deformation and may by caused by the significant surface roughness.

**Author Contributions:** Conceptualization, R.V.; Data curation, R.V. and O.Č.; Formal analysis, R.V., P.M. and D.K.; Funding acquisition, D.P.; Investigation, R.V. and O.Č.; Methodology, R.V. and P.M.; Project administration, R.V.; Resources, D.P.; Supervision, P.M., D.K. and D.P.; Validation, R.V., O.Č., P.M., D.K. and D.P.; Visualization, R.V.; Writing—original draft, R.V., O.Č. and D.K.; Writing—review & editing, R.V. and O.Č.

**Funding:** This research was funded by the ESIF, EU Operational Programme Research, Development and Education within the research project [Architectured materials designed for additive manufacturing] grant number [CZ.02.1.01/0.0/0.0/16_025/0007304].

**Conflicts of Interest:** The authors declare no conflict of interest.

## References

1. Karagiozova, D. Dynamic buckling of elastic-plastic square tubes under axial impact—I: Stress wave propagation phenomenon. *Int. J. Impact Eng.* **2004**, *30*, 143–166.
2. Li, X.; Zhang, P.; Wang, Z.; Wu, G.; Zhao, L. Dynamic behavior of aluminum honeycomb sandwich panels under air blast: Experiment and numerical analysis. *Compos. Struct.* **2014**, *108*, 1001–1008.
3. Olabi, A.G.; Morris, E.; Hashmi, M.S.J. Metallic tube type energy absorbers: A synopsis. *Thin Walled Struct.* **2007**, *45*, 706–726.
4. Dharmasena, K.P.; Wadley, N.G.; Xue, Z.; Hutchinson, J.W. Mechanical response of metallic honeycomb sandwich panel structures to high-intensity dynamic loading. *Int. J. Impact Eng.* **2008**, *35*, 1063–1074.
5. Kopanidis, A.; Theodorakakos, A.; Gavaises, E.; Bouris, D. 3D numerical simulation of flow and conjugate heat transfer through a pore scale model of high porosity open cell metal foam. *Int. J. Heat Mass Transf.* **2010**, *53*, 2539–2550.
6. Shimizu, T.; Matsuzaki, K.; Nagai, H.; Kanetake, N. Production of high porosity metal foams using EPS beads as space holders. *Mater. Sci. Eng. A* **2012**, *558*, 343–348.
7. Zhu, L.; Guo, K.; Li, Y.; Yu, T.X.; Zhou, Q. Experimental study on the dynamic behaviour of aluminium foam sandwich plates under single and repeated impacts at low temperature. *Int. J. Impact Eng.* **2018**, *114*, 123–132.
8. Sun, B.; Zhang, R.; Zhang, Q.; Gideon, R.; Gu, B. Drop-weight impact damage of three-dimensional angle-interlock woven composites. *J. Compos. Mater.* **2013**, *47*, 2193–2209.
9. Vrana, R.; Koutny, D.; Paloušek, D. Impact Resistance of Different Types of Lattice Structures Manufactured by SLM. *MM Sci. J.* **2016**, *2016*, 1579–1585.
10. Mines, R.A.W.; Tsopanos, S.; Shen, Y.; Hasan, R.; McKown, S.T. Drop weight impact behaviour of sandwich panels with metallic micro lattice cores. *Int. J. Impact Eng.* **2013**, *60*, 120–132.
11. Harris, J.A.; Winter, R.E.; McShane, G.J. Impact response of additively manufactured metallic hybrid lattice materials. *Int. J. Impact Eng.* **2017**, *104*, 177–191.

12. Yadroitsev, I. *Selective Laser Melting: Direct Manufacturing of 3D-Objects by Selective Laser Melting of Metal Powders*; LAP Lambert: Saarbrücken, Germany, 2009.
13. Thijs, L.; Kempen, K.; Kruth, J.-P.; van Humbeeck, J. Fine-structured aluminium products with controllable texture by selective laser melting of pre-alloyed AlSi10Mg powder. *Acta Mater.* **2013**, *61*, 1809–1819.
14. Qiu, C.; Yue, S.; Adkins, N.J.E.; Ward, M.; Hassanin, H.; Lee, P.D.; Withers, P.J.; Attallah, M.M. Influence of processing conditions on strut structure and compressive properties of cellular lattice structures fabricated by selective laser melting. *Mater. Sci. Eng. A* **2015**, *628*, 188–197.
15. Koutny, D.; Palousek, D.; Pantelejev, L.; Hoeller, C.; Pichler, R.; Tesicky, L.; Kaiser, J. Influence of scanning strategies on processing of aluminum alloy EN AW 2618 using selective laser melting. *Materials* **2018**, *11*, 1–17.
16. Han, X.; Zhu, H.; Nie, X.; Wang, G.; Zeng, X. Investigation on Selective Laser Melting AlSi10Mg Cellular Lattice Strut: Molten Pool Morphology, Surface Roughness and Dimensional Accuracy. *Materials* **2018**, *11*, 392
17. Ilcik, J.; Koutny, D.; Palousek, D. Geometrical accuracy of the metal parts produced by selective laser melting: Initial tests. In Proceedings of the 54th International Conference of Machine-Design-Departments (ICMD), Hejnice, Czech Republic, 10–12 September 2013; pp. 573–582.
18. Skalicky, P.; Koutny, D.; Pantelejev, L.; Palousek, D. Processing of aluminum alloy EN AW 7075 using selective laser melting: Initial study. In Proceedings of the 58th International Conference of Machine-Design-Departments (ICMD2017), Prague, Czech Republic, 6–8 September 2017; pp. 330–335.
19. Vrana, R.; Koutny, D.; Palousek, D.; Pantelejev, L.; Jaros, J.; Zikmund, T.; Kaiser, J. Selective laser melting strategy for fabrication of thin struts usable in lattice structures. *Materials* **2018**, *11*, 1–21.
20. Koutny, D.; Vrana, R.; Paloušek, D. Dimensional accuracy of single beams of AlSi10Mg alloy and 316L stainless steel manufactured by SLM. In Proceedings of the 5th International Conference on Additive Technologies (iCAT2014), Vienna, Austria, 16–17 October 2014; pp. 142–147.
21. Suard, M.; Lhuissier, P.; Dendievel, R.; Vignat, F.; Blandin, J.J.; Villeneuve, F. Impact of EBM fabrication strategies on geometry and mechanical properties of titanium cellular structures. In Proceedings of the Fraunhofer Direct Digital Manufacturing Conference (DDMC 2014), Berlin, Germany, 12–13 March 2014.
22. Vrana, R.; Koutny, D.; Paloušek, D.; Zikmund, T. Influence of selective laser melting process parameters on impact resistance of lattice structure made from AlSi10Mg. In Proceedings of the World PM 2016 Congress and Exhibition, Hamburg, Germany 9–13 October 2016.
23. Grytten, F.; Børvik, T.; Hopperstad, O.S.; Langseth, M. Low velocity perforation of AA5083-H116 aluminium plates. *Int. J. Impact Eng.* **2009**, *36*, 597–610.
24. Grytten, F.; Holmedal, B.; Hopperstad, O.S.; Børvik, T. Evaluation of identification methods for YLD2004-18p. *Int. J. Plast.* **2008**, *24*, 2248–2277.
25. Mohmmed, R.; Ahmed, A.; Elgalib, M.A.; Ali, H. Low Velocity Impact Properties of Foam Sandwich Composites: A Brief Review. *Int. J. Eng. Sci. Innov. Technol.* **2014**, *3*, 579–591.
26. Mohmmed, R.; Zhang, F.; Sun, B.; Gu, B. Finite element analyses of low-velocity impact damage of foam sandwiched composites with different ply angles face sheets. *Mater. Des.* **2013**, *47*, 189–199.
27. Labeas, G.; Ptochos, E. Investigation of sandwich structures with innovative cellular metallic cores under low velocity impact loading. *Plast. Rubber Compos.* **2013**, *42*, 194–202.
28. Ozdemir, Z.; Tyas, A.; Goodall, R.; Askes, H. Energy absorption in lattice structures in dynamics: Nonlinear FE simulations. *Int. J. Impact Eng.* **2017**, *102*, 1–15.
29. Banerjee, A.; Dhar, S.; Acharyya, S.; Datta, D.; Nayak, N. Determination of Johnson cook material and failure model constants and numerical modelling of Charpy impact test of armour steel. *Mater. Sci. Eng. A* **2015**, *640*, 200–209.
30. Milani, A.S.; Dabboussi, W.; Nemes, J.A.; Abeyaratne, R.C. An improved multi-objective identification of Johnson-Cook material parameters. *Int. J. Impact Eng.* **2009**, *36*, 294–302.
31. Brandl, E.; Heckenberger, U.; Holzinger, V.; Buchbinder, D. Additive manufactured AlSi10Mg samples using Selective Laser Melting (SLM): Microstructure, high cycle fatigue, and fracture behavior. *J. Mater. Des.* **2012**, *34*, 159–169.
32. Vaverka, O.; Koutný, D.; Vrána, R.; Pantělejev, L.; Paloušek, D. Effect of heat treatment on mechanical properties and residual stresses in additively manufactured parts. In Proceedings of the Engineering Mechanics 2018 24th International Conference, Svratka, Czech Republic, 14–17 May 2018.

33. Kempen, K.; Thijs, L.; van Humbeeck, J.; Kruth, J.-P. Mechanical properties of AlSi10Mg produced by selective laser melting. *Phys*. *Procedia* **2012**, *39*, 439–446.
34. Tsopanos, S.; Mines, R.A.W.; Mckown, S.; Shen, Y.; Cantwell, W.J.; Brooks, W.; Sutcliffe, C.J. The influence of processing parameters on the mechanical properties of selectively laser melted stainless steel microlattice structures. *J. Manuf. Sci. Eng*. **2010**, *132*, 1–12.
35. Xiao, L.; Song, W. Additively-manufactured functionally graded Ti-6Al-4V lattice structures with high strength under static and dynamic loading: Experiments. *Int*. *J*. *Impact Eng*. **2018**, *111*, 255–272.
36. Palousek, D.; Omasta, M.; Koutny, D.; Bednar, J.; Koutecky, T.; Dokoupil, F. Effect of matte coating on 3D optical measurement accuracy. *Opt*. *Mater*. **2015**, *40*, 1–9.
37. Ravari, M.R.K.; Kadkhodaei, M.; Ghaei, A. Effects of asymmetric material response on the mechanical behavior of porous shape memory alloys. *J. Intell. Mater. Syst. Struct.* **2016**, *27*, 1687–1701.

materials

MDPI

*Article*

# Computational Approaches of Quasi-Static Compression Loading of SS316L Lattice Structures Made by Selective Laser Melting

**Ondřej Červinek [1,*], Benjamin Werner [2], Daniel Koutný [1], Ondřej Vaverka [1], Libor Pantělejev [3] and David Paloušek [1]**

[1] Institute of Machine and Industrial Design, Brno University of Technology, Technická 2896/2, 616 69 Brno, Czech Republic; Daniel.Koutny@vut.cz (D.K.); Ondrej.Vaverka@vut.cz (O.V.); palousek@fme.vutbr.cz (D.P.)
[2] Institute of Lightweight Design and Structural Biomechanics, Vienna University of Technology, Gumpendofer Straße 7, 1060 Vienna, Austria; bwerner@ilsb.tuwien.ac.at
[3] Institute of Materials Science and Engineering, Brno University of Technology, Technická 2896/2, 616 69 Brno, Czech Republic; pantelejev@fme.vutbr.cz
* Correspondence: Ondrej.Cervinek@vut.cz; Tel.: +420-541-143-256

**Abstract:** Additive manufacturing methods (AM) allow the production of complex-shaped lattice structures from a wide range of materials with enhanced mechanical properties, e.g., high strength to relative density ratio. These structures can be modified for various applications considering a transfer of a specific load or to absorb a precise amount of energy with the required deformation pattern. However, the structure design requires knowledge of the relationship between nonlinear material properties and lattice structure geometrical imperfections affected by manufacturing process parameters. A detailed analytical and numerical computational investigation must be done to better understand the behavior of lattice structures under mechanical loading. Different computational methods lead to different levels of result accuracy and reveal various deformational features. Therefore, this study focuses on a comparison of computational approaches using a quasi-static compression experiment of body-centered cubic (BCC) lattice structure manufactured of stainless steel 316L by selective laser melting technology. Models of geometry in numerical simulations are supplemented with geometrical imperfections that occur on the lattice structure's surface during the manufacturing process. They are related to the change of lattice struts cross-section size and actual shape. Results of the models supplemented with geometrical imperfections improved the accuracy of the calculations compared to the nominal geometry.

**Keywords:** selective laser melting; finite element analysis; body centered cubic; quasi-static compression test; stainless steel 316L



**Citation:** Červinek, O.; Werner, B.; Koutný, D.; Vaverka, O.; Pantělejev, L.; Paloušek, D. Computational Approaches of Quasi-Static Compression Loading of SS316L Lattice Structures Made by Selective Laser Melting. *Materials* **2021**, *14*, 2462. https://doi.org/10.3390/ma14092462

Academic Editor: Aniello Riccio

Received: 30 March 2021
Accepted: 16 April 2021
Published: 10 May 2021



## 1. Introduction

### *1.1. Lightweight Structures*

Lightweight structures and materials have become interesting for industries including transportation, aerospace, and space applications [1]. One category of lightweight structures are metallic cellular structures where metal foams, honeycombs, and lattices belong. Properties like low thermal conductivity, acoustic absorption, mechanical vibration damping, high stiffness to volume fraction ratio, and energy absorption are required within these materials [2–4]. Some of these properties are well represented by closed-cell and open-cell metallic foams [5]. However, both topological configurations are mostly irregular, which can cause randomly distributed damage during loading [6]. Furthermore, closed-cell foams form gas capsules that are usually non-desirable, and open-cell foams tend to be deformed by bending instead of the more convenient stretching-dominated mode [7–9].

Additive manufacturing (AM) brings new production possibilities of stretching-dominated lattice structures with enhanced mechanical properties such as high energy

absorption related to their weight or damping properties [10–12]. One of the frequently used AM technologies called selective laser melting (SLM) allows manufacturing from different materials, e.g., stainless steel 316L [13], titanium alloy $Ti_6Al_4V$ [14], or aluminum alloy $AlSi_{10}Mg$ [15,16].

With the AM, the topology of lattice structures can be customized to a wide range of applications, including a different kind or direction of loading behavior [17,18]. This advantage can be used when lightweight components are designed for the transmission of accurately defined loading [8,19]. Structures can also be designed to absorb a specific amount of energy and undergo predefined deformation patterns [20]. A deeper knowledge of loading behavior and manufacturing technology is required to increase the efficiency of lattice structures, for example, in terms of energy-absorbing capabilities [21]. It includes information about the deformation mechanism within a specific geometry configuration, which can be investigated via finite element analysis (FEA) [22]. Significant inaccuracies and imperfections can occur [23], as far as the geometry of lattice structures produced by SLM technology is strongly influenced by the heat transfer phenomenon. In the computational model of lattice, the structure geometry should be considered with deviations from the nominal computer-aided designed (CAD) data [24].

### *1.2. Computational Approaches*

Some methods of finite element discretization of geometry have been developed to study the properties of lattice structures under mechanical loading. Luxner et al. [25] focused on the uniaxial compression properties of lattice structures with circular cross-sections and constant diameter. Timoshenko beam element models were utilized for the simulation of large structures. A stiffness correction in the vicinity of the vertices was introduced by using elements with artificially increased Young's modulus in these domains [26,27]. For a highly detailed representation of the structure topology, solid tetrahedron elements were used, giving higher modeling effort and computational cost.

Ravari et al. [28] developed a Python 6.6.6. script for creating models of lattice structure geometry using quadratic beam element B32 and solid tetrahedron elements C3D10M from the Abaqus library. The script divided the lattice struts into at least 9 equally spaced intervals variating in the strut's diameter with a circular cross-section. A diameter according to probability was assigned to each interval. Furthermore, Dong et al. [29] dealt with the concept of loading only a single strut in the structure. To indicate the influence of the joint on the stiffness of the lattice, strut, beam, and solid element models were generated. A similar approach was invented by Geng et al. [30] who used finite element models based on combined elements. Some of the Timoshenko beam elements in a unit cell in the middle of the loaded lattice structure were replaced with solid tetrahedral elements C3D10.

Vrana et al. [31] described methods of optical digitalization to achieve a model of lattice structure with the actual manufactured cross-section area and shape. The actual shape of the tilted lattice struts produced by SLM was approximated by an ellipse. Besides, Lei et al. [24] used micro computed tomography (μ-CT) to capture the realistic geometrical information of the lattice strut surface including imperfections. A Python script was developed to automatically create a 3D model using B31 beam elements. Actual distribution characteristics of imperfection were taken into account in the FEA model as the opposite of Ravari et al. [28]. The quasi-static FE simulations were conducted in the ABAQUS 6.14 Explicit solver. The same solver used also Gümrük et al. [32], Li et al. [33], and Liu et al. [34] for solving quasi-static compression behavior of body-centered cubic (BCC) lattice structure under large deformation. The ratio of artificial energy to internal energy and the ratio of kinetic energy to internal energy were held below 5% to ensure that the dynamic effect is insignificant. The different models presented by Lozanovski et al. [35] captured the 'waviness' of a struts' varying diameter along its length. They used a series of elliptical cross-sections derived from μ-CT measurements to develop a model geometry that includes manufacturing imperfections.

Several teams focused also on the development of a model of the material. Tsopanos et al. [36] used tensile tests of thin struts complemented with compression tests of BCC lattice cubes. The experimental results were used to obtain the mechanical properties of the structure produced by SLM. The elastic modulus varied until a good match between the finite element analysis and experiment was achieved. This knowledge used Smith et al. [3] for numerical modeling of the lattice structure compressive response. Initially, the material properties based on conventional tensile tests and a strut diameter of 0.2 mm was used for the FE models. The strut diameter then varied until both the experimental and FE stress-strain curves coincided. The ends of the struts were modeled with an increased diameter similar to the Luxner et al. [25] study.

Tancogne et al. [10] used a piece-wise linear hardening curve (a simple rate-independent J2-plasticity model with isotropic hardening) based on calibrated tensile experiments performed on SLM-made samples for a description of lattice structures made of SS316L. The effect of possible anisotropy, rate dependency, kinematic hardening, and martensitic phase transformation was neglected. A similar approach was used by Gümrük et al. [32]. Tancogne et al. [19] continued the research with the numerical investigation of the BCC lattice structure with tapered beams. Simulations were performed on a single unit cell to investigate the effect of tapering on the elastic moduli and the structure when large deformation occurs. The base material was a homogeneous isotropic Levy-von Mises material with isotropic strain hardening.

The material model was improved by Amani et al. [37], who studied the compression behavior of face-centered cubic (FCC) lattice structures manufactured by SLM. The deformation process of the lattice was captured by in situ and ex situ X-ray tomography illustrating a macroscopic structure and local micro-porosity. A 3D image-based conformal finite element model was then built for the simulation of the compression test using Gurson–Tvergaard–Needleman (GTN, in Abaqus) porous plasticity (based on von Mises yield criterion of ductile porous materials). A new procedure allowing to inform each element about the local porosity directly from high-resolution tomography was used. Simulation considering a homogenous matrix with an average initial porosity everywhere was compared to the new heterogeneous model.

Unfortunately, published studies usually involve simulations considering of only some of the most important characteristics of lattice structures. Some authors focus on the correct determination of input data for the model of the material using numerical corrections usually restricted to linear elastic behavior. Other researchers focus on the exact determination of the model of geometry including imperfections using μ-CT. These studies usually compare the mechanical properties of lattice structures in terms of compression modulus or collapse stress. However, a study with correctly determined models of material and geometry beyond the linear elastic area, is missing. The description of lattice structure behavior in the nonlinear area is crucial for future applications that consider progressive collapse, e.g., energy absorbers in the transport industry. Therefore, the main objective of further research should aim to the development and verification of computational models that allow the prediction of lattice structures' nonlinear deformation. The models will allow the designing of vehicle protection segments using lattice structures with minimal experimental effort. This study focuses on the development of computational analysis considering the abovementioned input parameters and the determination of their relevancy compared to experimental data.

## 2. Materials and Methods

To realize the aim of this study, it is necessary to perform a series of procedures connected to material testing, optical digitalization, and finite element analysis. The main processes described in the following sections are shown in the scheme in Figure 1.

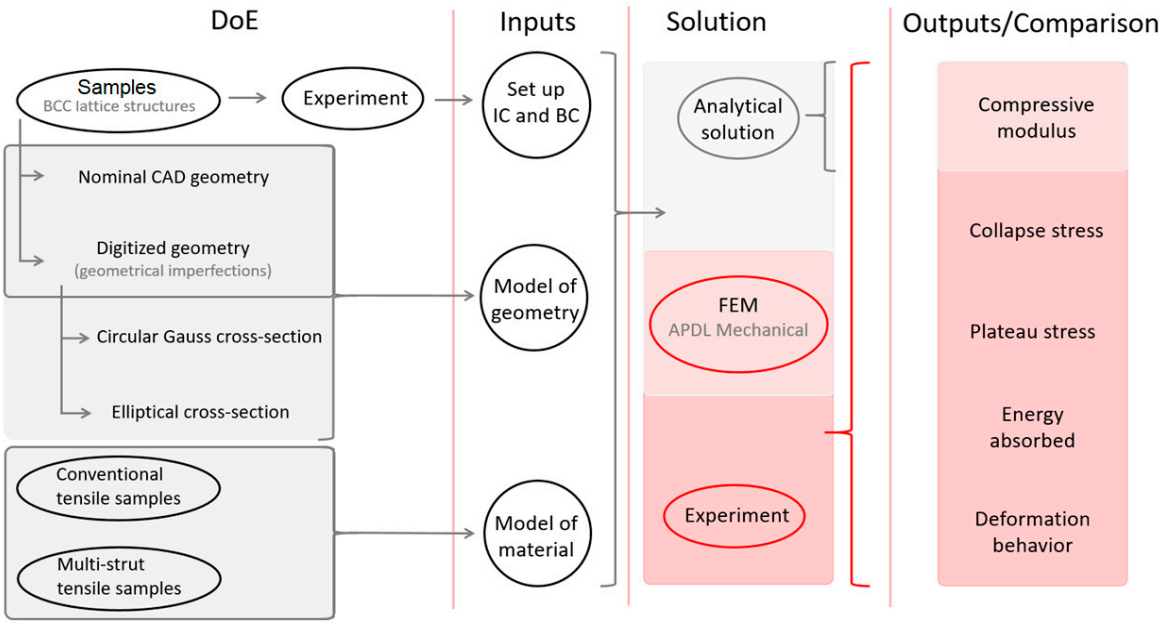


**Figure 1.** Scheme of the main working points in study.

### 2.1. Powder Material

For the production of lattice cubes and multi-strut tensile samples, the 1.4404 (316L) stainless steel metal powder (TLS Technik GmbH, Bitterfeld-Wolfen, Germany) was selected. The manufacturability of this material has reached a level allowing the production of parts with complex geometry such as lattice structures. Furthermore, stainless steel 316L is a ductile material with high elongation at failure (41 ± 1% without heat treatment [38]), which predetermines it to a good resistance during loading assumed for energy absorption. The chemical powder chemical composition of the 316L is given in Table 1. The gas atomization method was used to produce the powder. The particle size requirement was given by values between 15 µm and 45 µm for 50 µm layer thickness. The powder particle size analysis showed a distribution with the following characteristics that met the expectations: $Q_{10}$ = 10.07 µm, $Q_{50}$ = 29.44 µm, and $Q_{90}$ = 48.21 µm.

**Table 1.** Chemical analysis of TLS stainless steel 316L powder.

| Elem. | Fe | C | Si | Mn | Cr | Mo | Ni |
|---|---|---|---|---|---|---|---|
| wt.% | Bal. | 0.03 | 0.8 | 1.8 | 17.5 | 2.2 | 11.3 |

### 2.2. Lattice Structure

The present study focuses on a basic lattice structure that has a unit cell assembled by four struts along the body diagonals of a cube (see Figure 2a), which is typically called body-centered cubic (BCC). Lattice structured cubes with nominal dimensions of 20 × 20 × 20 mm and 4 mm unit cell size (see Figure 2b) were designed for a quasi-static compression test. The nominal strut diameter of the structure in CAD design varied from 0.3 mm to 1 mm. The samples were manufactured using an SLM 280$^{HL}$ machine (SLM Solutions, Lübeck, Germany) with the following standard set-up process parameters according to SLM Solutions recommendations: 100 °C platform heating, $N_2$ inert atmosphere, bidirectional hatching scanning strategy with two contours, and 50 µm layer thickness. The melting parameters were: 100 W laser power and 300 mm·s$^{-1}$ scanning speed for scanning contours, 275 W laser power and 700 mm·s$^{-1}$ scanning speed for hatching, 150 W laser power, and 400 mm·s$^{-1}$ scanning speed for fill contours.

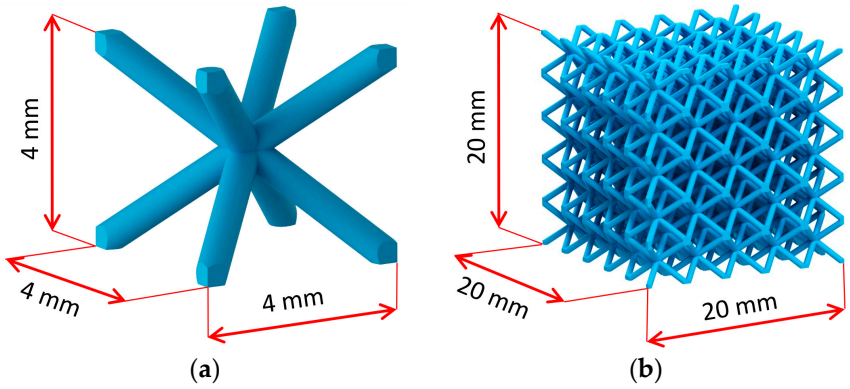


**Figure 2.** (**a**) BCC unit cell; (**b**) BCC lattice structure sample.

### *2.3. Multi-Strut Tensile Samples*

Tensile tests were carried out to determine the mechanical properties of 316L stainless steel. Conventional tensile samples manufactured according to usually used Standards (ISO, DIN) are not representing the mechanical properties of the lattice structure closely enough [36,38]. Already mentioned in Vrana et al. [39], the surface area of all parts manufactured via SLM technology is influenced by heat transfer and other phenomena during the manufacturing process. Therefore, this area is characterized by different values of mechanical properties. The percentage portion of these areas in samples manufactured according to abovementioned standards is significantly lower compared to the lattice structure struts. Therefore, strut tensile samples with a nominal strut diameter equal to the lattice structure struts were used (see Figure 3).

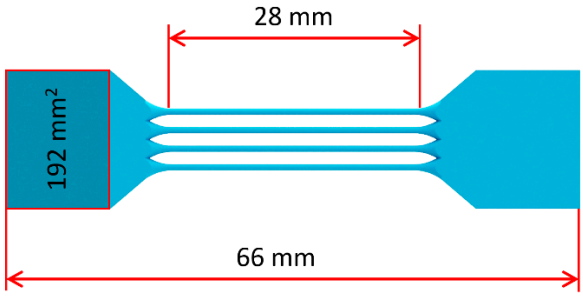


**Figure 3.** Multi-strut tensile sample with 12 struts.

Furthermore, the manufacturing angle of the samples was considered. According to Koutny et al. [40], the actual strut diameter measured after the manufacturing process differs from the nominal ones. Actual shape and size depend on many aspects, e.g., the settings of process parameters, powder distribution, manufacturing conditions, and manufacturing angle [23]. All tensile samples were manufactured with a 35° angle regarding the platform to achieve similar strut manufacturing conditions as in the BCC lattice structure. This ensures (together with equal process parameters) a very similar strut diameter, shape of cross-section, and mechanical properties of the multi-strut tensile samples compared to the BCC lattice structures.

Besides the multi-strut tensile samples, a series of conventional samples was manufactured with the same process parameters. Testing samples were prepared from billets built with a 90° angle regarding the platform and machined according to DIN 50125—(Form B, dimensions of the gauge length Ø6 × 30 mm).

### *2.4. Dimension and Shape Analysis*

The previous series of structured samples was used to inspect the actual diameter and cross-section area of the struts after the manufacturing process. After post-processing,

these samples were subjected to the optical digitalization process. An optical scanner ATOS Triple Scan (GOM GmbH, Braunschweig, Germany) with an MV170 lens was used (calibration was carried out according to VDI/VDE 2634). The samples were coated with titanium dioxide powder before scanning to prevent reflection of light projection (coating thickness approx. 5 µm [41]). The samples were scanned on the rotation table using a script written for maximizing the total area of the scanned surface.

The scans of lattice structures were evaluated using GOM Inspect v8.0 software. Eight measurements were carried out on struts at middle height (corner struts) for every sample. These struts were interlaced with cylinders based on the Gaussian best fit method (points 3 sigma) [40]. Diameters of the cylinders were measured. In the next step, the struts were cut at half of their length. The cross-section created by the section plane was interlaced by an ellipse with the same Gaussian best fit function (see Figure 4), and the major and minor axis diameter of the ellipse were determined.

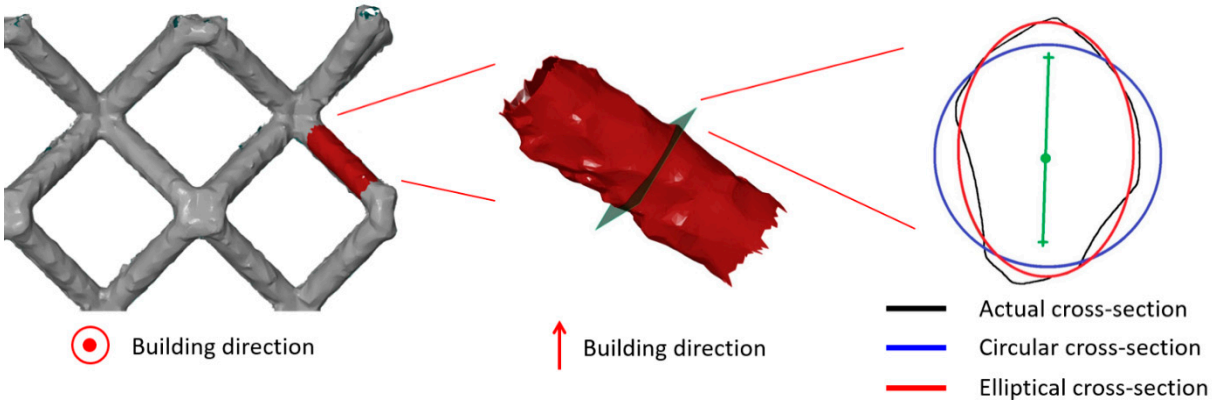


**Figure 4.** Comparison of different cross-section approximations.

### 2.5. Quasi-Static Mechanical Tests

Tensile tests (multi-strut samples, standard tensile samples) and compression tests of lattice cubes were performed on a universal testing machine Zwick Z250 (ZwickRoell GmbH & Co. KG, Ulm, Germany) equipped with dynamometer enabling load of 150 kN. The declared positioning accuracy of the device measurement (with repeatability) is ±2 µm. Ends of multi-strut tensile samples were fixed into the centered jaws and preloaded with 20 N force. Self-locking grips prevented the slipping of samples during the test.

The lattice cubes were placed without any fixing between the flat adapters in the device. The lower adapter was fixed on a bar movable in a vertical direction and the upper adapter was mounted on a static joint connection (slight tilting of the adapter was allowed). Both tensile and compression samples were loaded with a strain rate of approximately $10^{-3}$ $s^{-1}$; therefore, no strain rate effect was expected.

### 2.6. Analytical Formulation

Analytical approaches were developed for the simplified evaluation of cellular structure deformation behavior [2,42]. This study is using one of the newest approaches presented by Yang et al. [43], which accounts for the unit cell length, nominal strut radius, and boundary conditions of the BCC lattice structure. Equations described in this study were based on the earlier Timoshenko beam theory and Euler–Bernoulli theory [19] neglecting shear deflection terms. The equations used in this study do not contain the boundary plates constraints of the investigated lattice structure representing free strut deformation patterns (Equations (1) and (2)). With these equations, an elastic modulus $E^{e}_{c1}$ of lattice structure is calculated as follows:

Timoshenko solution

$$E_{c1}^{e} = \frac{9\sqrt{3}\pi E_s}{(17+12v_s)\left(\frac{1}{r_n}\right)^2 + 2\left(\frac{1}{r_n}\right)^4} \quad (1)$$

Euler–Bernoulli solution

$$E_{c1}^{e} = \frac{9\sqrt{3}\pi E_s}{3\left(\frac{1}{r_n}\right)^2 + 2\left(\frac{1}{r_n}\right)^4} \quad (2)$$

where $E_s$ is the elastic modulus of bulk material, $v_s$ is Poisson's constant of bulk material, $r_n$ is strut radius, and l is half of the unit cell diagonal. It should be mentioned that the analytical models take into account only nominal strut radius; therefore, the imperfections connected with change of cross-section area and its shape are neglected here.

### *2.7. Finite Element Analysis*

Numerical simulations were carried out in ANSYS Workbench 19.2 in module for structural analysis (Static structural). The subject of the simulation was a quasi-static compression test of the BCC lattice structure produced by SLM technology. Two different approaches were introduced and compared with experiments, including linear and nonlinear deformation behavior. The beam element model was developed as a computationally cheap solution for the simulation of bigger structures. For analysis requiring higher accuracy and stress analysis, a solid element model was used. Manufacturing imperfections connected with the change of strut cross-section and cross-sections' shape were considered in the beam element model simulation.

#### 2.7.1. Solid Element Model (Continuum Model)

The model of geometry consisted of tetrahedron elements (SOLID 187) with a quadratic interpolation function. This approach is computationally expensive and is restricted to smaller bodies, but gives information about the stress evolution in the lattice structure during loading. Because of higher computational requirements, a mesh sensitivity study was performed on a smaller lattice structure with a configuration of $3 \times 3 \times 3$ unit cells to achieve reasonably accurate results [35]. During the study, the level of plateau stress and the convergence of the solution were validated through the series with different element sizes [3,37,43]. At least six elements were used to discretize the diameter of the strut for geometry with and without imperfections [19,26]. Struts in the model with imperfections were represented by a constant elliptical cross-section based on measurement. Nodes created by intersecting struts were modelled with sharp corners without radiuses.

#### 2.7.2. Beam Element Model

The model was created using a script written in APDL by copying a single unit cell represented by a wireframe. Struts of unit cells were divided into mid-part and ends. Each strut consisted of minimal five beam elements (BEAM 188) according to the mesh sensitivity study performed in previous studies [30,44]. The behavior of nodes was adjusted at nodes where at least three ends of the struts met [26]. This step was done to achieve more realistic behavior of intersecting struts represented by the spherical domain rather than one point. It is caused by additional material accumulated in the struts after the manufacturing process. It included higher stiffness and material volume increase in the near vicinity of nodes. The artificial increase of stiffness was achieved by a thousand times increased value of Young's modulus. The higher material volume was achieved by an increase in nominal strut diameter about 0.2 mm (see Figure 5 (red)). This approach ensures bending and cracking struts rather than reinforced nodes during compression loading [45,46]. This approach is based on previous studies such as Luxner [26], Labeas [47], Smith [3], and

Gümrük [32], and supplemented with imperfections of the manufacturing process (see Figure 6).

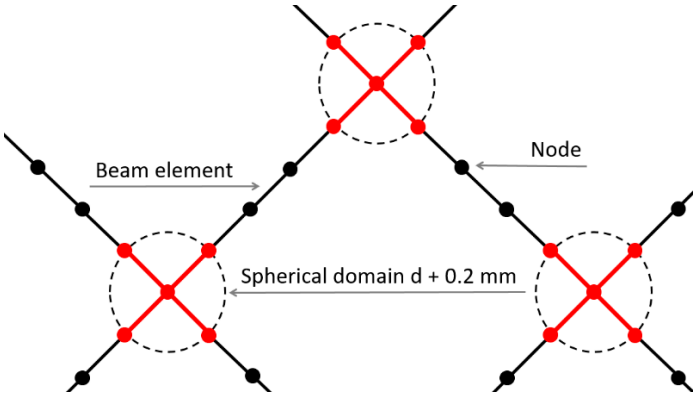


**Figure 5.** Schematic composition of elements and nodes with different properties.

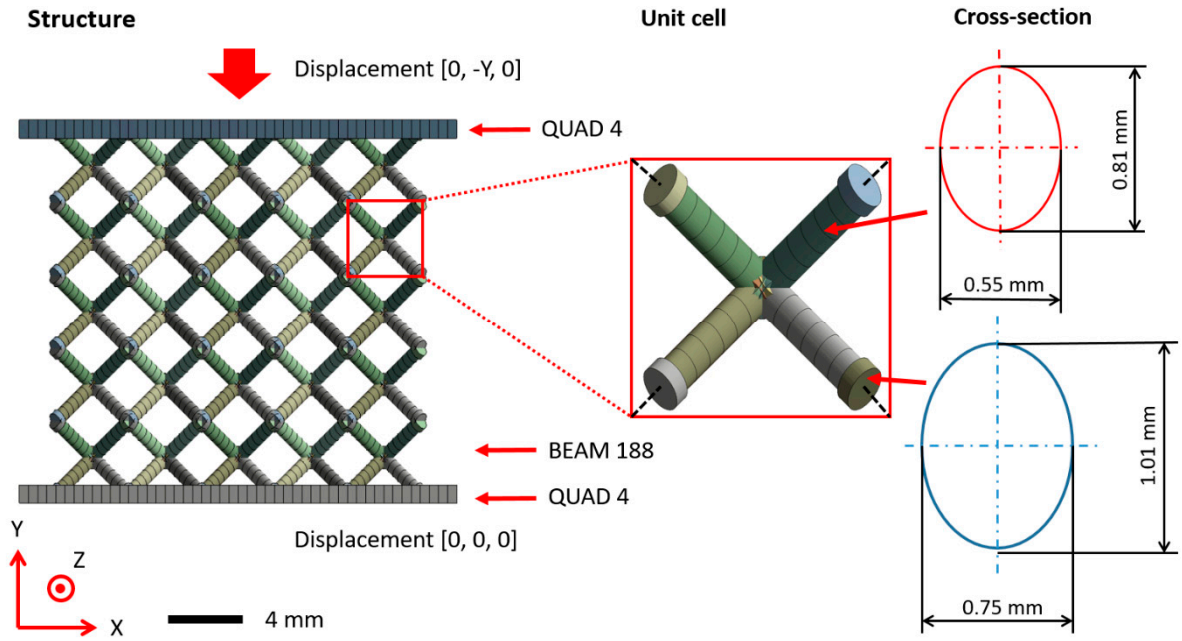


**Figure 6.** Segmented beam element model of BCC lattice structure including geometrical imperfection (for 0.6 mm nominal strut diameter).

Besides the lattice structure, the FE model included a top and bottom surface discretized with quadrilateral shell elements (SHELL 181), where boundary conditions were applied [24]. A standard Structural Steel model was assigned to the shells supplemented with a thousand times higher values of Young's modulus to account for the rigidity of adapters [26]. Between the beam elements of the lattice structure and the top and bottom surfaces, contact with a static friction coefficient [10,35] of 0.15 was applied (tabular steel-steel contact).

The model of the material of the lattice structure was based on a quasi-static tensile test of multi-strut samples. The data obtained by tensile test in the form of force-displacement curves were further evaluated. The optical scanning methods described in Section 2.4 were used for the determination of the actual cross-section of struts in the multi-strut sample. Results were used for the construction of a simple nonlinear elastic-plastic model of the material with isotropic hardening according to stress-strain curves [24,25,37]. No

failure criterion was considered due to the ductile properties of stainless steel 316L, which preserved the continuity of structure, even under large deflection [18].

The compressive loading was applied as a displacement in the y-direction on the top surface. In addition, the bottom surface was constrained in all degrees of freedom. Except for this movement, no other constraints were applied. Quarter-symmetry conditions cannot be introduced to make possible a small sliding structure along the diagonal during its deformation. The step end time was set to 1 s during one step and auto time stepping to program control. Large deflection settings were turned off.

## 3. Results and Discussion

### *3.1. Strut Dimension Analysis/Samples Morphology*

After-manufacturing weight inspection revealed variations in the mass of the samples compared to nominal weight values based on CAD data. A similar phenomenon was observed by Gümrük [32] within BCC lattice structures manufactured from the same material by SLM. This variation differed for all manufactured structures with a nominal diameter value between 0.3–1.0 mm. The residues of supporting cones used in the manufacturing process were excluded as a probable cause of the weight increment because support material was milled down during the post-processing phase to make the samples equally high. The detailed microscope photo shows a large number of metal particles melted on the surface of the sample strut. Most of these particles occurring on the bottom of the struts in the form of irregular clusters (see Figure 7, aggregates in red circles). It is caused by an increased heat transfer into the powder layer beneath, compared to the surrounding area. This phenomenon leads to a change of the geometry of down-skin surfaces known as the staircase (stair-step) effect [48]. The conditions of this effect led to a change of strut cross-section shape and size [3,21], dominantly in a direction perpendicular to the built platform. This led to a deviation in sample weight compared to nominal data (see Figure 8). It must be mentioned that the calculation of nominal weight is based on data not considering the strut porosity [48], which probably occurred during sample manufacturing. For standard process parameters tuned by the machine manufacturer, a negligibly low porosity value is assumed.

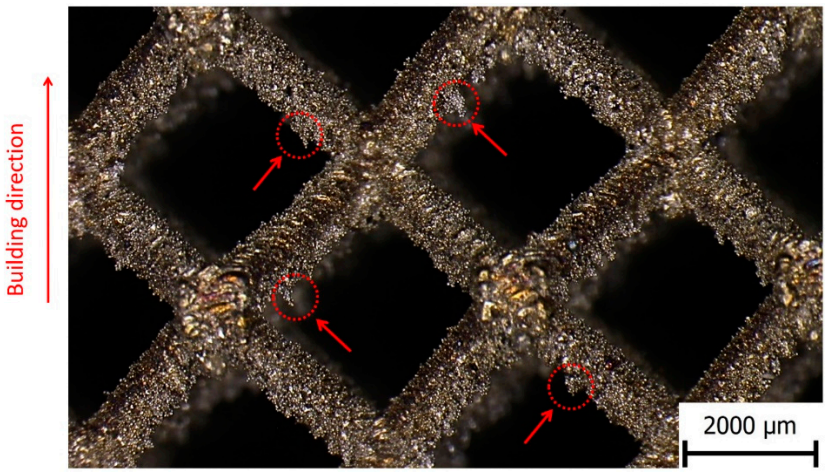


**Figure 7.** Detail of lattice structure surface with imperfections.

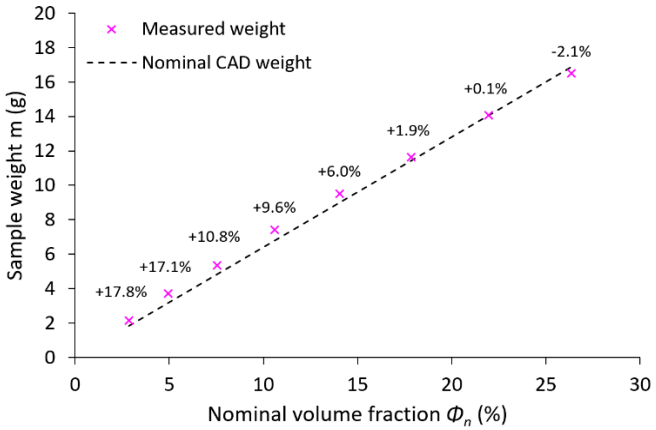


**Figure 8.** Comparison of the actual average and nominal weight of samples according to the nominal volume fraction; the numbers above points show the percentage of weight variation.

The lattice structures were digitalized as described in Section 2.4 to determine the accurate strut cross-section geometry. Based on these measurements, the strut cross-section geometry was approximated with a circular (according to Gauss distribution) and an elliptical shape to represent the manufactured strut geometry more precisely. The diameter of both Gauss circular and elliptical cross-sections based on optical measurements is bigger than the nominal CAD diameter values for all samples. The increase of diameter for the Gauss circular approximation is thereby between +4.0% and +22.5% (see Figure 9a). The major axis of the elliptical cross-section varies between +15.0% and +50.0%. The minor axis for all strut sizes is slightly smaller than the nominal value (between −8.0% and −12.9%; see Figure 9b). These values are reflected in the load-bearing strut cross-section area (see Table 2). Together with the results of weight measurement and the knowledge from a previous study [41], the following can be concluded: there is probably a strut diameter beyond the range of diameters investigated in this study for which increments in cross-section area caused by imperfections became negligible if the trend remains. Detail assessment of the border nominal strut value for which geometrical imperfections connected to the change of its cross-section has to be considered and should be further investigated.

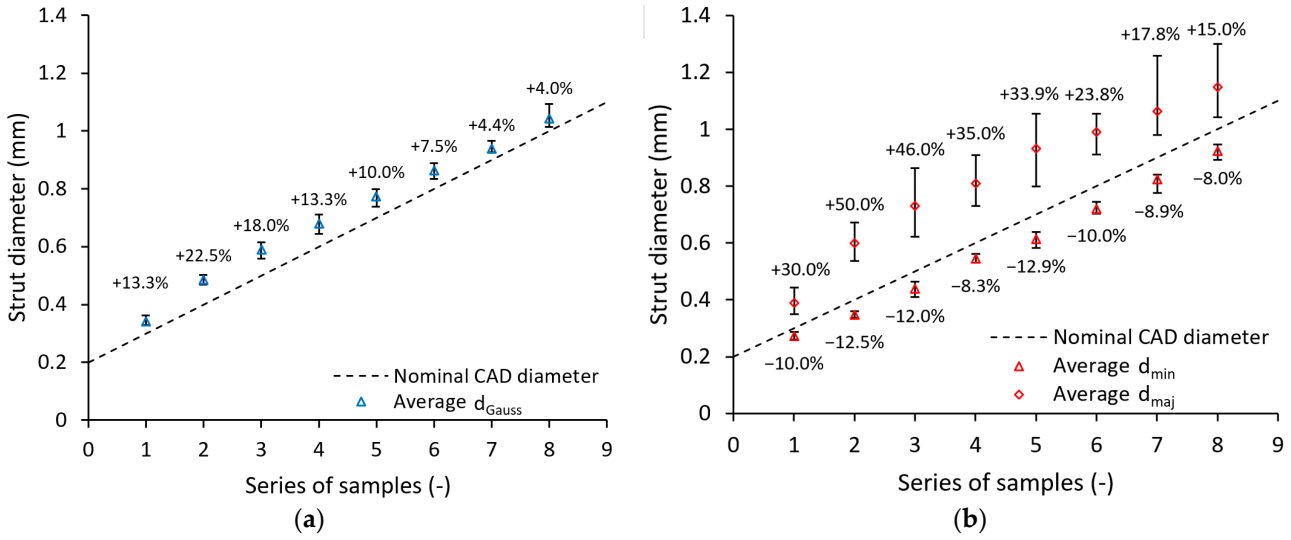


**Figure 9.** Difference between nominal and measured dimensions for (**a**) Gauss circular and (**b**) elliptical measurement; numbers above/beneath points show the percentage of dimension increase/decrease compared to CAD data.

**Table 2.** Average strut dimensions according to different measurement methods.

| $d_n$ (mm) | $d_{Gauss}$ (mm) | $S_{Gauss}/S_n$ (%) | $d_{maj}$ (mm) | $d_{min}$ (mm) | $S_{ellipse}/S_n$ (%) |
|---|---|---|---|---|---|
| 0.3 | 0.34 | +13.7 | 0.39 | 0.27 | +41.4 |
| 0.4 | 0.49 | +21.5 | 0.60 | 0.35 | +108.3 |
| 0.5 | 0.59 | +18.0 | 0.73 | 0.44 | +46.2 |
| 0.6 | 0.68 | +13.4 | 0.81 | 0.55 | +34.9 |
| 0.7 | 0.77 | +10.5 | 0.93 | 0.61 | +33.2 |
| 0.8 | 0.86 | +7.9 | 0.99 | 0.72 | +23.8 |
| 0.9 | 0.94 | +4.1 | 1.06 | 0.82 | +18.1 |
| 1 | 1.04 | +4.2 | 1.15 | 0.92 | +14.9 |

Optical measurements of struts in a previous study [40] revealed that an elliptical approximation is more accurate to the actual manufactured strut compared to a circular cross-section. Therefore, it was decided to use primarily the average values of elliptical measurements given in Figure 9b for creating models of geometry in numerical simulation. This approach allowed the introduction of one of the manufacturing imperfections with a crucial impact on lattice structure mechanical properties. According to the measurements, two geometrical configurations were adopted. The first considers only the change of circular strut diameter measured according to Gauss distribution (see Figure 9a), while the second also changes its shape to elliptical (see Figure 9b).

### *3.2. Multi-Strut Tensile Test Evaluation*

The engineering stress-strain curves as a result of the multi-strut tensile tests are related to the sum of all strut cross-sections in the sample. Strut dimensions and their actual cross-sections were measured by optical digitalization methods similar to those used for the lattice structure struts measurement. The samples were loaded until all 12 struts in the sample were broken (see Figure 10). All struts failed in different heights of the sample, which indicates approximately homogeneous mechanical properties across its length. This phenomenon is in contrast to conventional samples, which usually fail in the diagonal direction. The failures were probably driven by the random distribution of larger pores in thin struts, which caused local weakening of cross-sections. On the other hand, if the failure manners of separate struts are judged, a trend similar to the conventional samples occurs.

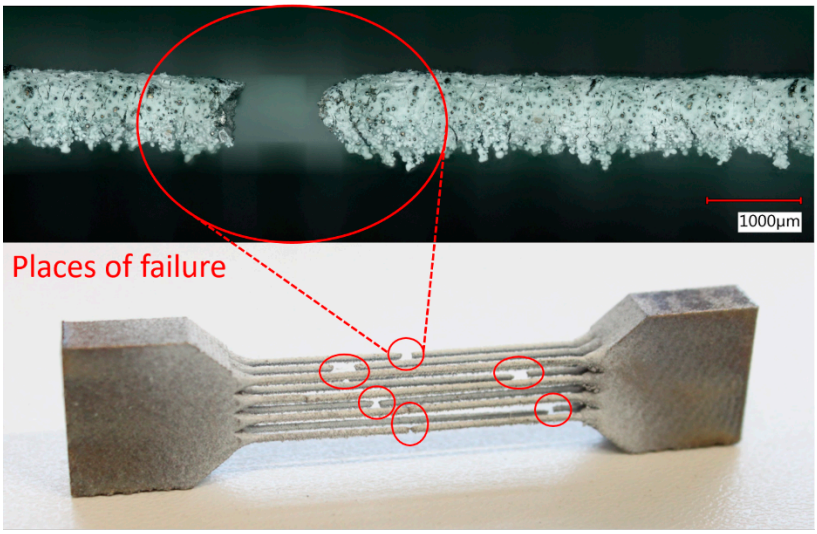


**Figure 10.** Multi-strut tensile sample after experiment including the detail of strut failure.

Because the process parameters and the tilt angle of the multi-strut samples are identical compared to the struts in the BCC lattice structure, similar cross-section deviations,

as well as mechanical properties, were expected. A comparison of the actual manufactured strut cross-section between the multi-strut tensile samples and the lattice structures revealed a deviation of the minor axis smaller than 25 µm. Based on the tensile tests of multi-strut tensile samples, true stress-strain values were calculated unencumbered by imperfections. From the calculated dependency, a bilinear elastic-plastic behavior was defined with Young's modulus $E_s$ of 94 GPa, yield strength (0.2% proof stress) $R_{p0.2\%}$ of 338 MPa, and tangent modulus $E_t$ of 787 MPa (see Table 3).

**Table 3.** Comparison of mechanical properties of conventional samples and samples with thin struts.

| | $E_s$ | $R_{p0.2\%}$ | $E_t$ | $R_m$ | $A$ |
|---|---|---|---|---|---|
| | **(GPa)** | **(MPa)** | **(MPa)** | **(MPa)** | **(%)** |
| Multi-strut tensile samples | 94 ± 10 | 338 ± 20 | 787 | 397 | 5.3 |
| Conventional samples | 166 ± 15 | 450 ± 5 | 89 | 541 | 40.7 |

Mechanical properties obtained by tensile tests of conventional and multi-strut tensile samples showed the following:

- Young's modulus $E_s$ and yield strength $R_{p0.2\%}$ determined by testing of multi-strut tensile samples achieved only 57% and 75% of the conventional samples values;
- Elongation at failure $A$ of multi-strut tensile samples was significantly lower compared to conventional samples, which is appointed to the increased fragility of the thin strut described in previous studies [3,32,36];
- Young's modulus $E_s$ obtained by multi-strut tensile samples testing is approximately 49% lower compared to the results achieved by single strut samples testing combined with the numerical correction presented by Tsopanos [36] and Smith [3]. Contrary to this, yield strength $R_{p0.2\%}$ was more than two times higher compared to previous studies;
- A good correlation of mechanical properties between multi-strut samples test and Gümrük [32] study was found. Young's modulus $E_s$ and yield strength $R_{p0.2\%}$ values deviated up to 5%;
- A good correlation of mechanical properties between conventional samples and the data sheet from SLM Solutions was found. Young's modulus $E_s$, yield strength $R_{p0.2\%}$, and elongation at break $A$ values deviated up to 7%.

### *3.3. Comparison of Analytical Approaches and Experiment*

For comparison of the experimental and analytical results, two different approaches considering the unconstrained movement of struts' free ends introduced by Yunhui [44] were used (Equations (1) and (2)). To calculate the compression modulus of the lattice structure $E_c$, Young's modulus value $E_s$, introduced in Table 3, with 94 GPa is used. Furthermore, the nominal strut cross-sections are applied without considering imperfections (see Figure 11a). The analytical approach based on the Euler–Bernoulli theory (see Equation (2)) predicts the results of $E_c$ closer to the experimentally determined compression modulus of the lattice. The analytical approach based on the Timoshenko beam theory (see Equation (1)) shows a similar trend but predicts a slightly smaller $E_c$. For a nominal strut diameter of 0.4 mm, the results of both analytical approaches deviate the most compared to the experiment (45% and 46% lower).

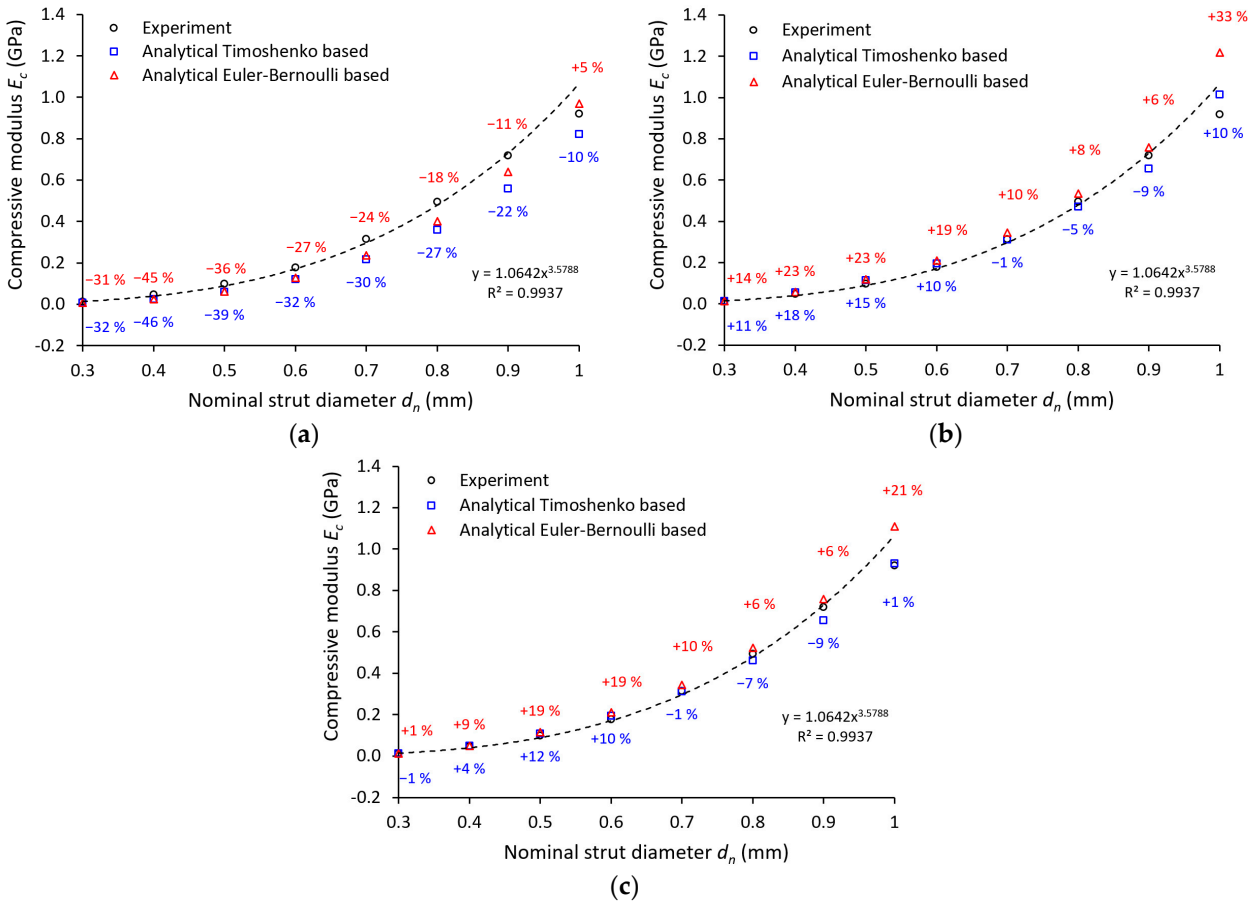


**Figure 11.** Comparison of quasi-static compression experiment with an analytical approach for: (**a**) nominal strut diameter; (**b**) Gauss circular approximation; (**c**) elliptical approximation.

This behavior can be attributed to the boundary conditions of the analytical approach. Both equations assume a frictionless contact on interfaces: the free ends of the lattice structure and the loading surface, and the free ends of the lattice structure and the supporting surface. On the contrary, in the experiments, the contact between the free ends and the surface of the testing machine adapter is characterized by contact with friction. Furthermore, the analytical model did not consider the imperfections of the manufacturing process. The only geometry involved in both models is the nominal strut diameter, which differs greatly from the actual ones according to abovementioned measurements (see Table 2). Therefore, two additional analytical computations were performed for Equations (1) and (2) considering the Gauss circular (see Figure 11b) and elliptical (see Figure 11c) strut cross-section. The input value $r_n$ for the elliptical cross-section was defined from the average major axis $d_{maj}$ and minor axis $d_{min}$ measurements.

The best agreement with the experiment was achieved by the analytical computations considering the elliptical cross-section for the Timoshenko equation. The biggest deviation from the average experimental values reached 12% at strut equal to 0.5 mm diameter. Contrary to this, the worst accuracy was determined by the computations considering the Gauss circular cross-section for the Euler–Bernoulli equation. The biggest deviation from the average experimental values reached 33% at a strut equal to 1.0 mm diameter. For a better assessment of the analytical approaches, further investigations in terms of structure morphology, boundary conditions, and geometrical imperfections must be done.

### *3.4. Comparison of FEM and Experiment*

#### 3.4.1. Linear Material

In the first step, the experiment was compared to FE analysis considering the nominal strut diameter with a circular cross-section. In addition, the material accumulation due to the manufacturing process was considered by increasing the strut diameter by 0.2 mm as described in Section 2.7. The model of the material was restricted to linear elastic behavior (Young's modulus 94 GPa). The resulting structure compressive modulus ($E_c$) versus slenderness ratio ($r_n/l$) are shown in Figure 12, with the slenderness ratio defined as strut radius $r_n$ divided by the strut length $l$. As clearly visible from the results, the simulation is in good agreement with the experiment (FEM—Beam model, orange rhombus). An inaccuracy within the last value can be caused by experimental results deviating from the overall trend or lower stiffness of structures, which are then sensitive to deviations. Repeatability tests of mechanical properties showed a good correlation (range < 5% in plateau area, see Figure 13); nevertheless, better stability of the results can be achieved when more samples with the same nominal strut diameter are tested.

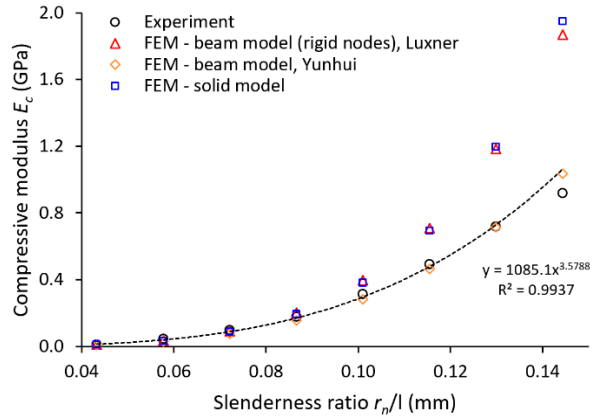


**Figure 12.** Comparison of lattice structure compressive modulus with a numerical solution.

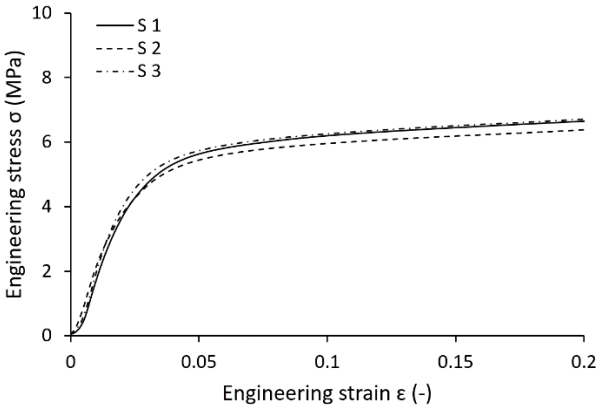


**Figure 13.** Compression test of BCC lattice cubes with nominal strut diameter 0.6 mm.

This approach worked well in the linear deformation region (see Figure 14), and therefore, allowed us to compare the lattice structure properties in terms of compressive modulus or initial stiffness. On the other hand, it was not possible to inspect the internal stress evolution during the loading of the structure. Therefore, a solid element model was introduced (Figure 12, FEM—Solid model, blue squares) to simulate the realistic connection of struts in the vicinity of the node, which is rather represented by the domain than point connection. The loading and the boundary conditions remained the same. The numerical approach was, furthermore, supported with the beam element model (FEM—Beam model

(rigid nodes), red triangles) with adapted stiffness (Young's modulus ×1000) in the near area of nodes according to the Luxner study [26]. The length of the adapted node beams was equal to the nominal strut diameter increased by 0.2 mm (see Figure 5).

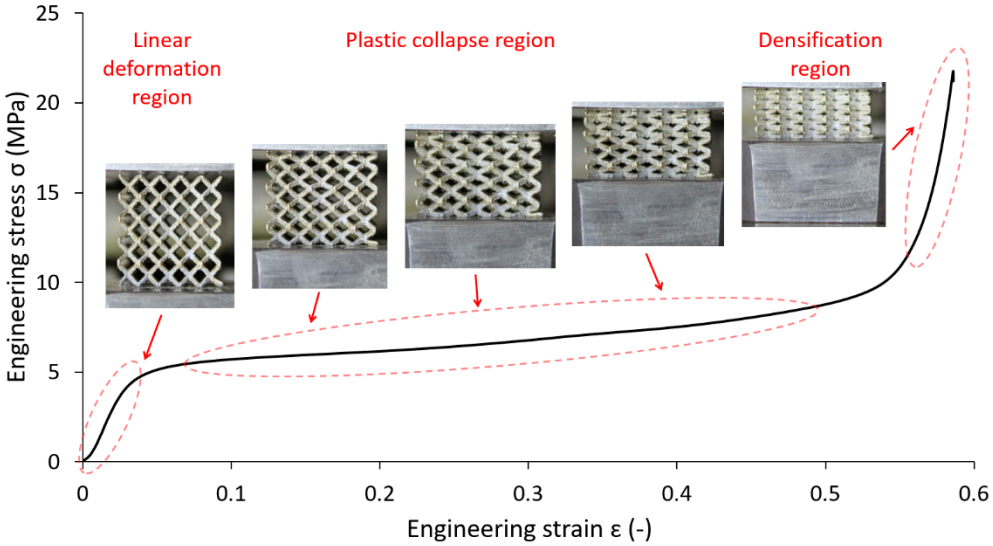


**Figure 14.** BCC lattice structure behavior in different regions of deformation.

The compressive modulus was calculated by both approaches with actual strut connection achieve similar values, but their difference compared to the experiment increased with the rising slenderness ratio. This difference is appointed to high stiffness when only the linear elastic behavior of the material is considered. The stiff behavior manifests, especially in the near vicinity of structure nodes, where the highest stress occurs during structure loading (see Figures 15 and 16). On the other hand, it must be mentioned that the experimental values were determined at the beginning of the linear area of the stress-strain deformation curve with the assumption of nearly elastic linear material. However, the possible explanation could be that plastic deformations can also occur in this area. It could happen despite a linear manner because the area usually takes up to a few percent of the lattice deformation. Therefore, a comparison of the experiment has to be extended to the calculation of nonlinear elastic-plastic material behavior.

#### 3.4.2. Non-Linear Material

Besides the beam element model with elastic-plastic material behavior (Figure 17 FEM–Beam model, orange rhombus), three additional beam element models with nonlinear behavior are compared to the experimental outcome. These include a model with rigid nodes and a nominal strut cross-section (FEM–Beam model (rigid nodes), red triangles), a model with rigid nodes and an elliptical strut cross-section (FEM–Beam model elliptical (rigid nodes), blue cross), and a model characterized by rigid nodes and circular strut cross-section (FEM–Beam model Gauss (rigid nodes), purple squares). The cross-section diameter is derived from the optical measurements of the struts (the Gauss best fit function; Section 2.4).

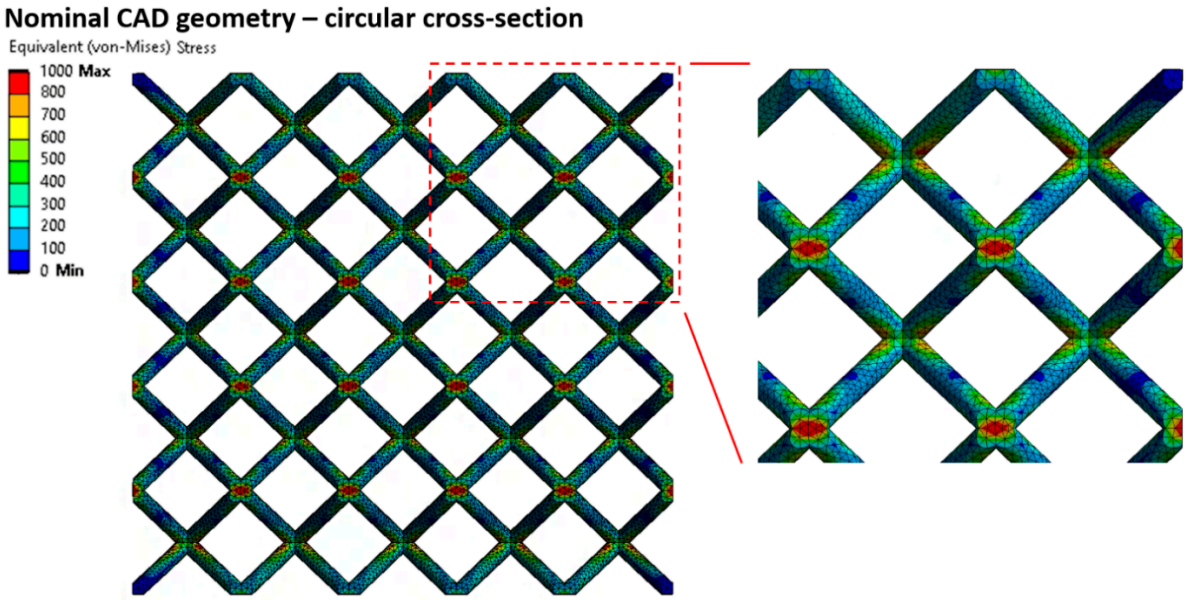


**Figure 15.** Equivalent (von Mises) stress distribution for a structure considering linear elastic material behavior—Circular cross-section (2.5% structure deflection).

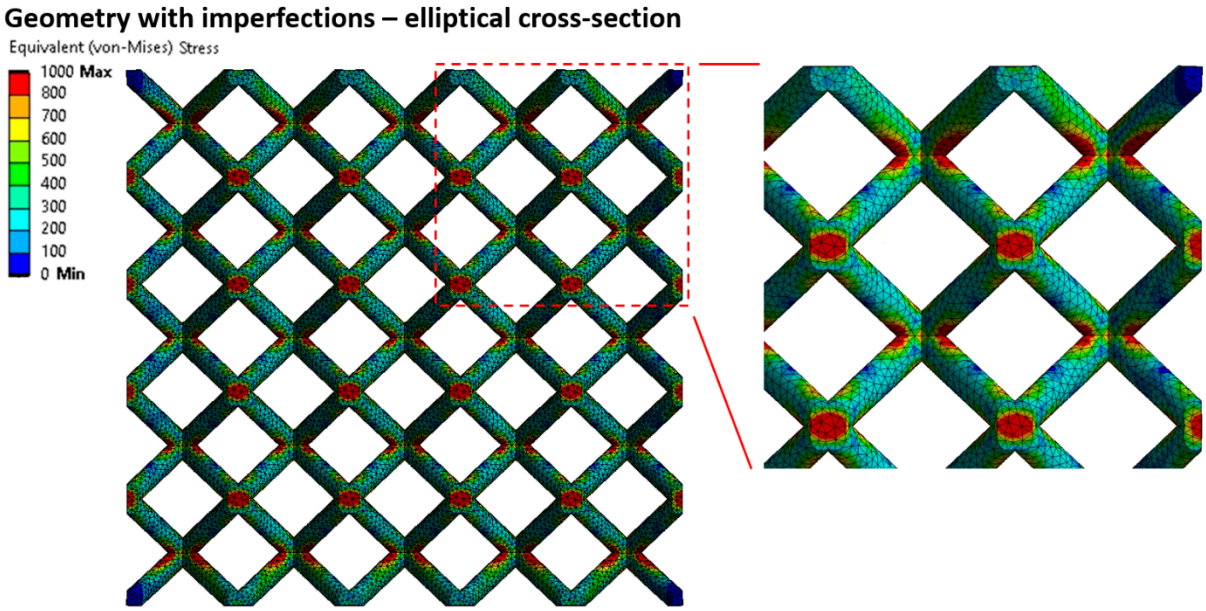


**Figure 16.** Equivalent (von Mises) stress distribution for a structure considering linear elastic material behavior—Elliptical cross-section (2.5% structure deflection).

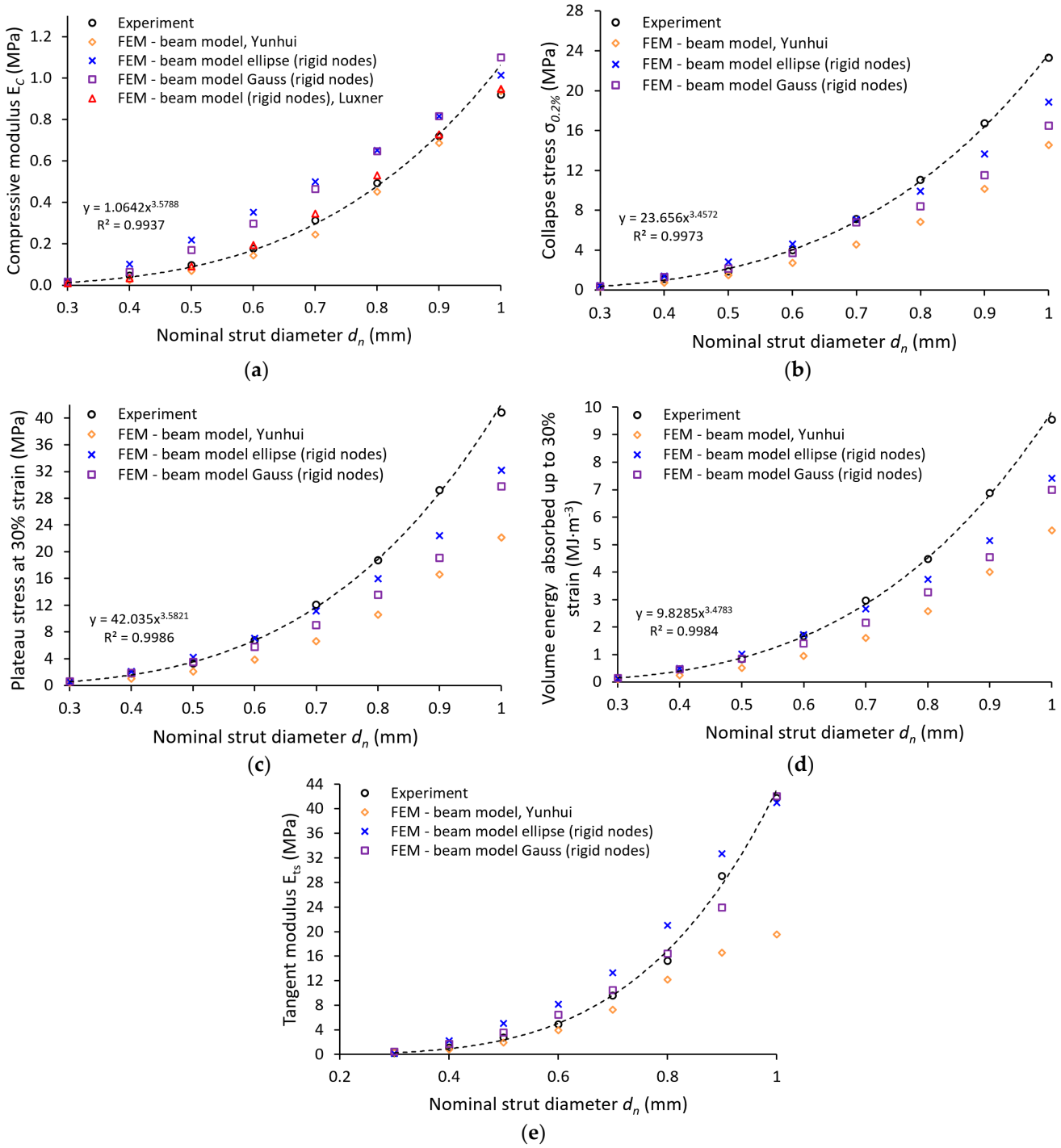


**Figure 17.** Comparison of quasi-static compression experiment with numerical solutions using different approaches—(**a**) compressive modulus; (**b**) collapse stress (0.2% structure strain); (**c**) Plateau stress; (**d**) volume energy absorbed; (**e**) tangent modulus of the structure.

Different trends occur when nonlinear material behavior is considered. Plastic deformation influences the calculated compressive modulus of the structure in the linear regime. Despite this fact, the calculated results of compressive modulus are still in good agreement with the experiment (see Figure 17a FEM–Beam model). Even more accurate results are achieved if rigid nodes in the vicinity of the lattice structure strut nodes are considered (FEM–Beam model (rigid nodes)). Contrary to this, calculations considering elliptical (FEM–Beam model ellipse (rigid nodes)) or Gauss circular (FEM–Beam model Gauss (rigid nodes)) cross-section exhibit higher percentage values of structure compressive modulus

$E_c$ compared to experiments. The biggest difference is visible when the values of structures with strut diameters 0.6 mm and 0.7 mm are compared.

The different trend of deviations occurs when the elastic-plastic material behavior is considered beyond the linear deformation of the structure. The deviation of engineering stress-strain dependency in this area indicates the beginning of structure collapse–Zone of active energy absorption. The first calculations performed with the model considering the nominal strut diameter (see Figure 17b FEM–Beam model) showed overall lower values of engineering stress with 0.2% deformation beyond the linear regime (collapse strain). The decrease is more significant with a rising strut diameter up to 0.9 mm, which corresponds to only 60% of the experimental stress. Contrary to this, slightly more accurate results achieve computations considering rigid nodes and circular Gauss cross-section (FEM—Beam model Gauss (rigid nodes)). Up to a diameter equivalent to 0.5 mm, the computation achieved engineering stress higher than experimental. Then, it started to decrease with a rising strut diameter up to the diameter equivalent to 1.0 mm, which corresponds to 70% of the experimental stress. Even closer to the experiment result an analysis can be achieved considering rigid nodes and elliptical cross-section (FEM–Beam model ellipse (rigid nodes)), which achieves the lowest value of 81% experimentally measured stress for the strut diameter equivalent to 1.0 mm.

A similar trend can be observed for the considered strut diameters also when the engineering stress (plateau stress) at 30% deformation is compared (see Figure 17c). According to the expectations, the lowest engineering stress achieves the calculation considering the nominal strut diameter without increased stiffness in the near vicinity of structure nodes (FEM–Beam model). Overall, lower engineering stress also leads to lower absorbed energy during the lattice structure deformation (see Figure 17d). Supplementing the model with rigid nodes and modified cross-sections leads to a more accurate prediction of the collapse stress in the FE analyses (see Figure 17b, FEM–Beam model ellipse (rigid nodes), and FEM–Beam model Gauss (rigid nodes)). The stress values of the performed analysis that consider the elliptical strut cross-section closely approach the experimental results (up to the nominal diameter of 0.7 mm). Beyond the linear deformation of the structure, a small influence of rigid nodes was observed, and therefore, its separate meaning is no further described in graphs.

The overall levels of engineering stress compared to the experiments in the area of lattice structure progressive collapse exhibit lower values with increasing nominal strut diameter. This behavior could be caused by the same issue that occurs when the material properties of lattice structures are determined based on conventional bulk samples (see Section 2.3) [23,31]. Furthermore, the internal area of tensile sample struts is usually manufactured with process parameters and strategies that differ from those that are applied to surface and subsurface areas because of the manufacturing technology. It leads to different values of mechanical properties. As the strut diameter changes, the ratio of both types of areas changes, and the mechanical properties are expected to variate. Therefore, the material properties should be determined for every strut configuration separately.

On the opposite, the tangent modulus values $E_{ts}$ (see Figure 17e) seem to be in a good correlation with the experiment for nominal strut diameters up to 0.8 mm diameter (FEM—Beam model). Above this strut diameter only models supplemented with geometrical imperfections can provide reasonably good results.

According to the FE simulations, an increment of partly melted material has a bigger significance on the loading force transmission. The deviations of the actual strut diameter can be caused by the different heat conductivity of powder and base parts, which causes the melting of the material with different intensities. This finding has a limitation because only a small range of structure geometrical configurations was tested (nominal CAD diameter $\leq$ 1 mm).

3.4.3. Comparison with Specific Structured Component

A further comparison of experiment and FE simulation was performed to verify the computational approaches in terms of material and geometry. A BCC lattice structure sample with dimensions of 40 × 40 × 20 mm$^3$ (see Figure 18a) was manufactured with a bottom and upper plate with a thickness of 3 mm and 5 mm. A nominal strut diameter of 0.8 mm was chosen for the structure. The size of the unit cell remained the same as in the previous series. The experiment of quasi-static compression was performed under the same conditions described in Section 2.5. The resulting engineering stress-strain curve was compared to the simulations using the beam element models introduced in Section 3.4.2. (see Figure 19). The nonlinear behavior of the material was considered.

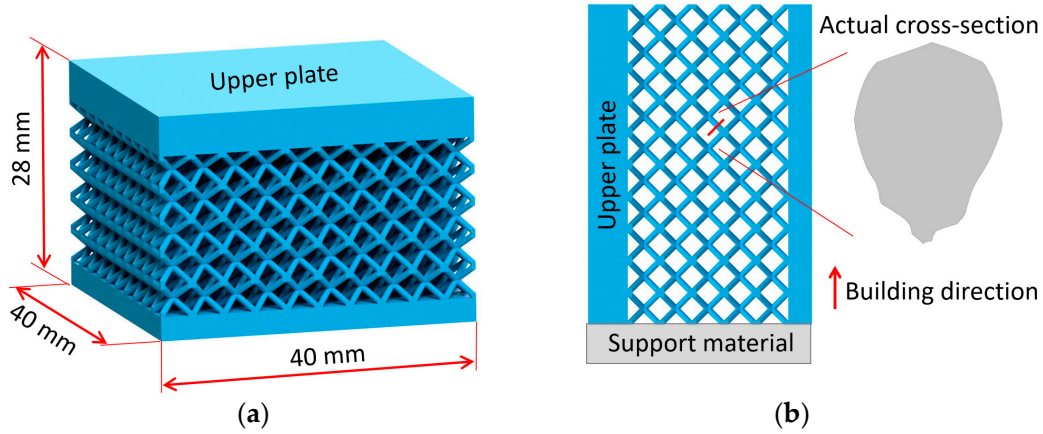


**Figure 18.** (**a**) Geometry of verification part; (**b**) building configuration with oriented cross-section imperfections.

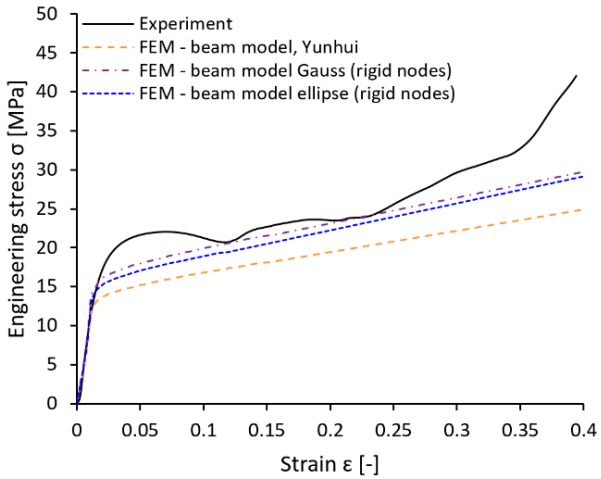


**Figure 19.** Engineering stress-strain comparison of reference structured part.

The verification part had to be manufactured rotated about 90° (see Figure 18b) due to the technological limits of the SLM process. Therefore, the geometrical imperfections that occurred in the manufacturing process were also oriented differently. This orientation was reflected in the model of geometry in simulations considering the elliptical cross-section of the strut.

The results showed a different level of engineering stress deviation for each computational model and experiment. In the first stage of structure loading, the compression modulus determined by simulation and experiment exhibits similar behavior. The difference occurs when the collapse strain is reached. According to the expectations, the worst result achieves for the model that considered the nominal strut diameter (FEM—Beam

model, see Table 4). The model reaches only 75% of the experimentally determined stress at 0.3 strain. Compared to that, models supplemented with geometrical imperfections achieve far better results. The simulation considering the elliptical cross-section (FEM—Beam model ellipse (rigid nodes)) reaches 87% of the experimentally determined stress at 0.3 strain, and the simulation considering Gauss circular cross-section (FEM—Beam model Gauss (rigid nodes)) reaches even 89%. Similar results can be achieved when the stress level at 10% and 20% of deformation or absorbed energy is compared (see Table 4).

**Table 4.** Comparison of stress and absorbed energy for different structure deflection.

| Experiment | | | Simulations | | | | | |
|---|---|---|---|---|---|---|---|---|
| | | | Beam Element | | Beam Element Gauss | | Beam Element Ellipse | |
| $\varepsilon$ | $\sigma$ | $E_a$ | $\sigma$ | $E_a$ | $\sigma$ | $E_a$ | $\sigma$ | $E_a$ |
| (-) | (MPa) | (MJ·m$^{-3}$) | (MPa) | (MJ·m$^{-3}$) | (MPa) | (MJ·m$^{-3}$) | (MPa) | (MJ·m$^{-3}$) |
| 0.1 | 21.24 | 1.88 | 16.84 | 1.4 | 19.96 | 1.65 | 18.94 | 1.56 |
| 0.2 | 23.51 | 4.17 | 19.41 | 3.18 | 23.09 | 3.77 | 22.2 | 3.58 |
| 0.3 | 29.61 | 6.69 | 22.15 | 5.26 | 26.41 | 6.24 | 25.66 | 5.98 |

In contrast to the previous comparison in Figure 17c, it seems to be more efficient to use a Gauss circular cross-section instead of an elliptical for a nominal strut diameter of 0.8 mm in simulations. However, it must be mentioned that the results obtained by simulations of samples with different strut diameters focused mainly on the description of geometrical imperfections in the loading direction, which corresponds to the building direction (where imperfections manifest probably the most, see Figure 7). A different situation can occur when other loading directions are considered. Therefore, imperfections in directions that do not correspond to the building direction could be better described by different cross-section approximations. To confirm this hypothesis, a further comparison of imperfections' influence on the mechanical properties in different loading directions has to be done.

## 4. Conclusions

The quasi-static compression behavior of the BCC lattice structure made of stainless steel 316L by selective laser melting technology was investigated experimentally, analytically, and through finite element modeling. A good correlation between the experiment and analytical-based approach using the Timoshenko theory was achieved for the equivalent of elliptical cross-section (up to 12% within diameter 0.5 mm). Analytical approaches were further supplemented with numerical simulations. In the first step, a nominal CAD-designed geometry discretized by Timoshenko beam elements and solid tetrahedron elements was used. A linear elastic material behavior was used for the simulation. In the second step, two additional numerical approaches considering geometrical imperfections were introduced into the simulation with the non-linear elastic-plastic model of the material. The main conclusions of this study can be described in the following points:

1. It is efficient to use specially designed tensile samples that consist of more thin struts to determine the actual mechanical properties of lattice structures. A good correlation (up to 5%) between mechanical properties determined in this study and described in the literature [32] was found. The analytical models support the credibility of the mechanical properties in the linear-elastic regime;
2. The geometrical imperfections can acquire different significance across variating strut diameter for one structure manufactured with the same process parameters and different geometrical parameters, e.g., strut diameter;
3. The FE analyses with solid and beam element models can predict the lattice structure compressive modulus with similar accuracy if an artificial stiffness increase in the vicinity of nodes is used within the beam element model;

4. The significance of geometrical imperfections increased after reaching 0.2% deformation beyond the linear regime (collapse strain). Including the imperfections improve the accuracy of calculations for both introduced approaches, whereas the change of cross-section to the elliptical seems to be more effective than the change to Gaussian circular for all diameters in the tested range;
5. The calculated levels of engineering stress compared to experiments in the area of lattice structure progressive collapse (30% deflection of structure) exhibit lower values with increasing nominal strut diameter. This phenomenon can indicate different values of mechanical properties of different strut diameters;
6. According to the FE simulation, an increment of partly melted material has a bigger significance for the loading force transmission. The finding is similar to the study of Vrana [31], who determined geometrical imperfections for $AlSi_{10}Mg$ with similar methods. It would be interesting to investigate the strut diameters beyond the range of diameters in this study (nominal CAD diameter > 1 mm) to determine the influence of the described imperfections in the future.

**Author Contributions:** Conceptualization, O.Č.; methodology, O.Č.; software, B.W. and O.Č.; validation, D.K., O.V., L.P. and D.P.; formal analysis, B.W.; investigation, O.Č.; resources, D.K., L.P. and D.P.; data curation, O.Č. and B.W.; writing—Original draft preparation, O.Č.; writing—Review and editing, B.W., D.K., O.V., L.P. and D.P.; visualization, O.Č.; supervision, D.K.; project administration, D.K., L.P. and D.P.; funding acquisition, D.K., D.P and L.P. All authors have read and agreed to the published version of the manuscript.

**Funding:** This research was funded by the ESIF, EU Operational Programme Research, Development and Education within the research project [Architectured materials designed for additive manufacturing] grant number [CZ.02.1.01/0.0/0.0/16_025/0007304] and faculty specific research projects FSI-S-20-6290 and FSI-S-20-6296.

**Institutional Review Board Statement:** Not applicable.

**Informed Consent Statement:** Not applicable.

**Data Availability Statement:** The data presented in this study are available on request from the corresponding author.

**Conflicts of Interest:** The authors declare no conflict of interest.

## Abbreviations

| | |
|---|---|
| AM | additive manufacturing |
| BCC | Body-centered cubic |
| FEA | finite element analysis |
| SLM | Selective laser melting |
| FCC | face-centered cubic |
| CAD | computer-aided design |
| μ-CT | micro computed tomography |
| $Q_{10}$ | 10% quantile of particles distribution |
| $Q_{50}$ | 50% quantile of particles distribution |
| $Q_{90}$ | 90% quantile of particles distribution |
| $E^e_{c1}$ | elastic modulus of lattice structure |
| $E_s$ | elastic modulus of bulk material |
| $v_s$ | Poisson's constant of bulk material |
| $r_n$ | nominal strut radius |
| $l$ | half of unit cell diagonal |
| $m$ | weight of sample |
| $m_a$ | measured weight of sample |

| | |
|---|---|
| $m_n$ | nominal CAD weight of sample |
| $\sigma_{0.2\%}$ | collapse stress (0.2% structure strain) |
| $R_m$ | ultimate tensile strength |
| $\Phi_n$ | nominal volume fraction |
| $d_n$ | nominal strut diameter |
| $S_n$ | cross-section area of nominal strut diameter |
| $d_{Gauss}$ | diameter given by Gauss distribution |
| $S_{Gauss}$ | cross-section area of Gauss strut diameter |
| $d_{maj}$ | major axis diameter |
| $d_{min}$ | minor axis diameter |
| $S_{ellipse}$ | cross-section area of elliptical strut |
| $R_{p0.2\%}$ | yield strength (0.2% proof stress) |
| $E_t$ | tangent modulus |
| $E_c$ | structure compressive modulus |
| $\sigma$ | engineering stress |
| $\varepsilon$ | engineering strain |
| $E_{ts}$ | tangent modulus of structure |
| $A$ | elongation at break |
| $E_a$ | volume energy absorbed |

## References


1. Bonatti, C.; Mohr, D. Mechanical Performance of Additively-Manufactured Anisotropic and Isotropic Smooth Shell-Lattice Materials: Simulations & Experiments. *J. Mech. Phys. Solids* **2019**. [CrossRef]
2. Gibson, L.J.; Ashby, M.F. *Cellular Solids: Structure and Properties*, 2nd ed.; Cambridge University Press: Cambridge, UK, 2014; ISBN 9781139878326.
3. Smith, M.; Guan, Z.; Cantwell, W.J. Finite Element Modelling of the Compressive Response of Lattice Structures Manufactured Using the Selective Laser Melting Technique. *Int. J. Mech. Sci.* **2013**, *67*, 28–41. [CrossRef]
4. Harris, J.A.; Winter, R.E.; McShane, G.J. Impact Response of Additively Manufactured Metallic Hybrid Lattice Materials. *Int. J. Impact Eng.* **2017**, *104*, 177–191. [CrossRef]
5. Deshpande, V.S.; Fleck, N.A. Isotropic Constitutive Models for Metallic Foams. *J. Mech. Phys. Solids* **2000**, *48*, 1253–1283. [CrossRef]
6. Rashed, M.G.; Ashraf, M.; Mines, R.A.W.; Hazell, P.J. Metallic Microlattice Materials: A Current State of the Art on Manufacturing, Mechanical Properties and Applications. *Mater. Des.* **2016**, *95*, 518–533. [CrossRef]
7. Banhart, J. Manufacture, Characterisation and Application of Cellular Metals and Metal Foams. *Prog. Mater. Sci.* **2001**, *46*, 559–632. [CrossRef]
8. Salimon, A.; Bréchet, Y.; Ashby, M.F.; Greer, A.L. Potential Applications for Steel and Titanium Metal Foams. *J. Mater. Sci.* **2005**, *40*, 5793–5799. [CrossRef]
9. Ozdemir, Z.; Hernandez-Nava, E.; Tyas, A.; Warren, J.A.; Fay, S.D.; Goodall, R.; Todd, I.; Askes, H. Energy Absorption in Lattice Structures in Dynamics: Experiments. *Int. J. Impact Eng.* **2016**, *89*, 49–61. [CrossRef]
10. Tancogne-Dejean, T.; Spierings, A.B.; Mohr, D. Additively-Manufactured Metallic Micro-Lattice Materials for High Specific Energy Absorption under Static and Dynamic Loading. *Acta Mater.* **2016**, *116*, 14–28. [CrossRef]
11. Ozdemir, Z.; Tyas, A.; Goodall, R.; Askes, H. Energy Absorption in Lattice Structures in Dynamics: Nonlinear FE Simulations. *Int. J. Impact Eng.* **2017**, 102. [CrossRef]
12. Zhao, M.; Liu, F.; Fu, G.; Zhang, D.; Zhang, T.; Zhou, H. Improved Mechanical Properties and Energy Absorption of BCC Lattice Structures with Triply Periodic Minimal Surfaces Fabricated by SLM. *Materials* **2018**, *11*, 2411. [CrossRef]
13. Labeas, G.; Ptochos, E. Investigation of Sandwich Structures with Innovative Cellular Metallic Cores under Low Velocity Impact Loading. *Plast. Rubber Compos.* **2013**, *42*, 194–202. [CrossRef]
14. Xiao, L.; Song, W. Additively-Manufactured Functionally Graded Ti-6Al-4V Lattice Structures with High Strength under Static and Dynamic Loading: Experiments. *Int. J. Impact Eng.* **2018**, *111*, 255–272. [CrossRef]
15. Chen, Z.; Wang, Z.; Zhou, S.; Shao, J.; Wu, X. Novel Negative Poisson's Ratio Lattice Structures with Enhanced Stiffness and Energy Absorption Capacity. *Materials* **2018**, *11*, 1095. [CrossRef]
16. Vrana, R.; Vaverka, O.; Cervinek, O.; Pantelejev, L.; Hurnik, J.; Koutny, D.; Palousek, D. Heat Treatment of the SLM Processed Lattice Structure Made of AlSi10Mg and Its Effect on the Impact Energy Absorption. In Proceedings of the Conference: Euro PM2019 Congress & Exhibition, Maastricht, The Netherlands, 13–16 October 2019; p. 6.
17. Maskery, I.; Hussey, A.; Panesar, A.; Aremu, A.; Tuck, C.; Ashcroft, I.; Hague, R. An Investigation into Reinforced and Functionally Graded Lattice Structures. *J. Cell. Plast.* **2017**, *53*, 151–165. [CrossRef]
18. Zhang, L.; Feih, S.; Daynes, S.; Chang, S.; Wang, M.Y.; Wei, J.; Lu, W.F. Energy Absorption Characteristics of Metallic Triply Periodic Minimal Surface Sheet Structures under Compressive Loading. *Addit. Manuf.* **2018**, *23*, 505–515. [CrossRef]

19. Tancogne-Dejean, T.; Mohr, D. Stiffness and Specific Energy Absorption of Additively-Manufactured Metallic BCC Metamaterials Composed of Tapered Beams. *Int. J. Mech. Sci.* **2018**, *141*, 101–116. [CrossRef]
20. Al-Saedi, D.S.J.; Masood, S.H.; Faizan-Ur-Rab, M.; Alomarah, A.; Ponnusamy, P. Mechanical Properties and Energy Absorption Capability of Functionally Graded F2BCC Lattice Fabricated by SLM. *Mater. Des.* **2018**, *144*, 32–44. [CrossRef]
21. Mines, R.A.W.; Tsopanos, S.; Shen, Y.; Hasan, R.; McKown, S.T. Drop Weight Impact Behaviour of Sandwich Panels with Metallic Micro Lattice Cores. *Int. J. Impact Eng.* **2013**, *60*, 120–132. [CrossRef]
22. Crupi, V.; Kara, E.; Epasto, G.; Guglielmino, E.; Aykul, H. Static Behavior of Lattice Structures Produced via Direct Metal Laser Sintering Technology. *Mater. Des.* **2017**, *135*, 246–256. [CrossRef]
23. Vrána, R.; Koutný, D.; Paloušek, D.; Pantělejev, L.; Jaroš, J.; Zikmund, T.; Kaiser, J. Selective Laser Melting Strategy for Fabrication of Thin Struts Usable in Lattice Structures. *Materials* **2018**, *11*, 1763. [CrossRef]
24. Lei, H.; Li, C.; Meng, J.; Zhou, H.; Liu, Y.; Zhang, X.; Wang, P.; Fang, D. Evaluation of Compressive Properties of SLM-Fabricated Multi-Layer Lattice Structures by Experimental Test and μ-CT-Based Finite Element Analysis. *Mater. Des.* **2019**, *169*, 107685. [CrossRef]
25. Luxner, M.H.; Stampfl, J.; Pettermann, H.E. Linear and Nonlinear Numerical Investigations of Regular Open Cell Structures. In Proceedings of the ASME International Mechanical Engineering Congress and Exposition, Anaheim, CA, USA, 13–19 November 2004; American Society of Mechanical Engineers, Aerospace Division (Publication) AD: New York, NY, USA, 2004; Volume 47004, pp. 469–475.
26. Luxner, M.H.; Stampfl, J.; Pettermann, H.E. Finite Element Modeling Concepts and Linear Analyses of 3D Regular Open Cell Structures. *J. Mater. Sci.* **2005**, *40*, 5859–5866. [CrossRef]
27. Luxner, M.H.; Woesz, A.; Stampfl, J.; Fratzl, P.; Pettermann, H.E. A Finite Element Study on the Effects of Disorder in Cellular Structures. *Acta Biomater.* **2009**, *5*, 381–390. [CrossRef] [PubMed]
28. Karamooz Ravari, M.R.; Kadkhodaei, M.; Badrossamay, M.; Rezaei, R. Numerical Investigation on Mechanical Properties of Cellular Lattice Structures Fabricated by Fused Deposition Modeling. *Int. J. Mech. Sci.* **2014**, *88*, 154–161. [CrossRef]
29. Dong, G.; Zhao, Y.F. Numerical and Experimental Investigation of the Joint Stiffness in Lattice Structures Fabricated by Additive Manufacturing. *Int. J. Mech. Sci.* **2018**, *148*, 475–485. [CrossRef]
30. Geng, X.; Ma, L.; Liu, C.; Zhao, C.; Yue, Z.F. A FEM Study on Mechanical Behavior of Cellular Lattice Materials Based on Combined Elements. *Mater. Sci. Eng. A* **2018**, *712*, 188–198. [CrossRef]
31. Vrána, R.; Cervinek, O.; Manas, P.; Koutný, D.; Paloušek, D. Dynamic Loading of Lattice Structure Made by Selective Laser Melting-Numerical Model with Substitution of Geometrical Imperfections. *Materials* **2018**, *11*, 2129. [CrossRef] [PubMed]
32. Gümrük, R.; Mines, R.A.W. Compressive Behaviour of Stainless Steel Micro-Lattice Structures. *Int. J. Mech. Sci.* **2013**, *68*, 125–139. [CrossRef]
33. Li, P.; Wang, Z.; Petrinic, N.; Siviour, C.R. Deformation Behaviour of Stainless Steel Microlattice Structures by Selective Laser Melting. *Mater. Sci. Eng. A* **2014**, *614*, 116–121. [CrossRef]
34. Liu, Y.; Dong, Z.; Liang, J.; Ge, J. Determination of the Strength of a Multilayer BCC Lattice Structure with Face Sheets. *Int. J. Mech. Sci.* **2019**, *152*, 568–575. [CrossRef]
35. Lozanovski, B.; Leary, M.; Tran, P.; Shidid, D.; Qian, M.; Choong, P.; Brandt, M. Computational Modelling of Strut Defects in SLM Manufactured Lattice Structures. *Mater. Des.* **2019**, *171*, 107671. [CrossRef]
36. Tsopanos, S.; Mines, R.A.W.; McKown, S.; Shen, Y.; Cantwell, W.J.; Brooks, W.; Sutcliffe, C.J. The Influence of Processing Parameters on the Mechanical Properties of Selectively Laser Melted Stainless Steel Microlattice Structures. *J. Manuf. Sci. Eng. Trans. ASME* **2010**, *132*, 0410111–04101112. [CrossRef]
37. Amani, Y.; Dancette, S.; Delroisse, P.; Simar, A.; Maire, E. Compression Behavior of Lattice Structures Produced by Selective Laser Melting: X-Ray Tomography Based Experimental and Finite Element Approaches. *Acta Mater.* **2018**, *159*, 395–407. [CrossRef]
38. SLM Solutions. Material Data Sheet. Fe-Alloy 316L (1.4404)[1]. Available online: https://www.slm-solutions.com/fileadmin/Content/Powder/MDS/MDS_Fe-Alloy_316L_0820_V0.91_EN_LS.pdf (accessed on 10 October 2019).
39. Gümrük, R.; Mines, R.A.W.; Karadeniz, S. Determination of Strain Rate Sensitivity of Micro-Struts Manufactured Using the Selective Laser Melting Method. *J. Mater. Eng. Perform.* **2018**, *27*, 1016–1032. [CrossRef]
40. Koutny, D.; Vrana, R.; Palousek, D. Dimensional Accuracy of Single Beams of AlSi10Mg Alloy and 316L Stainless Steel Manufactured by SLM. In Proceedings of the 5th International Conference on Additive Technologies iCAT2014, Vienna, Austria, 16–17 October 2014; Pogacar, D., Ed.; Interesansa Zavod: Ljubljana, Slovenia, 2014.
41. Palousek, D.; Omasta, M.; Koutny, D.; Bednar, J.; Koutecky, T.; Dokoupil, F. Effect of Matte Coating on 3D Optical Measurement Accuracy. *Opt. Mater.* **2015**, *40*. [CrossRef]
42. Ushijima, K.; Cantwell, W.J.; Mines, R.A.W.; Tsopanos, S.; Smith, M. An Investigation into the Compressive Properties of Stainless Steel Micro-Lattice Structures. *J. Sandw. Struct. Mater.* **2011**, *13*, 303–329. [CrossRef]
43. Yang, Y.; Shan, M.; Zhao, L.; Qi, D.; Zhang, J. Multiple Strut-Deformation Patterns Based Analytical Elastic Modulus of Sandwich BCC Lattices. *Mater. Des.* **2019**, *181*, 107916. [CrossRef]
44. Ren, X.; Xiao, L.; Hao, Z. Multi-Property Cellular Material Design Approach Based on the Mechanical Behaviour Analysis of the Reinforced Lattice Structure. *Mater. Des.* **2019**, *174*, 107785. [CrossRef]
45. Werner, B.; Todt, M.; Pettermann, H.E. Nonlinear Finite Element Study of Beams with Elasto-Plastic Damage Behavior in the Post-Buckling Regime. *PAMM* **2019**, *19*, 2. [CrossRef]

46. Labeas, G.N.; Sunaric, M.M. Investigation on the Static Response and Failure Process of Metallic Open Lattice Cellular Structures. *Strain* **2010**, *46*, 195–204. [CrossRef]
47. Trevisan, F.; Calignano, F.; Lorusso, M.; Pakkanen, J.; Aversa, A.; Ambrosio, E.P.; Lombardi, M.; Fino, P.; Manfredi, D. On the Selective Laser Melting (SLM) of the AlSi10Mg Alloy: Process, Microstructure, and Mechanical Properties. *Materials* **2017**, *10*, 76. [CrossRef] [PubMed]
48. Qiu, C.; Yue, S.; Adkins, N.J.E.; Ward, M.; Hassanin, H.; Lee, P.D.; Withers, P.J.; Attallah, M.M. Influence of Processing Conditions on Strut Structure and Compressive Properties of Cellular Lattice Structures Fabricated by Selective Laser Melting. *Mater. Sci. Eng. A* **2015**, *628*, 188–197. [CrossRef]

Available online at www.sciencedirect.com

jmr&t Journal of Materials Research and Technology

journal homepage: www.elsevier.com/locate/jmrt

Original Article

# Non-linear dynamic finite element analysis of micro-strut lattice structures made by laser powder bed fusion

*Ondřej Červinek* [a,*], *Heinz Pettermann* [b], *Melanie Todt* [b], *Daniel Koutný* [a], *Ondřej Vaverka* [a]

[a] *Institute of Machine and Industrial Design, BUT Brno, Technická 2896/2, 616 69 Brno, Czech Republic*
[b] *Institute of Lightweight Design and Structural Biomechanics, TU Wien, Gumpendorfer Straße 7, 1060 Vienna, Austria*

ARTICLE INFO

*Article history:*
Received 23 February 2022
Accepted 11 April 2022
Available online 15 April 2022

*Keywords:*
Laser powder bed fusion
Lattice structure
Split hopkinson bars test
Impact test
Dynamic loading
Finite element analysis

ABSTRACT

The development of additive manufacturing technologies enables the production of a new type of porous materials for the absorption of mechanical energy. These are, for example, metallic lattice structures produced by laser powder bed fusion. The structures can be made from a wide range of alloys, achieve high specific energy absorption, and can be manufactured as hybrid parts with conventional bulk components. To effectively develop lattice structures, it is necessary to complement experimental tests with simulations using the finite element method (FEM) performed under conditions of increased loading velocities. Therefore, this study focuses on the development of the FEM modelling strategy that reflects the effect of strain rate sensitivity of the base material (SS316L) and the most significant geometrical imperfections of the manufacturing process. The strain rate is reflected by the Cowper-Symonds constitutive law, which parameters are determined by the dynamic tensile test on Hopkinson split bars. The imperfections are captured by optical digitalization. The significance of the Cowper-Symonds parameters and geometric imperfections are studied independently, whereas agreement with the experiment is observed. Tests are performed for several lattice structures with different strut orientations and velocities to evaluate the versatility of the proposed approaches. A good correlation between computational and experimental results in terms of energy absorption is found for structures with an experimentally determined strut diameter and the proposed Cowper-Symonds input parameters.



* Corresponding author.
E-mail address: Ondrej.Cervinek@vut.cz (O. Červinek).
https://doi.org/10.1016/j.jmrt.2022.04.051

## 1. Introduction

Lightweight porous materials have become interesting in many industrial fields such as aerospace, transportation, biomedical engineering, and defence [1,2]. Properties such as low thermal conductivity, acoustic absorption, mechanical vibration damping, and topology adaptation for high energy absorption have been required for these materials [3–5]. The possibility of their production by additive manufacturing (AM) has introduced various architectures of porous materials with improved mechanical properties [6]. Their deformational behaviour could be adjusted according to specific requirements [7,8]. The most common porous materials are cellular structures that have regularly repeated cubic cells [9]. They can be manufactured as a single part together with bulk elements and designed for a precisely defined load case [10,11]. A frequently used AM technology is laser powder bed fusion (LPBF) that allows the processing of different materials, for example, stainless steel 316L [12], titanium alloy $Ti_6Al_4V$ [13], or aluminium alloy $AlSi_{10}Mg$ [14,15].

Regardless of the material or technology used, it has been found that mechanical properties can be significantly improved by adjusting the process parameters [7,16]. Unfortunately, the result of the tuning process is limited by the mechanical properties of the parent material. When considering strut systems, properties decrease even more as defects are more pronounced in thin geometries [4,17]. Changes in internal lattice arrangement have also led to different types of deformation [18]. This behaviour has been associated with the bending or stretching dominated character of the lattice structure [19,20]. The approach can be applied to many structures, but, except for topology (connectivity of the struts and the degrees of freedom), it does not take into account other factors such as direction and loading conditions or node shape [21].

The performance of the structure can be further improved by local modifications of the struts. For example, a structure with slightly parabolic tapered struts could achieve higher stiffness and lead to a lighter configuration [7]. Similarly, square honeycomb configurations can achieve higher strength and energy absorption efficiency under dynamic loading if thin walls are replaced with deformed strut shapes with equivalent relative density [5]. Another way to improve performance is to redesign the geometry of the entire structure with implicit mathematical equations using tapered struts and fillets at the central nodes to increase mechanical properties [6,22]. Further improvement of energy absorption could be achieved when relative density is continuously changed. This can be done by changing the dimensions of the smallest unit element called a unit cell, in the loading direction [13].

It is necessary to perform detailed finite element analyses (FEA) of the deformation response to predict the mechanical properties of the lattice structures [16,23]. The computational model must contain information about the behaviour of the parent material obtained by mechanical tests on the thin strut [24,25]. Cervinek et al. [26] have already discussed a detailed analysis of the material models used for the lattice structure.

The higher the loading rates and the larger the deformations, the more complex the constitutive law must describe the behaviour. Higher velocities are associated with the propagation of shock waves, significant inertial forces, and an increase in adiabatic temperature [27,28]. The simple approach uses the properties of specially shaped tensile samples with multiple struts tested on modified Hopkinson bars to obtain material parameters used in the Cowper-Symonds (C-S) law [29] as a function of the strain rate. A more sophisticated constitutive law uses the Johnson-Cook equation, which considers large strains, high loading rates, and an adiabatic temperature rise together with the failure criterion [30,31]. It is possible to neglect the adiabatic increase in temperature for a lower strain rate loading using the simplified Johnson-Cook law [32,33].

The model of the geometry that represents the structure in the simulation can be defined in different ways depending on its complexity. The most effective method uses a balanced simplification of the geometry created by the beam elements (based on the theory of Timoshenko [34] or Belytschko-Schwer [32]). The beams usually have circular cross-sections with diameters given by nominal CAD data [25,35]. However, the simulation accuracy is not very high because the model suffers from several inaccuracies in the strut geometry, the definition of the nodal connection, and the contact. An improvement in the accuracy of the Timoshenko beam element model is possible by artificially increasing the stiffness of the structural nodes [36]. A stiffness correction is made in the vicinity of the vertices using elements with artificially increased Young's modulus [21,37]. With this approach used, the beam connection better represents the actual connection of the struts, which behaves more like a spherical domain than a single point. In addition, the element diameters in these domains are increased to compensate for the larger mass of the melted material caused by a material overlap in the nodes. An advantage of beam elements is the ability to analyse larger structures with less computational effort.

In addition, increased simplification is possible [12,15,38] by replacing each unit cell with one or more solid cubic elements. The elements represent the effective properties of the structure under mechanical loading (homogenization). The next approach uses solid tetrahedral elements to model the geometry of the struts with real strut connections [16,37,39].

The purpose of this study is to explore the structural simulations of lattice structures' dynamic loading. The simulation has to consider the effects of the strain rate and the actual cross-section of the struts, which have usually been treated separately. For one of the elementary structures, the range of velocities is set from quasi-static to high-velocity loading. The simulations are compared with experiments of structures made of stainless steel by laser powder bed fusion.

## 2. Materials and methods

To achieve the main objectives of the study, it is necessary to perform a series of procedures related to dynamic compressive and tensile mechanical testing, optical digitalization, and finite element analysis. The most important processes are described in the following sections (see Fig. 1).

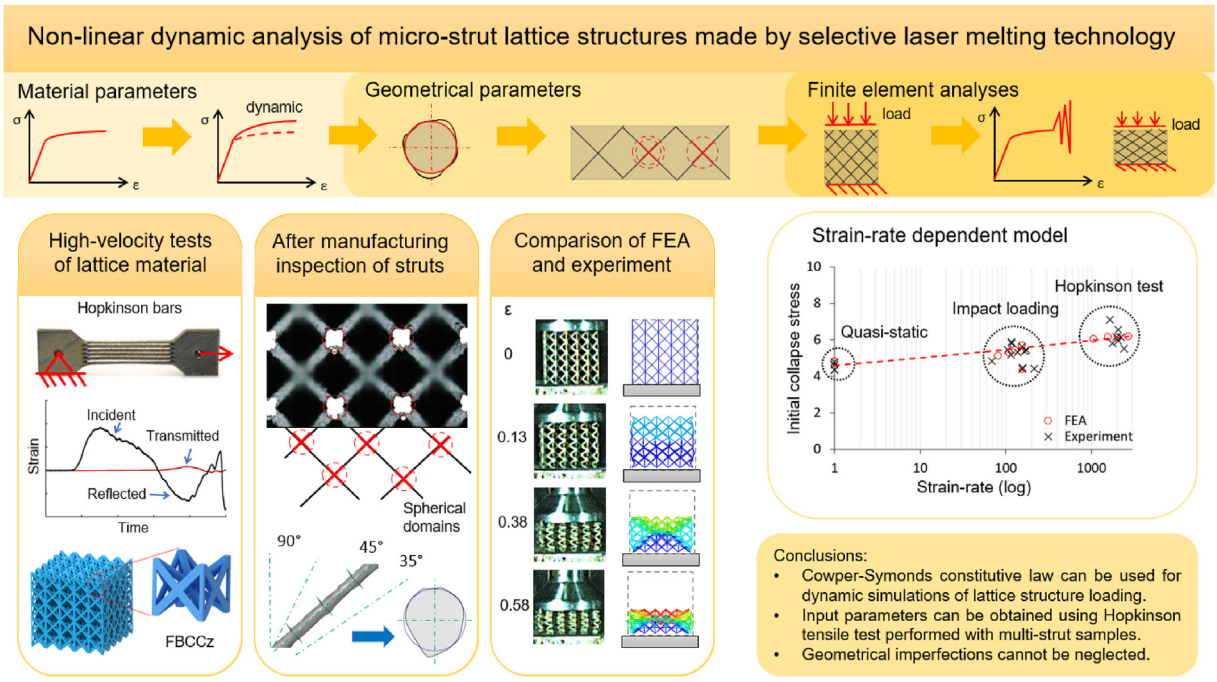


**Fig. 1 – Scheme of the most important process steps of the research.**

Stainless steel 1.4404 (SS 316L) metal powder (TLS Technik GmbH, Bitterfeld-Wolfen, Germany) is chosen to produce all samples on the SLM 280$^{HL}$ machine (SLM Solutions, Lübeck, Germany). The distribution of powder particles, chemical analysis, and process parameters were presented in the previous study [28]. The manufacturing process parameters remained the same to preserve consistent mechanical properties.

### 2.1. *Dimension and shape analysis*

Groups of struts with a length of 20 mm (nominal diameter 0.6 mm) are manufactured at the corners of the building platform to inspect the actual dimensions of the struts in the lattice structures. The layout should reflect potentially different conditions across the platform caused by the irregular flow of inert gas. The different angles of the struts are used to cover all angles that appeared within the manufactured structures (90°, 45°, and 35.26°). The struts were subjected to an optical digitalization process. An ATOS Triple Scan optical scanner (GOM GmbH, Braunschweig, Germany) with an MV170 lens is used (calibration is carried out according to VDI/VDE 2634). Samples were coated with titanium dioxide powder before scanning to prevent the reflection of light projection (coating thickness approximately 5 μm [40]).

The strut scans are evaluated using the GOM Inspect v8.0 software (GOM GmbH, Braunschweig, Germany). Measurements are evaluated at several regularly spaced cross-sections of the strut (see Fig. 2 a)). Each measurement is made using circle that approximated the actual cross-section of the struts based on the Gaussian best fit method (3-point sigma, see Fig. 2 b)) [41].

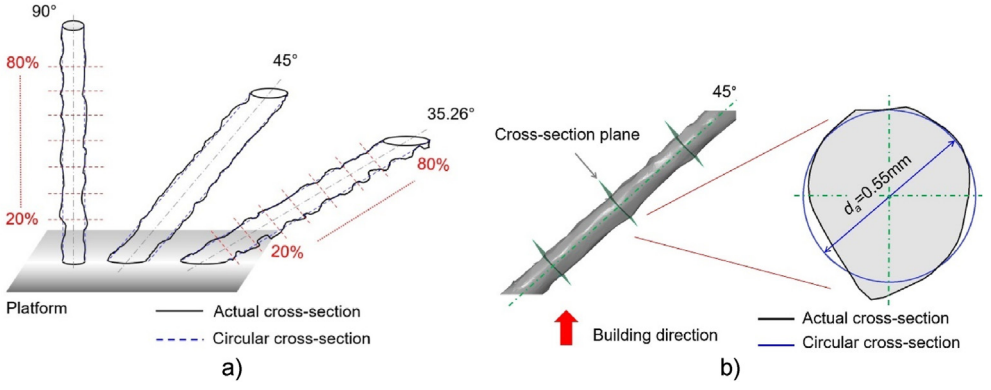


**Fig. 2 – a) height of the cross-sections, b) derivation of different cross-sections.**

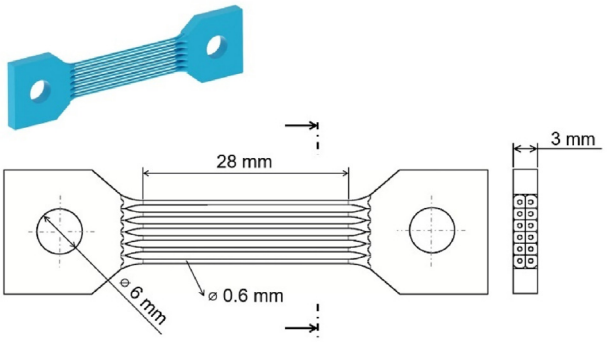


**Fig. 3 – Multi-strut tensile sample for SHBT.**

### 2.2. *Split hopkinson bars test (SHBT)*

Conventional tensile samples manufactured according to common standards (ISO, DIN 50 125) have been found to not accurately represent the mechanical properties of the lattice structure [41,42]. Therefore, strut tensile samples with a nominal strut diameter equal to the lattice structure struts are used (strut diameter 0.6 mm, 12 struts, see Fig. 3) [4,42,43].

Dynamic tensile tests are carried out using modified split Hopkinson tensile bars (see Fig. 4, SVS FEM, Brno, Czech Republic) to determine the mechanical properties of 316L stainless steel under dynamic loading. The initial loading velocity was 30 m $s^{-1}$. The samples are attached to the bars of the device using a bolt connection. The incident and transmission bars are made of structural steel (with Young's modulus 205 GPa, density 7850 kg $m^{-3}$, and Poisson's ratio 0.3). Semiconductor strain gauges EP140-3-35-G (VTS Zlín s.r.o., Zlín, Czech Republic) with a nominal resistance of 350 Ω, a grid length of 3 mm, and a k-factor of +140 are placed in pairs in the middle of both bars. The strain gauges are connected in the half Wheatstone bridge configuration to eliminate any flexural stress on the bars. The signal emitted from the Wheatstone bridge is strengthened with amplifiers. The signal is further recorded with a high-speed oscilloscope with a recording frequency of 10 MHz.

At the beginning of the SHBT, the striker bar impacts the loading block, indicating negative pulse propagation [29]. The pulse travels along the parallel bars until it reaches the second block. Then an elastic wave is reflected, causing a positive stress load in the incident bar. It generates tension wave propagation through the incident bar into the sample from the loading side. When the elastic wave arrives at the interface sample-incident bar, a part of the tension wave reflects as a compression wave from the interface, while the other part continues to propagate along with the sample and into the transmit bar until the sample breaks. Massive wave reflection is caused due to the impedance difference between the sample and the incident bar. The sample loading time is given by the time it takes for the tension wave to reflect itself in the form of an unloading compression wave from the transmit bar free end and for this unloading wave to interact with the sample.

In the next step, a similar device based on the principle of moving bars toward each other is used for high-velocity dynamic compression of structured cubes, as described by Nolting et al. [44].

The signals coming from the gauges are evaluated in the form of engineering stress $\sigma$, strain rate $\dot{\varepsilon}$, and strain $\varepsilon$, using the following known Eq. (1–3) [29,44,45] (assuming for one dimensional stress wave theory):

$$\sigma = \frac{A_0 E_0}{A}\varepsilon_t(t) \tag{1}$$

$$\dot{\varepsilon} = -\frac{2C_0}{L}\varepsilon_r(t) \tag{2}$$

$$\varepsilon(t) = -\frac{2C_0}{L}\int_0^t \varepsilon_r dt \tag{3}$$

where $\varepsilon_t(t)$ represents the transmitted wave, whilst $\varepsilon_r(t)$ represents a reflected wave. $A_0$ and $E_0$ represent the cross-sectional area and the Young's modulus of the bars, while A indicates the cross-sectional area summed over all struts in the multi-strut sample. In addition, $L$ indicates the initial length of the sample in loading direction, whilst $C_0$ indicates the elastic wave velocity given by Eq. (4) [44]:

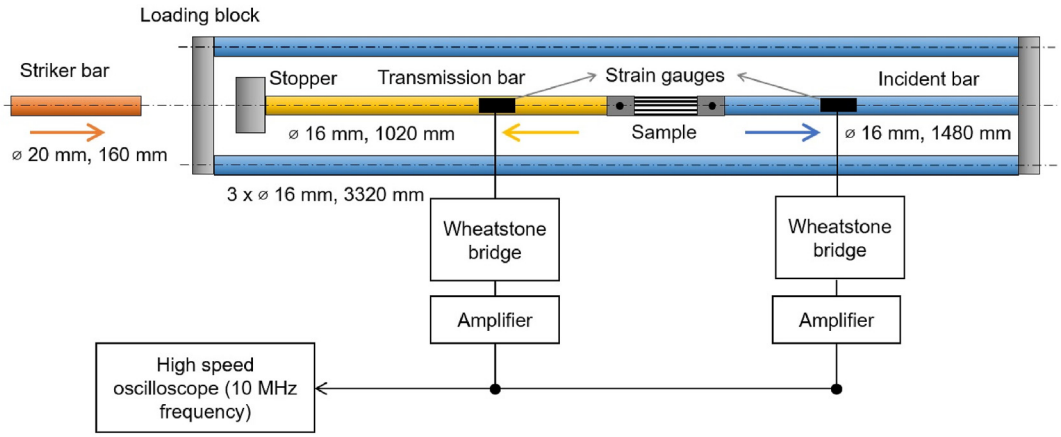


**Fig. 4 – Schematic picture of Hopkinson bars used for dynamic tensile tests.**

**Table 1 – C-S proposed parameters.**

| Authors | $D$ [$s^{-1}$] | $q$ [-] | Description |
|---|---|---|---|
| Langdon & Schleyer [46] | 429–2 721 | 4.1–5.8 | Standard bulk samples, strain rates $10^{-4}$-50 $s^{-1}$ |
| Burgan [47] | 240 | 4.74 | Sheets with thickness 10 mm |
| Gümrük [29] (1) | 4 851,9 | 4.078 | To 100 $s^{-1}$, based on yield stress |
| Gümrük [29] (2) | 80 736,69 | 5.0075 | To 6600 $s^{-1}$, based on yield stress |
| Gümrük [29] (3) | $252 \cdot 10^6$ | 8.054 | Up to 6600 $s^{-1}$, based on max. tensile stress |
| Gümrük [29] (4) | $17 \cdot 10^6$ | 12 | Estimation |

$$C_0 = \sqrt{\frac{E_0}{\rho_0}} \tag{4}$$

where $\rho_0$ is the density of the bars.

### 2.3. C-S material parameters

The C-S constitutive law accounts for the basic mechanism of strain rate dependence [16,27]. It is possible to use the model because the range of relatively low velocities is applied. The formulation of the model is given by the following Eq. (5) [27]:

$$\sigma_d = \sigma_0 \left[1 + \left(\frac{\dot{\varepsilon}}{D}\right)^{1/q}\right] \tag{5}$$

where $\sigma_d$ and $\sigma_0$ represent the yield or maximum tensile stress observed during the dynamic and static test, respectively, whilst $D$ and $q$ are constants obtained by performing curve fitting with the experimental data. Mechanical tests at different velocities, including quasi-static loading, are usually performed to obtain these constants for a specific material.

The literature shows C-S constants for different conditions obtained by curve fitting (see Table 1).

### 2.4. Impact test

The present study focuses on lattice structures with a cubic unit cell assembled by struts along the body diagonals or faces (see Fig. 5). These are specifically called body-centered cubic (BCC), face-centered cubic (FCC), and their modifications supplemented with vertical struts in the corners (BCCz, FCCz) or their combinations (FBCC, FBCCz). Lattice structure cubes with nominal dimensions of 20 × 20 × 20 mm and 4 mm unit cell size are designed for a dynamic compression test (5 samples of each structure). The nominal diameter of the structure strut in the CAD design is set to 0.6 mm.

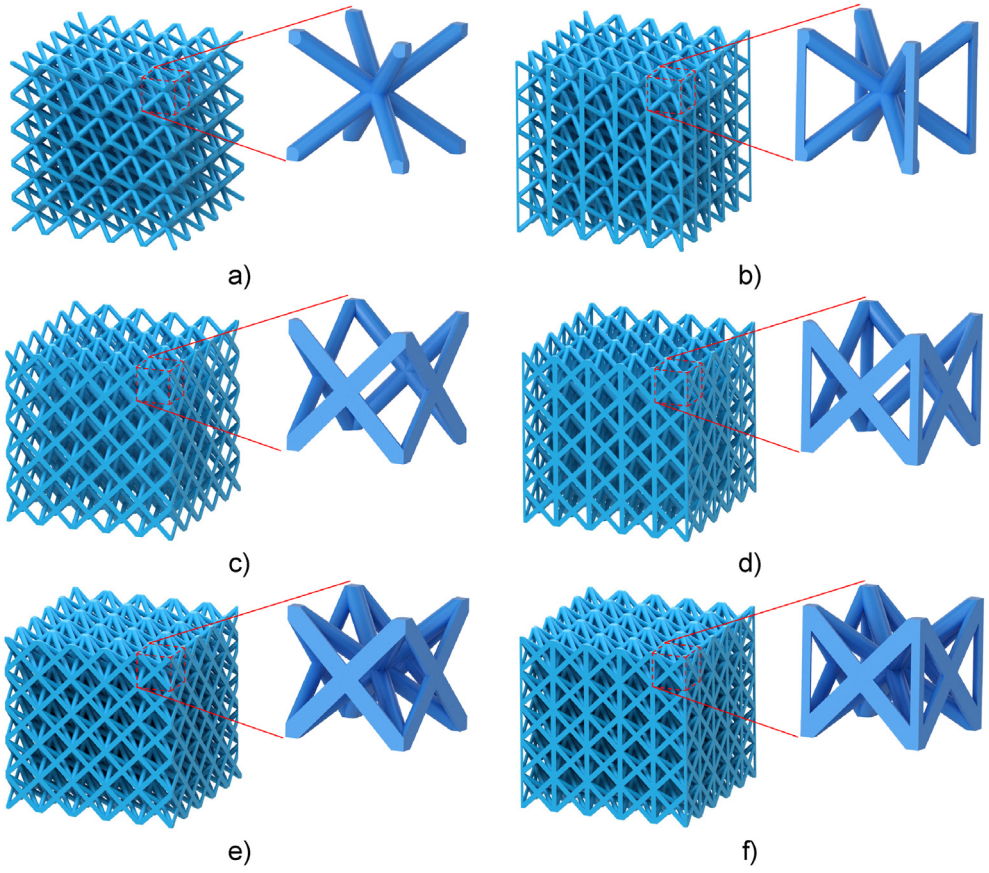


**Fig. 5 – Unit cell of a) BCC, b) BCCz, c) FCC, d) FCCz, e) FBCC, and f) FBCCz lattice structure.**

Drop-weight impact tests of the lattice structures are performed with the impact tester developed at the Brno University of Technology (BUT, Fig. 6). The device is equipped with a Phantom V710 high-speed camera (Vision Research, Wayne, New Jersey) and a strain gauge XY31-3/120 (HBM GmbH, Darmstadt, Germany). The strain gauge measures the reaction force during the deformation of the lattice sample, whereas the high-speed camera measures the position of the marker on the falling head to capture the deformation of the sample. A strain gauge signal is recorded using the Quantum X MX410B data acquisition system (HBM GmbH, Darmstadt, Germany) with a sampling frequency of 96 kHz. Data from the high-speed camera are recorded using Phantom Camera Control software version 3.5 (Vision Research, Wayne, NJ) with a sampling frequency of 56.808 kHz. Both records are compounded and evaluated in the MATLAB R2021a software (MathWorks, Natick, Massachusetts). The following outputs are obtained by signal evaluation: time dependence of the force reaction, deformation, and falling head velocity.

During impact tests, the overall weight of the crosshead is 13.45 kg, and the height of the drop is 1 m. For these parameters, a crosshead achieves a drop velocity of approximately 3 m $s^{-1}$, equal to an impact energy of 60.5 J. The testing device belongs to low-velocity test devices [14,48,49].

### 2.5. Finite element analysis

Numerical simulations are performed in the Explicit Dynamics module of ANSYS Workbench 20.2 (Ansys Inc., Canonsburg, Pennsylvania). The main subject of the simulations is the dynamic compression of lattice structure samples using a split Hopkinson pressure bars test and an impact test described in Sections 2.2 and 2.4.

#### 2.5.1. Model of material

The model of material given by the elastic-plastic behaviour is determined with the quasi-static tensile test of specially shaped samples performed in the study by Cervinek [26]. The original true stress-strain response $\sigma_T$ is fitted with the Hollomon Eq. (6) [5] to achieve the material parameters (strength coefficient $K_H$ and hardening exponent $n_H$):

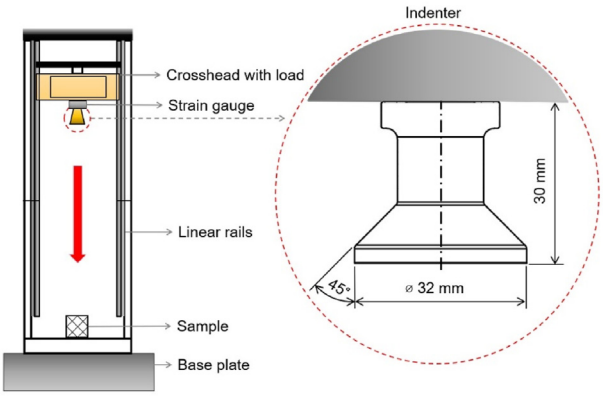


**Fig. 6 – Impact tester scheme with indenter.**

$$\sigma_T = \sigma_0 + K_H \varepsilon_p^{n_N} \quad (6)$$

where $\sigma_0$ is yield stress value, while $\varepsilon_p$ is an effective plastic strain. The non-linear behaviour is then assigned to beam elements in the Workbench together with the C-S constitutive law definition [50,51] (see Table 2). The failure criterion is not considered due to the ductile properties of stainless steel, which preserves the continuity of the structure, even under large deflection [52].

#### 2.5.2. Model of geometry

The model is created using a Python API V20 script that allows the cutting of the struts along their axis. It allows to use half or quarter cross-section at the structure surface or to define the cross-section of a random shape. All struts are further divided along the length of the axis into the mid-part and ends. Each strut consists of 2-noded beam elements (BEAM 188) based on Timoshenko beam theory, which encounters shear deformation effects. At least seven elements are used for discretization in the middle of the part. It is done according to the mesh sensitivity study performed in previous studies [14,34]. Young's modulus is ten times higher at the intersections of the struts [21]. The diameters of these elements are increased to 0.8 mm to compensate for the increase in material (see Fig. 7). The procedure ensures bending the struts rather than deforming the nodes during compression loading [53].

#### 2.5.3. Finite element analysis setup

Except for the lattice structure, the simulation includes a top (indenter) and bottom (base) surface. Surfaces are discretized with 4-noded quadrilateral shell elements (QUAD 4 with a thickness of 3 mm) and assigned with boundary conditions [50]. The compressive loading is introduced by applying the initial velocity on an upper plate in the Y direction [displacements Ux = 0; Uy = -Y; Uz = 0] (see Fig. 7). In addition, the bottom surface is constrained in all degrees of freedom of displacement. No other constraints are applied.

A standard structural steel model of the material is assigned to the shells supplemented with ten times higher values of Young's modulus to account for the increased stiffness of the plates. The indenter surface is supplemented with an artificially increased density to represent the weight of the load head (13.45 kg). At the interfaces of the structure-indenter (vertices-face) and the structure-based plate (vertices-face), contact with a static friction coefficient of 0.15 [7,54] and a dynamic coefficient of 0.1 [2,55] is applied.

**Table 2 – Material parameters of stainless-steel elastic-plastic behaviour.**

| Mechanical property | Value | Unit |
|---|---|---|
| Density of parent material $\rho_s$ | 7900 | kg·$m^{-3}$ |
| Young's modulus $E$ | 94000 | MPa |
| Poisson's ratio $\nu$ | 0.31 | – |
| Yield strength $\sigma_0$ | 338 | MPa |
| Strength coefficient $K_H$ | 481.45 | MPa |
| Hardening exponent $n_H$ | 0.17 | – |
| Ultimate tensile strength $\sigma_{UTS}$ | 397 | MPa |

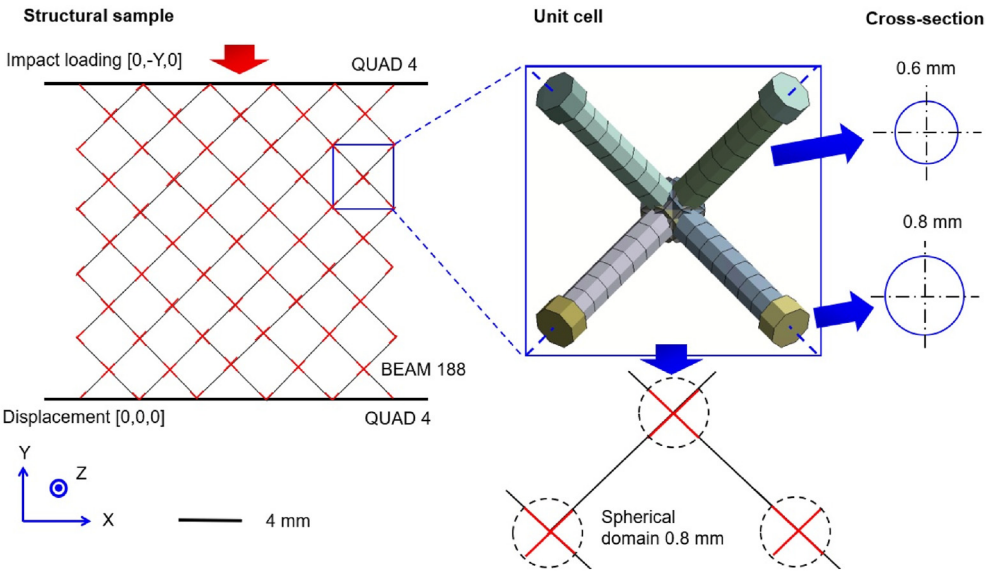


**Fig. 7 – Schematic composition of the BCC lattice structure beam element model including geometrical imperfection.**

## 3. Results and discussion

### 3.1. *Strut dimension analysis/samples morphology*

#### 3.1.1. *Lattice structure samples*

After the sample manufacturing, post-processing operations and inspections are performed. Weight measurement is carried out using Sartorius MA35 with a resolution of ±0.5 mg (Sartorius, Göttingen, Germany). The measured weights are divided by the total volume of the cubic space (8000 $mm^3$) to obtain the actual density of the structure $\rho^*$. Based on the calculation, the relative density $\rho'_{RE}$ is determined using the following Eq. (7) [10]:

$$\rho'_{RE} = \frac{\rho^*}{\rho_S} \cdot 100\% \tag{7}$$

where $\rho_S$ is the density of parent material given by the supplier's datasheet (7 900 kg $m^{-3}$). The same calculation is used for the nominal CAD relative density $\rho'_{CAD}$, where the density of the structure is calculated by CAD software Inventor 2021 (Autodesk, San Rafael, California).

The further comparison reveals a good agreement between measured and CAD-based densities for FCC, FCCz, FBCC, and FBCCz samples (see Fig. 8 a)). On the other hand, significant differences occur between the BCC and BCCz lattice structures. Fig. 8 b) shows that the range of relative density deviations $\rho'_{RED}$ is approximately 8% ± 1%, which is similar for all inspected structures. For most structures, the deviations are regularly distributed around the CAD-based relative density represented by zero value on a vertical axis. The different phenomena occur for BCC and BCCz lattice structures, where deviations go to positive values only. It is probably caused by the struts with an orientation of 35.26° regarding the building platform, as they incline to the most irregular aggregations. The increased transfer of heat to the powder layer beneath causes the particles in the larger area compared to the other strut orientations [16,17,28,41]. The phenomenon could occur on a smaller scale when FBCC and FBCCz structures are considered with differently oriented struts. For the standard process parameters delivered by the machine manufacturer, a negligibly low porosity value is assumed. The assumption is based on equal relative densities calculated from actual weight [56] and optical digitization.

The microscope photos (Olympus SZX7, magnification ×25, Shinjuku, Japan) show partially melted metal particles on the surface of the sample strut. Most of these particles occur at the bottom of the struts in the form of irregular clusters (see Fig. 9; arrows) due to the phenomenon mentioned above. It leads to a change in the geometry of downskin surfaces. If the phenomenon is strong enough, it can influence the shape and size of the cross section of the strut [4,56], dominantly in a direction parallel to the building direction.

#### 3.1.2. *Single struts inspection*

The single struts are digitalized as described in Section 2.1. to determine the accurate cross-section geometry of the strut. The graph in Fig. 10 shows the diameters of struts manufactured at different angles with results organized according to a measurement position.

Based on the comparison, it can be concluded that measured diameters are smaller than the CAD-designed diameters within all inspected angles. No specific correlation was found between the change in diameters and the increase in height. Therefore, the possible increase in heat conduction at a low altitude over the building platform has no significant meaning, at least for thin struts made of SS316L up to 16 mm height above the platform (altitude of the highest cross-section). The cross-section areas of all inspected struts reach between 83.1% and 84.3% of a CAD-designed cross-section (see Table 3). This range appoints to a minimal difference in cross-sections across inspected angles but highlights the importance of differences between measured and CAD-designed geometry.

Based on the results, several points must be considered when the lattice structure geometry is prepared:

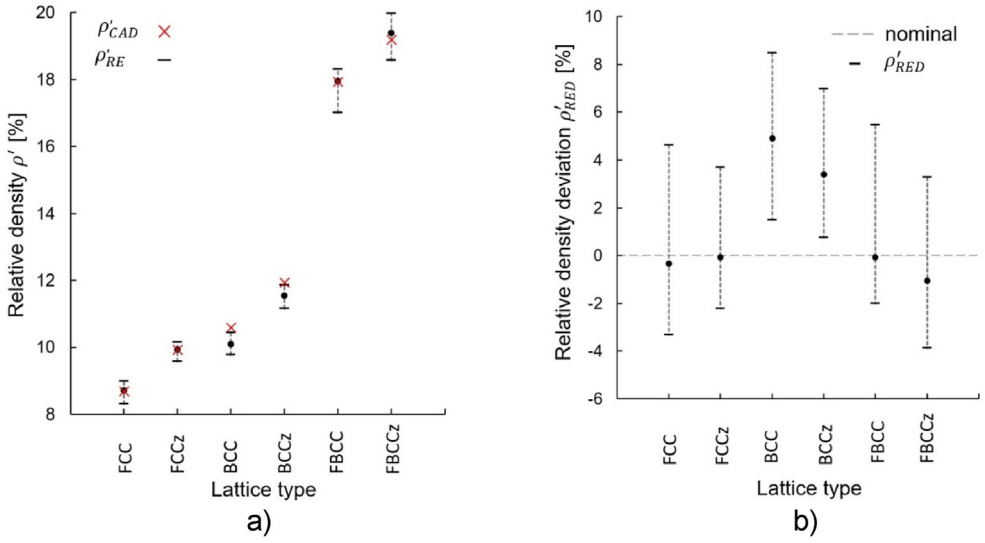


**Fig. 8 – a) Comparison of measured and CAD based densities; b) deviation in relative density.**

- It is possible to neglect the differences between the diameters of the struts built at different angles since the average variation is less than 3%.
- If the geometry of struts is represented by a circular cross-section based on measurements, the nominal dimension reduced by -0.05 mm can be used (see Table 3).
- The negligible range of measured strut diameters could indicate a similar influence of the laser on differently oriented struts positioned in the corners of the platform. Therefore, the mutual position of the sample-laser source can have a greater influence on the final geometry than strut orientation.
- The measurements show that the cross-sectional shape tends to certain non-circularities that can be approximated by an ellipse, which was already discussed in Cervinek et al. [26]). However, the significance of this imperfection is less important and, therefore, is not discussed within the study.

### 3.2. *SHBT evaluation*

Fig. 11 gives an example of the results obtained by the high-velocity tensile test described in Section 2.2. The relatively low amplitude of the initiated signal produces excessive noise.

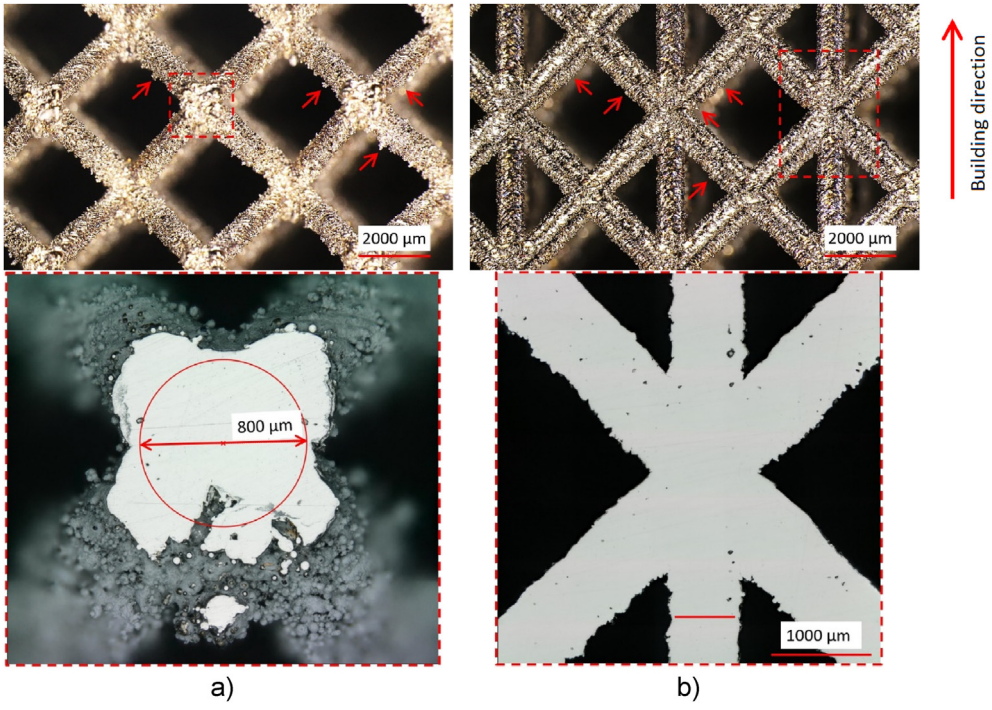


**Fig. 9 – Details of manufactured a) BCC and b) FCCz structure.**

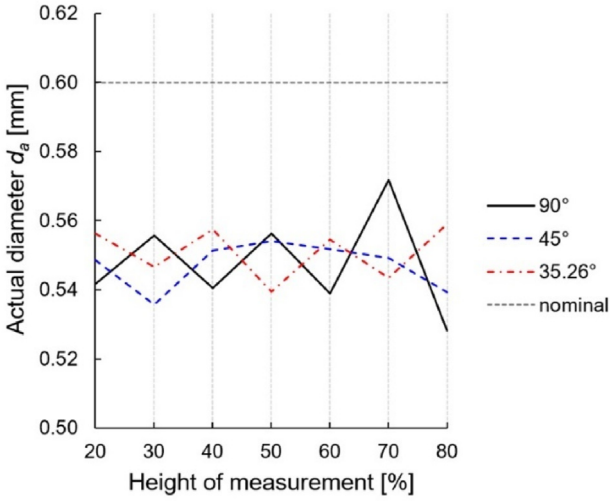


**Fig. 10 – Actual strut diameter with circular approximation.**

**Table 3 – Results of single strut dimension measurement.**

| Angle [°] | Average actual diameter $d_a$ [mm] | Cross-section area [mm$^2$] | Compared to nominal [%] |
|---|---|---|---|
| 90 | 0.548 | 0.236 | 83.3 |
| 45 | 0.547 | 0.235 | 83.1 |
| 35.26 | 0.551 | 0.238 | 84.3 |

Therefore, the signal is cut after the first reflection to obtain readable information. The low amplitude of the transmitted signal is associated with the large difference in impedance at the sample–bar interfaces. Therefore, the signals captured on the incident bar and the transmit bar are amplified. Sample fastening conditions should be investigated in detail in the future to decrease this effect.

The response of the lattice structure in terms of acting stress, strain, and strain rate is evaluated using Eq. (1–3). The results are compared in terms of the ultimate tensile strength $\sigma_{UTS}$, maximal strain $\varepsilon_{MAX}$, and maximal strain rate $\dot{\varepsilon}_{MAX}$. A comparison of $\sigma_{UTS}$ and quasi-static testing in a previous study

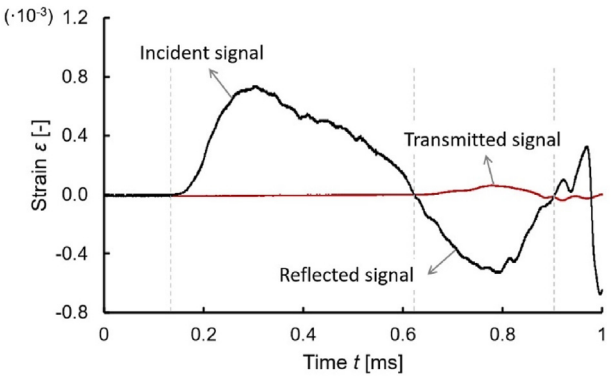


**Fig. 11 – An example of SHBT result showing the incident, reflected, and transmitted strain signals with time.**

**Table 4 – Properties given by the Split Hopkinson tensile test of multi-strut samples.**

| Sample No. [-] | $\sigma_{UTS}$ [MPa] | $\dot{\varepsilon}_{MAX}$ [s$^{-1}$] | $\varepsilon_{MAX}$ [-] |
|---|---|---|---|
| 1 | 597 | 193 | 0.069 |
| 2 | 573 | 196 | 0.075 |
| 3 | 557 | 292 | 0.168 |
| 4 | 530 | 226 | 0.032 |
| 5 | 522 | 208 | 0.050 |
| Average | 556 | 223 | 0.079 |

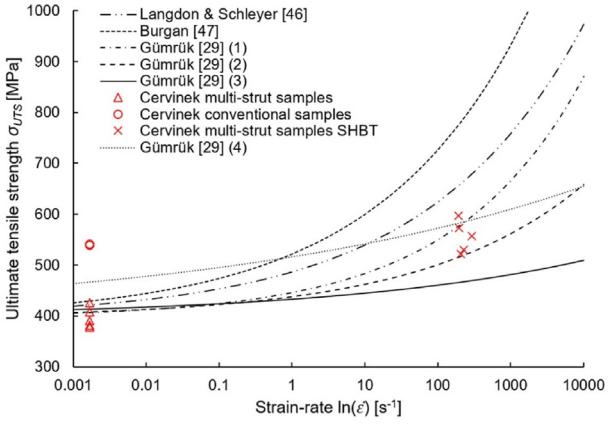


**Fig. 12 – Comparison of strain rate dependent curves of the C-S equation using experimental data.**

conducted with similar samples shows a 28% increase (see Table 2 and Table 4) [26].

In the next step, material data determined in the literature are fitted to the C-S model (Eq. 5). Fig. 12 shows semi-logarithmic scale curves that use parameters found by Langdon and Schleyer [46], Burgan [47], and Gümrük [29], and the quasi-static ultimate tensile strength presented by Cervinek [26] (see Table 1 and Table 2). Differences between curves are visible even for strain rates lower than 100 s$^{-1}$. Based on the resulting stress levels, the curves can be divided into two groups, where two upper curves are given by constants obtained by conventional samples testing [46,47], while other curves are given by constants obtained by thin strut samples testing [29].

The graph shows good agreement between the experimental results of dynamic loading (with a loading rate of approximately 220 s$^{-1}$) and some of the curves based on testing of thin-strut samples. Among them are two considering higher loading rates (Gümrük (2) and Gümrük (4)). As the experimental strain rates are still relatively low, also good agreement can be seen with Gümrük (1).

The experimental results of standardized DIN samples (at a loading rate of approximately $10^{-3}$ s$^{-1}$) are added to the graph to obtain complete information about the correlation between quasi-static and dynamic testing. Their comparison shows a significant difference between the results of thin strut samples and conventional volume samples. This difference has even a greater impact on the ultimate tensile strength than the increased loading rates in the low-velocity testing regime.

The result appoints to the importance of obtaining the mechanical properties of samples designed for a specific configuration, which has been discussed in [4,28,42,56].

Based on the compliance between the suggested curves and the experimental results, the parameters $D$ and $q$ giving curves Gümrük (1,2,4) are used.

### 3.3. *Impact test evaluation*

The data recorded by a high-speed camera and a strain gauge are evaluated to give the force reaction course and the position of the indenter over time. Based on it, the velocity of the structure deformation and indenter deceleration are calculated. An engineering stress value is calculated as a force reaction divided by the initial area of the sample (400 $mm^2$). The strain is defined from the overall deformation of the sample divided by the initial sample height given by 20 mm. The strain rate values vary between 77 $s^{-1}$ and 125 $s^{-1}$ within the tested structures – the highest strain rate is measured for the BCC structure with the lowest stiffness.

Despite the equivalent loading weight, the structures achieve different stress-strain responses due to their internal strut organisation and variable relative density; Fig. 13. The graphs show that the structure deformation starts in an approximately linear manner. After reaching the critical level of stress, initial collapse stress $\sigma_{IC}$ (see Appendix 1), [4,42]), the deformation of the structure starts to gradually turn into a region of progressive collapse. The level of critical stress increases with increasing stiffness in the direction of loading of the structures. The highest values are achieved within the FBCCz lattice structure with an average value of 25.22 MPa.

The region of progressive collapse characteristic of an approximately constant stress level is called the plateau stress area. This behaviour is better applicable within structures without struts that have an axis in the loading direction (see Fig. 13 a), c), and e)). Their collapse is caused by bending the struts rather than buckling failure, which manifests itself by a direct change in stress level [57].

BCC, BCCz, and FCC structures (see Fig. 13 a), b), and c)) with the lowest stiffness are loaded until contact occurred between struts in neighbouring unit cells. The state is called densification [20,58]. It is defined by deformation, at which the energy absorption efficiency is the highest [52]. The ability of the material to absorb energy has its maximum at a specific stress value. The increase in absorbed energy is less than an equivalent increase in stress when the specific value is exceeded. Optimal energy absorption can be judged by efficiency (see Fig. 13) Eq. (8) [2,5,59]:

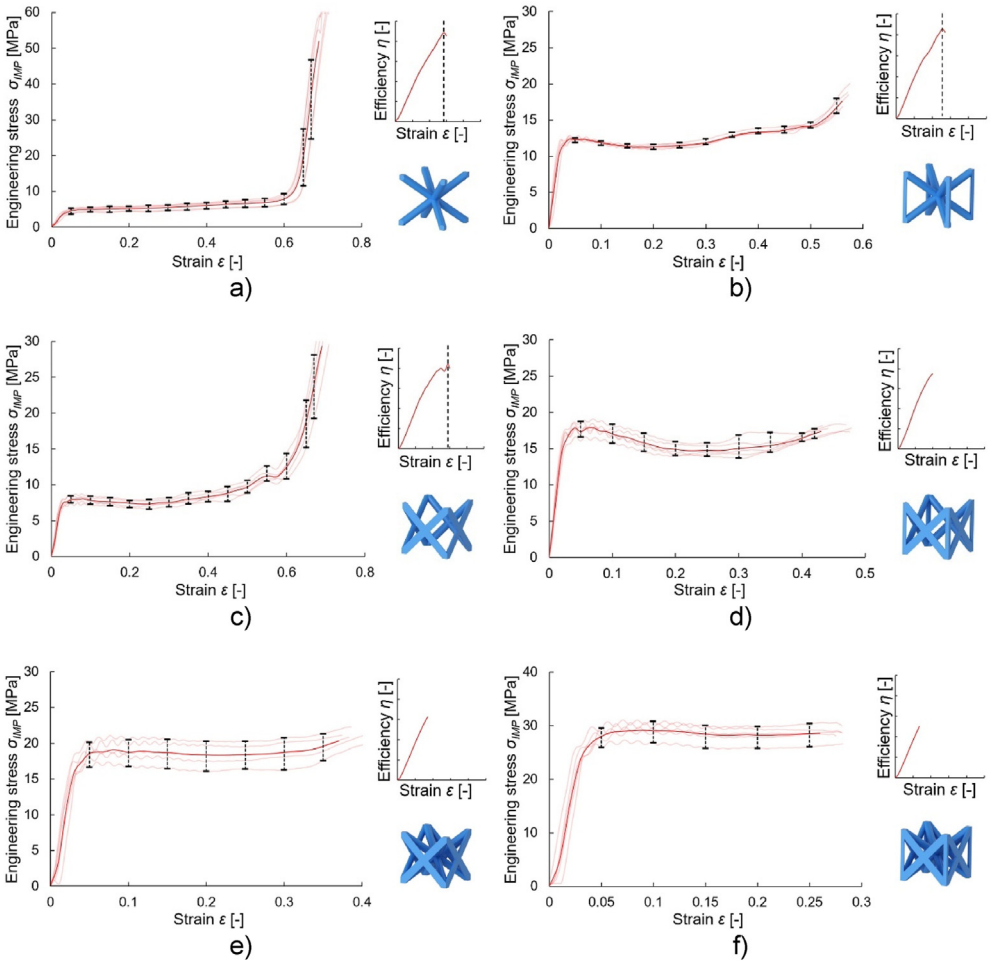


**Fig. 13 – The engineering stress-strain response of a) BCC; b) BCCz; c) FCC; d) FCCz; e) FBCC; f) FBCCz lattice structures.**

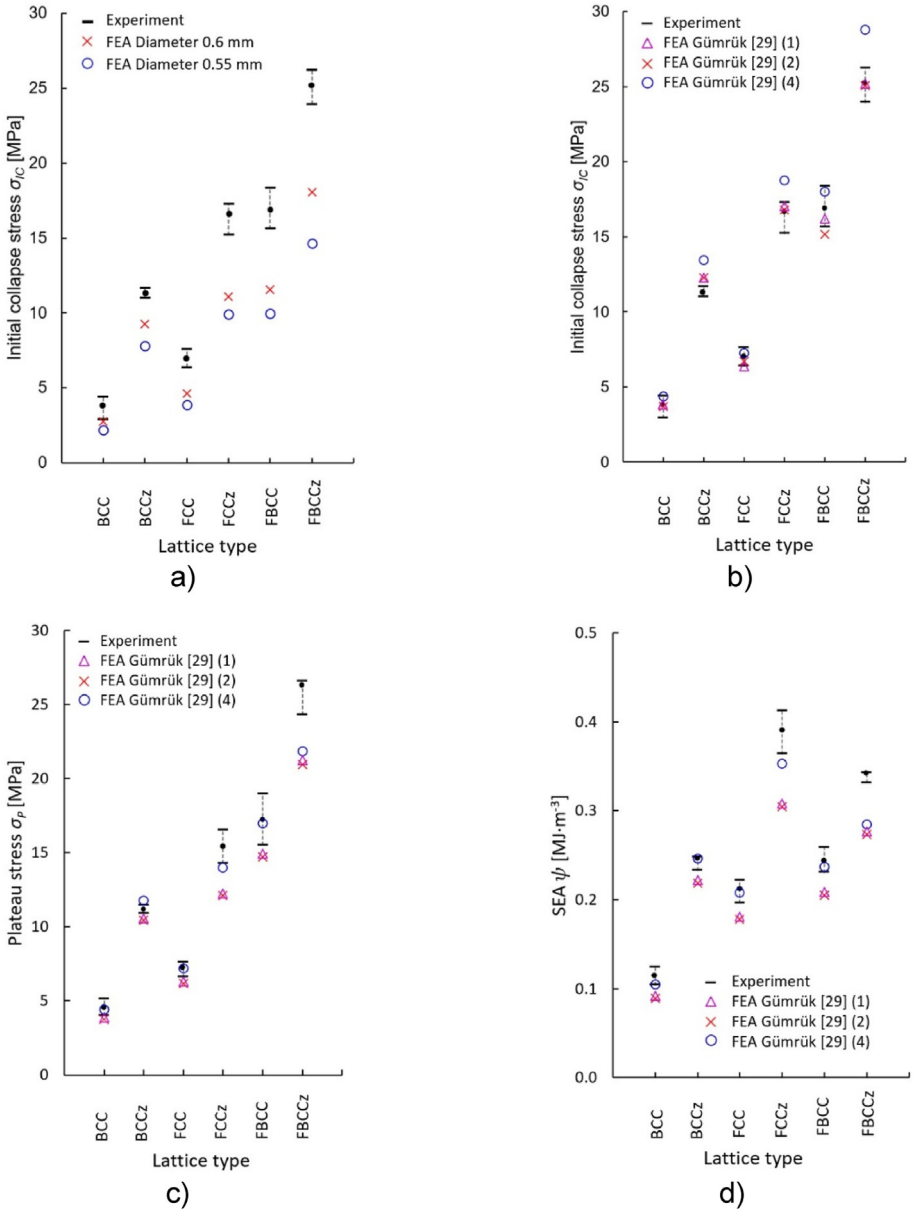


**Fig. 14 – a) Comparison of initial collapse stress for nominal geometry and geometry with corrections; b) initial collapse stress with imperfection and different C-S parameters; c) plateau stress; d) SEA.**

$$\eta(\varepsilon) = \frac{1}{\sigma(\varepsilon)} \int_0^{\varepsilon} \sigma(\varepsilon) d\varepsilon \tag{8}$$

The value at the beginning of densification $\varepsilon_{d0}$ is given at the point, where energy absorption efficiency reaches its maximal value according to Eq. (9), which means:

$$\left.\frac{d\eta(\varepsilon)}{d\varepsilon}\right|_{\varepsilon=\varepsilon_{d0}} = 0 \tag{9}$$

A comparison of stress-strain response and images from the high-speed camera shows that a steep increase of stress occurred early before contact of the struts (see Fig. 13 and Appendix 1, BCC and FCC). It could be caused by the partially melted residual material between the struts, which enhances the stress response during compression loading, while within tension loading does not. The lowest strain achieves the FBCCz structure, which has the highest volume fraction. The graphs in Fig. 13 show an increasing plateau stress level when the maximal strain is decreased.

The amount of energy dissipated can be expressed as the area under engineering stress until a certain amount of deformation is achieved (up to 0.25 strain, which is approximately the strain achieved within structure deformation with

the highest stiffness). Therefore, the stress-strain response could be quantified by volume energy absorption [20] given by Eq. (10) [7]:

$$W_{25\%} = \int_0^{\varepsilon_{MAX}} \sigma(\varepsilon) d\varepsilon \tag{10}$$

In this case $\varepsilon_{MAX}$= 0.25. From energy absorption, the plateau stress can be calculated by Eq. (11) [60]:

$$\sigma_P = \frac{W_{25\%}}{\varepsilon} \tag{11}$$

Comparison of volume energy absorption up to 25% strain could provide only partial information about the overall absorption of the structures. With this indicator, according to expectations, the highest volume energy absorption achieves the structure with the highest stiffness. Therefore, to describe the effectivity of lattice structure configurations, volume energy absorption up to 25% strain has to be normalized by the relative density of the structure – specific energy absorption $\psi$ (SEA). According to this metric, the efficiency of the average SEA values of the structures is compared according to Eq. (12) [7]:

$$\psi = \frac{W_{25\%}}{\rho_s \rho'_{RE}} \tag{12}$$

The FCCz configuration achieves the highest SEA $\psi$ level (see Fig. 14 d)). The second and third most efficient structures are FBCCz and BCCz, respectively. The high SEA values for the mentioned structures are assigned to the efficiency of the struts in the loading direction. The effectivity of similar configurations can be increased if the vertical struts are prevented from early buckling. In contrast, the basic BCC lattice structure usually mentioned in many studies achieved the worst result. At least its deformation behaviour can be described by plateau stress without the stress peak typical for buckling strut failure in the loading direction.

### 3.4. *Comparison of FEA and experiment*

For the preparation of the simulation of the drop-weight test, two main factors are considered. The first of them is the implementation of the geometrical imperfections that occurred during the manufacturing process. Based on the measurement results in Section 3.1.2., the circular cross-section of the struts with a diameter of 0.6 mm is changed to 0.55 mm (for nodes from 0.8 mm to 0.75 mm) with the diameter approximating the actual ones. The second factor is related to the C-S strain rate sensitive constitutive law added to the material model. It is decided to investigate several parameters sets because a good agreement between the values given by the literature and the experiment has been obtained (see Fig. 12). The factors are evaluated in the dynamic simulations to quantify the influence and to compare them with experiments. Both are done separately and together.

#### 3.4.1. *Influence of geometrical imperfection*

Fig. 14 a) shows the differences between the structures with and without geometrical corrections. Differences are expressed in terms of stress at 0.2% strain beyond linear deformation – initial collapse stress $\sigma_{IC}$. The simulation uses an elastic-plastic model of the material described in Table 2. From the comparison, it can be concluded that involving the corrections using decreasing the cross-section of the strut leads to a decrease in the initial collapse stress for all inspected lattice configurations. The cross-section decreases of about 15% causes deviation variation in the range between -12% and -25% of stress. Stress level differences show the significance of the manufacturing deviations inclusion. Therefore, it has to be considered individually for each structure as the influence on each parameter configuration differs.

#### 3.4.2. *Influence of strain rate effects*

In the next step, the elastic-plastic nonlinear behaviour is supplemented with the C-S strain rate dependent law, and the geometrical corrections are included (diameter 0.55 mm). The response of the structures is compared in terms of the most important properties – initial collapse stress $\sigma_{IC}$ (see Fig. 14 b)), plateau stress $\sigma_P$ (see Fig. 14 c)), and SEA $\psi$ (see Fig. 14 d)).

The importance of the strain rate dependent model can be observed when Fig. 14 a) FEA Diameter 0.55 mm and Fig. 14 b) FEA are compared. It can be concluded that even for low loading velocities, the strain rate dependence of SS 316L cannot be neglected. Furthermore, despite the excessively different input parameters between Gümrük (1) and Gümrük (2) (see Table 1), the results in terms of observed quantities are almost the same (see Fig. 14 b)). The significant difference

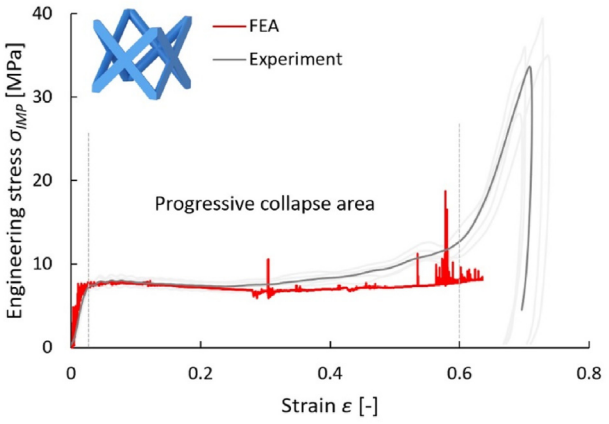


**Fig. 15 – Comparison of FEA with strain rate dependency included and experiment for FCC lattice structure.**

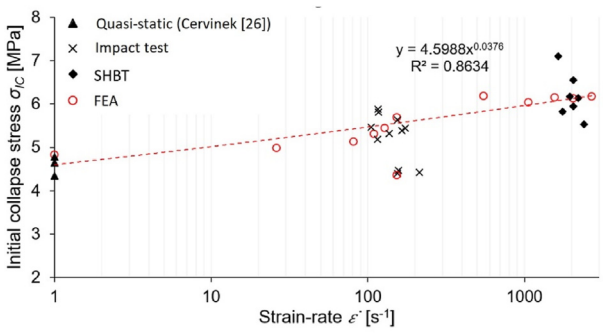


**Fig. 16 – Comparison of strain rates from quasi-static to high velocities.**

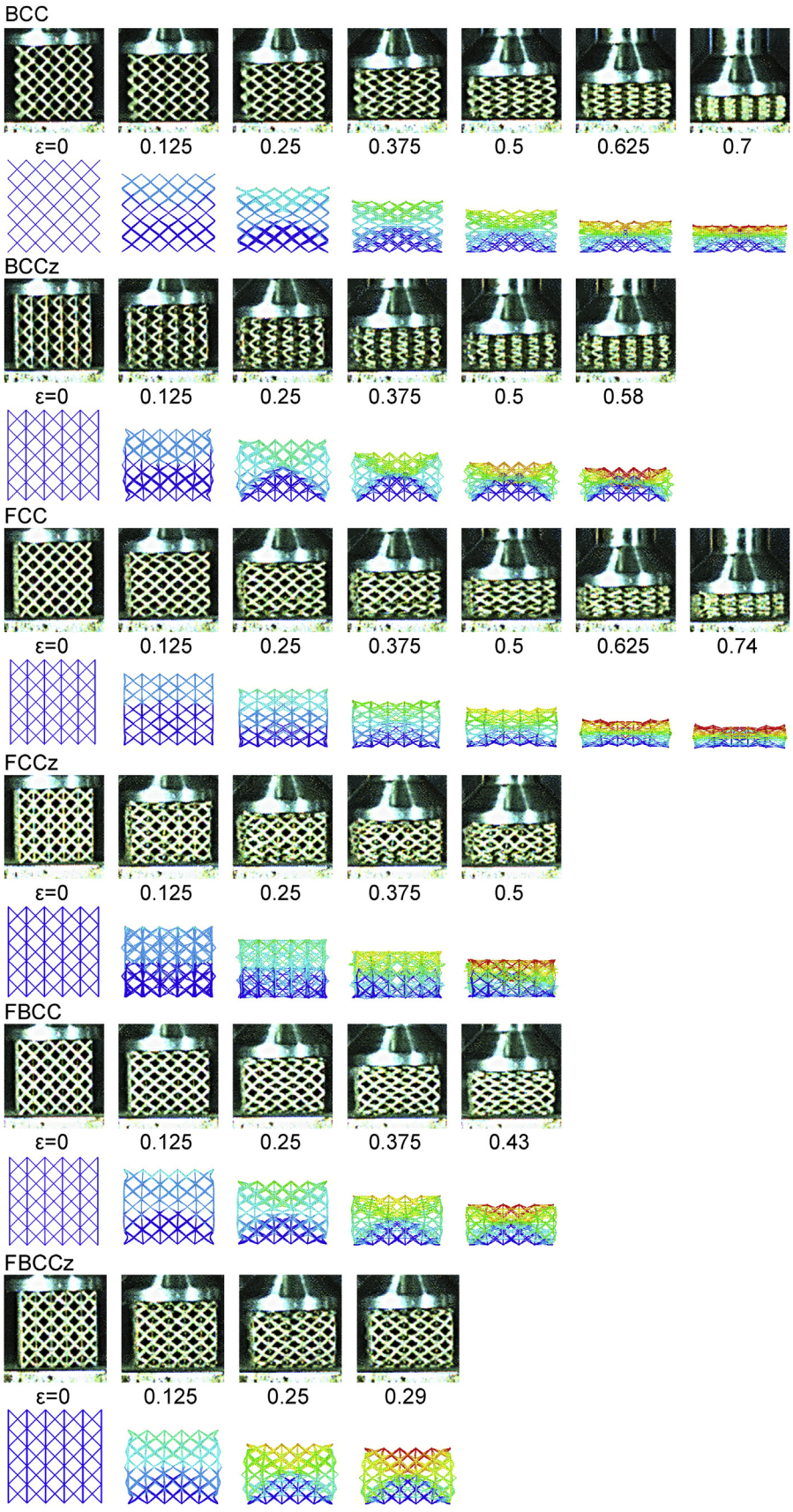


**Fig. 17 – High speed images of deformation pattern of lattice structures and FEA at certain stages.**

occurs when the parameters Gümrük (4) are considered. Based on the initial collapse stress comparison, it can be judged that the simulations with parameters Gümrük (1) and Gümrük (2) match better than the simulation with parameters Gümrük (4). On the contrary, if the plateau stress or SEA is compared, the simulations with Gümrük (4) parameters are closer to the experiment. It is also visible that the initial collapse stress can be predicted using FE analysis efficiently, while the energy absorption is more difficult to predict with increased structure deflection.

The simulations suffer from several simplifications when a large deformation occurs (see Appendix 1). Powder particle aggregations in the nearest area of the lattice nodes are missing in the model, which could lead to the lack of hardening during compression loading. In addition to that, the other major problem is the contact of struts in the beam element model. The true contact in the vicinity of the structural nodes is replaced by spheres of influence with artificially increased stiffness. However, when large deformations occur, the structure is deformed until the beam elements without increased stiffness touch each other. The point where the first contact of the beams occurs could be a limitation, as the only contact of the strut axis is considered in simulations. Therefore, after reaching this critical point, it cannot be expected that the simulation reflects the physically correct behaviour of the structure under loading. In the FEA reaction force response, reaching this level is manifested by excessive noise in the output signal (see Fig. 15).

In the future, the APDL commands can be used to develop a computational approach that improves the contact formulation between the struts in the lattice structure and involves a hardening effect connected with the deformation of the aggregation in the nearest area of the structure nodes.

Finally, the initial collapse stress of the BCC lattice structure deformed at different strain rates (from approximately $10^{-3}$ $s^{-1}$ to $2.2 \cdot 10^{3}$ $s^{-1}$) is assessed. Material parameters were chosen according to the compliance of initial collapse stress with the experiment (Gümrük (1)). At several strain rates, the verification of the computational model is provided by comparison with the experiment (see Fig. 16). The FEA gives an approximately linear dependency which can be expressed by the function $y$. The comparison shows good agreement in the measured points and, therefore, the applicability of the model for different loading rates.

## 4. Conclusion

In the study, a series of computational simulations of the lattice structures dynamic loading are performed using ANSYS Workbench. The model of material is defined as the nonlinear elastic-plastic model of stainless steel 316L made by laser powder bed fusion. The plastic behaviour is defined by the Hollomon equation. The strain rate dependent behaviour given by the C-S constitutive equation is included. A new method is applied to determine the input parameters using experiments with split Hopkinson tensile bars and specially shaped thin-strut samples. The experimental results and the curves obtained from previous studies with thin struts [29] show good agreement. Optical digitization methods are used to reflect the main imperfections of the manufacturing process. Thin struts corresponding to those of the tested structures are scanned. Their cross-sections are approximated by circles to obtain a simplified shape and dimension of the strut for implementation in FEA. The models are created using a Python script, which allows us to define struts with any cross-sectional shapes. Simulations of the lattice structure impact test are performed for all configurations and compared with those of the experiment. The main conclusions of this study can be described in the following points:

1. A good agreement between the tensile tests on multi-strut samples and results given by equations from the literature is found for a low strain rate (approximately $220s^{-1}$).
2. The imperfections of the manufacturing process related to the variation in the strut cross-section cannot be neglected. For the parameters used in this study, the circular diameter reduced by about 15% can be used for all strut orientations. This leads to a deviation in the range between -12% and -25% of the stress compared to the simulation without imperfections.
3. The most efficient structure in terms of SEA is FCCz. The high efficiency is probably caused by struts with an axis in the loading direction, which are also well supported against buckling.
4. The consideration of different C-S input parameters can lead to different stress-strain responses at certain loading stages of the lattice structure. At least for the initial collapse stress, good agreement was achieved for multiple parameters and different structures.
5. The lack of contact between the struts in the beam element model seems to be the main weakness of this approach. In this study, only the contact of the beam axis is defined, which does not reflect reality if a large deflection occurs. This manifests itself in excessive noise in the force reaction response. Therefore, the contact between the beams should be redefined in the future to minimize this effect.

## Declaration of Competing Interest

The authors declare that they have no known competing financial interests or personal relationships that could have appeared to influence the work reported in this paper.

## Acknowledgement

This research was funded by the AKTION – bilateral cooperation in science and education between the Czech Republic and Austria in the tertiary sector, ESIF, EU Operational Programme Research, Development and Education within the research project [Architectured materials designed for additive manufacturing] grant number [CZ.02.1.01/0.0/0.0/16_025/0007304] and faculty specific research project FSI-S-20-6296. The creation of this study was allowed and supervised by the Institute of Lightweight Design and Structural Biomechanics of the TU Wien and the Institute of Machine and Industrial Design of BUT.

## Appendix 1

Based on Figure 17, good compliance in the deformation pattern can be observed at small structure strains. The plastic hinges leading to locally large deformation on the diagonals are visible for the BCC lattice structure in the experiment as well as in the FEA. For the rest of the structures, the local deformation is visible on the surface of the sample. As the strain increases, the structure surfaces of the struts begin to touch, leading to a rapid increase of the acting stress. Unfortunately, this effect cannot be captured with the geometry representation of beam elements in FEA. Therefore, the FEA results should be considered valid until the strut surfaces first contact.

## REFERENCES


[1] Bonatti C, Mohr D. Mechanical performance of additively-manufactured anisotropic and isotropic smooth shell-lattice materials: simulations & experiments. J Mech Phys Solid 2019. https://doi.org/10.1016/j.jmps.2018.08.022.

[2] Xiao L, Song W, Xu X. Experimental study on the collapse behavior of graded Ti-6Al-4V micro-lattice structures printed by selective laser melting under high speed impact. Thin-Walled Struct 2020. https://doi.org/10.1016/j.tws.2020.106970.

[3] Yan C, Hao L, Hussein A, Bubb SL, Young P, Raymont D. Evaluation of light-weight AlSi10Mg periodic cellular lattice structures fabricated via direct metal laser sintering. J Mater Process Technol 2014;214. https://doi.org/10.1016/j.jmatprotec.2013.12.004.

[4] Smith M, Guan Z, Cantwell WJ. Finite element modelling of the compressive response of lattice structures manufactured using the selective laser melting technique. Int J Mech Sci 2013;67:28–41. https://doi.org/10.1016/j.ijmecsci.2012.12.004.

[5] Harris JA, Winter RE, McShane GJ. Impact response of additively manufactured metallic hybrid lattice materials. Int J Impact Eng 2017;104. https://doi.org/10.1016/j.ijimpeng.2017.02.007.

[6] Zhao M, Liu F, Fu G, Zhang D, Zhang T, Zhou H. Improved mechanical properties and energy absorption of BCC lattice structures with triply periodic minimal surfaces fabricated by SLM. Materials 2018;11:2411. https://doi.org/10.3390/ma11122411.

[7] Tancogne-Dejean T, Spierings AB, Mohr D. Additively-manufactured metallic micro-lattice materials for high specific energy absorption under static and dynamic loading. Acta Mater 2016;116:14–28. https://doi.org/10.1016/j.actamat.2016.05.054.

[8] Ozdemir Z, Tyas A, Goodall R, Askes H. Energy absorption in lattice structures in dynamics: nonlinear FE simulations. Int J Impact Eng 2017;102. https://doi.org/10.1016/j.ijimpeng.2016.11.016.

[9] Singh J, Upadhyay A, Sehgal SS. A review on metallic micro lattice. Mater Today Proc 2019. https://doi.org/10.1016/j.matpr.2020.07.375.

[10] Salimon A, Bréchet Y, Ashby MF, Greer AL. Potential applications for steel and titanium metal foams. J Mater Sci 2005. https://doi.org/10.1007/s10853-005-4993-x.

[11] Tancogne-Dejean T, Mohr D. Stiffness and specific energy absorption of additively-manufactured metallic BCC metamaterials composed of tapered beams. Int J Mech Sci 2018. https://doi.org/10.1016/j.ijmecsci.2018.03.027.

[12] Labeas G, Ptochos E. Investigation of sandwich structures with innovative cellular metallic cores under low velocity impact loading. Plast Rubber Compos 2013. https://doi.org/10.1179/1743289811Y.0000000056.

[13] Xiao L, Song W. Additively-manufactured functionally graded Ti-6Al-4V lattice structures with high strength under static and dynamic loading: Experiments. Int J Impact Eng 2018;111:255–72. https://doi.org/10.1016/j.ijimpeng.2017.09.018.

[14] Geng X, Ma L, Liu C, Zhao C, Yue ZF. A FEM study on mechanical behavior of cellular lattice materials based on combined elements. Mater Sci Eng, A 2018. https://doi.org/10.1016/j.msea.2017.11.082.

[15] Labeas GN, Sunaric MM. Investigation on the static response and failure process of metallic open lattice cellular structures. Strain 2010. https://doi.org/10.1111/j.1475-1305.2008.00498.x.

[16] Gümrük R, Mines RAW. Compressive behaviour of stainless steel micro-lattice structures. Int J Mech Sci 2013. https://doi.org/10.1016/j.ijmecsci.2013.01.006.

[17] Qiu C, Yue S, Adkins NJE, Ward M, Hassanin H, Lee PD, et al. Influence of processing conditions on strut structure and compressive properties of cellular lattice structures fabricated by selective laser melting. Mater Sci Eng, A 2015. https://doi.org/10.1016/j.msea.2015.01.031.

[18] Maskery I, Tuck C, Aremu AO, Maskery I, Tuck C, Ashcroft IA, et al. A comparative Finite Element study of cubic unit cells for Selective Laser Melting. Int Solid Free Fabr Symp 2014:1238–49.

[19] Deshpande VS, Fleck NA. Isotropic constitutive models for metallic foams. J Mech Phys Solid 2000. https://doi.org/10.1016/S0022-5096(99)00082-4.

[20] Gibson LJ, Ashby MF. Cellular solids: structure and properties. 2nd ed 2014. https://doi.org/10.1017/CBO9781139878326.

[21] Luxner MH, Stampfl J, Pettermann HE. Finite element modeling concepts and linear analyses of 3D regular open cell structures. J Mater Sci 2005. https://doi.org/10.1007/s10853-005-5020-y.

[22] Yan C, Hao L, Hussein A, Young P, Raymont D. Advanced lightweight 316L stainless steel cellular lattice structures fabricated via selective laser melting. Mater Des 2014. https://doi.org/10.1016/j.matdes.2013.10.027.

[23] Crupi V, Kara E, Epasto G, Guglielmino E, Aykul H. Static behavior of lattice structures produced via direct metal laser sintering technology. Mater Des 2017. https://doi.org/10.1016/j.matdes.2017.09.003.

[24] Hasan R, Mines RAW, Shen E, Tsopanos S, Cantwell WJ, Brooks W, et al. Comparison of the drop weight impact performance of sandwich panels with aluminium honeycomb and titanium alloy micro lattice cores. Appl Mech Mater 2010;24–25:413–8. https://doi.org/10.4028/www.scientific.net/AMM.24-25.413.

[25] Ushijima K, Cantwell WJ, Mines RAW, Tsopanos S, Smith M. An investigation into the compressive properties of stainless steel micro-lattice structures. J Sandw Struct Mater 2011. https://doi.org/10.1177/1099636210380997.

[26] Červinek O, Werner B, Koutný D, Vaverka O, Pantělejev L, Paloušek D. Computational approaches of quasi-static compression loading of SS316L lattice structures made by selective laser melting. Materials 2021. https://doi.org/10.3390/ma14092462.

[27] Buchar J, Voldřich J. Terminální balistika. 1st ed. Brno: Academia; 2003.

[28] Červinek O, Vrána R, Koutný D, Paloušek D. Static and dynamic compression performance of lattice structures made by selective laser melting [n.d].

[29] Gümrük R, Mines RAW, Karadeniz S. Determination of strain rate sensitivity of micro-struts manufactured using the selective laser melting method. J Mater Eng Perform 2018;27:1016–32. https://doi.org/10.1007/s11665-018-3208-y.
[30] Banerjee A, Dhar S, Acharyya S, Datta D, Nayak N. Determination of Johnson cook material and failure model constants and numerical modelling of Charpy impact test of armour steel. Mater Sci Eng, A 2015. https://doi.org/10.1016/j.msea.2015.05.073.
[31] Grytten F, Børvik T, Hopperstad OS, Langseth M. Low velocity perforation of AA5083-H116 aluminium plates. Int J Impact Eng 2009;36:597–610. https://doi.org/10.1016/j.ijimpeng.2008.09.002.
[32] Chen Z, Wang Z, Zhou S, Shao J, Wu X. Novel negative Poisson's ratio lattice structures with enhanced stiffness and energy absorption capacity. Materials 2018;11. https://doi.org/10.3390/ma11071095.
[33] Murugesan M, Jung DW. Johnson cook material and failure model parameters estimation of AISI-1045 medium carbon steel for metal forming applications. Materials 2019. https://doi.org/10.3390/ma12040609.
[34] Ren X, Xiao L, Hao Z. Multi-property cellular material design approach based on the mechanical behaviour analysis of the reinforced lattice structure. Mater Des 2019. https://doi.org/10.1016/j.matdes.2019.107785.
[35] Labeas G, Ptochos E. Homogenization of selective laser melting cellular material for impact performance simulation. Int J Struct Integr 2015;6:439–50. https://doi.org/10.1108/IJSI-10-2014-0059.
[36] Luxner MH, Stampfl J, Pettermann HE. Linear and nonlinear numerical investigations of regular open cell structures. Am Soc Mech Eng Aerosp Div AD 2004. https://doi.org/10.1115/IMECE2004-62545.
[37] Luxner MH, Pettermann HE. Modeling and simulation of highly porous open cell structures: elasto-plasticity and localization versus disorder and defects. IUTAM Bookseries 2009. https://doi.org/10.1007/978-1-4020-9404-0_14.
[38] Pettermann HE, Hüsing J. Modeling and simulation of relaxation in viscoelastic open cell materials and structures. Int J Solid Struct 2012. https://doi.org/10.1016/j.ijsolstr.2012.04.027.
[39] 2020 ERG Aerospace Corp. ERG materials and aerospace n.d. http://ergaerospace.com/technical-data/duocel-foam-energy-absorption/.
[40] Palousek D, Omasta M, Koutny D, Bednar J, Koutecky T, Dokoupil F. Effect of matte coating on 3D optical measurement accuracy. Opt Mater 2015. https://doi.org/10.1016/j.optmat.2014.11.020.
[41] Koutny D, Engineering M, Republic C. Dimensional accuracy of single beams of AlSi10Mg alloy and 316Lstainless steel manufactured by SLM. In: Proc 5th int conf addit technol; 2014.
[42] Tsopanos S, Mines RAW, McKown S, Shen Y, Cantwell WJ, Brooks W, et al. The influence of processing parameters on the mechanical properties of selectively laser melted stainless steel microlattice structures. J Manuf Sci Eng Trans ASME 2010;132. https://doi.org/10.1115/1.4001743. 0410111–04101112.
[43] Vrána R, Cervinek O, Manas P, Koutný D, Paloušek D. Dynamic loading of lattice structure made by selective laser melting-numerical model with substitution of geometrical imperfections. Materials 2018;11. https://doi.org/10.3390/ma11112129.
[44] Nolting AE, Arsenault R, Bolduc M. Increased accuracy of SHPB test apparatus to better evaluate naval steels. Procedia Eng 2011. https://doi.org/10.1016/j.proeng.2011.04.375.
[45] Split Hopkinson pressure bar: design parameters and prediction of the experiment output. Eng Mech 2018;2018. https://doi.org/10.21495/91-8-213.
[46] Langdon GS, Schleyer GK. Unusual strain rate sensitive behaviour of AISI 316L austenitic stainless steel. J Strain Anal Eng Des 2004. https://doi.org/10.1177/030932470403900106.
[47] Burgan B. Elevated temperature and high strain rate properties of offshore steels. 2001.
[48] Banhart J. Manufacture, characterisation and application of cellular metals and metal foams. Prog Mater Sci 2001;46:559–632. https://doi.org/10.1016/S0079-6425(00)00002-5.
[49] Mohmmed R, Zhang F, Sun B, Gu B. Finite element analyses of low-velocity impact damage of foam sandwiched composites with different ply angles face sheets. Mater Des 2013;47:189–99. https://doi.org/10.1016/j.matdes.2012.12.016.
[50] Lei H, Li C, Meng J, Zhou H, Liu Y, Zhang X, et al. Evaluation of compressive properties of SLM-fabricated multi-layer lattice structures by experimental test and μ-CT-based finite element analysis. Mater Des 2019. https://doi.org/10.1016/j.matdes.2019.107685.
[51] Amani Y, Dancette S, Delroisse P, Simar A, Maire E. Compression behavior of lattice structures produced by selective laser melting: X-ray tomography based experimental and finite element approaches. Acta Mater 2018. https://doi.org/10.1016/j.actamat.2018.08.030.
[52] Zhang L, Feih S, Daynes S, Chang S, Wang MY, Wei J, et al. Energy absorption characteristics of metallic triply periodic minimal surface sheet structures under compressive loading. Addit Manuf 2018. https://doi.org/10.1016/j.addma.2018.08.007.
[53] Werner B, Todt M, Pettermann HE. Nonlinear finite element study of beams with elasto-plastic damage behavior in the post-buckling regime. Proc Appl Math Mech 2019;19:2. https://doi.org/10.1002/pamm.201900248.
[54] Lozanovski B, Leary M, Tran P, Shidid D, Qian M, Choong P, et al. Computational modelling of strut defects in SLM manufactured lattice structures. Mater Des 2019. https://doi.org/10.1016/j.matdes.2019.107671.
[55] Xie F, He X, Cao S, Mei M, Qu X. Influence of pore characteristics on microstructure, mechanical properties and corrosion resistance of selective laser sintered porous Ti-Mo alloys for biomedical applications. Electrochim Acta 2013. https://doi.org/10.1016/j.electacta.2013.04.105.
[56] Mines RAW, Tsopanos S, Shen Y, Hasan R, McKown ST. Drop weight impact behaviour of sandwich panels with metallic micro lattice cores. Int J Impact Eng 2013;60:120–32. https://doi.org/10.1016/j.ijimpeng.2013.04.007.
[57] Werner B, Červinek O, Koutný D, Reisinger A, Pettermann HE, Todt M. Numerical and experimental study on the collapse of a triangular cell under compression. Int J Solid Struct 2022. https://doi.org/10.1016/j.ijsolstr.2021.111295.
[58] Choy SY, Sun CN, Leong KF, Wei J. Compressive properties of Ti-6Al-4V lattice structures fabricated by selective laser melting: design, orientation and density. Addit Manuf 2017. https://doi.org/10.1016/j.addma.2017.06.012.
[59] Avalle M, Belingardi G, Montanini R. Characterization of polymeric structural foams under compressive impact loading by means of energy-absorption diagram. Int J Impact Eng 2001. https://doi.org/10.1016/S0734-743X(00)00060-9.
[60] Cao X, Xiao D, Li Y, Wen W, Zhao T, Chen Z, et al. Dynamic compressive behavior of a modified additively manufactured rhombic dodecahedron 316L stainless steel lattice structure. Thin-Walled Struct 2020. https://doi.org/10.1016/j.tws.2019.106586.

# 7 CONCLUSIONS

This thesis focused on the development of the non-linear computational model of lattice structures under different loading velocities with the inclusion of geometrical imperfections. The most important issues were addressed to scientific questions identified based on the review of the literature. To use the lattice structures produced by additive technologies for energy absorption purposes, it was necessary to make a precise estimation of their deformational behavior. Such an estimation required consideration of the specific material properties of the thin struts and geometric deviations.

Unfortunately, current analytical models did not reflect specific features and were designed to estimate the behavior of the structure only for linear elastic deformation. Therefore, it was necessary to use FEA to make a precise prediction. Some of the models developed in previous years already considered the above-mentioned features. But so far, a model that would encounter all of them and furthermore reflect the effects of dynamic loading did not exist. Therefore, this thesis brought a computational strategy that allowed to combine the mentioned features and determine their influence. The model was verified by experiments for different topologies, sizes, and loading velocities.

The first part focused on the determination of the effect of the most significant geometrical imperfections – change in strut cross-sectional shape and area. It was found that the nominal geometry did not fully represent the actual topology of the thin struts. Its use for the creation of geometry models in FEA led to distorted information about the deformation resistance and the deformation pattern. Therefore, the model was supplemented with the measured cross-sectional shape and diameter, which provided enough accurate results. The measured values were not universally applicable; however, a similar approach could be used for different topologies, parent materials or LPBF process parameters. The most important outputs were described as follows:

1. An optical digitization method revealed a ‘water drop’ shape of the cross-section of the strut. The best approximation of the shape was obtained by an ellipse with a minor-to-major axis ratio of 0.71.

2. The elliptic strut cross-section significantly increased the accuracy of the FEA compared to the Gaussian circular cross-section (from 12% to 2% difference).

3. Partially melted powder particles on the strut surface caused a significant increase in structure weight (from 4.72 g to 6.97 g for a nominal strut diameter of 0.8 mm). Including the imperfections changed the weight to a value that corresponded to the measurement (6.94 g).

4. Tensile tests showed the differences in the mechanical properties of the samples with angles of 90° and 45° with respect to the building platform. Samples with 45° orientations had a yield strength about 10% higher, ultimate tensile stress about 20% higher, Young's modulus about 40% higher, and a tangent modulus about 30% lower.

The second part was focused on the correct determination of the input parameters of the non-linear material model that represented the properties of the lattice structure made of SS 316L. It was shown that conventional samples manufactured according to DIN standards were unable to represent properties of thin-strut geometries. Furthermore, it was difficult to determine properties based on a single strut. However, specially shaped samples that combined multiple struts and conventional samples in one multi-strut sample appeared to be suitable for this purpose. Moreover, the definition of the beam element model suffered from several simplifications. To improve its accuracy, the diameter of the strut in the near area of the nodes had to be increased by approximately 0.2 mm and Young's modulus in this area had to be increased 1000 times. The approach had its limitations and did not allow to reflect the behavior of a heavily deflected structure. The main conclusions of this part were described in the following points:

1. The test of specially shaped samples showed good agreement in properties compared to the literature dealing with similar multi-strut samples [19, 27] (Young's modulus in the literature was 97 GPa; determined in the thesis was 94 GPa). Analytical models based on Euler-Bernoulli and Timoshenko beam theory [117] supported the credibility of mechanical properties in the linear-elastic area.

2. The determination of the mechanical properties for very thin struts had limitations. If the diameter of the struts changed a lot ($<\pm 0.3$ mm), then the properties also changed. Therefore, to accurately represent the material properties of different strut diameters, it is required to determine properties for each diameter separately.

3. Geometrical imperfections acquired different significance for different strut diameters. The most significant were for lower strut diameters (about +0.09 mm for a Gaussian circular diameter). The least significant were for larger strut diameters (about +0.04 mm for a Gaussian circular diameter).

4. FE analyses using solid and beam element models predicted the compressive modulus of the lattice structure with similar accuracy if an increase in artificial stiffness in the vicinity of the nodes was used for the beam element model.

5. Including imperfections improved the accuracy of both FEM approaches beyond the yield point. The elliptical cross-section was more beneficial than the Gaussian circular for all diameters (initial collapse stress for the equivalent strut diameter was 81% for the elliptical cross-section, whereas only 70% for the Gaussian circular).

7. The powder particles partially melted on the surface of the structure had an important significance for the transmission of force. The finding was similar to the study by Vrana [118], who determined geometrical imperfections for $AlSi_{10}Mg$ with similar methods. Structures with nominal diameters >1mm have to be investigated in the future to determine the threshold where the influence of imperfections becomes negligible.

The third part focused on the inclusion of an effect that caused a change in the material stress response under dynamic loading. The experimental findings of previous studies focused on dynamic loading of lattice structures were used and combined with the results of the Hopkinson tensile test of multi-strut samples. Based on this combination, the most suitable parameter setup was chosen. The model included the strain hardening represented by Hollomon and the C-S constitutive law, which modified the stress-strain response based on the strain rate. It was possible to use the model for various structure topologies considering the strut diameter similar to those used for multi-strut tensile samples. The biggest disadvantage was a limitation to a certain range of diameters. The main conclusions of this study were described in the following ways:

1. A good agreement of results obtained by the tensile tests of multi-strut samples and equations from the literature was found for a low strain-rate (approximately 220 $s^{-1}$).

2. The imperfections of the manufacturing process related to the variation in the strut cross-section could not be neglected. The Gaussian circular diameter reduced by approximately 15% was used for all strut orientations. It resulted in a deviation in the range between -12% and -25% of the stress compared to the simulation without imperfections.

3. The most efficient structure in terms of SEA was FCCz (average 0.39 $MJ \cdot m^{-3}$). The high efficiency was probably due to struts with an axis in the loading direction, which were also well supported against buckling.

4. The consideration of different C-S input parameters led to different stress-strain responses at certain loading stages of the lattice structure. For the initial collapse stress, good agreement was achieved for all parameters tested and different structures.

5. The lack of contact between the struts in the beam element model appeared to be the main weakness of this approach. Only the contact of the beam axis was defined, which did not reflect reality when a large deflection occurred (up to approx. 0.58 strain). It caused excessive noise in the force reaction response. Therefore, the contact between the beams should be redefined in the future to minimize this effect.

Regarding the tested hypotheses, the obtained results are summarized in the following remarks:

Q1 How do geometric imperfections of the cross-sectional shape and size affect the compression response of the lattice structures with a nominal strut diameter in the range of 0.6-1.2 mm?

Computational analyzes that studied the effects of described imperfections showed a significant impact of their inclusion in the geometry model in the investigated range. Both contributed to an increase in the stiffness of the structure. Without their consideration, the resulting structure properties were underestimated in terms of deformation resistance. The influence of both types of imperfections was observed to decrease with increasing nominal strut diameter. The obtained results were valid only for specific ranges of diameters, material and process parameters set, and could not be universally applied. Furthermore, some configurations tended to only mild non-circularities strut cross-sections. Therefore, it had to be considered whether an elliptical approximation of the strut cross-section was beneficial or if a circular cross-section was representative enough. In any case, reflecting imperfections related to the change in shape and size was beneficial and improved the accuracy of the simulation. **Thus, the first hypothesis was not falsified.**

Q2 How does the non-linear material model based on multi-strut tensile samples with stiffness corrections influence the deformation behavior of the lattice structure with nominal strut diameter in the range of 0.3-1.0 mm made of 316L stainless steel by SLM technology?

The tensile tests of specially shaped multi-strut samples achieved a more accurate resulting properties of lattice structures in comparison to the conventional samples. The non-linear elastic-plastic material model based on these results appeared to sufficiently represent the behavior of the lattice structure for loading beyond the yield point. The disadvantage of this approach was its limitation for a certain range of strut diameters. If the nominal strut diameter of the tensile sample differed significantly from the strut diameter of the lattice structure, then the resulting models suffered from significant inaccuracies. Furthermore, the material model used for the beam element model required additional local corrections in the near vicinity of the nodes. According to the compression test result, the range of material corrections and stiffness adjustments was identified. These corrections appeared to be significant in the area of plastic deformation, where they replaced the lack of beam connectivity. **Thus, the second hypothesis was not falsified.**

Q3 How does the implementation of strain-rate sensitivity into model of material influence the behavior of the 316L stainless steel lattice structure under dynamic compression loading in the range of $10^2$-$10^3$ $s^{-1}$ strain-rate?

It was proved that for the tested range of strain-rates, it was beneficial to include the effect of the sensitivity of the parent material on the strain-rate. Furthermore, the combination with deformation hardening in the form of linear or exponential dependence, appeared to be beneficial for accuracy of the simulation. Without strain-rate dependence, the simulation suffered from the decreased dynamic resistance. The difference was significant even for lower values of strain-rates ($10^2$ $s^{-1}$) as the stainless steel 316L showed a strong dependence on strain-rate sensitivity. **Thus, the third hypothesis was not falsified.**

# 8 LIST OF PUBLICATIONS

## 8.1 Papers published in journals with impact factor

VRÁNA, R.; ČERVINEK, O.; MAŇAS, P.; KOUTNÝ, D.; PALOUŠEK, D. Dynamic Loading of Lattice Structure Made by Selective Laser Melting-Numerical Model with Substitution of Geometrical Imperfections, 2018, vol. 11, no. 11, p. 1-22. ISSN 1996-1944

ČERVINEK, O.; WERNER, B.; KOUTNÝ, D.; VAVERKA, O.; PANTĚLEJEV, L.; PALOUŠEK, D. Computational Approaches of Quasi-Static Compression Loading of SS316L Lattice Structures Made by Selective Laser Melting. Materials, 2021, vol. 14, no. 9, p. 1-24. ISSN: 1996-1944.

WERNER, B.; ČERVINEK, O.; KOUTNÝ, D.; REISINGER, A.; PETTERMANN, H.E.; TODT, M. Numerical and experimental study on the collapse of a triangular cell under. International Journal of Solids and Structures, 2021, vol. 236, no. 76, p. 1-12. ISSN: 0020-7683.

ČERVINEK, O.; PETTERMANN, H.; TODT, M.; KOUTNÝ, D.; VAVERKA, O. Non-linear dynamic finite element analysis of micro-strut lattice structures made by laser powder bed fusion. Journal of Materials Research and Technology, 2022, vol. 18, no. 1-16, p. 3684-3699. ISSN: 2238-7854.

VRÁNA, R.; KOUTECKÝ, T.; ČERVINEK, O.; ZIKMUND, T.; PANTĚLEJEV, L.; KAISER, J.; KOUTNÝ, D. Deviations of the SLM produced Lattice Structures and Their Influence on Mechanical properties. Materials, 2022, vol. 15, no. 9, p. 1-20. ISSN: 1996-1944.

## 8.2 Papers in conference proceedings

VRÁNA, R.; VAVERKA, O.; ČERVINEK, O.; PANTĚLEJEV, L.; HURNÍK, J.; KOUTNÝ, D.; PALOUŠEK, D. Heat Treatment of the SLM Processed Lattice Structure Made of AlSi10Mg and Its Effect on the Impact Energy Absorption

ČERVINEK, O.; VRÁNA, R. KOUTNÝ, D.; PALOUŠEK, D. Static and Dynamic Compression Performance of Lattice Structures Made by Selective Laser Melting.

## 8.3 Other results

functional specimen (RIV-G/B) – Protective element based on energy absorption

# 9 LITERATURE


[1] AHMAD, Zaini. *Impact and Energy Absorption of Empty and Foam-filled Conical Tubes*. 2009.

[2] HUTCHINSON, John W. a Zhenyu XUE. *Metal sandwich plates optimized for pressure impulses*. 2005. ISBN 0020-7403. doi:10.1016/j.ijmecsci.-2004.10.012

[3] DHARMASENA, Kumar P., H. N G WADLEY, Zhenyu XUE a John W. HUTCHINSON. Mechanical response of metallic honeycomb sandwich panel structures to high-intensity dynamic loading. *International Journal of Impact Engineering*. 2008, **35**(9), 1063–1074. ISSN 0734743X. doi:10.1016/j.ijimpeng.2007.06.008

[4] MOHMMED, Ramadan, Azzam AHMED, Mohamed Ahmed ELGALIB a Hashim ALI. Low Velocity Impact Properties of Foam Sandwich Composites : A Brief Review. *International Journal of Engineering Science and Innovative Technology (IJESIT)*. 2014, **3**(2), 579–591.

[5] MOHMMED, Ramadan, Fa ZHANG, Baozhong SUN a Bohong GU. Finite element analyses of low-velocity impact damage of foam sandwiched composites with different ply angles face sheets. *Materials and Design*. 2013, **47**, 189–199. ISSN 18734197. doi:10.1016/j.matdes.2012.12.016

[6] LABEAS, G. N. a M. M. SUNARIC. Investigation on the static response and failure process of metallic open lattice cellular structures. *Strain*. 2010. ISSN 00392103. doi:10.1111/j.1475-1305.2008.00498.x

[7] WANG, Yonghui, Ximei ZHAI, Wenjian YING a Wei WANG. Dynamic crushing response of an energy absorption connector with curved plate and aluminum foam as energy absorber. *International Journal of Impact Engineering*. 2018, **121**, 119–133. ISSN 0734743X. doi:10.1016/j.ijimpeng.2018.07.016

[8] FANG, Dai Ning, Yu Long LI a Han ZHAO. *On the behaviour characterization of metallic cellular materials under impact loading*. 2010. ISBN 0567-7718. doi:10.1007/s10409-010-0392-x

[9] DESHPANDE, V. S. a N. A. FLECK. Isotropic constitutive models for metallic foams. *Journal of the Mechanics and Physics of Solids*. 2000. ISSN 00225096. doi:10.1016/S0022-5096(99)00082-4

[10] DESHPANDE, V. S., M. F. ASHBY a N. A. FLECK. Foam topology: Bending versus stretching dominated architectures. *Acta Materialia*. 2001. ISSN 13596454. doi:10.1016/S1359-6454(00)00379-7

[11] AHMAD, Z. a D. P. THAMBIRATNAM. Crushing response of foam-filled conical tubes under quasi-static axial loading. *Materials and Design*. 2009, **30**(7), 2393–2403. ISSN 02641275. doi:10.1016/j.matdes.2008.10.017

[12] BANHART, J. *Manufacture, characterisation and application of cellular metals and metal foams*. 2001. ISBN 0079-6425. doi:10.1016/S0079-6425(00)00002-5

[13] LABEAS, G a E PTOCHOS. Investigation of sandwich structures with innovative cellular metallic cores under low velocity impact loading. *Plastics, Rubber and Composites*. 2013. ISSN 1465-8011. doi:10.1179/1743289811Y.-0000000056

[14] TANCOGNE-DEJEAN, Thomas, Adriaan B. SPIERINGS a Dirk MOHR. Additively-manufactured metallic micro-lattice materials for high specific energy absorption under static and dynamic loading. *Acta Materialia*. 2016, **116**. ISSN 13596454. doi:10.1016/j.actamat.2016.05.054

[15] *ERG materials & aerospace*. 2019. http://ergaerospace.com/applications/-duocel-foam-energy-absorbers/

[16] 2020 ERG AEROSPACE CORP. *ERG materials and aerospace*. http://ergaerospace .com/technical-data/duocel-foam-energy-absorption/

[17] MINES, R. A.W., S. TSOPANOS, Y. SHEN, R. HASAN a S. T. MCKOWN. Drop weight impact behaviour of sandwich panels with metallic micro lattice cores. *International Journal of Impact Engineering*. 2013, **60**, 120–132. ISSN 0734743X. doi:10.1016/j.ijimpeng.2013.04.007

[18] TANCOGNE-DEJEAN, Thomas a Dirk MOHR. Stiffness and specific energy absorption of additively-manufactured metallic BCC metamaterials composed of tapered beams. *International Journal of Mechanical Sciences*. 2018, **141**, 101–116. ISSN 00207403. doi:10.1016/j.ijmecsci.2018.03.027

[19] GÜMRÜK, Recep, R. A.W. MINES a Sami KARADENIZ. Determination of Strain Rate Sensitivity of Micro-struts Manufactured Using the Selective Laser Melting Method. *Journal of Materials Engineering and Performance*. 2018, **27**(3), 1016–1032. ISSN 15441024. doi:10.1007/s11665-018-3208-y

[20] LABEAS, G. a Evangelos PTOCHOS. Homogenization of selective laser melting cellular material for impact performance simulation. *International Journal of Structural Integrity*. 2015, **6**(4), 439–450. ISSN 17579872. doi:10.1108/IJSI-10-2014-0059

[21] HASAN, Rafidah, Robert A.W. MINES, E. SHEN, S. TSOPANOS, Wesley J. CANTWELL, W. BROOKS a C.J. SUTCLIFFE. Comparison of the Drop Weight Impact Performance of Sandwich Panels with Aluminium Honeycomb and Titanium Alloy Micro Lattice Cores. *Applied Mechanics and Materials*. 2010, **24**–**25**, 413–418. ISSN 1662-7482. doi:10.4028/www.scientific.net/AMM.24-25.413

[22] USHIJIMA, K., W. J. CANTWELL, R. A.W. MINES, S. TSOPANOS a M. SMITH. An investigation into the compressive properties of stainless steel micro-lattice structures. *Journal of Sandwich Structures and Materials*. 2011. ISSN 10996362. doi:10.1177/1099636210380997

[23] XIAO, Lijun a Weidong SONG. Additively-manufactured functionally graded Ti-6Al-4V lattice structures with high strength under static and dynamic loading: Experiments. *International Journal of Impact Engineering*. 2018, **111**, 255–272. ISSN 0734743X. doi:10.1016/j.ijimpeng.2017.09.018

[24] CHEN, Zeyao, Zhe WANG, Shiwei ZHOU, Jianwang SHAO a Xian WU. Novel negative poisson's ratio lattice structures with enhanced stiffness and energy absorption capacity. *Materials*. 2018, **11**(7). ISSN 19961944. doi:10.3390 /ma11071095

[25] RADEK VRANA, ONDREJ VAVERKA, ONDREJ CERVINEK, LIBOR PANTELEJEV, JAKUB HURNIK, DANIEL KOUTNY, David Palousek. Heat Treatment of the SLM Processed Lattice Structure Made of AlSi10Mg and Its Effect on the Impact Energy Absorption. In: *Conference: Euro PM2019 Congress & Exhibition*. 2019, s. 6.

[26] OZDEMIR, Zuhal, Andrew TYAS, Russell GOODALL a Harm ASKES. Energy absorption in lattice structures in dynamics: Nonlinear FE simulations. *International Journal of Impact Engineering*. 2017, **102**. ISSN 0734743X. doi:10.1016 /j.ijimpeng.2016.11.016

[27] GÜMRÜK, R. a R. A W MINES. Compressive behaviour of stainless steel micro-lattice structures. *International Journal of Mechanical Sciences*. 2013. ISSN 00207403. doi:10.1016/j.ijmecsci.2013.01.006

[28] LI, P., Z. WANG, N. PETRINIC a C. R. SIVIOUR. Deformation behaviour of stainless steel microlattice structures by selective laser melting. *Materials Science and Engineering A*. 2014. ISSN 09215093. doi:10.1016/j.msea.2014.07.015

[29] WANG, Bing, Lin-Zhi WU, Li MA a Ji-Cai FENG. Low-velocity impact characteristics and residual tensile strength of carbon fiber composite lattice core sandwich structures. *Composites Part B: Engineering*. 2011, **42**(4), 891–897. ISSN 13598368. doi:10.1016/j.compositesb.2011.01.007

[30] ŽMINDÁK, Milan, Zoran PELAGIĆ, Peter PASTOREK, Martin MOČILAN a Martin VYBOŠŤOK. Finite element modelling of high velocity impact on plate structures. In: *Procedia Engineering*. 2016, s. 162–168. ISSN 18777058. doi:10.1016 /j.proeng.2016.01.191

[31] MASKERY, I., N. T. ABOULKHAIR, A. O. AREMU, C. J. TUCK a I. A. ASHCROFT. Compressive failure modes and energy absorption in additively manufactured double gyroid lattices. *Additive Manufacturing*. 2017, **16**. ISSN 22148604. doi:10.1016/j.addma.2017.04.003

[32] MASKERY, Ian, Alexandra HUSSEY, Ajit PANESAR, Adedeji AREMU, Christopher TUCK, Ian ASHCROFT a Richard HAGUE. An investigation into reinforced and functionally graded lattice structures. *Journal of Cellular Plastics*. 2017. ISSN 15307999. doi:10.1177/0021955X16639035

[33] GRYTTEN, F., T. BØRVIK, O. S. HOPPERSTAD a M. LANGSETH. Low velocity perforation of AA5083-H116 aluminium plates. *International Journal of Impact Engineering*. 2009, **36**(4), 597–610. ISSN 0734743X. doi:10.1016/j.-ijimpeng. 2008.09.002

[34] LUXNER, Mathias H., Juergen STAMPFL a Heinz E. PETTERMANN. Linear and nonlinear numerical investigations of regular open cell structures. In: *American Society of Mechanical Engineers, Aerospace Division (Publication) AD*. 2004. ISSN 07334230. doi:10.1115/IMECE2004-62545

[35] LUXNER, Mathias H., Juergen STAMPFL a Heinz E. PETTERMANN. Finite element modeling concepts and linear analyses of 3D regular open cell structures. In: *Journal of Materials Science*. 2005. ISSN 00222461. doi:10.1007/s-10853-005-5020-y

[36] LUXNER, Mathias H., Alexander WOESZ, Juergen STAMPFL, Peter FRATZL a Heinz E. PETTERMANN. A finite element study on the effects of disorder in cellular structures. *Acta Biomaterialia*. 2009. ISSN 17427061. doi:10.1016/j.-actbio. 2008.07.025

[37] KARAMOOZ RAVARI, M. R., M. KADKHODAEI, M. BADROSSAMAY a R. REZAEI. Numerical investigation on mechanical properties of cellular lattice structures fabricated by fused deposition modeling. *International Journal of Mechanical Sciences*. 2014. ISSN 00207403. doi:10.1016/j.-ijmecsci.2014.08.009

[38] DONG, Guoying a Yaoyao Fiona ZHAO. Numerical and experimental investigation of the joint stiffness in lattice structures fabricated by additive manufacturing. *International Journal of Mechanical Sciences*. 2018. ISSN 00207403. doi:10.1016 /j.ijmecsci.2018.09.014

[39] GIBSON, Lorna J. a Michael F. ASHBY. *Cellular solids: Structure and properties, second edition*. 2014. ISBN 9781139878326. doi:10.1017/CBO-9781139878326

[40] GENG, Xiaoliang, Liyang MA, Chao LIU, Chen ZHAO a Zhu Feng YUE. A FEM study on mechanical behavior of cellular lattice materials based on combined elements. *Materials Science and Engineering A*. 2018. ISSN 09215093. doi:10.1016 /j.msea.2017.11.082

[41] LEI, Hongshuai, Chuanlei LI, Jinxin MENG, Hao ZHOU, Yabo LIU, Xiaoyu ZHANG, Panding WANG a Daining FANG. Evaluation of compressive properties of SLM-fabricated multi-layer lattice structures by experimental test and μ-CT-based finite element analysis. *Materials and Design*. 2019. ISSN 18734197. doi:10.1016 /j.matdes.2019.107685

[42] YAN, Chunze, Liang HAO, Ahmed HUSSEIN, Philippe YOUNG a David RAYMONT. Advanced lightweight 316L stainless steel cellular lattice structures fabricated via selective laser melting. *Materials and Design*. 2014. ISSN 18734197. doi:10.1016/j.matdes.2013.10.027

[43] KOUTNY, Daniel, Radek VRANA a David PALOUSEK. Dimensional accuracy of single beams of AlSi10Mg alloy and 316L stainless steel manufactured by SLM. In: *5th International Conference on Additive Technologies iCAT2014*. 2014. ISBN 978-961-281-579-0.

[44] LIU, Lu, Paul KAMM, Francisco GARCÍA-MORENO, John BANHART a Damiano PASINI. Elastic and failure response of imperfect three-dimensional metallic lattices: the role of geometric defects induced by Selective Laser Melting. *Journal of the Mechanics and Physics of Solids*. 2017. ISSN 00225096. doi:10.1016 /j.jmps.2017.07.003

[45] LIU, Yabo, Zhichao DONG, Jun LIANG a Jingran GE. Determination of the strength of a multilayer BCC lattice structure with face sheets. *International Journal of Mechanical Sciences*. 2019. ISSN 00207403. doi:10.1016/j.-ijmecsci.2019.01.026

[46] SIMULIA, Dassault Systèmes. Abaqus 6.14 / Analysis User's Guide. *ABAQUS 6.14 Analysis User's Guide*. 2014, **I**, 862. ISSN 1098-6596. doi:10.1017/ CBO9781107415324.004

[47] BECKER, Roland a Boris VEXLER. Mesh refinement and numerical sensitivity analysis for parameter calibration of partial differential equations. *Journal of Computational Physics*. 2005. ISSN 10902716. doi:10.1016/j.-jcp.2004.12.018

[48] HALLQUIST, Jo. *LS-DYNA® theory manual*. 2006. ISBN 9254492507.

[49] LOZANOVSKI, Bill, Martin LEARY, Phuong TRAN, Darpan SHIDID, Ma QIAN, Peter CHOONG a Milan BRANDT. Computational modelling of strut defects in SLM manufactured lattice structures. *Materials and Design*. 2019. ISSN 18734197. doi:10.1016/j.matdes.2019.107671

[50] YADROITSEV, I. a I. SMUROV. Selective laser melting technology: From the single laser melted track stability to 3D parts of complex shape. In: *Physics Procedia*. 2010. ISBN 18753892. doi:10.1016/j.phpro.2010.08.083

[51] SMITH, M., Z. GUAN a W. J. CANTWELL. Finite element modelling of the compressive response of lattice structures manufactured using the selective laser melting technique. *International Journal of Mechanical Sciences*. 2013, **67**, 28–41. ISSN 00207403. doi:10.1016/j.ijmecsci.2012.12.004

[52] MINES, Robert A.W., Sozohn TSOPANOS a S.T. MCKOWN. Verification of a Finite Element Simulation of the Progressive Collapse of Micro Lattice Structures. *Applied Mechanics and Materials*. 2011, **70**, 111–116. ISSN 1662-7482. doi:10.4028/www.scientific.net/AMM.70.111

[53] TSOPANOS, S., R. A.W. MINES, S. MCKOWN, Y. SHEN, W. J. CANTWELL, W. BROOKS a C. J. SUTCLIFFE. The influence of processing parameters on the mechanical properties of selectively laser melted stainless steel microlattice structures. *Journal of Manufacturing Science and Engineering, Transactions of the ASME*. 2010, **132**(4), 0410111–04101112. ISSN 10871357. doi:10.1115/1.4001743

[54] CHAWLA, N. a X. DENG. Microstructure and mechanical behavior of porous sintered steels. *Materials Science and Engineering A*. 2005. ISSN 09215093. doi:10.1016/j.msea.2004.08.046

[55] LI, Chuanlei, Hongshuai LEI, Yabo LIU, Xiaoyu ZHANG, Jian XIONG, Hao ZHOU a Daining FANG. Crushing behavior of multi-layer metal lattice panel fabricated by selective laser melting. *International Journal of Mechanical Sciences*. 2018. ISSN 00207403. doi:10.1016/j.ijmecsci.2018.07.029

[56] CHEN, Liming, Jian ZHANG, Bing DU, Hao ZHOU, Houchang LIU, Yongguang GUO, Weiguo LI a Daining FANG. Dynamic crushing behavior and energy absorption of graded lattice cylindrical structure under axial impact load. *Thin-Walled Structures*. 2018, **127**, 333–343. ISSN 02638231. doi:10.1016/j.-tws.2017.10.048

[57] SILVA, Matthew J. a Lorna J. GIBSON. The effects of non-periodic microstructure and defects on the compressive strength of two-dimensional cellular solids. *International Journal of Mechanical Sciences*. 1997. ISSN 00207403. doi:10.1016/s0020-7403(96)00065-3

[58] LI, Xin, Peiwen ZHANG, Zhihua WANG, Guiying WU a Longmao ZHAO. Dynamic behavior of aluminum honeycomb sandwich panels under air blast: Experiment and numerical analysis. *Composite Structures*. 2014, **108**(1), 1001–1008. ISSN 02638223. doi:10.1016/j.compstruct.2013.10.034

[59] MINES, R. A. W., S. MCKOWN, W. CANTWELL, W. BROOKS a C. J. SUTCLIFFE. On the Progressive Collapse of Micro Lattice Structures. In: *Experimental Analysis of Nano and Engineering Materials and Structures*. 2007. doi:10.1007/978-1-4020-6239-1_369

[60] HARRIS, J. A., R. E. WINTER a G. J. MCSHANE. Impact response of additively manufactured metallic hybrid lattice materials. *International Journal of Impact Engineering*. 2017, **104**, 177–191. ISSN 0734743X. doi:10.1016/j.ijimpeng.2017.02.007

[61] J., Hollomon. Properties and structure of steel - tensile deformation. *AIME Trans*. 1945, **162**(268), 90.

[62] P., Ludwik. Elemente der technologischen mechanik. *Julius Springer*. 1909.

[63] E., Voce. A practical strain hardening function. *Metallurgia*. 1955, **91**(219).

[64] LUDWIGSON, D. C. Modified stress-strain relation for FCC metals and alloys. *Metallurgical Transactions*. 1971. ISSN 03602133. doi:10.1007/BF-02813258

[65] AMANI, Yasin, Sylvain DANCETTE, Pauline DELROISSE, Aude SIMAR a Eric MAIRE. Compression behavior of lattice structures produced by selective laser melting: X-ray tomography based experimental and finite element approaches. *Acta Materialia*. 2018. ISSN 13596454. doi:10.1016/j.actamat.2018.08.030

[66] TVERGAARD, V. a A. NEEDLEMAN. Analysis of the cup-cone fracture in a round tensile bar. *Acta Metallurgica*. 1984. ISSN 00016160. doi:10.1016/0001-6160(84)90213-X

[67] CHU, C. C. a A. NEEDLEMAN. Void nucleation effects in biaxially stretched sheets. *Journal of Engineering Materials and Technology, Transactions of the ASME*. 1980. ISSN 15288889. doi:10.1115/1.3224807

[68] *Abaqus Version 6.13 Documentation Collection*. 2013.

[69] ŠLAIS, Miroslav. *Studium vlivu rychlostních a teplotních parametrů na tvařitelnost Ti slitin*. B.m., 2012. Vysoké učení technické v Brně.

[70] WANG, Xuemei a Jun SHI. Validation of Johnson-Cook plasticity and damage model using impact experiment. *International Journal of Impact Engineering*. 2013. ISSN 0734743X. doi:10.1016/j.ijimpeng.2013.04.010

[71] DIETENBERGER, Michael, Murat BUYUK a Cing-Dao(Steve) KAN. Development of a high strain-rate dependent vehicle model. *LS-Dyna Anwenderforum*. 2005.

[72] KADHANE, Somnath a Hemant WARHATKAR. Review of Experimental Techniques used to Study the Mechanical Behaviour of Biological Soft Tissues. In: 2017. doi:10.2991/iccasp-16.2017.44

[73] LANGDON, G. S. a G. K. SCHLEYER. Unusual strain rate sensitive behaviour of AISI 316L austenitic stainless steel. *Journal of Strain Analysis for Engineering Design*. 2004. ISSN 03093247. doi:10.1177/030932470403900106

[74] BURGAN, B. *Elevated temperature and high strain rate properties of offshore steels*. 2001. ISBN 0 7176 2023 9.

[75] NOLTING, A. E., R. ARSENAULT a M. BOLDUC. Increased accuracy of SHPB test apparatus to better evaluate naval steels. In: *Procedia Engineering*. 2011. ISSN 18777058. doi:10.1016/j.proeng.2011.04.375

[76] YOUNG, Kevin. Development of a Tensile Split Hopkinson Pressure Bar Testing Facility. *Eletronic Theses and Dissertations*. 2015.

[77] MINES, R. A.W., S. MCKOWN, S. TSOPANOS, E. SHEN, W. CANTWELL, W. BROOKS a C. SUTCIIFFE. Local effects during indentation of fully supported sandwich panels with micro lattice cores. In: *Applied Mechanics and Materials*. 2008. ISSN 16627482. doi:10.4028/www.scientific.net/AMM.13-14.85

[78] *Data sheet: CTIII-1/4 -5056-0.001N-2.3*. 2012.

[79] RASHED, M. G., Mahmud ASHRAF, R. A.W. MINES a Paul J. HAZELL. Metallic microlattice materials: A current state of the art on manufacturing, mechanical properties and applications. *Materials and Design*. 2016. ISSN 18734197. doi:10.1016/j.matdes.2016.01.146

[80] MCKOWN, S., Y. SHEN, W. K. BROOKES, C. J. SUTCLIFFE, W. J. CANTWELL, G. S. LANGDON, G. N. NURICK a M. D. THEOBALD. The quasi-static and blast loading response of lattice structures. *International Journal of Impact Engineering*. 2008. ISSN 0734743X. doi:10.1016/j.ijimpeng.2007.10.005

[81] ASHBY, MF, A EVANS, NA FLECK, LJ GIBSON, JW HUTCHINSON, HNG WADLEY, a F DELALE,. Metal Foams: A Design Guide. *Applied Mechanics Reviews*. 2001. ISSN 0003-6900. doi:10.1115/1.1421119

[82] WINTER, R. E., M. COTTON, E. J. HARRIS, D. J. CHAPMAN, D. EAKINS a G. MCSHANE. Plate-impact loading of cellular structures formed by selective laser melting. In: *WIT Transactions on the Built Environment*. 2012, s. 145–156. ISBN 17433509. doi:10.2495/SU120131

[83] RADFORD, D. D., G. J. MCSHANE, V. S. DESHPANDE a N. A. FLECK. Dynamic compressive response of stainless-steel square honeycombs. *Journal of Applied Mechanics, Transactions ASME*. 2007. ISSN 00218936. doi:10.1115/1.2424717

[84] CAO, Xiaofei, Dengbao XIAO, Ying LI, Weibin WEN, Tian ZHAO, Zihao CHEN, Yongbo JIANG a Daining FANG. Dynamic compressive behavior of a modified additively manufactured rhombic dodecahedron 316L stainless steel lattice structure. *Thin-Walled Structures*. 2020. ISSN 02638231. doi:10.1016/j.tws.2019.106586

[85] XIAO, Lijun, Weidong SONG a Xiao XU. Experimental study on the collapse behavior of graded Ti-6Al-4V micro-lattice structures printed by selective laser melting under high speed impact. *Thin-Walled Structures*. 2020. ISSN 02638231. doi:10.1016/j.tws.2020.106970

[86] GIBSON, L.J. a M.F. ASHBY. Cellular Solids: Structure & Properties. *Advances in Polymer Technology*. 1989. ISSN 1365-2850.

[87] L. J. GIBSON, M. F. Ashby. Cellular Solids: Structure and Properties, 2d ed. *Cambridge University Press*. 1997.

[88] OZDEMIR, Zuhal, Everth HERNANDEZ-NAVA, Andrew TYAS, James A. WARREN, Stephen D. FAY, Russell GOODALL, Iain TODD a Harm ASKES. Energy absorption in lattice structures in dynamics: Experiments. *International Journal of Impact Engineering*. 2016. ISSN 0734743X. doi:10.1016/j.ijimpeng.2015.10.007

[89] ZHAO, Miao, Fei LIU, Guang FU, David ZHANG, Tao ZHANG a Hailun ZHOU. Improved Mechanical Properties and Energy Absorption of BCC Lattice Structures with Triply Periodic Minimal Surfaces Fabricated by SLM. *Materials*. 2018, **11**(12), 2411. ISSN 1996-1944. doi:10.3390/ma11122411

[90] ZHANG, Lei, Stefanie FEIH, Stephen DAYNES, Shuai CHANG, Michael Yu WANG, Jun WEI a Wen Feng LU. Energy absorption characteristics of metallic triply periodic minimal surface sheet structures under compressive loading. *Additive Manufacturing*. 2018. ISSN 22148604. doi:10.1016/j.addma.2018.08.007

[91] LI, Dawei, Wenhe LIAO, Ning DAI, Guoying DONG, Yunlong TANG a Yi Min XIE. Optimal design and modeling of gyroid-based functionally graded cellular structures for additive manufacturing. *CAD Computer Aided Design*. 2018. ISSN 00104485. doi:10.1016/j.cad.2018.06.003

[92] INTERNATIONAL ORGANIZATION FOR STANDARDIZATION. Mechanical testing of metals – Ductility testing – Compression test for porous and cellular metals. *International Organization for Standardization*. 2011.

[93] LUXNER, Mathias H., Juergen STAMPFL a Heinz E. PETTERMANN. Numerical simulations of 3D open cell structures - influence of structural irregularities on elasto-plasticity and deformation localization. *International Journal of Solids and Structures*. 2007. ISSN 00207683. doi:10.1016/j.ijsolstr.2006.08.039

[94] YAN, Chunze, Liang HAO, Ahmed HUSSEIN, Simon Lawrence BUBB, Philippe YOUNG a David RAYMONT. Evaluation of light-weight AlSi10Mg periodic cellular lattice structures fabricated via direct metal laser sintering. *Journal of Materials Processing Technology*. 2014, **214**(4). ISSN 09240136. doi:10.1016 /j.jmatprotec.2013.12.004

[95] MATACHE, L. C., P. LIXANDRU, T. CHERECHES, A. MAZURU, D. CHERECHES, V. GEANTA, I. VOICULESCU, E. TRANA a A. N. ROTARIU. Determination of material constants for high strain rate constitutive model of high entropy alloys. In: *IOP Conference Series: Materials Science and Engineering*. 2019. ISSN 1757899X. doi:10.1088/1757-899X/591/1/012057

[96] BANERJEE, A., S. DHAR, S. ACHARYYA, D. DATTA a N. NAYAK. Determination of Johnson cook material and failure model constants and numerical modelling of Charpy impact test of armour steel. *Materials Science and Engineering A*. 2015. ISSN 09215093. doi:10.1016/j.msea.2015.05.073

[97] WANG, Yonghui, J. Y.Richard LIEW, Siew Chin LEE a Wei WANG. Experimental and analytical studies of a novel aluminum foam filled energy absorption connector under quasi-static compression loading. *Engineering Structures*. 2017. ISSN 18737323. doi:10.1016/j.engstruct.2016.10.020

[98] ZHANG, Pan, Yuansheng CHENG, Jun LIU, Yong LI, Changzai ZHANG, Hailiang HOU a Chunming WANG. Experimental study on the dynamic response of foam-filled corrugated core sandwich panels subjected to air blast loading. *Composites Part B: Engineering*. 2016, **105**. ISSN 13598368. doi:10.1016/j.compositesb.2016.08.038

[99] MASKERY, I., C. TUCK, A.O. AREMU, I. MASKERY, C. TUCK, I.A. ASHCROFT, R.D. WILDMAN a R.I.M HAGUE. A comparative Finite Element study of cubic unit cells for Selective Laser Melting. *International Solid Freeform Fabrication Symposium2*. 2014, 1238–1249.

[100] VRÁNA RADEK, KOUTNÝ DANIEL, PALOUŠEK DAVID, Zikmund Tomáš. Influence of Selective Laser Melting Process Parameters on Impact Resistance of Lattice Structure made from AlSi10Mg. 2016, 6.

[101] QIU, Chunlei, Sheng YUE, Nicholas J.E. ADKINS, Mark WARD, Hany HASSANIN, Peter D. LEE, Philip J. WITHERS a Moataz M. ATTALLAH. Influence of processing conditions on strut structure and compressive properties of cellular lattice structures fabricated by selective laser melting. *Materials Science and Engineering A*. 2015. ISSN 09215093. doi:10.1016/j.msea.2015.01.031

[102] PYKA, Grzegorz, Greet KERCKHOFS, Ioannis PAPANTONIOU, Mathew SPEIRS, Jan SCHROOTEN a Martine WEVERS. Surface Roughness and Morphology Customization of Additive Manufactured Open Porous Ti6Al4V Structures. 2013, 4737–4757. doi:10.3390/ma6104737

[103] PYKA, Grzegorz, Greet KERCKHOFS, Jan SCHROOTEN a Martine WEVERS. The effect of spatial micro-CT image resolution and surface complexity on the morphological 3D analysis of open porous structures. *Materials Characterization*. 2014, **87**. ISSN 10445803. doi:10.1016/j.matchar.2013.11.004

[104] FÍLA, Tomáš, Petr KOUDELKA, Jan FALTA, Petr ZLÁMAL, Václav RADA, Marcel ADORNA, Stefan BRONDER a Ondřej JIROUŠEK. Dynamic impact testing of cellular solids and lattice structures: Application of two-sided direct impact Hopkinson bar. *International Journal of Impact Engineering*. 2021. ISSN 0734743X. doi:10.1016/j.ijimpeng.2020.103767

[105] VRÁNA, R. *Návrh porézních struktur pro aditivní výrobu technologií selective laser melting*. B.m., 2014. Vysoké učení technické v Brně.

[106] BREMEN, Sebastian, Wilhelm MEINERS a Andrei DIATLOV. Selective Laser Melting A manufacturing technology for the future ? *Laser Technik Journal*. 2012. ISSN 16137728. doi:10.1002/latj.201290018

[107] ČIŽMÁROVÁ, Elena a Jana SOBOTOVÁ. *Nauka o materiálu I. a II.: cvičení*. Praha: České vysoké učení technické, 2014. ISBN 978-80-01-05550-2.

[108] THIJS, Lore, Karolien KEMPEN, Jean Pierre KRUTH a Jan VAN HUMBEECK. Fine-structured aluminium products with controllable texture by selective laser melting of pre-alloyed AlSi10Mg powder. *Acta Materialia*. 2013, **61**(5), 1809–1819. ISSN 13596454. doi:10.1016/j.actamat.2012.11.052

[109] PALOUSEK, David, Milan OMASTA, Daniel KOUTNY, Josef BEDNAR, Tomas KOUTECKY a Filip DOKOUPIL. Effect of matte coating on 3D optical measurement accuracy. *Optical Materials*. 2015. ISSN 09253467. doi:10.1016 /j.optmat.2014.11.020

[110] URBÁNEK, Aleš. *Kontrola součástí pomocí metod reverzního inženýrství: Bakalářská práce*. B.m., 2008. Vysoké učení technické v Brně.

[111] ČERMÁK, Jan. Metody 3D skenování objektů. *B.m.* 2015.

[112] YAHAYA, M. A., D. RUAN, G. LU a M. S. DARGUSCH. Response of aluminium honeycomb sandwich panels subjected to foam projectile impact - An experimental study. *International Journal of Impact Engineering*. 2015, **75**, 100–109. ISSN 0734743X. doi:10.1016/j.ijimpeng.2014.07.019

[113] AHMAD, Z., D. P. THAMBIRATNAM a A. C C TAN. Dynamic energy absorption characteristics of foam-filled conical tubes under oblique impact loading. *International Journal of Impact Engineering*. 2010, **37**(5), 475–488. ISSN 0734743X. doi:10.1016/j.ijimpeng.2009.11.010

[114] VRANA, RADEK, Daniel KOUTNY a David PALOUSEK. IMPACT RESISTANCE OF DIFFERENT TYPES OF LATTICE STRUCTURES MANUFACTURED BY SLM. *MM Science Journal*. 2016, (06), 1579–1585. doi:10.17973/MMSJ.2016_12_2016186

[115] VRANA, R., D. KOUTNY, D. PALOUSEK a T. ZIKMUND. Impact resistance of lattice structure made by selective laser melting from AlSi12 alloy. *MM Science Journal*. 2015, **2015**(DECEMBER), 849–852. ISSN 18050476 18031269. doi:10.17973/MMSJ.2015_12_201547

[116] SHEET, Material Data. Material daten blatt.

[117] YANG, Yunhui, Meijuan SHAN, Libin ZHAO, Dexuan QI a Jianyu ZHANG. Multiple strut-deformation patterns based analytical elastic modulus of sandwich BCC lattices. *Materials and Design*. 2019. ISSN 18734197. doi:10.1016 /j.matdes.2019.107916

[118] VRÁNA, Radek, Daniel KOUTNÝ, David PALOUŠEK, Libor PANTĚLEJEV, Jan JAROŠ, Tomáš ZIKMUND a Jozef KAISER. Selective Laser Melting Strategy for Fabrication of Thin Struts Usable in Lattice Structures. *Materials*. 2018. doi:10.3390 /ma11091763

# LIST OF FIGURES AND TABLES

## 9.1 List of figures

## 9.2 List of tables

# LIST OF ABBREVIATIONS AND SYMBOLS

| | | | |
|---|---|---|---|
| BCC | based cubic centered | BCCz | BCC with struts in z-direction |
| CAD | computer aided design | C-S | Cowper-Symonds |
| DAF | dynamic amplification factor | DIC | digital image correlation |
| DIF | dynamic increase factor | FCC | faced cubic centered |
| FEA | finite element analysis | FEM | finite element method |
| GTN | GursonTvergaardNeedleman | J-C | Johnson-Cook |
| PFCC | FCC with struts in z-direction | SEA | specific energy absorption |
| SEM | scanning electron microscope | SHPB | split Hopkinson pressure bars |
| SIE | specific impact energy | SLA | stereolithography |
| SLM | selective laser melting | SLS | selective laser sintering |
| TPMS | triply periodic minimal surf. | 1-D | one dimensional |
| 3-D | three dimensional | FE | finite element |
| SS | stainless steel | PLA | polylactid acid |
| FDM | fused deposition modeling | MPC | multipoint constraint |
| µ-CT | micro-computed tomography | FCCCz | FCC with struts in z-direction |
| Mat26 | Mat Honeycomb | Mat40 | *Mat_Nonlinear_Orthotropic |
| MAT98 | simplified Johnson-Cook | UTS | ultimate tensile stress |
| SHC | square honeycomb | LWSHC | lattice-walled square honeycomb |
| FLWSHC | fine LWSHC | | |

| | | | |
|---|---|---|---|
| $\sigma_{peak}$ | stress peak | $\sigma_{plateau}$ | uniform plateau stress |
| $\varepsilon_{compact}$ | compaction strain | $E^*$ | modulus of elasticity of structure |
| $E^S$ | parent mat. modulus of elasticity | $x$ | translation in x direction |
| $y$ | translation in y direction | $z$ | translation in z direction |
| $t^*$ | total loading time | $U$ | axial displacement |
| $t$ | actual time | $v$ | velocity of the rigid wall |
| $a$ | radius of major axis | $b$ | radius of minor axis |
| $d_x$ | horiz. disp. of the gravity center | $d_y$ | vertical disp. of the gravity center |
| $x'$ | rotated horizontal axis | $y'$ | rotated vertical axis |
| $E$ | Young's modulus | $\sigma_y$ | yield stress |
| $\varepsilon_p$ | logarithmic deformation | $n_i$ | interpolation fitting exponent |
| $C_i$ | interpolation fitting coefficient | $\sigma_t$ | true plastic |
| $\Phi$ | yield function | $\sigma_{eq}$ | von Mises equivalent stress |
| $\sigma_H$ | hydrostatic stress | $q_i$ | calibrating parameter |

| | | | |
|---|---|---|---|
| $f$ | void volume fraction | $f_0$ | initial volume fraction |
| $\dot{f}_{gr}$ | void growth rate | $\dot{\varepsilon}^{pl}$ | plastic strain-rate tensor |
| $\varepsilon_{eq}^{pl}$ | equivalent plastic strain | $\varepsilon_N$ | mean val. of nucleation dis. |
| $s_N$ | standard dev. of nucleation dis. | $f_N$ | volume fraction of nucleated voids |
| $\sigma_0$ | initial flow stress | $N$ | hardening exponent |
| $G$ | elastic shear modulus | $\sigma_{zz}$ | nominal stress |
| $\varepsilon_z$ | nominal strain | $\sigma$ | stress |
| $\dot{\varepsilon_0}$ | quasi-static strain-rate | $\dot{\varepsilon}$ | dynamic strain-rate |
| $A$ | yield strength | $B$ | hardening modulus |
| $C$ | strain-rate hardening coefficient | $n$ | hardening exponent |
| $m$ | coefficient of thermal softening | $\bar{\sigma}$ | von Mises stress |
| $\bar{\varepsilon}^{pl}$ | equivalent plastic strain | $\dot{\bar{\varepsilon}}^{pl}$ | equivalent plastic strain-rate |
| $T^*$ | homologous temperature | $T$ | material temperature |
| $T_{melt}$ | melting temperature | $T_{room}$ | room temperature |
| $p$ | pressure | $d_i$ | exper. determined constant |
| $\sigma_o'$ | dynamic ultimate tensile stress | $\dot{\varepsilon_p}$ | strain-rate |
| $D$ | material fitting coefficient | $q$ | material fitting exponent |
| $\varepsilon_i$ | incident wave | $\varepsilon_t$ | transmitted wave |
| $\varepsilon_r$ | reflected wave | $A_0$ | cross-section area of the bar |
| $E_0$ | elasticity modulus of the bar | $A$ | cross-section area of the strut |
| $C_0$ | elastic wave velocity | $\rho_0$ | density of the bar |
| $E_B$ | elasticity modulus of the bar | $A_B$ | cross-section area of the bar |
| $F_{input}$ | input force | $F_{output}$ | output force |
| $L_0$ | initial length of the sample | $\Delta L$ | sample deflection |
| $E_{BCC}^*$ | initial stiffness of the BCC lattice | $\rho_s$ | density of the parent material |
| $\rho^*$ | overall density of the structure | $\sigma_{pl,BCC}^*$ | plastic coll. strength of the BCC |
| $d$ | strut diameter | $L$ | strut length |
| $m_b$ | measured sample weight | $\rho_p$ | density of parent material |
| $N$ | length of structure in unit cells | $\bar{\rho}$ | relative density |
| $W$ | structure compression work | $\psi_s$ | parent mat. absorption capacity |
| $\varepsilon_i$ | specific strain | $\sigma_m$ | max. nominal compressive stress |
| $\varepsilon_d$ | maximum strain | $m_{ct}$ | total weight of hybrid absorber |
| $F$ | compressive force | $H$ | height of porous sample |
| $x_y$ | displacement at yield | $x_D$ | densification displacement |
| $x_D'$ | highest energy absorption disp. | $F_{max}$ | maximal force |
| $F_m$ | mean force reaction | $\sigma^*$ | specific strength |
| $\sigma_{pl}^*$ | specific plateau stress | $\sigma_s$ | strength of parent material |
| $R_n$ | strut diameter | α | strut tapering |
| $\sigma_{min}$ | lowest stress value | $\sigma_b$ | initial plastic failure |
| $W_v$ | changes in absorbed energy | $Q_{10}$ | 10% quantile |
| $Q_{50}$ | median | $Q_{90}$ | 90% quantile |
| $Ys$ | Offset yield strength | | |

www.ustavkonstruovani.cz